université PARIS-SACLAY

Fast Atom Diffraction at Crystal Surfaces, the Role of Attractive Forces

Diffraction d'atomes rapides sur des surfaces, le rôle des forces attractives

Thèse de doctorat de l'université Paris-Saclay

École doctorale n° 572, ondes et matière (EDOM)
Spécialité de doctorat : Physique
Graduate School : Physique. Référent : Faculté des sciences d'Orsay

Thèse préparée dans l'unité de recherche : **Institut des Sciences Moléculaires d'Orsay** (Université Paris-Saclay, CNRS), sous la direction de **Philippe RONCIN**, Directeur de recherche

Thèse soutenue à Paris-Saclay, le 8 juillet 2022, par

Peng PAN

Composition du jury

Anne LAFOSSE Professeur, Université Paris-Saclay	Présidente
Salvador MIRET-ARTÉS Professeur, IFF/CSIC (Madrid)	Rapporteur & Examinateur
Thierry ANGOT Professeur, Aix-Marseille Université (Marseille)	Rapporteur & Examinateur
Paola ATKINSON Chargé de recherche, Sorbonne Université (Paris)	Examinatrice
Philippe RONCIN Directeur de Recherche, ISMO/CNRS (Orsay)	Directeur de thèse

THESE DE DOCTORAT

NNT : 2022UPASP065

université PARIS-SACLAY

ÉCOLE DOCTORALE
Ondes et matière
(EDOM)

Titre : Diffraction d'atomes rapides sur des surfaces, le rôle des forces attractives

Mots clés : analyse des surfaces, diffraction inélastique, matériaux 2D, couches minces, epitaxie par jets moléculaires, vibrations thermiques, Facteur de Debye-Waller, physisorption

Résumé : Ce travail est consacré à l'étude de la diffraction d'atomes rapides en incidence rasante (~ 1 °) à la surface des cristaux, une technique découverte à Orsay et baptisée GIFAD. Nous identifions deux composantes dans les images de diffraction des atomes d'énergie proches du keV. L'une est associée à la diffraction élastique et l'autre à la diffraction inélastique où de l'énergie a été échangée avec la surface. Nous avons établi une transformation de coordonnées telle que l'une montre les angles de Bragg de la diffraction et l'autre se projette sur un profil de diffusion polaire sans aucun signe de diffraction. Ce profil s'avère indépendant de l'axe cristallographique sondé. Les composants inélastiques sont bien reproduits par un profil log-normal, permettant une évaluation simple du rapport de diffraction élastique et inélastique connu sous le nom de facteur Debye-Waller. Les forces qui agissent sur le projectile sonde, généralement un atome d'hélium, sont de deux natures, attractives et répulsives. A ce jour, seules les forces repulsives, en l'occurrence la répulsion de Pauli(proportionnelle à la densité électronique en surface) étaient prises en compte. Nous montrons l'importance des forces attractive, de type van der Waals, aussi bien pour la diffraction que pour la diffusion inélastique. Nous proposons le concept de raideur effective du potentiel que nous évaluons par un modèle analytique reposant sur un potentiel de Morse. Le modèle prédit que la largeur log-normal w est régie par la raideur effective, calculée à partir du travail de surface et de la profondeur du puits de physisorption D. Nous utilisons également ce modèle de Morse pour évaluer la dépendance à la température du facteur Debye-Waller entre 130K et 1017 K. Il fournit une mesure de l'amplitude thermique des atomes de surface perpendiculaires à la surface. La plupart des études ont été réalisées à l'aide de sondes à l'hélium et au néon. Nous étendons ces études en utilisant les gaz nobles Ar, Kr et Xe. La diffraction inélastique des atomes rapides peut ainsi être utilisée comme une nouvelle méthode pour mesurer la profondeur des puits de physisorption (forces de van der Waals).

université PARIS-SACLAY

ÉCOLE DOCTORALE
Ondes et matière
(EDOM)

Title : Fast Atom Diffraction at Crystal Surfaces, the Role of Attractive Forces
Keywords : surface analysis, inelastic diffraction, 2D material, ultra thin layers, molecular beam epitaxy, thermal vibration, Debye-Waller factor, physisorption

Abstract : This work is devoted to the study of grazing incidence ($\sim 1\ ^\circ$) fast atom (keV energies) diffraction (GIFAD) at crystal surfaces. We identify two components in the diffraction images. One is associated with elastic diffraction, and the other is inelastic diffraction where energy has been exchanged with the surface. We separate the scattering profile such that diffraction is observed only in one direction while the other does not exhibit any diffraction feature. This polar scattering profile is found to be independent of the probed crystallographic axis. The inelastic components are well-fitted by a log-normal profile, allowing straightforward evaluation of elastic and inelastic diffraction ratio known as the Debye-Waller factor. It's well accepted that the probe atoms are sensitive to the surface electron density, *i.e.*, considering short-range Pauli repulsion and long-range van der Waals forces. We propose a new model taking into account the attractive forces. It is based on the description of the mean planar potential as a Morse potential. The model predicts that the width w is governed by the effective stiffness, depending on the surface work function and physisorption well depth D. We also use this Morse description model to evaluate the temperature dependence of the Debye-Waller factor between 130K and 1017 K. It provides a measure of the thermal amplitude of the surface atoms perpendicular to the surface. Most studies were performed using helium and neon probes. We extend these studies using Ar, Kr, and Xe noble gases. Compared with the previous thesis on the subject, we demonstrate the significant role of the attractive forces. We conclude this work by identifying five different techniques to measure physisorption well-depth with fast atoms diffraction. Some are adapted to light atoms and shallow depth, but others work with heavy atoms and should also allow investigation of the attractive well-depth.

I would like to dedicate this thesis to my loving parents, my grandparents, and my supervisor
...

Acknowledgements

First of all, I would like to express my sincerest gratitude to my supervisor, Philippe Roncin, whose support, encouragement, and guidance from the initial to the final level enabled me to finish my doctoral study. I appreciate all the efforts he has made to teach me the knowledge, in physics and a broad range of other fields all over my doctoral career. His pursuit of excellence, rigorous and pragmatic style has benefited me a lot. It's a great honor for me to work with such an advisor who acts not only like a supervisor but also like a father. I've been invited to visit his home and have meals with his family many times during the difficult time, COVID-19 lockdown, and my beginning time in Paris, make me feel at home.

I want to express my warmest gratitude to Prof. Ximeng CHEN, Prof. Jianxiong SHAO, and Prof. Lin CHEN from Lanzhou University in China, for their guiding me to the particle scattering field, support, and encouragement in my research career. Their support allowed me to study at Lanzhou University, Strasbourg University (IPHC), Aix-Marseilles University (CPPM), and Paris-Saclay University, where I learned about particle detector and calibration knowledge, which helped me in my PhD projects.

I am also grateful to the members of my dissertation committee, Prof. Salvador MIRET-ARTÉS, Prof. Thierry ANGOT, Prof. Anne LAFOSSE, and Prof. Paola ATKINSON. Special thanks to Prof. Miret-artés and Prof. Angot, for their careful reading and valuable comments on my thesis. I appreciate your time and help.

Thanks for the former members of the group: M. Debiossac, P. Rousseau, P. Soulisse, H. Khemliche , A. Momeni. The theory supports from A.G. Borisov and A. Zugarramurdi. Your contributions provide me a shoulder to stand.

It is a great pleasure to thank those in ISMO, who helped me during my graduate study, namely M. Baudier for the CAD, J. Guigand, J.P. Dugal and H. Bauduin for the machining. C. Charrière for the motor-control systems, and S. Lupone for the sample preparation. And thanks to A. Ouvrard, A. Mayne, W.Q. Zheng, L. Guillemont, L. Amiaud, H. Oughaddou, A. Santander-Syro, ... for introducing or training me on their instruments, for the numerous

insightful discussions ...Thanks for Jülich research center hosted me in 50th IFF school on particles (X-ray, neutron, electron) scattering. Prof. Philippe Mendels from LPS teaches me Solid-state physics courses.

I also treasure old and ongoing friendships at Paris-Saclay University: Jingwen, Xue LI, Wei ZHANG, Xiaomin, Miaobo, Mingxiang, NianJheng, Mengli, Xiangmeng, Wenbo, Xiao ZHANG, Bocheng, Hailong, Shengwen, Cong WANG, Xuefeng, Ren Li, Arindam, Abdel, Céline, Delphine, Hamza, Jaafar, Killian, Remi, Samrit, ... And some friends from Paris: Xi CHEN, Weiyi Li, and Wen WEN for fruitful discussion, and they are repeatedly helped me in all kinds of problems which happen to an international student...Thanks to my angel Maria present in my life, who always backed me up.

Finally, this is an occasion to show my deepest love for my dear parents, my grandparents in heaven, their love full of my backpack for adventure in the world, and they backed me up all the time. I would not finish my graduate study without their support and encouragement.

I hope this thesis is not the end of my thinking in the field of particle scattering, especially fast-atom diffraction/scattering academic research.

I take this opportunity to sincerely acknowledge the China Scholarship Council for providing me with financial support for four years in France.

Contents

1 Introduction **1**

1.1 A Brief History of Matter-wave diffraction 1
1.2 Why Surface? 4
1.3 Surface Analytical Techniques 5
1.4 Probing the Surface by Fast-atoms Diffraction 7
1.5 Probing the Lattice Dynamics by Inelastic Fast-atoms Scattering 8
1.6 Specificity of Grazing Incidence Fast-atoms Diffraction 9
1.7 Organization of this Thesis 9

2 Experimental Setup **11**

2.1 Introduction 11
2.2 The Ion Source 12
2.2.1 Filament Ion Source 12
2.2.2 ECR Ions Source 13
2.2.3 The Wien Filter 13
2.3 The Beamline 14
2.3.1 The Charge Exchange Cell 14
2.3.2 The Beam collimation 15
2.3.3 The Pizza Slice. 15
2.4 The UHV Chamber 18
2.4.1 The Manipulator 18
2.4.2 Sample Heating and Cooling System 19
2.5 The Detector System 21
2.5.1 The Phosphor Screen 22
2.5.2 The Lens and Camera 22
2.5.3 The Direct Beam Attenuator 24
2.6 Additional Equipment 24

2.6.1 The Deflectors and Chopping System . . . 24
2.6.2 The Retractable Resistive Anode Detector . . . 25
2.6.3 The Recoil Ion Detectors . . . 25
2.6.4 Direct Recoil Spectroscopy . . . 26
2.6.5 The Sputtering Ion Gun . . . 26
2.6.6 The Co-linear Laser . . . 27
2.6.7 The Webcam and perpendicular laser . . . 28
2.7 Sample Preparation . . . 30
2.8 Atomic Beam Preparation . . . 31

3 Experimental Methods and Data Analysis 33
3.1 Introduction . . . 33
3.2 Scattering Geometry and Diffraction Conditions . . . 33
3.2.1 Primary beam, Laue circle, and incidence plane . . . 35
3.3 Experimental Methods . . . 36
3.3.1 ϕ-can and Atomic Triangulation . . . 37
3.3.2 Polar Angle Scan(θ-can) . . . 38
3.3.3 Atom Beam Energy Scan (E-Scan) . . . 39
3.3.4 Sample Temperature Scan (T-Scan) . . . 40
3.4 Data Treatment and Analysis . . . 41
3.4.1 Background Subtraction . . . 42
3.4.2 Polar-like Transformations . . . 42
3.5 Specific Distributions . . . 43
3.5.1 The Normal (Gaussian) Distribution . . . 43
3.5.2 The Log-normal Distribution . . . 44
3.6 Elastic Diffraction and Inelastic Scattering Patterns . . . 44
3.6.1 Polar Profiles . . . 45
3.6.2 Lateral(Transverse) Profiles . . . 45
3.6.3 Separation into Elastic and Inelastic Scattering . . . 47
3.6.4 Elastic and Inelastic Scattering Width and Intensity . . . 48

4 Elastic Diffraction and Theoretical Description 49
4.1 Overview . . . 49
4.2 Description of Probes: Neutral Atoms . . . 50
4.3 Description of Surface . . . 50
4.3.1 Structure of LiF Crystal . . . 51
4.3.2 Surface Work Function . . . 53

4.4 Theory of Elastic diffraction at Surfaces . . . 53
4.4.1 Axial surface channeling approximation . . . 54
4.4.2 Theoretical methods in elastic diffraction . . . 58
4.4.3 The Hard Corrugated Wall Model . . . 59
4.5 The Atom-Surface Potential Energy Landscape (PEL) . . . 60
4.5.1 Decomposition into Binary Interaction Potentials . . . 61
4.5.2 A Purely Repulsive Single Exponential Model . . . 63
4.5.3 A Bi-exponential Model . . . 66
4.5.4 The Lennard-Jones potential . . . 67
4.5.5 Buckingham Potential . . . 68
4.5.6 Tang-Toennies Potential . . . 69
4.6 The 1D means planar potential V(z) . . . 70
4.6.1 The Morse planar potential . . . 70
4.6.2 Equilibrium Position, well-depth . . . 71
4.6.3 Turning Points and Allowed Regions of Motion . . . 71
4.6.4 The Atom-surface Interaction Forces . . . 72
4.6.5 Beeby Correction in GIFAD . . . 73
4.6.6 Summary of 1D potentials . . . 74
4.7 Summary of elastic diffraction . . . 75

5 Inelastic Diffraction, Models and Challenges 77
5.1 Overview . . . 77
5.2 Lattice Dynamics . . . 79
5.3 The Debye-Waller Factor in TEAS . . . 82
5.4 Classical Motion in an Exponential Potential . . . 84
5.5 Quantum Binary Collision Model (QBCM) . . . 85
5.6 The Modified Debye-Waller factor . . . 86
5.6.1 conclusion . . . 88

6 Experimental Results: Polar Inelastic Profiles in Fast Atom diffraction at Surfaces 91
6.1 GIFAD Polar Inelastic Profiles . . . 91
6.1.1 The Polar Profiles . . . 92
6.1.2 Inelastic diffraction, the surface stiffness Γ . . . 100
6.1.3 Discussion . . . 105
6.1.4 Conclusion . . . 107

7 Experimental Results: Temperature Dependence in Fast-atom Diffraction at Surfaces **109**
7.1 Introduction . . . 109
7.2 Experimental procedure . . . 110
7.3 Results . . . 114
7.3.1 DWF: Sample quality issues . . . 115
7.3.2 DWF: Energy dependence . . . 116
7.3.3 DWF: Temperature dependence . . . 117
7.3.4 The inelastic scattering width w . . . 118
7.4 Discussion . . . 120
7.5 Conclusions . . . 120

8 Experimental Results: Noble Gases Atoms (Ar Kr Xe) as Probes in GIFAD **123**
8.1 Overview . . . 123
8.2 A brief comparison of noble gases . . . 124
8.3 Ar results . . . 125
8.4 Conclusion . . . 127

9 Measuring physisorption well-depth with fast atom scattering **131**
9.1 Overview . . . 131
9.2 Bound states resonances BSR . . . 131
9.3 Beeby correction . . . 132
9.4 Comparing elastic intensities with the exact quantum scattering . . . 133
9.5 Refraction effect . . . 134
9.6 Inelastic scattering width, the effective stiffness . . . 135
9.7 Conclusion . . . 135

10 Outlook and Conclusion **137**
10.1 Outlook . . . 137
10.2 Conclusion . . . 137
10.3 Conclusion in French: . . . 139

Bibliography **141**

Appendix A Surface effective stiffness derivation **155**

Appendix B Wavelength calculation of atom beam **157**

Appendix C Application of the Distribution and Programming **159**
C.0.1 Application of Morse Potential 161
C.0.2 Programming in CodeBlocks 162

Appendix D Jacobian Transformation **165**

Appendix E Temperature Measurements with type N and type K thermocouples **169**
E.0.1 General Description 172

Appendix F Auto-control Camera by Labview **177**

Appendix G CAD design for retractable detector **179**

Chapter 1

Introduction

There's plenty of room at the bottom.

Richard Feynman

1.1 A Brief History of Matter-wave diffraction

Many physical phenomena appear only in classical form because underlying quantization can not be resolved experimentally, and the coherence degree is too small. However, the quantum effect reveals itself as soon as the measurement is accurate enough, in such a way and when the conditions that the coherence is not destroyed. In 1924, de Broglie formulated the de Broglie hypothesis in his PhD thesis[1], claiming that all matter has a wave-like nature, a concept of wave-particle duality. This is a central part of the theory of quantum mechanics. He was awarded the Nobel Prize in Physics in 1929 for his discovery of the wave nature of electrons. Furthermore, his formula was experimentally confirmed by Davisson-Germer[2] and G.P.Thomson[3], and awarded Nobel Prize in Physics in 1937 for their experimental discovery of electrons by crystals. In 1930, the first observation of slow (thermal energy) Helium atoms diffraction experiment was completed by Estermann and Stern on LiF(100) surface[4], and Stern was awarded the Nobel Prize in Physics in 1943 for his contribution to the development of the molecular beam method. In 1945, the first neutron diffraction experiments were performed by Ernest O. Wollen using the Graphite nuclear Reactor at Oak Ridge. In 1946, Clifford Shull joined, and together they established the basic principles of the technique, and applied it successfully to many different materials for structure and magnetic research. While Shull studied "where the atoms are located", and eventually how the magnetic moments are arranged in the solid. Brockhouse observed" how the atoms are

moving" in the solid for the first time. The two pioneers of neutron diffraction and inelastic neutron scattering, Schull and Brockhouse, shared the 1994 Nobel Prize in Physics.

From theory to experiments, these outstanding achievements were first predicted by de Broglie hypothesis, then confirmed experimentally by matter-wave (electrons, neutron, atoms, and molecules) diffraction. Taking advantage of the wave-particle duality of those probe particles, scattering (particle-like), and diffraction (wave-like) experimental methods developed as modern powerful tools, currently used for determining the atomic structure of materials and can also be used for energy and momentum-resolved measurements of dispersion of lattice dynamics. Energy-wavelength relationship of various scattering probe particles shows in Fig. 1.1.

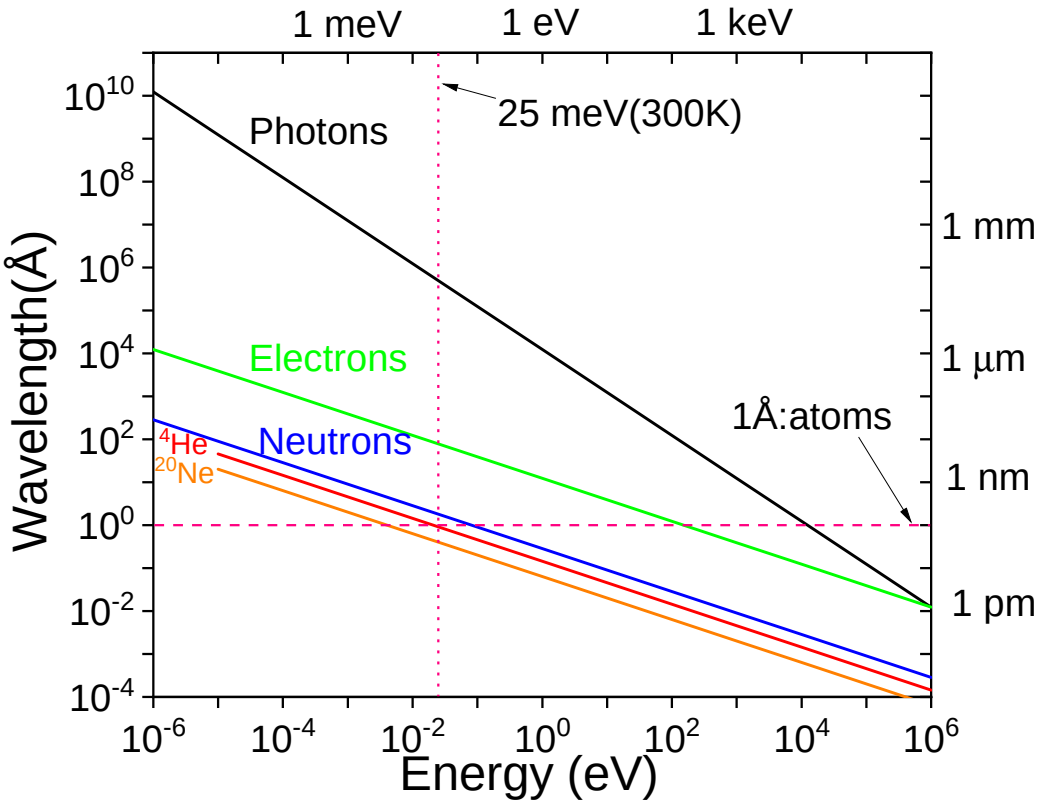

Figure 1.1 The comparison of the wavelength-energy dispersion relation for the different probes- photons, electrons, neutrons, and atoms.

An interesting development of atom diffraction at surfaces was reported in the scattering angular distributions for grazing incidence fast atoms diffraction (GIFAD[5] or FAD[6]) in recent years. Such quantum scattering effects use keV fast-atom as probes observed from insulators and demonstrated for conductors (*e.g.* metals[7, 8]) and semiconductors[9, 10]. which is based on probe atoms and surface atoms interaction.

The interactions of atoms with surfaces play a fundamental role in a wide range of scientific and technological problems for the characterization of materials, thin-film growth inside MBE [10, 11], and catalysis, to analyze and understand their physical and chemical properties at the atomic scale. These can be real space microscopic techniques such as scanning tunneling microscope (STM) and atomic force microscopy (AFM)[12, 13], but also reciprocal space techniques by scattering and diffraction of particles, such as x-ray, neutrons, electrons, and atoms. Since atoms with energies below one eV cannot penetrate below the surface (only sensitive to the topmost layer), no charging effect on the surface (Nondestructive), thermal energies atom scattering (TEAS, also known as HAS[14, 15]) is a valuable tool to investigate surfaces. Grazing Incidence Fast Atom Diffraction (GIFAD) appears as the natural extension of TEAS, just as Reflection High Energy Electron Diffraction (RHEED) does compare with Low Energy Electron Diffraction (LEED), the comparison of key parameters see table.1.1.

Table 1.1 Comparison of LEED, TEAS, and their grazing incidence is equivalent to RHEED and GIFAD. Here E is the total kinetic energy, θ_{in} is the polar incidence angle, and $E_\perp$, $\lambda_\perp$ are the perpendicular energy and wavelength. The table is adapted from Ref.[16]

	Probes	E(eV)	θ_{in} (°)	$E_\perp$(meV)	$\lambda_\perp$ (Å)
GIFAD	He	100-5000	< 1	1-1000	0.1-5
TEAS	He	$10^{-3} - 10^{-1}$	10-170	1-100	0.5-5
RHEED	e^-	$10^4 - 10^5$	< 5.0	$10^3 - 10^5$	0.5-10
LEED	e^-	50-100	90	$5 \times 10^4 - 10^5$	~ 1

However, the diffraction of keV atoms was a surprise due to their typical de Broglie wavelength $\lambda_{dB} = \frac{h}{p}$ (for E=1 keV ^{4}He, λ_{dB}= 0.45 pm), below the picometer scale, three orders of magnitude smaller than crystal lattice parameter (few Å). The kinematic relationships of ^{4}He monochromatic beam linking the de Broglie wavelength λ_i and the corresponding wavevector k_i to its kinetic energy E_i are given by (the detailed calculation shown in Appendix. B),

$$\lambda_i[\text{Å}] = \frac{2\pi}{k_i[\text{Å}]} = \frac{4.5418}{\sqrt{E_i[meV]}} \tag{1.1}$$

It was rapidly understood that the fast motion in the low index orientation, considered here as the x axis, is strongly decoupled from the slow-motion normal to the crystallographic axis in the (y,z) plane. The relevant energy $E_\perp = E\sin^2\theta_{in} \approx E\theta_{in}^2$ is reduced by 3 to 4

orders of magnitude. Therefore, the associated wavelength is $\lambda_\perp = \frac{h}{\sqrt{2mE_\perp}}$ in Eq. 1.1, which is a fraction of Å, and comparable with the crystal lattice length. Those features in the regime of surface channeling lead to quantum effects for scattering the fast-atoms beams on a well-ordered crystal surface[5–7] or thin-film[17]—a new powerful tool for surface science[18, 16].

1.2 Why Surface?

In recent decades, especially after discovering 2D materials, surface science has become an increasingly crucial interdisciplinary field between physics, chemistry, crystallography, biology, and materials science. There are several driving forces for the development of the field, among them molecular beam epitaxy (MBE) technology, surface catalysis, and low-dimensional materials. For instance, in the semiconductor industry, the world's leading semiconductor manufacturing company, TSMC, plans to put a 3 nm semiconductor node into commercial production in 2022. In such a small-scale manufacturing device, so-called nanotechnology is one of the most challenging topics at the forefront of science today. Nanoscience or nanotechnology can be viewed as the evolutionary outgrowth of surface science[19]. Since the concepts were first discussed by Richard Feynman in 1959, in his talk "There's Plenty of Room at the Bottom". Being able to analyze, manufacture, assemble, arrange, and modify matter (such as 2D materials, *i.e.* surface or interface) directly by atoms or molecules at an atomic scale has been a dream of scientists for more than half a century. Nanotechnology depends on surfaces, near-surface, and interface phenomena. In such low dimensions (typically 1D or 2D), it has been discovered that many novel phenomena do not appear in simple bulk materials, such as topological insulators[20], quantum Hall effect[21], and superconductors. The challenge is to understand more details about the surface, and how the atoms and electrons move on the surface. The surface atoms are only visible in surface-sensitive experimental techniques or by studying properties or processes which are determined by surface atoms only. For instance, to study phenomena like adsorption, crystal growth, etching, or catalysis. A microscopic understanding of the growth processes requires investigating the surface process at an atomic level.

The environment of the surface is crucially important. It requires ultra-high vacuum (UHV) conditions to keep the surface clean for long periods, and even at the best vacuum, this does not last forever. From the point of view of the highest quality, under atmospheric pressure and room temperature, the quality of the real surface is far removed from the ideal systems desirable in physical investigations. A freshly prepared material surface usually is very

reactive toward atoms and molecules in the environment. For instance, strong chemisorption and weak physisorption give rise to ad-atoms or ad-layer on the topmost atomic layers of the surface. It's often needed in the early step of the demonstration of a specific physical-electronic or chemical behavior. There is a marked desire to create a perfect surface with as few defects as possible.

1.3 Surface Analytical Techniques

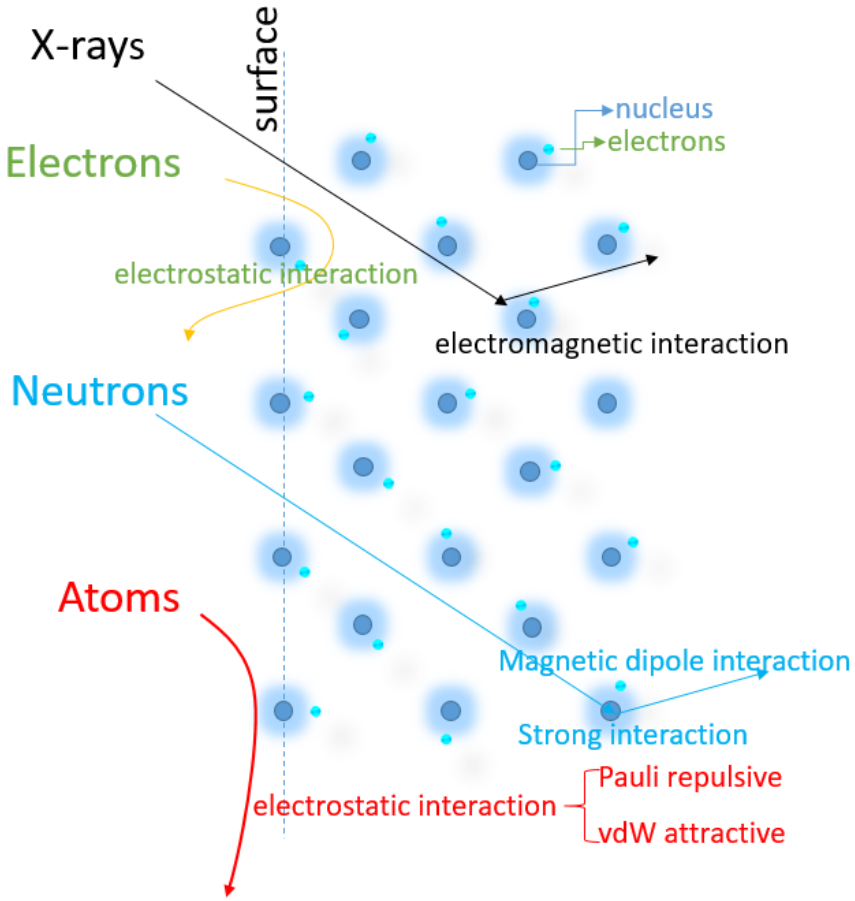

Figure 1.2 Schematic diagram of the scattering process and interaction mechanism of different probes. Note that atoms are mainly scattered at the surface. Figure inspired by a lecture note[22].

There are not too many techniques to rapidly diagnose the surface quality. In the spectrum of surface science analytical tools, methods based on diffraction phenomena for photons, electrons, neutrons, and atoms play an essential role[22], the comparison of the scattering process in Fig. 1.2 and key parameters in Tab. 1.2. since these provide immediate information on the symmetry of periodic structures of surface, adsorbed atoms or molecules, or ultra-thin

Table 1.2 Basic parameters are for the diffraction of x-ray, electrons, neutrons, and atoms.

	E(eV)	θ_{in} (°)	$E_{\perp}$(meV)	$\lambda_{\perp}$ (Å)	Penetration depth(Å)
GIFAD	100-5000	< 1	1-1000	0.1-5	0
TEAS	$10^{-3} - 10^{-1}$	10-170	1-100	0.5-5	0
LEED	50-100	90	$5 \times 10^4 - 10^5$	~ 1	5-10
RHEED	$10^4 - 10^5$	< 5.0	$10^3 - 10^5$	0.5-10	$10^2 - 10^3$
X-ray	10^4	~ 90	$5 \times 10^4 - 10^5$	~ 1	$> 10^4$
Neutron	10^{-2}	~ 90	10	~ 1	$> 10^5$

films. The X-ray diffraction (XRD) technique is one of the most standard methods for determining bulk crystal structure at atomic resolution. Since X-ray weakly interacts with materials, the probe can penetrate deep into the sample, so they are usually not very sensitive to the surface. To investigate the surface, synchrotron radiation facilities are necessary to acquire high-brilliant beam and reliable data. Furthermore, a well-established reciprocal technique for surface and interface investigation is the grazing incidence small-angle X-ray diffraction (GIXD[23] or GISAXS[24]) technique, which limits X-ray penetration into the bulk.

However, among all the surface techniques, those using atoms as probes are the most sensitive to the top-most layer. The technique understudy in this manuscript is probably one of the most sensitive to the presence of surface defects.

It relies on a long history of research on atoms and ions-surface interactions[25, 26], energy scales ranging from the thermal (meV) to high energy (MeV), various phenomena are observed, and many techniques and applications based on atoms or ions are developed. For example, clean the surface by ion sputtering, modify the surface by focused ion beam (FIB)[27], and analyze the composition of solid surfaces and thin films by secondary ion mass spectrometry (SIMS)[28]. Helium ion microscope[29], and ion back-scattering methods such as low and medium-energy ion scattering (LEIS[26, 30, 31] and MEIS, respectively) are also powerful tools for surface structure analysis. The specificity of GIFAD is the use of grazing incidence geometry which provides extremely low effective interaction energies with the surface(Sec. 4.4.1). GIFAD connects atoms scattering with standard optics and

with quantum optics[32]. Using incidences angle close to 1° with sub eV values of $E_{\perp}$ (see Tab. 1.1). GIFAD uses neutral projectiles because the self acceleration towards the surface due to image charge acceleration is usually in the order of 1 eV [33, 34]. The following topics will be discussed in this manuscript: (1) Polar inelastic scattering profile; (2) Lateral elastic diffraction profile; (3) Atomic triangulation; (4) The presence of diffraction and its interpretation; (5) The temperature effect in fast atom diffraction; (6) The methods of measuring the physisorption by fast atom diffraction;

All of these provide quantitative information on the surface quality and topology at the atomic level. Furthermore, it can combine with atoms or ion-TOF SAR or SIMS to provide a chemical analysis.

For all these applications, a better understanding of the fundamental aspects of the atoms-surface scattering is needed. This is in part the purpose of this manuscript which explores the limits of the present understanding in this domain.

This work presents experimental investigations to understand the surface structures and dynamical processes occurring at surfaces. Processes occurring at surfaces can be broken down into two components: elastic and inelastic, which can be extracted from the analysis of these polar inelastic scattering angular distribution and intensity ratio of these profiles. Lateral elastic diffraction angular distribution and intensities of different diffraction orders. Temperature effect on those angular distribution profiles.

1.4 Probing the Surface by Fast-atoms Diffraction

The spatial arrangement of the atoms or nuclei (ion cores) in a condensed matter system is often called its "atomic structure." In general, it is experimentally measured by elastic scattering or diffraction experiments, so-called reciprocal space probe techniques, in which photons, electrons, neutrons, or atoms as probes are scattered, and the nuclei or ion cores in the system act as scattering centers. Although the state-of-art modern real space probe techniques such as scanning tunneling microscopy (STM) and atomic force microscopy (AFM) have allowed direct imaging of the spatial positions of individual atoms. These scattering techniques play a very important role in physics, chemistry, and biology when investigating the matter on the atomic scale. Especially in high-temperature regions where low-temperature probe techniques have limitations, the fast-atoms scattering technique can work at sample temperatures up to 1000 K, and it's only sensitive to the top-most layer, which avoids the contribution from substrate layers. Similar to other diffraction techniques,

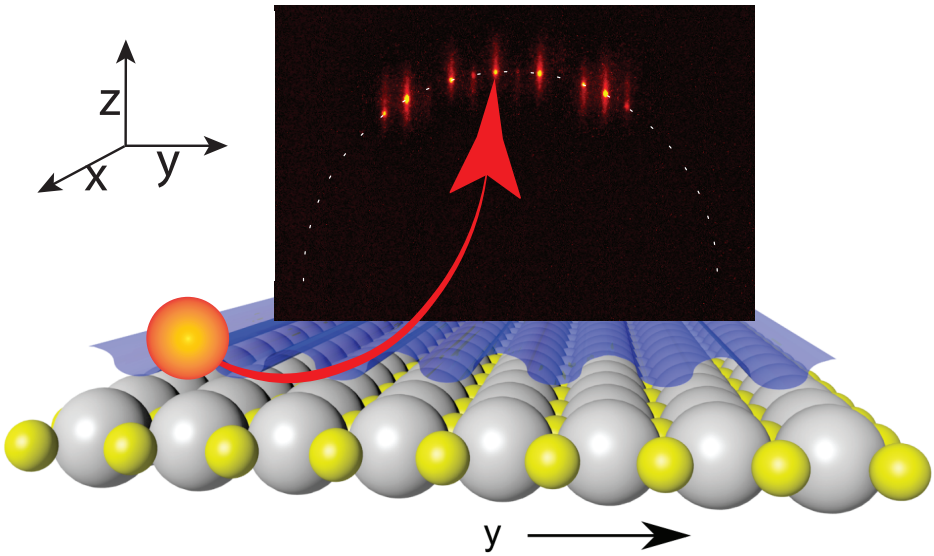

Figure 1.3 Schematic view of a GIFAD experiment. The image in the background is the diffraction pattern of 500 eV helium atoms impinging at $\theta_i = 1.2°$ on a LiF surface along the $\langle 110 \rangle$ direction. The white line where bright spots are observed is the Laue circle corresponding to elastic diffraction along the y direction only, as if the matter-wave of the projectile would diffract on the row of atoms along the probed axis as x as illustrated by the blue surface.

GIFAD can be observed in two different regimes, elastic and inelastic. The elastic regime where no energy is exchanged with the probed system corresponds to a situation where no information is available on the exact trajectory of the projectile. Corresponds to a perfectly periodic surface giving access to the topology of the probed system. In addition, the structure of matter can be simulated and predicted theoretically by advanced computers to solve the Schrödinger equation and find the structure with the lowest total ground-state energy of the electrons and nuclei[35].

1.5 Probing the Lattice Dynamics by Inelastic Fast-atoms Scattering

Inelastic diffraction or scattering measurements include energy transfer between surface and probe atoms, revealing information about the surface dynamics. Thus, probe atoms scatter inelastically by excitation or de-excitation of the surface thermal vibrational. Since grazing incidence is the multi-collision domain, we get the temperature effect of the averaging thermal vibrational amplitudes of surface phonon modes at low temperature (LN2 cooling) T=130K, and high temperature up to 1000K.

1.6 Specificity of Grazing Incidence Fast-atoms Diffraction

Atomic beams have many advantages over conventional surface probes, such as electrons as a surface probe. The key features of GIFAD are the following:

- (1) The probes of GIFAD (He, Ne, Ar, Kr, Xe) are inert and neutral atoms with no charging effect and are non-destructive to the surface;
- (2) GIFAD is one of the most sensitive surface analysis techniques. Since the effective energy $E_\perp$ is adjustable from 1 meV to 10 eV, the classical turning point usually lies at about 1-3 Å above the surface plane;
- (3) The wave-particle duality of probe atoms, which has de Broglie wavelengths λ_{dB} in the *pm* range, but an effective energy $E_\perp$ and effective wavelength $\lambda_\perp = \lambda_{dB} \cdot \sin\theta$ in Å range make diffraction (wave nature) and scattering (particle nature) phenomenons both observable;
- (4) High temperature tolerable for sample surface, up to 1000 K (LiF);
- (5) Detector with high quantum efficiency 50%, all scattered particles recorded on a D∼80 mm MCP, which makes online monitoring thin-film growth possible;
- (6) High spatial accuracy close to pm on the topology of the electronic density;

1.7 Organization of this Thesis

In Chapter 1, We presented the first introduction to the background and basic concepts of matter-wave diffraction and a brief comparison of different diffraction/scattering techniques. Chapter 2 then introduce the UHV setup for grazing incidence fast atom diffraction (GIFAD) experiments. Chapter 3 describes the experimental methods and data analysis methods in GIFAD. Chapter 4 and Chapter 5 are devoted to the theoretical background for the fast-atoms diffraction technique. The features of probe atoms and surfaces are described separately. Chapter 6 presents the experimental results for inelastic scattering angular distribution along the z-axis (polar profiles), mainly Helium atom scattering at LiF single crystal. And in chapter 7, temperature dependence results of fast atoms diffraction at LiF crystal surface are presented. Chapter 8 summarizes some results from heavier elements as probes (Ar Kr Xe), and Chapter 9 summarizes how to measure physisorption well-depth with fast atom scattering. Finally, chapter 10 will present this thesis conclusion and an outlook of possible future work related to my studies.

Chapter 2

Experimental Setup

2.1 Introduction

This chapter introduces a UHV setup for grazing incidence fast atom diffraction (GIFAD) experiments[36]. The overall geometry is simply a source of fast atoms facing an imaging detector, just as for reflection high energy electron diffraction (RHEED) experiments. Several instrumental developments are described making GIFAD operation more efficient and straightforward.

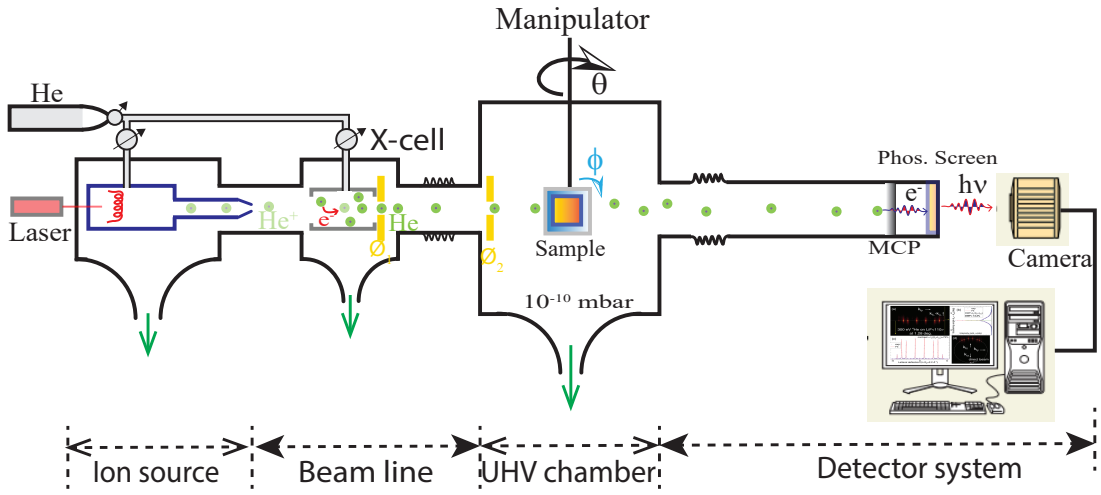

Figure 2.1 The schematic of the GIFAD setup contains four main sections, *i.e.*, ion source, beamline, UHV chamber, and detector system.

Discovered independently in Orsay[5] and Berlin[6], grazing incidence fast atom diffraction has developed as a powerful analytic tool in surface science (see *e.g.* ref.[18, 37] for a review). The general GIFAD setup in Fig. 2.1 consists of four sections:

- (I) An ion source to generate ion beam;
- (II) Beamline combined with a neutralization or charge exchange cell (X-cell) and collimated by two slits or diaphragms to limit beam divergence;
- (III) A 5D (X, Y, Z, θ, ϕ) adjustable manipulator holding the sample in the UHV chamber;
- (IV) Imaging detector system, with a combination of MCP, phosphor screen, and CMOS/CCD camera.

2.2 The Ion Source

As detailed below, GIFAD requires an atom beam injected through small diaphragms with a reduced divergence to guarantee the resolution. In other words, the brightness is most important and, *in fine*, requires a limited energy dispersion. The latter is limited by the extraction field's ionization mechanism, geometry, and intensity. The maximum current is usually expressed in μA corresponding to $\sim 5 \times 10^{12}$ ions per second, while only a few 10^3 - 10^4 atoms per second will be needed, but having the best possible properties.

2.2.1 Filament Ion Source

Hot filament ion sources have the reputation of providing bright ion beams in the keV energy range, as required for spatially resolved secondary ion mass spectroscopy (SIMS) or depth profiling [38] applications.

We use the EX05 model ion source from VG Ortec with a differential pumping port allowing a beamline vacuum of better than 5×10^{-7} mbar. This compact ion source provides a high flux, small spot beam of noble gas ions at energies up to 5 keV. This electron impact ion source is equipped with two tungsten filaments suitable for use with high purity noble gases. Gas is supplied from high pressure (< 1 atm.) supply source to the ionization region through the gas inlet leak valve. Only one filament is in use at a time. Selecting the second filament is accomplished by a single switch button.

The ion source power supply controls the emission current up to 10 mA, by controlling the current through the filament up to 2 A. Helium, or another noble gas, is injected into the ionization region where the electrons impact and ionize a part of the gas atoms. An electrode at the exit from the ionization region and co-axial with it is held at a negative potential with respect to the grid. This electrode is the extractor and accelerates the ions out of the ionization region and into the remaining part of the ion lens section. The EX05 is a two-lens condenser and focus design by changing the potential on the lens to control the beam current.

2.2.2 ECR Ions Source

Electron cyclotron ion sources (ECR) use a magnetic structure and microwave to heat a plasma. Polygon Physics TES-35 is a compact, lightweight, high-performance ECR ion source designed for surface science and processing based on ions, atoms, electrons, or plasma in a UHV environment. The advantage of the ECR ion source is that it has no fragile filament. It can ionize not only noble gases like He, Ne, Ar, Kr, Xe, but also reactive gases like O_2, N_2, H_2, etc. The core element of TES is a microwave discharge system that operates at ultra-low power and is as small as a thumb. The extraction system connected to the cavity determines the nature of the particles that leave the source. For a given aperture size, the particle flow rate can be varied over a wide range by tuning the gas flow rate and the applied microwave power. In the case of ions or electrons, the beam current can also be tuned by the strength of the extraction field.

2.2.3 The Wien Filter

A Wien filter is a device consisting of orthogonal electric and magnetic fields such that particles with the correct speed will be unaffected and pass it. In contrast, other charged particles will be deflected. The charged particles from the ion source pass its electric field and will feel a force proportional to the charge and field strength such that $\vec{F} = q\vec{E}$. Similarly, the particles moving in a magnetic field will feel a force, $\vec{F} = q\vec{v} \times \vec{B}$, proportional to the velocity and charge of the particle. To select charged particles with only velocity $\vec{v}$ through the Wien filter, setting the electric field $(\vec{E})$ and magnetic field $(\vec{B})$ force to equal magnitude in opposite directions it can be shown that $v = \frac{E}{B}$.We measured the magnetic field using a gauss meter between the North and south poles and got the magnetic field strength B=0.675kG(kilo-Gauss) or 0.0675 T. We used a commercial Wien filter from non-sequitur-technologies where the permanent magnet is placed outside a vacuum and can be removed for baking purposes.

A mass filter is mandatory when operating the ECR ion source with molecular gas such as H_2 to produce H^+ or H_2^+ ions but we did not use it when working with high purity noble gas with the hot filament ion sources. It is important to misalign the ion source so that neutral atoms produced at the extraction level and having different energy do not contribute.

2.3 The Beamline

2.3.1 The Charge Exchange Cell

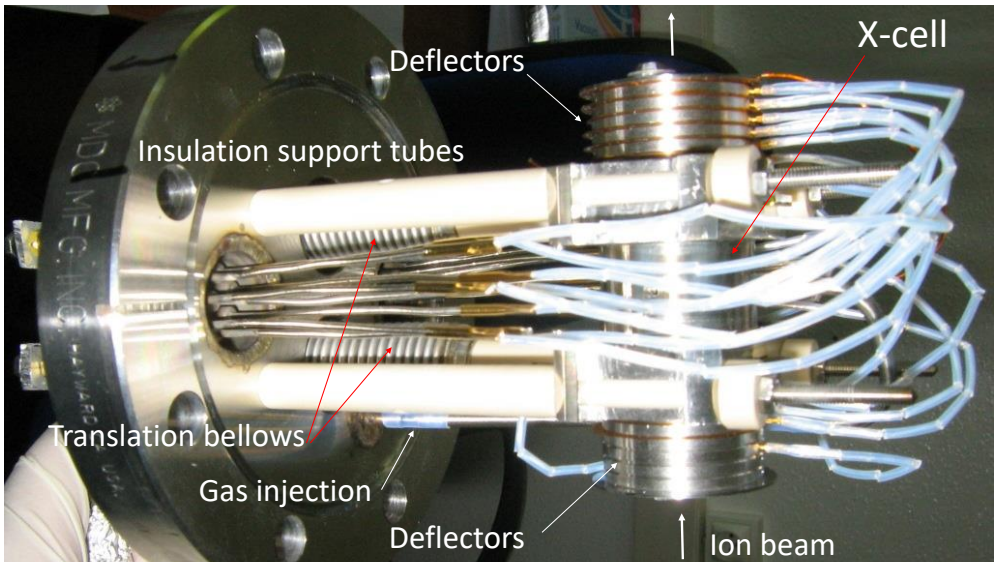

Figure 2.2 Photograph of the charge exchange cell. The cell is in the center, it is preceded by sets of deflectors to optimize the beam direction. It is also followed by another set of deflectors to remove the ionic part of the beam or to pulse it if desired.

The charge exchange cell in Fig. 2.2 is a $l = 2$ cm long tube with entrance and exit holes designed, so that the internal pressure can be adjusted in the 10^{-3} mbar range without a dramatic increase in the background pressure. The internal pressure is usually calculated so that single collisions dominate, *i.e.*, the collision probability P=$\sigma nL \approx 0.1$, where σ is the charge exchange cross-section for the ion of the beam to capture an electron from the target gas of the cell. For resonant neutralisation of 1 keV He^+ ions on helium, a total cross section $\sigma \approx 10^{-15}$ cm^2 was measured [39]. so that the calculated pressure should be such that $n \approx 0.5 \times 10^{14}$ particles per cm^3, *i.e.* a pressure inside the cell around 0.5×10^3 mbar. The beam's actual fraction of neutral helium can be lower due to angular scattering during the collision. At 1 keV, it typically amounts to 0.1 ° [39]. To limit the amount of gas to be pumped, the entrance and exit of the cell are collimated by two sets of diaphragms placed on

a linear translation. The entrance diaphragm $\oslash_0$ is still large enough to allow most of the ion beam into the cell, but the second one can be much smaller as it is used as $\oslash_1$, the first of the two divergence limiting diaphragms.

2.3.2 The Beam collimation

The Cell Diaphragm System

a) Pizza slice

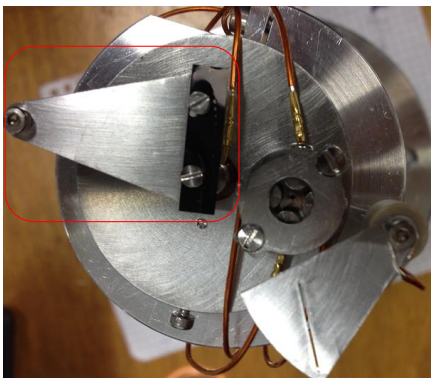

b) Dimension

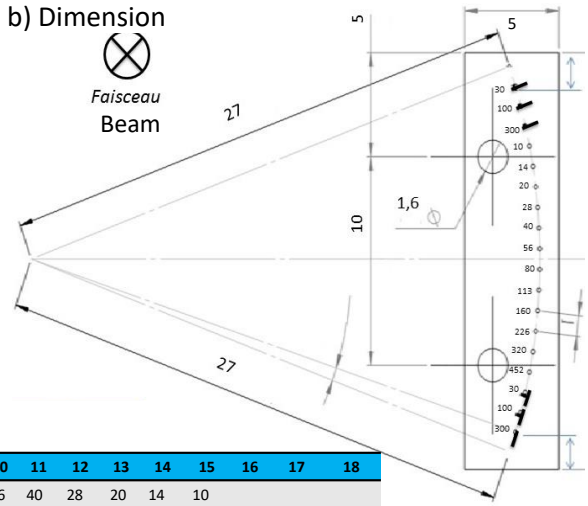

c) Aperture size

size #	1	2	3	4	5	6	7	8	9	10	11	12	13	14	15	16	17	18
D(μm)				452	320	226	160	113	80	56	40	28	20	14	10			
H(μm)	400	400	400													30	100	300
V(μm)	300	100	30													400	400	400

Figure 2.3 a) The pizza slice contains 18 different slits installed between the beamline and UHV chamber. b) Dimension of pizza slice and positions of those 18 slits with size list in c).

Compared with charged particles and photon beams, atomic beams usually can not be focused or deflected by lenses or deflectors. The atom beam diverges radially outward from an ion source point, and its solid angle is determined only by either the effective area of the detector or the collimator geometry. The beamline collimates the atomic beam before it is used in the UHV chamber. This is achieved by adjusting 3 collimators step by step, more details in Fig. 2.1, with two collimators located inside the charge exchange cell. Before interacting with the surface in the UHV chamber, the atomic beam passes through the first diaphragm $\oslash_0$, enters into the neutralization cell, then leaves from diaphragms $\oslash_1$. Finally, inject into the UHV chamber by diaphragm $\oslash_2$ in pizza slice (Fig. 2.3). It will be introduced later.

2.3.3 The Pizza Slice.

The atom beam is injected into the UHV chamber via diaphragm ($\oslash_2$). We have 18 different sizes and shapes of slits on $\oslash_2$. In GIFAD experiments, we will be able to adjust beam size

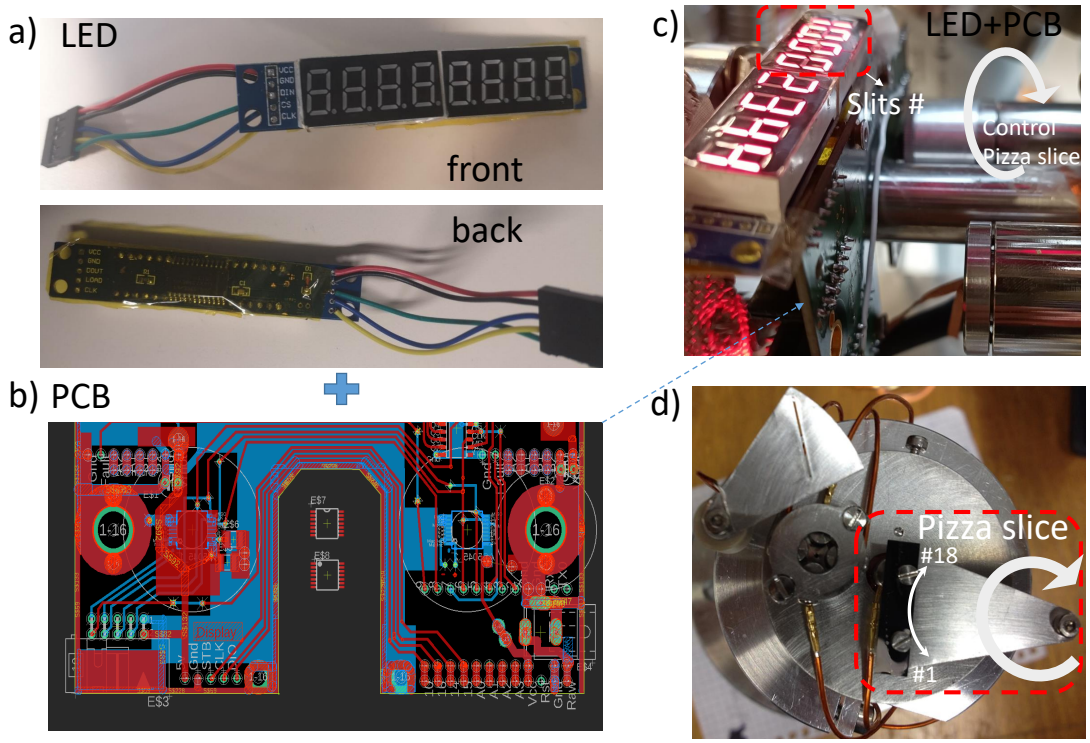

Figure 2.4 a) A LEDkey after wiring. b) PCB with an AS5140 contact-less magnetic sensor to read the portions of the slits. c) LED+PCB assembled in GIFAD setup to control diaphragm ($\oslash_2$), Here we read a number 10.00 | 2348, which means we using hole #10($\oslash_2$=113μm), the other digits provide higher accuracy to have better control. d) Pizza slice installed as the diaphragm $\oslash_2$.

and intensity via the different sizes of slits. It depends on the experimental requirement, such as resolution or time consumption.

In Fig. 2.4, we show a homemade slits number readout system. We use an AS5140 contact-less magnetic sensor to read the absolute angular position of the DN10 miniature rotary feed-trough. The position is read by an Arduino-nano and displayed on a LED display, in units of the regular hole. The pattern shape shown in Fig. 2.3 b), is engraved by electro-erosion on a thin nickel plate having the shape of a pizza slice. Without this display, it would be almost impossible to position a given hole precisely in the center of the beam where the rotation degree between two slits is only $\sim 2.7°$.

We use the co-linear laser (detailed in Sec. 2.6.6) as a light source to calibrate those apertures' diameter D and detector resolution through the different diameters of circle-apertures in Fig. 2.5 and rectangle slits in Fig. 2.7. Airy disk's width and diameter circle-apertures have a simple relationship, the comparison of experimental results and model shown in Fig. 2.6.

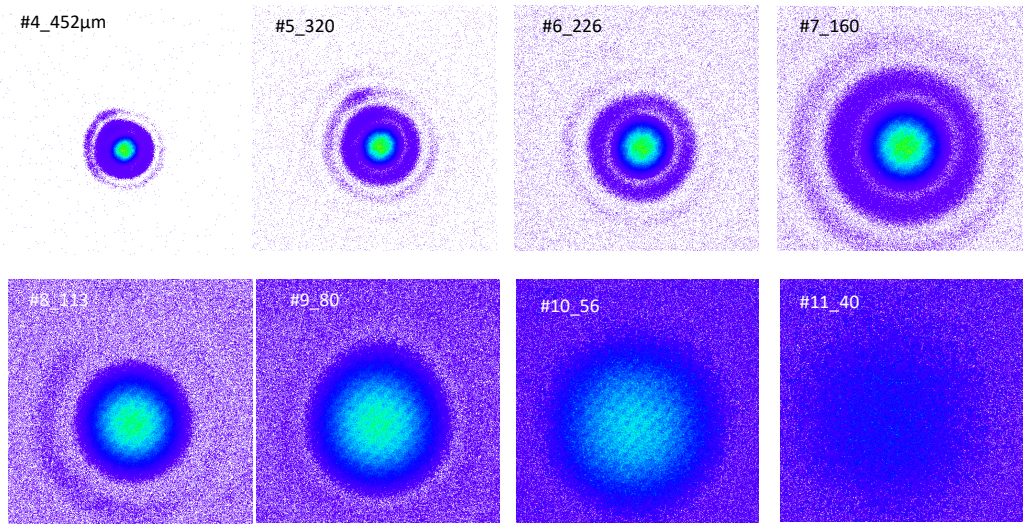

Figure 2.5 Laser diffraction through different sizes of circle-apertures, bigger apertures give smaller Airy disk.

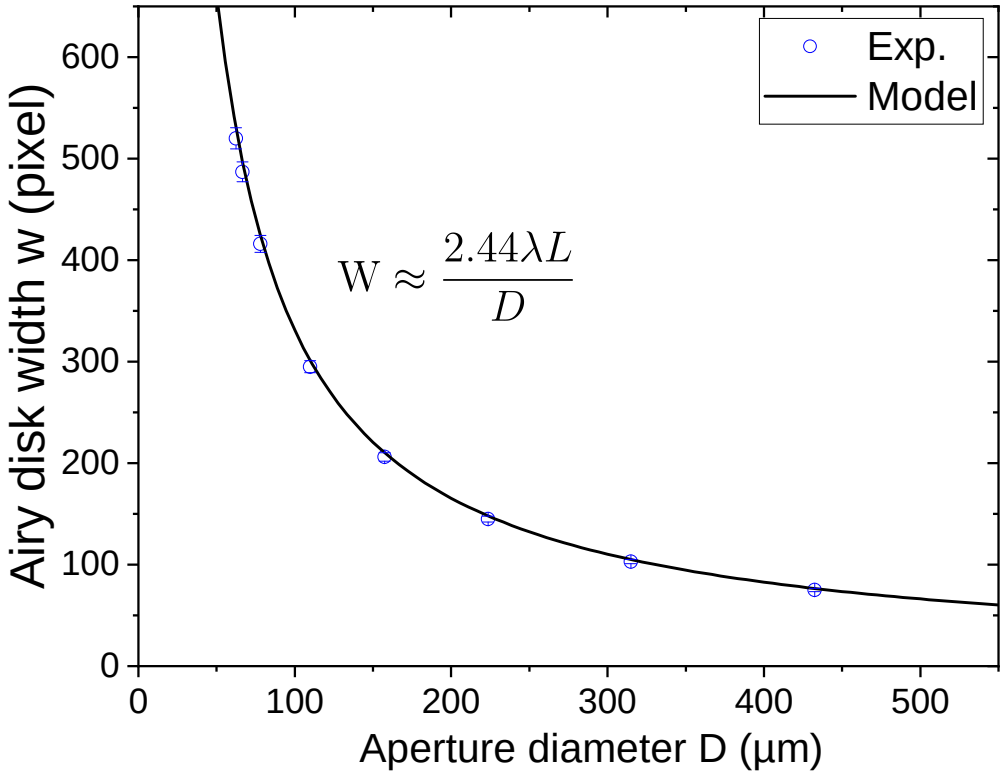

Figure 2.6 Laser diffraction through different sizes of circle-apertures. Eq. 2.1 gives the relation of aperture diameter D and Airy disk width w.

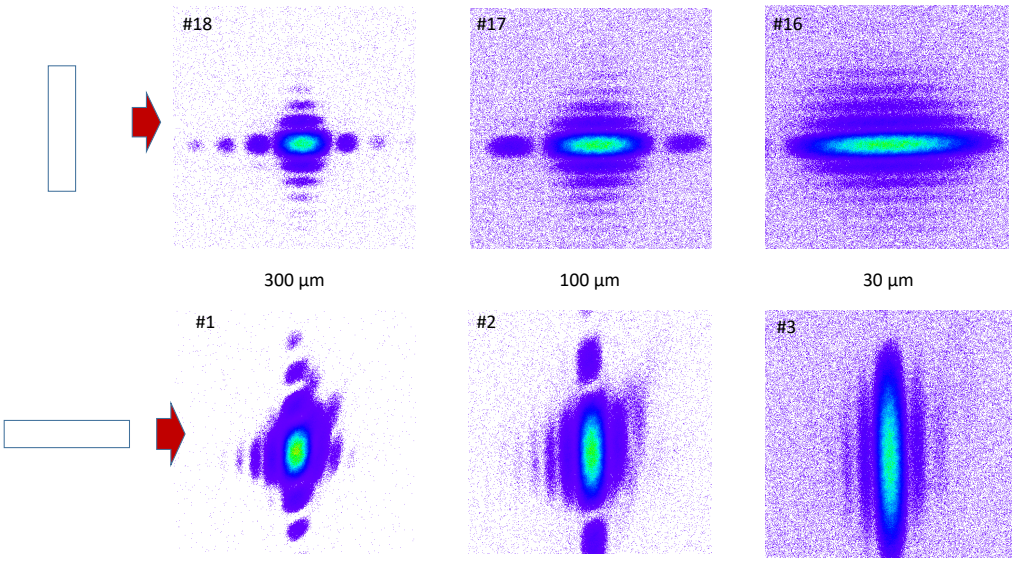

Figure 2.7 a) Laser diffraction through rectangle shape slits (Length=400 μm, Width =300, 100, and 30 μm), If we focus on the first-order diffraction pattern, bigger apertures (Length $\times$ Width) give smaller diffraction patterns.

2.4 The UHV Chamber

2.4.1 The Manipulator

GIFAD is a diffraction technique and therefore requires accurate control of two angles, the angle of incidence θ with the surface plane $\vec{k}_{in} \times \vec{S}$, $\hat{n}$ and the orientation of the surface ϕ, or the angle between the crystallographic axis labeled with miller index with the projection of $\vec{k}_{in}$ on the surface plane.

A holding flange characterizes a simple manipulator with a three-axis translation stage holding a primary rotation axis perpendicular to this flange and terminated by a sample holder. More sophisticated models support a co-axial translation or rotation mechanism to perform additional movements, such as an additional rotation.

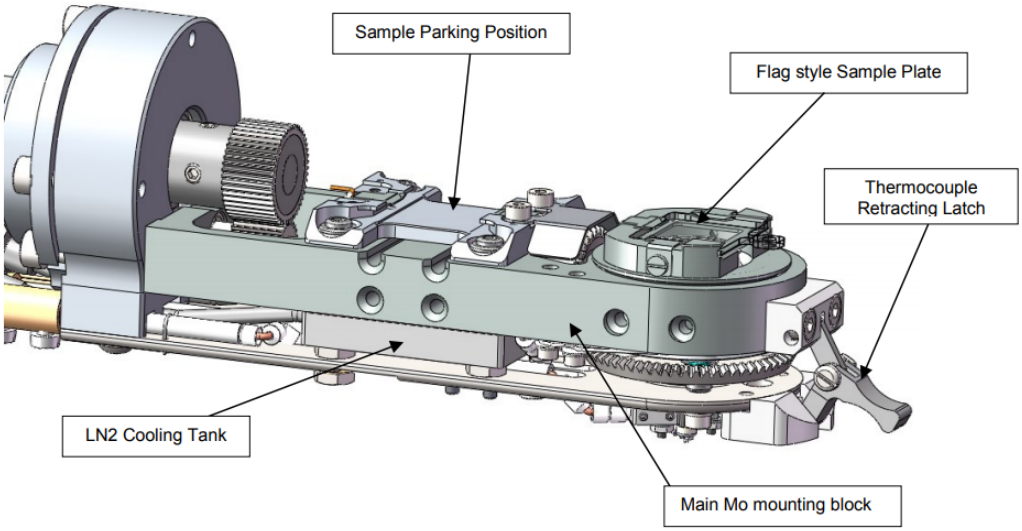

Figure 2.8 Sample plate with heating and cooling systems.

2.4.2 Sample Heating and Cooling System

The manipulator of the sample holder is connected to a heating and cooling system. The head is cabled to control the temperature of an Omicron Flag style sample plate over the range 130K(-143°) to 1473K (1200°) using a combination of the LN2 cooling and Ta foil heater. The head is equipped with an LN2 cooling system and a Ta foil heater module, as shown in Fig. 2.8.

Sample radiative and e-Beam Heating

The Heater is designed to heat Omicron flag style sample plates, is fitted with a Type N thermocouple located inside the Tantalum foil heater. The foil heater radiates heat onto the back face of the flag-style sample plate providing enough energy to enable continuous heating to 700 $^{\circ}C$. For the heating temperature much above 600-700 $^{\circ}C$ should be done using e-beam heating to avoid needlessly overheating the cathode. For this setup, the electron emission was observed at $\sim$ 5.8 A for the heater freshly coated with Yttria. The thermocouple must be retracted (unlocked) from the sample plate for transfer. Otherwise, the spring will push and hold the target to avoid movement. The sample holder heating temperature-power curve shown in Fig. 2.9.

Sample Cooling

Connect a supply of LN2 directly to the input tank of the liquid Nitrogen (LN2) feed-through using a 6.5mm OD Teflon tube insert into the 'O' ring fitting and tighten.

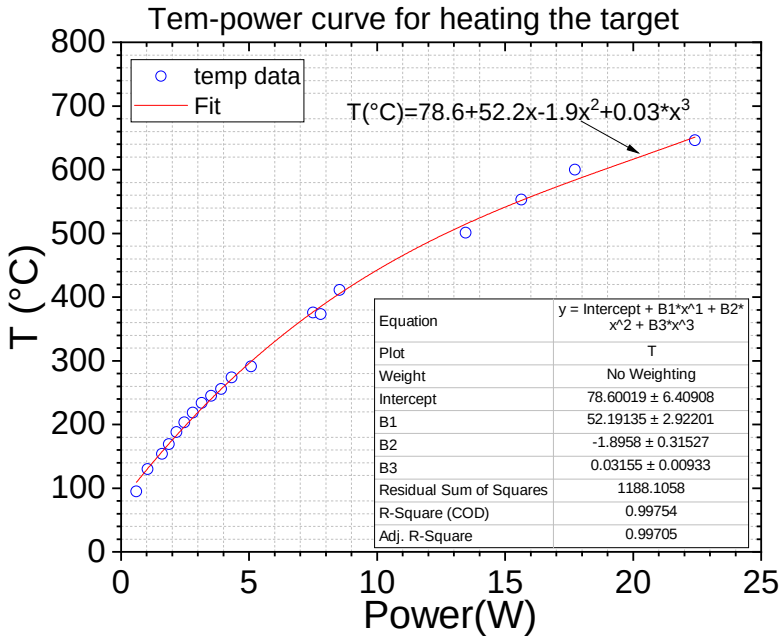

Figure 2.9 Sample heating temperature-power curve.

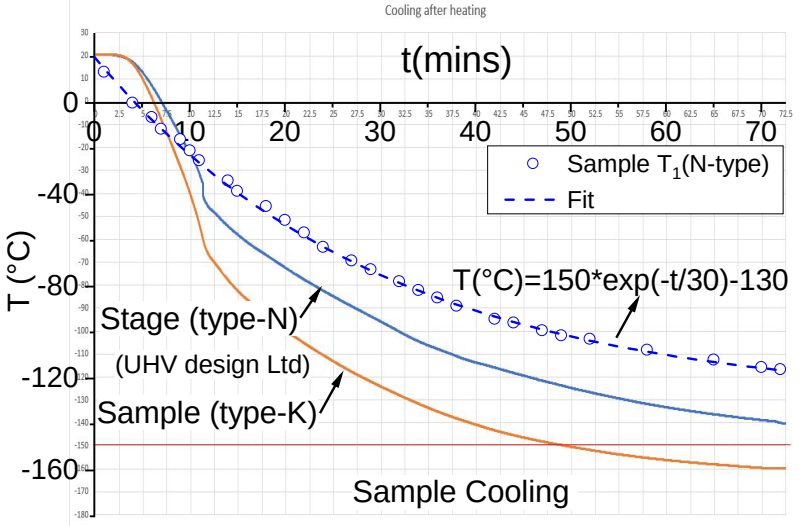

Figure 2.10 Sample cooling temperature-time curve.

Keep the connecting tubes as short as possible to reduce cooling time. After a few minutes, LN2 should appear at the exhaust port. The temperatures at the exit will be observed to fall quite rapidly, following curves as shown in Fig. 2.10, comparing results from the UHV design company and our experimental results. Exponential decay of temperature with time was observed, the starting point at $T(t = 0\,min) = 20°C$, then the empirical fit by such simple formula: $T(t)[°C] = 150 \cdot e^{(-t/30)} - 130$.

2.5 The Detector System

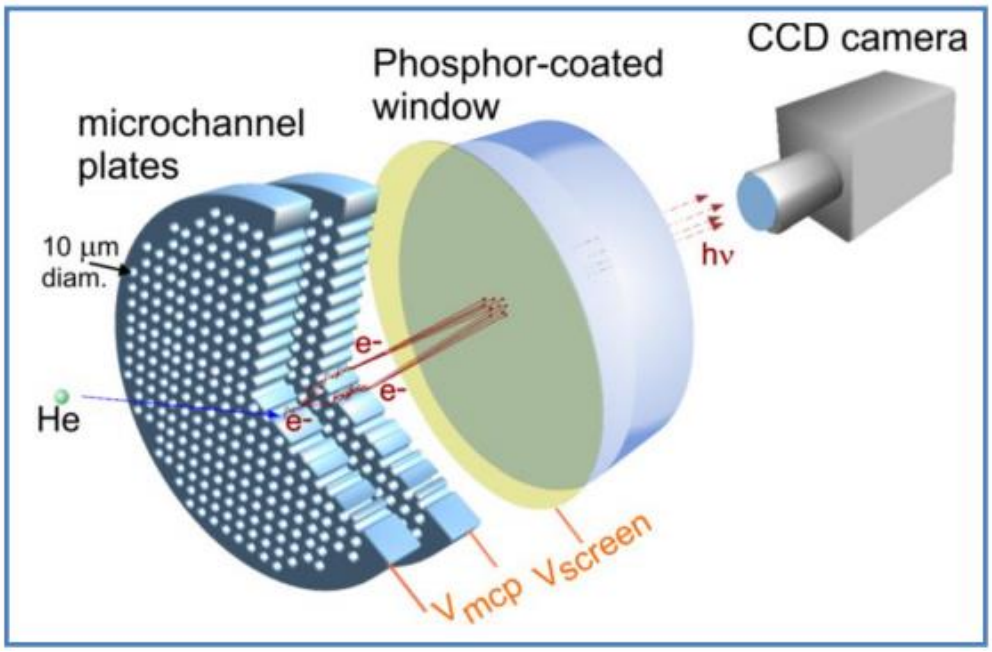

Figure 2.11 The schematic of the detector system, MCP+PhosphorScreen+CCD/CMOS

Imaging detector systems shown in Fig. 2.11, in our case, should be able to detect atoms efficiently in the keV energy range, for instance, photomultiplier tubes, channeltron, or microchannel plates. In all these cases, the impact of the atom in the material will be able to extract an electron from this material. The underlying process is simply the Pauli repulsion. When the atom tries to penetrate the material, it has to push surface electron density. One electron from materials has a chance to be ejected with an energy usually on the order of one eV.

The rest of the detector will convert this initial electron into an electron cascade by the successive acceleration of ejected electron around 100-400 eV and collision on dedicated material known to respond by emitting a few secondary electrons.

The successive energies are perfectly defined in the case of a PM tube and only statistically defined in Channeltron, where no straight line is possible due to the curvature or inside a MCP channel because of its very long aspect ratio (L/d: 50-60). As a result, around ten e-2e collisions or multiplication cascades can occur, producing between 10^3 to 10^4 electrons. In the case of MCP, these electrons are produced at the exit of a narrow tube of 20μm diameter, allowing localization of the atom impact. In our case, imaging detectors rely on MCP to convert the atom impact into an electron shower. They differ in the technique used to localize

the associated impact in space and time. When using two MCP, the number of electrons can reach $10^7 - 10^8$, enough to generate a pulse of a few tens of mV across a 50 Ω resistance. Since the second MCP produces the electrons, the voltage pulse is also present at the MCP output. It can be directed to a voltage comparator called discriminator, emitting a quasi synchronous logic signal from which the atom arrival time can be determined with a sub ns accuracy. A specific anode will collect the electrons and try to retrieve the impact location (see *e.g.*[40]).

2.5.1 The Phosphor Screen

The imaging detector uses a single MCP and a phosphor screen [41]. The setup of the phosphor screen (scintillator) is a standard 2-3 mm thickness cylindrical disk coated with an ITO layer and a 4 micron P34 Phosphor layer. Its diameter matches our MCP, which has high efficiency of less than 20 eV of electron energy to emit photons. The screen is stable under UHV conditions and can resist temperatures up to 200 $^{\circ}C$ without a problem.

2.5.2 The Lens and Camera

The optical system is expected to image the 60 mm phosphor screen with high resolution and as few distortions as possible. The CMOS camera is a Hamamatsu C11440-10C model with a 1440*1920 pixel allowing a 45 micron per pixel if the lens is adjusted to the full screen. The lens should collect as much light as possible without introducing aberrations. This is somewhat contradictory since the aberrations are weak only in the paraxial region. Therefore, placing the camera and lens as far away as possible is recommended, while the closer the camera, the more intensity will be collected. As a compromise, we used a high aperture F0.95 "Xenon" lens from Schneider [42] with a focal lens of 17 mm. It is placed 25 cm away from the Phosphor screen so that the maximum angle of the light collected is less than 9°.

The performance of the system has been evaluated in detail. The aberration of the lens has been tested by scanning a light spot generated by a laser illuminating a 10 micron hole and placed 250 mm from the camera entrance. We could then determine the correspondence between beam position and measured position. The measured aberration correspond to a barrel type aberration $r' = r + \alpha r^3$ with a coefficient $\alpha \sim 2 \times 10^{-9}$ [36]. The aberration is negligible in the center but affect particles detected at the edge by a few pixel.

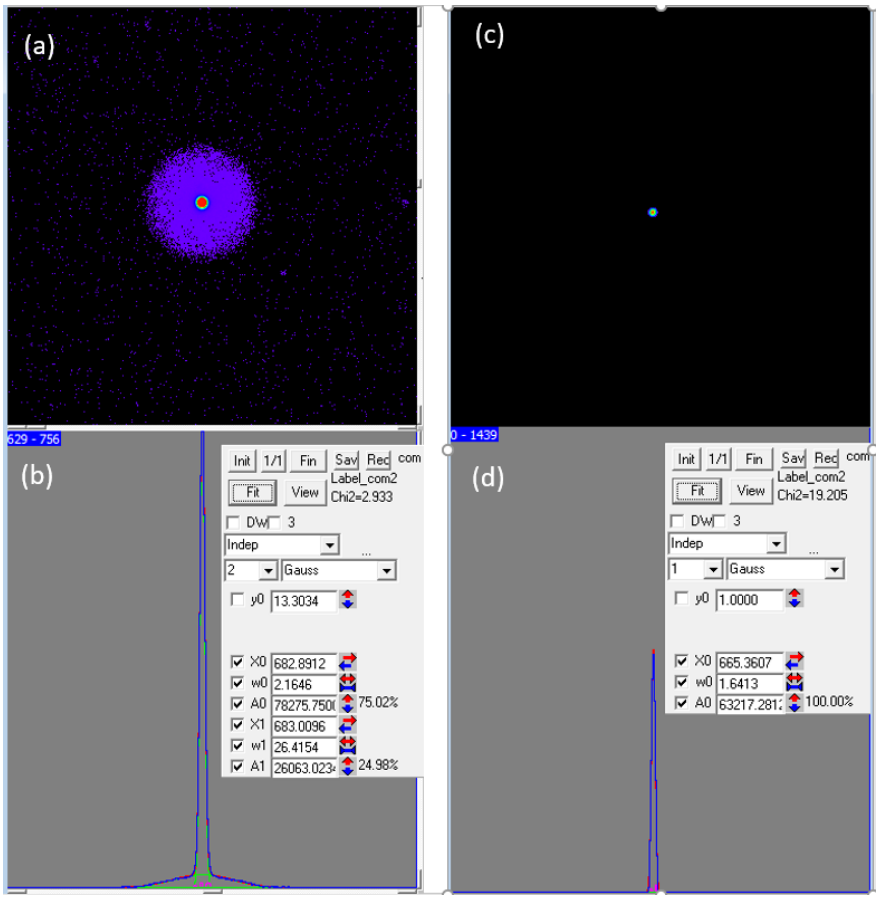

Figure 2.12 Comparison of direct beams recorded at the center position of the detector. (a) by analog integration mode (AIM), and (c) by photon counting mode (PCM) of CMOS camera. (b) and (d) are projection profiles of (a) and (c) along z (polar profiles), respectively.

Analog Integration Mode and Photon Counting Mode

The camera has several methods to record the data, we call these methods acquisition modes. There are four image acquisition modes: Live, Acquire, Analog Integration, and Photon counting. The last two are most often used in recording experimental data. In analog integration mode, many images accumulate in the frame memory. In the photon counting mode, single-particle events are added up in the frame memory. A very high signal-to-noise ratio can be achieved if the signal integration time is sufficiently long. A comparison of direct beams recorded by those two modes is shown in Fig. 2.12. The measured width is improved from σ=2.16 to 1.64. Considering that the improvement comes from the width of a single impact which is replaced by a centroid determination we add the associated variances, $1.4^2 + 1.64^2 = 2.16^2$, where $\sigma = 1.4$ could be interpreted as the resolution gained by pointing the center of a single spot. In Fig. 2.13, we shown the direct beam recorded from

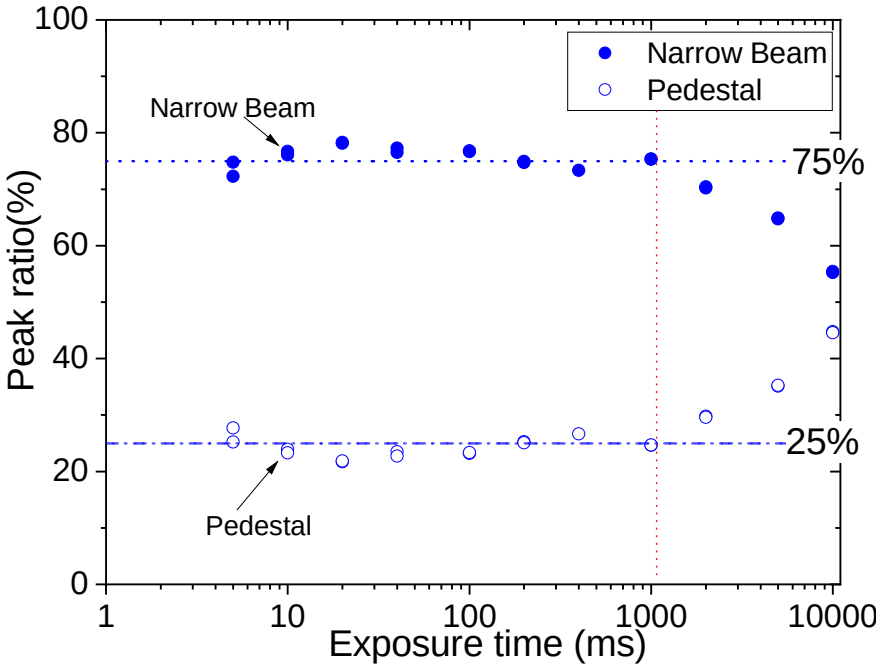

Figure 2.13 CMOS camera performance at different exposure times from 5ms to 10s. The pedestal intensity does not depend on exposure time. Beyond 1s exposure time (red dotted line) the pixels of the beam spot are saturated, and the measured Beam intensity is erroneous.

4ms to 10s in Analog Integration Mode, to avoid the saturation issue, it's better to keep the exposure time less than 1s per image.

2.5.3 The Direct Beam Attenuator

The exact position and profile of the direct beam is most important for accurate diffraction measurements. In particular, the proper positioning of the Laue circle encompasses the direct beam and all elastic diffraction spots [43]. To avoid damaging the MCP detector when recording the direct beam profile, two fine mesh grids with 10% and 1% transmission are mounted on a z translator that can be inserted into the beam with minimum perturbation of its angular profile.

2.6 Additional Equipment

2.6.1 The Deflectors and Chopping System

There are two pairs of deflectors for steering of the ion beam in X and Y directions. There are two methods to deflect the charged ion beam, While magnetic lenses are usually used at

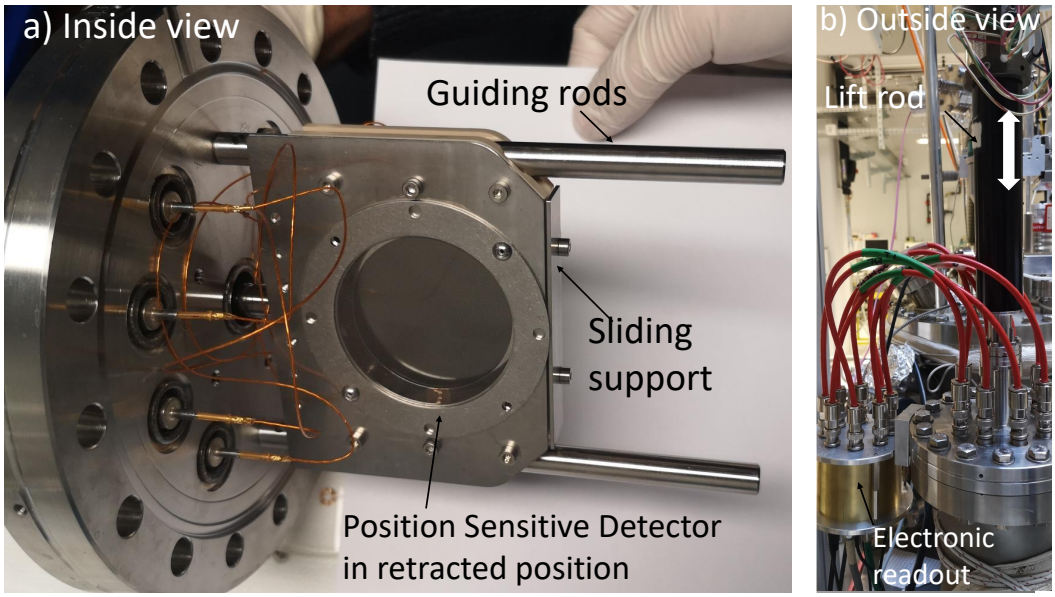

Figure 2.14 The retractable resistive anode detector has an active diameter of 40 mm and a sub-ns timing accuracy. It is sliding along the two metal rods taped into the 100 CF flange and is tied to a 100 mm linear actuator to be taken in or out of the beam.

high energies (E $>$ 50 keV) The chopping system consists of an entrance slit that determines the size of the beam spot.

2.6.2 The Retractable Resistive Anode Detector

The retractable resistive anode detector is a two-dimensional position-sensitive (2D-PSD), mainly[40] containing two pieces of the micro-channel plate (MCP) and a readout. It can be inserted into the beam and provide a 2D position (yz plane) of the atom or ion beam. The detector is an evolution of the similar ones used in the first GIFAD experiments[5] and in many different applications ranging for atomic collisions [44–47], collisions on surfaces[48], charge deposition on insulators and micro capillaries[49, 50]. The detector support is made of peek and slides between two stainless steel rods. It is covered by a stainless steel plate holding a high transparency grid almost invisible in Fig. 2.14.

2.6.3 The Recoil Ion Detectors

The recoil ion detectors are multi-purpose particle detectors. They can be configured to detect preferentially positive or negative particles by biasing the entrance at a voltage between -5 kV and 3 kV. The anode voltage does not exceed the 5 kV limit of electrical feed-through. They are fixed on DN40CF tubes directed to the target and intended to detect particles emitted

around 30-45 ° from the surface, either forward or backward. The time and position-sensitive detectors were designed to be compact with a large active area [51]. Typical applications are listed below.

2.6.4 Direct Recoil Spectroscopy

Direct Recoil Spectroscopy (DRS) is the generic name for several techniques where atoms or ions with a definite energy are sent onto a surface and the ejected or recoiling ions or atoms are analysed in energy. If a quasi binary collision took place, then the energy and momentum sharing follows those of the gas phase and the mass of the collision partner, initially at rest, can be identified. The most general technique is probably Time of Flight analysis (TOF SARS [52]) because, most often the particles are ejected as neutrals. This is usually achieved as a function of the target azimuthal and polar angle at a relatively large incidence angle because only quasi-binary collisions can be identified. Under grazing incidence, only ad-atoms or terrace edges can undergo a violent binary collision and the analysis of the recoils emitted in the forward or backward direction should help identification of poisoning impurities such as hydrogen contaminants that are difficult to pump. More interesting scientifically, identifying the chemical composition of island edges during growth is a challenging issue.

2.6.5 The Sputtering Ion Gun

Inside the UHV chamber, a commercial ion gun IG2 is a product for beam etching and sputter cleaning of samples for surface analysis. It is assembled with the UHV chamber and operates with inert gases such as Argon to remove the containment from the surface. Ions are generated by electron impact within the ion source's filament ionization chamber, then the ion beam is focused at the target with energies of up to 2 kV. A focusing lens permits high ion current density for a given pressure in the UHV chamber.

Inside the UHV chamber, a commercial ion gun IG2 was installed and directed to the sample holder for sputtering clean samples. We operate it with an inert gas such as Ne^+ or Ar^+ at an energy between 500 eV and 2 keV. It is equipped with a focusing lens, and we have added a pair of deflectors to scan the target with the ion beam. By recording the secondary electron yield with one of the recoil ion detectors described in Sec. 2.6.3 as a function of the voltage of the deflecting plates, a coarse image of the target can be formed. For LiF samples, sputter cleaning is associated with creating topological defects that we could not remove. Even after thermal treatment and grazing sputtering, the diffraction pattern does not exhibit sharp elastic spots with a dimension that compares with our primary beam. This is not the case for metals

where the diffraction on the Ag(110) surface could be observed only after repeated cycles of sputtering and annealing [7].

2.6.6 The Co-linear Laser

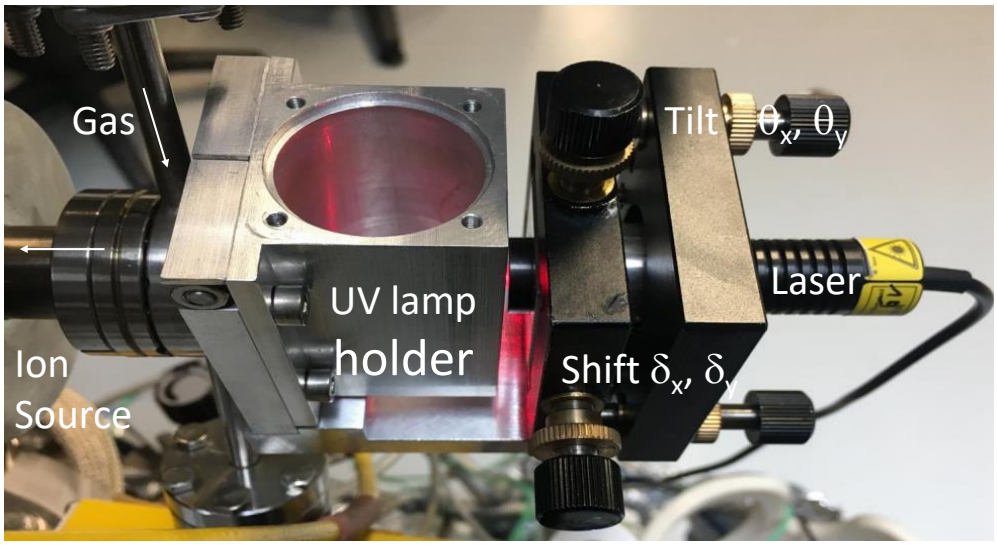

Figure 2.15 The laser is held on a miniature X, θ_X, Y, θ_Y platform hooked directly to the ion source. It passes through support, allowing the insertion of a UV lamp.

A compact spot red laser in Fig. 2.15 with 648nm wavelength is installed behind the ion source, co-axial with the beamline. The advantage of using the laser here is that it is much easier to trigger a laser beam by a switch button to replace the atom beam and find the good alignment of the beamline. This can also greatly save the service life of the ion source filament. In addition, we can use the laser to calibrate the detector's resolution by light diffraction. The diffraction geometry shown in Fig. 2.16 a), and a typical diffraction pattern of λ=648 nm visible red light through a D=160 μm circular aperture in Fig. 2.16 b). The diffraction pattern has a bright central region known as the Airy disk. A simple analysis of the Airy disk already gives the dimensions of the holes:

$$\sin\theta_1 \approx \frac{1.22\lambda}{D}$$
$$\text{For small angle approximation yields: } \theta_1 \approx \frac{1.22\lambda}{D} \tag{2.1}$$
$$\text{and, } D \approx \frac{2.44\lambda L}{w} \text{with } w \text{ measured from the 1st dark ring.}$$

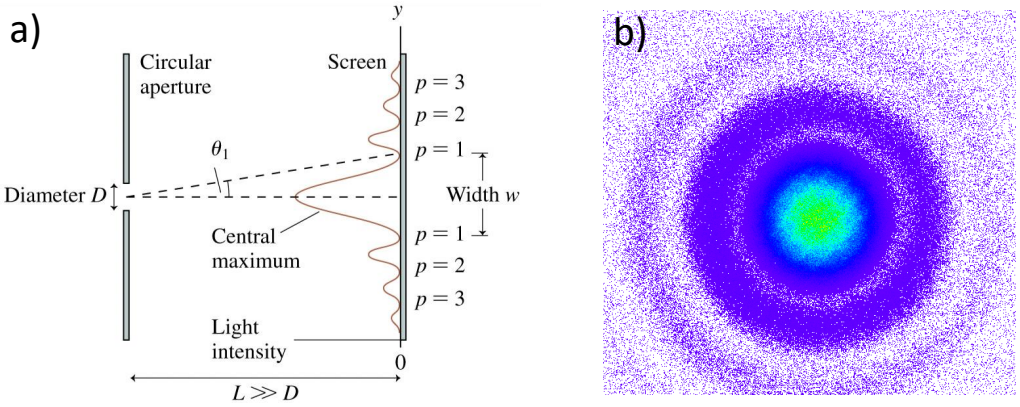

Figure 2.16 a) Circular-aperture diffraction geometry, where L(942mm) $\gg$ D(0.16mm). b) Diffraction pattern of the λ=648 nm laser through a D=160 μm circular aperture in the beam-line.

Alignment with the Laser

The Alignment procedure of all the diaphragms and differential pumping holes is easier with the miniature X, Y, θ_X, θ_Y platform attached directly to the EX05 ion source (section 2.2). As detailed in Sec. 2.5, when a single MCP is used together with a phosphor screen without an aluminum cover layer, enough light passes through the (unbiased) MCP to be imaged by the camera, allowing quantitative intensity optimization both in a vacuum or at atmospheric pressure. This is particularly convenient to calibrate the variable holes and slits along the beamline by the recorded Airy pattern. This also allows a very simple pre-positioning of the target surface into the beam.

2.6.7 The Webcam and perpendicular laser

The UHV chamber offers a DN100CF flange directly facing the target surface, shown in Fig. 2.17 a). When unused, it is closed by a window flange where we have installed a webcam and a miniature red laser. The red laser is shifted by $\approx$ 2 cm from the center and directed to intercept the surface around its center. If the target surface is indeed parallel to the flange, the reflected beam also lies 2cm from the center but opposite to the primary spot. During an azimuthal rotation, the reflected spot describes a circle with a center located at $2\theta_{laser}$ and a radius 2τ where τ is the misalignment of the surface normal with respect to the rotation axis and θ_{laser} is the arbitrary angle of the laser with the mean surface normal. Due to the 24 cm long path between the surface and the window, the position of the spot reflected from the surface is easily tracked by the camera. It can be used to follow the target azimuthal angle online and to correct for the possible tilt angle τ.

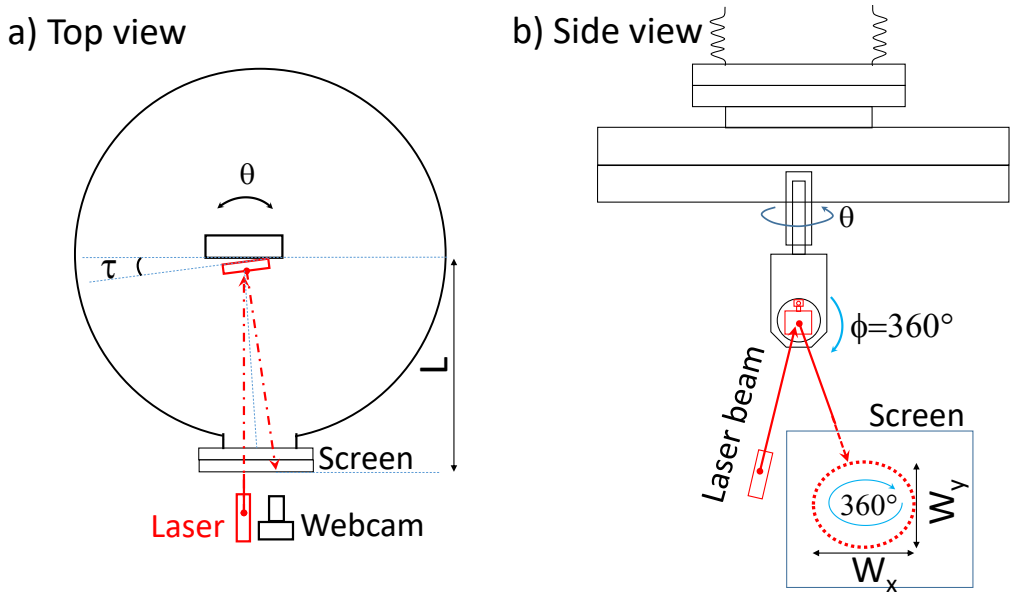

Figure 2.17 The Webcam and perpendicular laser installed around the UHV chamber. a) top view and b) side view of laser deflection geometry, where L≈24 cm. After a 360° rotation of the sample, the reflected spot follows a circle with W_x and $W_y \simeq W_x$ which can be measured by tracking the laser spot on a screen.

The Tilt Angle Correction

One of the difficulties associated with GIFAD is the shallow angle of incidence needs to be known with precision. This is not a problem during a standard diffraction experiment but it isn't easy to guarantee a sample positioning perfectly perpendicular to the manipulator rotation axis so that the angle of incidence could remain fixed during an azimuthal scan. Sereno *et al.* [53] have derived an active regulation to estimate the tilt angle τ based on experimental measurements in the (x, y) perpendicular plane.

$$W = 4L\tau \tag{2.2}$$

Where W is the width of tracked laser spot along x or y, L is the distance between the sample to the screen. Such calibration can also be performed using the specular reflection of the co-linear laser. But these correspond to separate measurements and can not be easily visualized during the diffraction experiment.

The other option is to use the window in front of the surface, perpendicular to the target. A miniature red laser is installed to shoot at the target and the spot of the reflected beam is imaged on the backside of a semi-transparent paper taped on the window and recorded by a basic Webcam. In this quasi-normal geometry, the spot follows a quasi-circular trajectory

whose radius is given by the tilt angle. In principle, the reflected spot position could be tracked and its position transferred to a perfect correction algorithm. In the present case, only the effective angle of incidence is corrected by adjusting the angle of incidence by the proper amount. Our manipulator does not have flexibility in the perpendicular plane so the specular reflection plane undergoes a weak oscillation by $\pm\tau$ in Eq. 2.2 during a full azimuthal scan.

2.7 Sample Preparation

Under normal conditions, atmospheric pressure (1 bar), and room temperature (300K), the real surface is far from the ideal systems desirable in physical investigations. A freshly prepared surface of a sample usually is very reactive toward atoms and molecules in the environment. The adsorption from weak physisorption to strong chemisorption gives rise to an adlayer on the topmost atomic layers of the solid. As an object of physical investigations, a well-defined surface has to be prepared on a particular solid, in a special preparation process, under well defined external conditions. There are essentially three ways to manufacture clean surfaces under UHV conditions[54]:

- (1) Cleavage of bulk crystal materials in a cleanroom or UHV. Of course, only surfaces that are cleavage planes of the crystal can be made in this way;
- (2) Treatment of imperfect and contaminated surfaces of arbitrary orientation by ion sputtering and thermal annealing in several cycles;
- (3) Epitaxial growth of crystal layers (or overlayers) by means of molecular beam epitaxy (MBE) or evaporation;

A typical GIFAD experiment begins with introducing or preparing a new sample surface and subsequent annealing. For a metallic sample, sputtering is needed to clean the surface contamination. Here, we used LiF single crystal, previously irradiated by γ-rays [55] giving a pronounced yellow to orange color, and cleaved just before transfer into sample holder in UHV chamber. Subsequent heating at 400 °C for a few hours is usually enough to recombine the color centers and record nice diffraction images with well-resolved elastic spots.

The ISMO moved to a new building in 2017 and all the experiments since then have been performed with the GIFAD setup connected to the UHV tunnel (Fig. 2.18) of the SIM2D group. The tunnel is still in development, allows the transfer of samples from one experiment to another. For instance, the Al_2O_3/Ni_3Al surface was prepared by A. Ouvrard before being

inserted in our chamber, and then transferred to our setup via UHV tunnel for triangulation and diffraction studies (see Chap. 3.3.1).

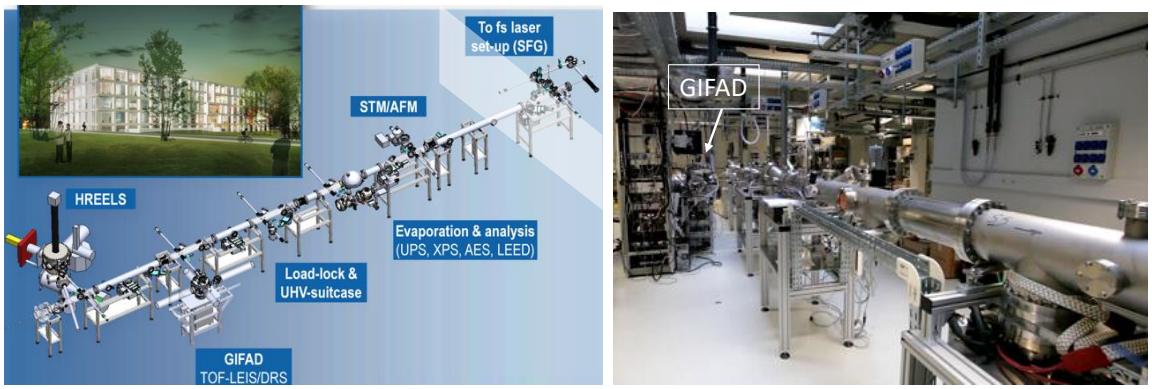

Figure 2.18 The UHV tunnel of the SIM2D group at ISMO, the sample can be transferred from different experimental setups through the UHV tunnel (1×10^{-9} mbar).

2.8 Atomic Beam Preparation

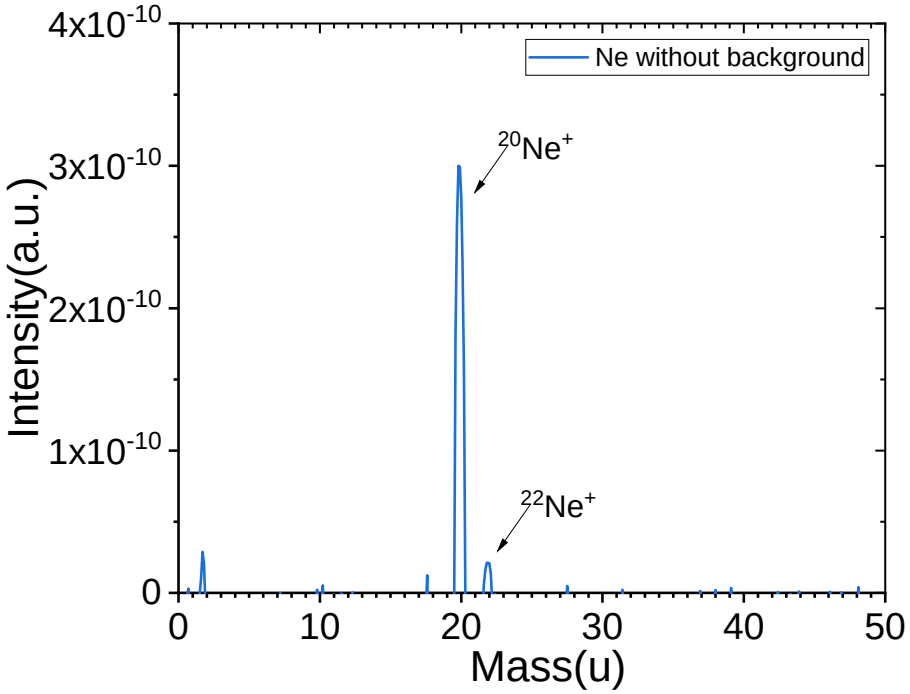

Figure 2.19 Ne gas mass spectrum, Main isotopes of neon 90.48% ^{20}Ne, 9.25% ^{22}Ne.

After a sample is installed in the sample holder of the manipulator, a stable and high-intensity atomic beam needs to be ready. A typically primary(direct) beam recorded in the detector

is shown in Fig. 2.12. When working with noble gases, the presence of a Wien filter is not mandatory but the gas purity should be checked mainly to avoid producing mixed beams and weird diffraction images and avoid damaging the filament. We have a quadrupolar residual gas analyzer that can be installed close to the charge exchange cell. When no gas is fed on the cell, the RGA essentially measures the gas injected in the source, which is enough to check the purity as illustrated in Fig. 2.19.

Chapter 3

Experimental Methods and Data Analysis

> Nothing in life is to be feared, it's only to be understood.
>
> *Marie Curie*

3.1 Introduction

3.2 Scattering Geometry and Diffraction Conditions

In Fig. 3.1, we show the scattering geometry for "Grazing incidence fast-atoms diffraction" (GIFAD) at a well-ordered (low index) surface LiF(100). The impact of the probe atoms on the surface proceeds under glancing angles of incidence $\theta_i \sim 1^\circ$, so that the scattering process can be characterized in small-angle collisions.

A common feature of all the grazing incidence diffraction techniques[56], the coordinate system is chosen to have the atom beam oriented parallel to the projection of this incident beam on the sample surface. With the y axis in the sample surface plane, the z-axis is oriented along the surface normal. With the wavelength λ, the wave vector transfer $\mathbf{q}$ is given by

$$\mathbf{q}_{x,y,z} = \mathbf{k}_f - \mathbf{k}_i = \frac{2\pi}{\lambda} \begin{pmatrix} \cos(\theta_f)\cos(\phi_f) - \cos(\theta_i) \\ \cos(\theta_f)\sin(\phi_f) \\ \sin(\theta_i) + \sin(\theta_f) \end{pmatrix}$$

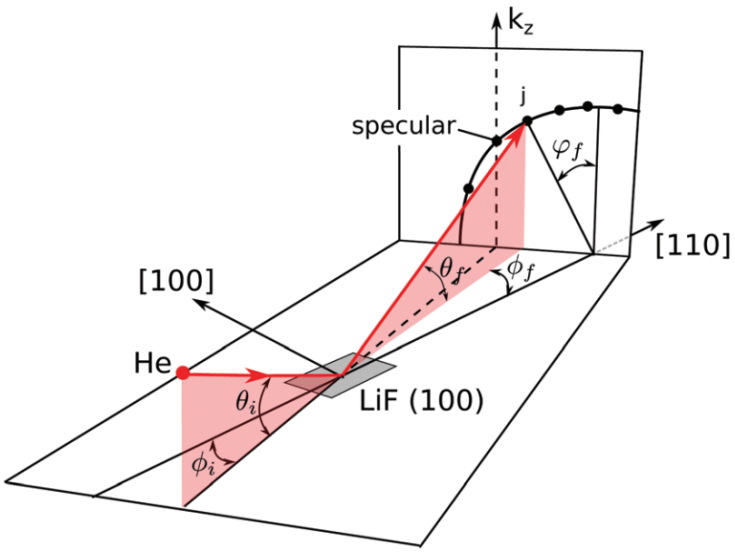

Figure 3.1 Schematic of scattering geometry under misalignment. Helium atoms beam scattering on a LiF(100) surface with a polar incidence angle θ_i and azimuthal (misalignment) incidence angle ϕ_i with respect to the [100] direction of the surface. A diffraction order j is located with the lateral deflection angle ϕ_f, the final polar exit angle θ_f, and the deflection angle φ_f, the scattering plane in red, corresponds to j=1. During a ϕ-Scan, the position of the specular spot on the detector remains fixed. Taken from[16].

The vertical component of kinetic energy governs the motion perpendicular to the surface.

$$E_\perp = E \cdot \sin^2 \theta_{in}$$

Where E is the kinetic energy of the primary beam, $E_\perp$ is the perpendicular energy of the atom beam normal to the surface.

The elastic diffraction spots fall on the Laue circle on energy conservation if the normal energy does not change ($E_\perp$=constant),

$$E_\perp = E_{iy} + E_{iz} = E_{fy} + E_{fz}$$

where $E = \frac{\hbar^2 k^2}{2m}$, which means the energy conservation in yz-palne motion, so called Laue circle shown in Fig. 3.2,

$$Constant = k_\perp^2 = k_{fy}^2 + k_{fz}^2$$

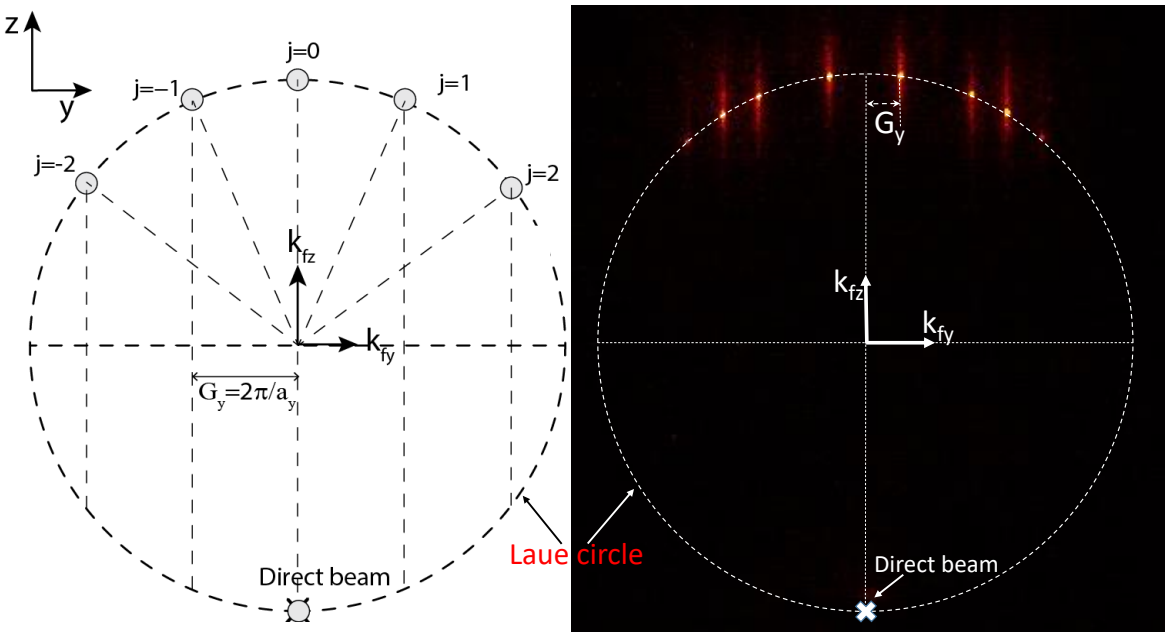

Figure 3.2 Schematic illustration of elastic (on Laue circle) diffraction geometry in the y-z plane. In an ideal case (purely elastic), those diffraction spots should have the same shape (or distribution) as the direct beam (*e.g.* Gauss distribution). In right panel, a typical diffraction pattern (from 300 eV ^{4}He on LiF[110] at 1.28°), elastic components(on Laue circle) and inelastic components (out of Laue circle) are present simultaneously.

The diffraction peaks are equally separated by the well known Bragg angle:

$$\theta_B = \arctan\left(G_y/\hbar k_{//}\right) \tag{3.1}$$

where $\hbar k_{//} = \hbar k \cos\theta_{in}$ is the projectile momentum parallel to the crystal axis. $G_y = 2\pi/a_y$ is the reciprocal lattice vector associated with the distance a_y between atomic rows perpendicular to the probed crystal axis, taken here as the x direction.

3.2.1 Primary beam, Laue circle, and incidence plane

The primary or direct beam (See Fig. 3.3 and Fig. 3.4) is very important to record for subsequent experimental analysis. The shape and intensity of the beam are the original information before scattering or diffraction, and the evolution of the beam is based on such a direct beam. For instance, for a purely elastic scattering, specular scattering, the shape of the scattered beam should be identical to the direct beam.

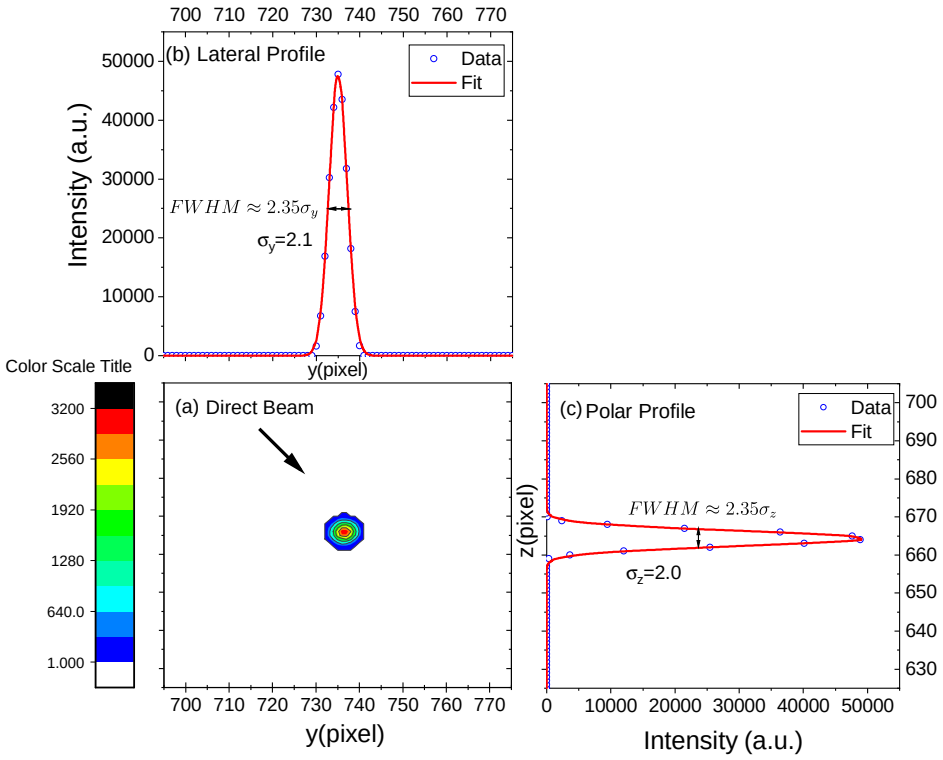

Figure 3.3 (a) A direct beam recorded at the center position of the detector by photon counting mode (PCM) of CMOS camera. (b) and (c) are lateral and polar profiles fitted by Gaussian distribution, *i.e.*, the projection profiles of (a) in y and z directions, respectively.

Angular distributions of scattered projectiles were recorded at a distance L=858 mm behind the target through an imaging detector system (see Sec. 2.5). Elastically scattered atom beam impacts the detector on the Laue circle of radius θ_{in} (Show as Fig. 3.1), owing to energy conservation of the normal motion for scattering from ordered surfaces.

3.3 Experimental Methods

A procedure called triangulation [57, 58, 16] where the angle of incidence θ ($\equiv k_{iz}$) should be kept constant. In practice, the relative width $\langle k_{fy}^2 \rangle^{1/2}/k_{iz}$ compensates for a eventual tilt τ between the surface normal and the rotation axis [58, 53]. After proper alignment on the desired axis, the surface is prepared by various methods until a good diffraction pattern is observed. The size of the diffraction spots provides a lower limit on the surface coherence length.

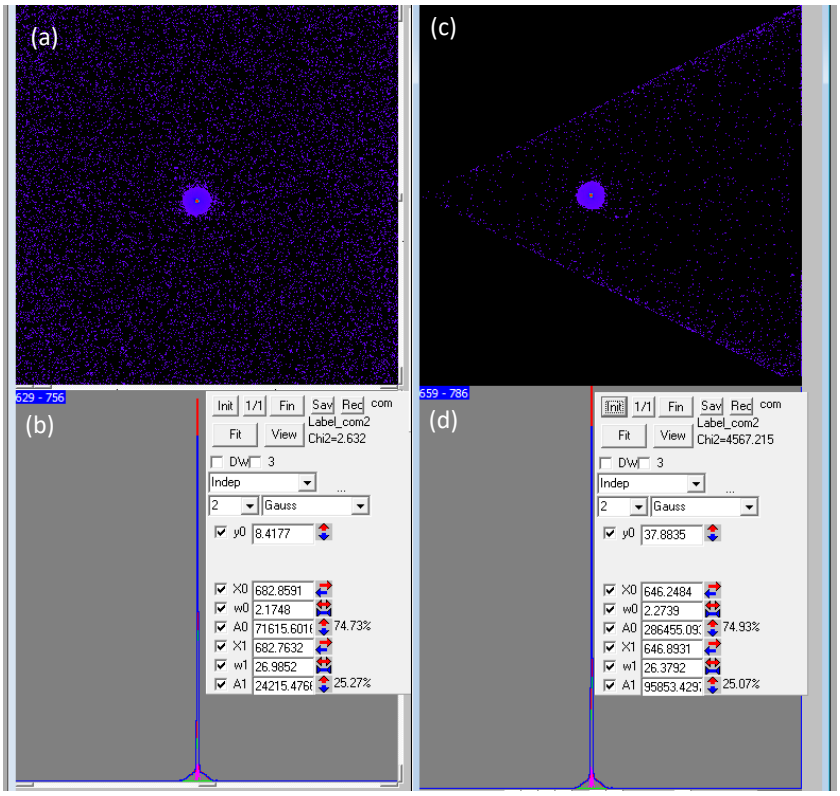

Figure 3.4 (a) A direct beam recorded at the center position of the detector by analog integration mode (AIM) of CMOS camera. (a) is the raw file, (c) is after polar transform. (b) and (d) are projection profiles of (a) and (c) along z (polar profiles), respectively, and two Gaussian distributions fit both. The pedestal is hardly affected by the Polar transform.

3.3.1 ϕ-can and Atomic Triangulation

The azimuthal angle scan (ϕ-Scan), a typical diffraction pattern in Fig. 3.5, is usually the first experiment performed after inserting a new sample in the UHV chamber. This allows precise measurement of the main crystallographic directions difficult to track precisely in a transfer system. The diffraction pattern is often not observed immediately because of molecular surface adsorption or other reasons such as limited coherence. ϕ-Scan corresponds to a variation of the azimuthal angle ϕ_i (see Fig. 3.1 for the definition of scattering angles.) Several low index directions can be identified during an azimuthal scan, providing the basis for atomic triangulation measurements[57, 58], a GIFAD results in Fig. 3.6.

The measurements consist of a rapid azimuthal scan, ϕ-scan, where the target surface is rotated in-plane (around the z axis) to identify its crystal axis. It does not require that diffraction is observed because a simple analysis of the width of scattered lateral profiles;

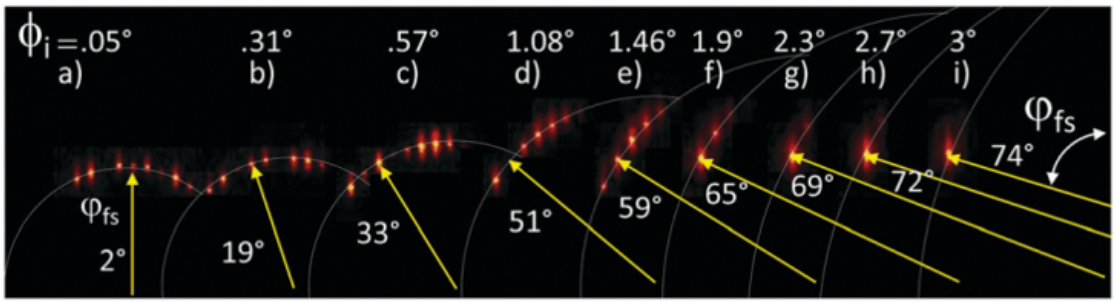

Figure 3.5 A typical result from ϕ-Scan, (a)-(i), 9 diffraction patterns of 460 eV He corresponding to an incidence azimuthal angle ϕ_i from 0.05° to 3° relative to the $\langle 110 \rangle$ direction.

($\langle k_{fy}^2 \rangle^{1/2}$ in Fig. 6.2a,6.2c,6.2d,7.2,7.3a), as a function of the target azimuthal angle ϕ is enough to identify the principal crystal axis.

When the energy is perpendicular to the surface, $E_\perp$ is close to or larger than 10 eV. The projectile penetrates the electronic density of the target at a distance close to one Å . Secondary electrons are emitted, for instance, by the promotion of quasi-molecular orbitals. By tracking the secondary electron yield during an azimuthal scan, some surface structure parameters such as the direction of the low index axis can be determined by ion beam triangulation [59]. At large enough projectile energy, $E_\perp$ reaches the few eV ranges even at a moderate angle of incidence θ. The electron emission can be recorded in coincidence with the scattered atoms or ions [60]. In our setup, only the retractable detector has a time resolution suitable for such coincidence detection allowing trajectory-dependent electron emission to be identified [61, 62]. The electron emission can be resolved in projectile energy loss with a pulsed beam [63]. For instance, this type of detector arrangement was used to identify the population of excitons and explain why large band-gap ionic insulators emit more electrons than metals under ion impact [64, 65].

3.3.2 Polar Angle Scan(θ-can)

The polar angle scan (θ-Scan) is one of the most often used working modes to acquire the experimental data in this thesis. A θ-Scan is a step-wise variation of the angle of incidence θ_i at fixed azimuthal angle ϕ_i and beam energy E_i (See Fig. 3.1 for the definition of the scattering geometry). For simplicity, we consider here that ϕ_i is zero so that the projection of the beam direction on the surface coincides with a low index direction of the crystal as in Fig. 4.2. A compact and visual way to display the evolution of the diffracted intensities in this θ-Scan is to plot the intensities on the Laue circle in a 2D color map (diffraction chart).

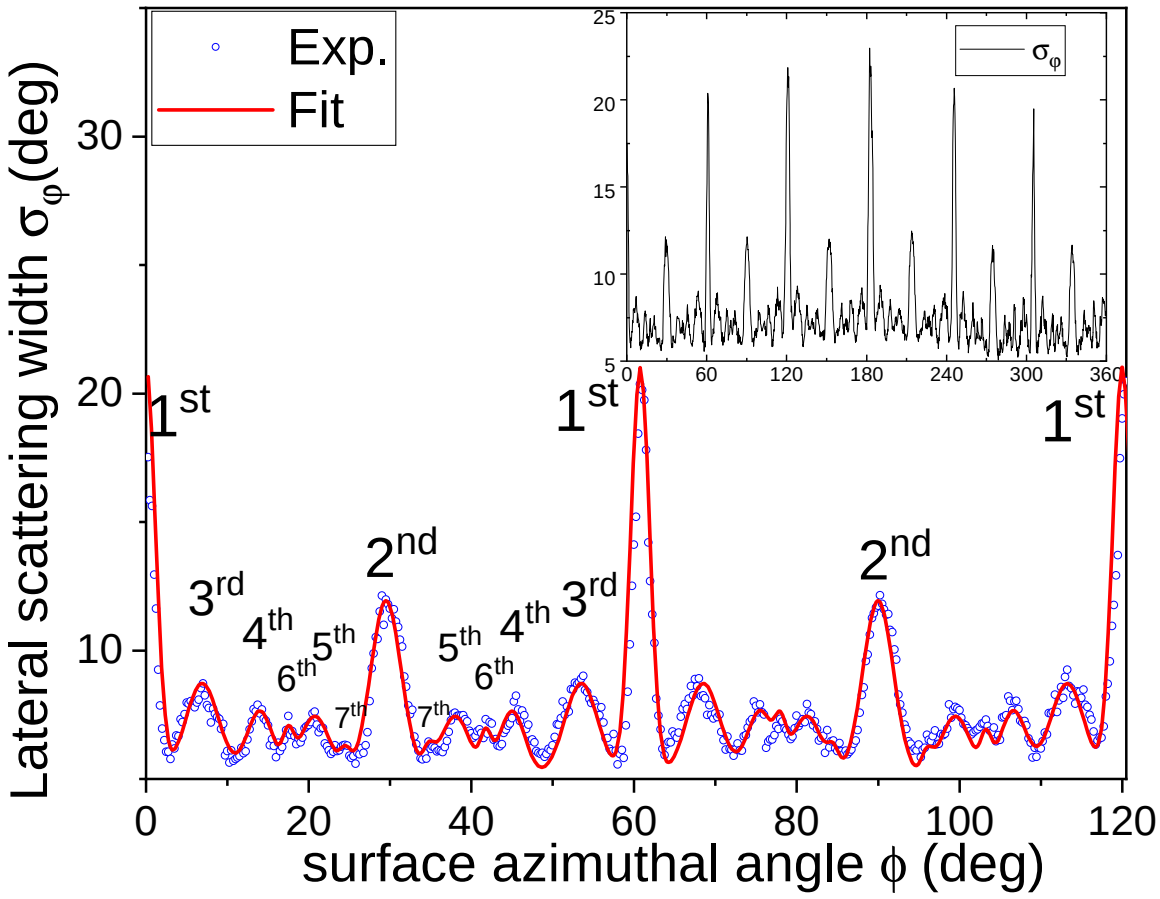

Figure 3.6 A triangulation curve identifying the topmost channeling directions corresponds to tracking the mean width σ_φ of the scattering profile during a ϕ-scan or in-plane rotation. With $\varphi = \arctan\frac{k_y}{k_z}$ is related to the deflection angle in the 2D perpendicular plane.

Since the diameter of the Laue circle is proportional to the angle of incidence, the length of the half-circle above the surfaces links to the incidence angle θ_{in}.

3.3.3 Atom Beam Energy Scan (E-Scan)

An energy scan (E-Scan) is a step-wise variation of the primary atom beam energy E, fixing the incidence angle θ_i and azimuthal ϕ_i. During an E-Scan, the radius of the Laue circle is constant. However, the Bragg angle $\phi_B = \arctan(G_y/kcos\theta_i)$ gets lower as the energy increases so that more diffraction orders can be observed until they cannot be resolved experimentally. In Fig. 3.9 show a typical E-scan of Ne atoms on a LiF(001) surface along $\langle 110 \rangle$ direction with θ_i=0.42° and ϕ_i=0°. Dotted white lines indicate the positions of Bragg peaks.

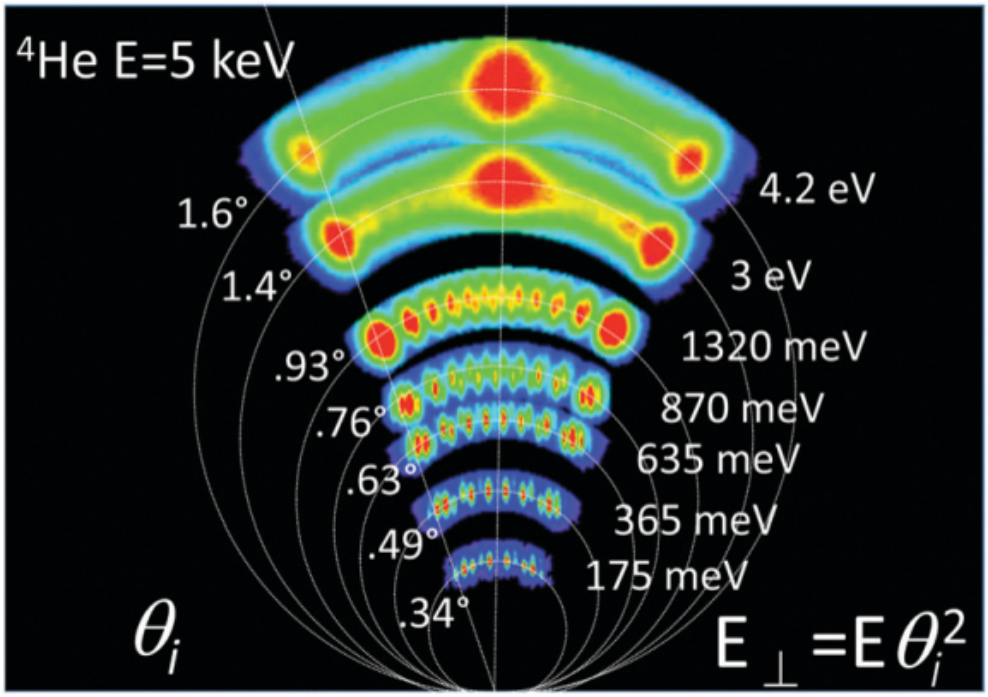

Figure 3.7 A typical result from θ-scan with 5 keV helium projectiles on LiF$\langle 110 \rangle$), superposition of 7 diffraction patterns at different polar incidence angles θ_i. Above 1 eV, there is no clear evidence of elastic diffraction as a well-defined Laue circle, but several quantum features remain present and progressively fade away at larger values of $E_\perp$. From ref[16].

3.3.4 Sample Temperature Scan (T-Scan)

The sample temperature scan (T-Scan) controls the temperature variation of the samples, by heating through a power supply connected to the sample holder or cooling down by liquid nitrogen (LN2).

In principle, a T-scan would consist of a simple variation of the target temperature leaving all other parameters unchanged. Unfortunately, this is not compatible with the extreme sensitivity of grazing incidence. In GIFAD, the target surface is easily positioned within 10 to 20 μm from the beam. If it is not enough inserted, the primary beam is still present on the image, whereas if it is too much inserted, even the scattered beam disappears. However, thermal expansion of the target crystal and the manipulator induce much larger displacements and minor angular tilts producing major effects in GIFAD. Instead, we waited for a stable temperature before realigning the target and performing a θ-scan. We interpolate between measured angular values from these variations to restore a temperature variation.

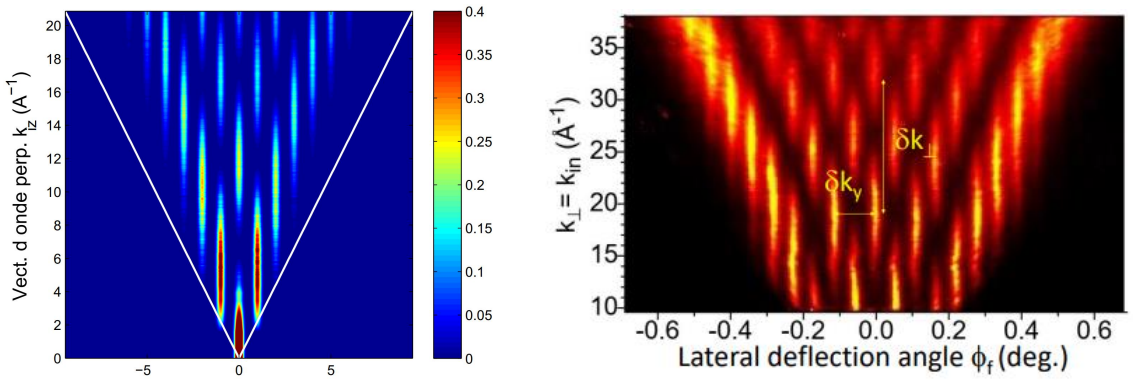

Figure 3.8 A θ-scan diffraction chart is constructed by selecting (for instance, from Fig.3.7), only the intensities on the Laue circle and also by adopting a very small step size giving the appearance of a continuous evolution with θ_i. On the left, the chart corresponds to He along LiF$\langle 110 \rangle$ (from ref.[66]) while on the right, it corresponds to Ne on LiF$\langle 110 \rangle$ (from ref.[67])

3.4 Data Treatment and Analysis

Several important corrections have to be applied to obtain absolute GIFAD intensities with the imaging detector system. The present procedure involves four different steps: (a) subtraction of the CMOS dark current and the offset of the analog to digital converter; (b) correction of the spatial distortion induced by the Hamamatsu-CMOS detector; (c) correction of the small spatial inhomogeneities in the quantum efficiency; (d) conversion of the raw data intensities to absolute value. The procedure is similar to other X-ray diffraction techniques recording scattered photons by the CCD camera system[68].

$$\Delta I_s = \frac{f_{corr}(I_{Data,raw} - I_{Bg,raw})}{I_{qe}}$$

After we recorded the diffraction pattern by the imaging detector system (see chapter. 2.5), we will not consider the nature of the position-sensitive detector used to record the diffraction pattern as a 2D image. We assume that the detector is far from the surface and perpendicular both to the surface plane and the plane of incidence, so that the number of counts in each pixel (x,y) corresponds to an intensity map in momentum space (k space) I(k_x,k_y). In the present case (see Fig. 2.1), one CMOS (1920*1440) pixel corresponds to a scattering angle of 0.00284° ($\sim 5 \times 10^{-5}$ rad). Similar to standard crystallography, two types of information can be extracted. The surface lattice unit is reflected in the peak spacing satisfied with the Bragg condition. Furthermore, the relative peak intensities depend on the scattering amplitudes determined by the shape of the electron density at the surface.

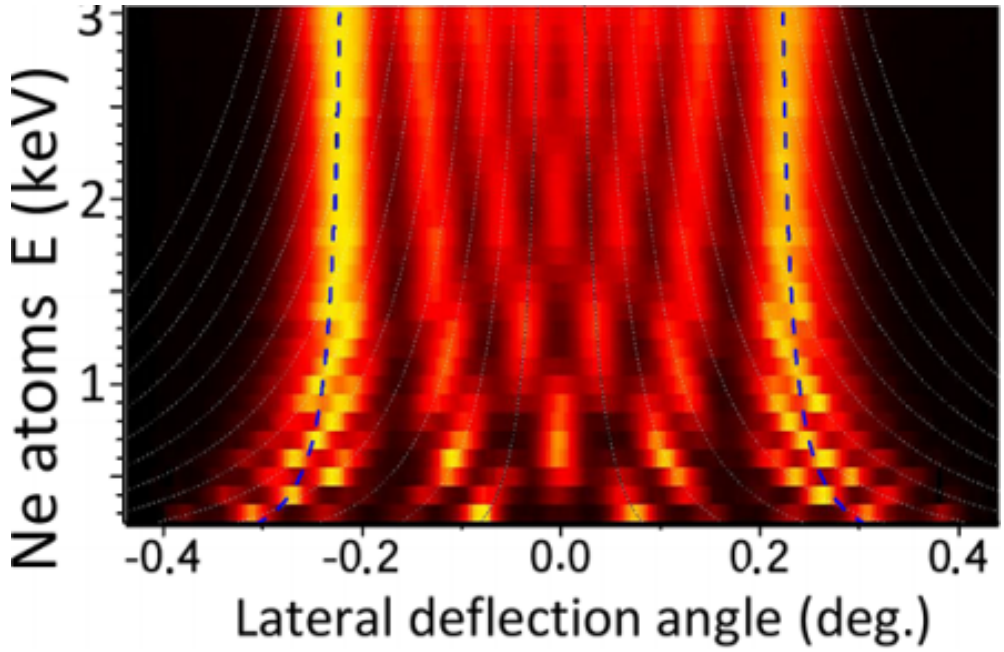

Figure 3.9 A typical result of diffraction charts from Ne atoms E-Scan along LiF⟨110⟩, the incidence angle is fixed at $\theta = 0.42°$, and the total kinetic energy E varied in the range of 0.3 to 3 keV. The blue dashed line is for an optical refraction model (see sec.9.5). Note that in an E-scan, the Bragg angle varies as pointed out by the dotted lines. Taken from ref.[67]

3.4.1 Background Subtraction

The background pattern of the detector without a beam is recorded at the beginning for the same exposure time as the diffraction pattern. In this way, the CMOS dark current and the fixed offset of the AD-conversion are subtracted in a single step. Dark images are taken before triggering the kinetic process during fast time-resolved experiments. In practice, multiple dark images are acquired and averaged after the camera has reached thermal equilibrium to reduce noise and avoid thermal noise.

3.4.2 Polar-like Transformations

We usually apply polar transformation[69] to convert the intensity on the Laue circle onto a line. A standard polar transform in Fig. 3.10 (a), centered on the Laue circle and associating $(k_x, k_y) \rightarrow (\alpha, \left|\vec{k_{out}}\right|)$ with $\alpha = \arcsin k_x/k_y$ and $\left|\vec{k_{out}}\right| = \sqrt{k_x^2 + k_y^2}$. Such transform will not preserve the Bragg comb structure $k_x = nG$. The polar-like transform is to keep the k_x coordinate unchanging and to consider the transformation as $(k_x, k_y) \rightarrow (k_x, \left|\vec{k_{out}}\right|)$, define the direct beam as original point (0,0), and the radius of this circle defines the effective momentum $k_{eff} = k_y/2 + k_x^2/k_y$. The associated polar transform now is $(k_x, k_y) \rightarrow (k_x, 2k_{eff})$, as sketched

in Fig. 3.10 (b). For a direct beam, it should be invariant after such a polar-transform as shown in Fig. 3.4.

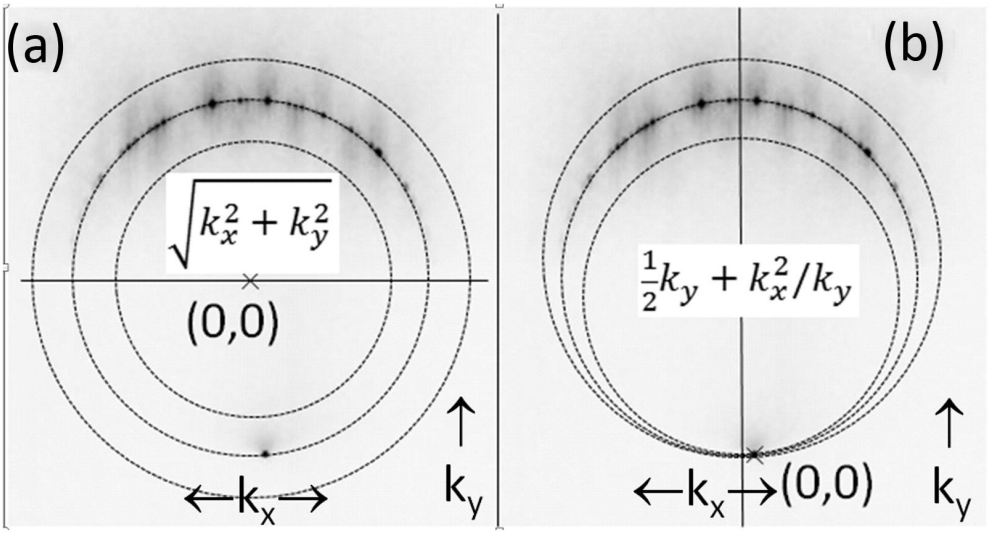

Figure 3.10 Schematic view of two options for polar-like transformations. In Fig. (a), the center of the Laue circle is the reference. In Fig. (b), the reference is the direct beam. The figure corresponds to the $\beta_2(2\times 4)$ GaAs surface.[10] and are taken from Ref. [69].

3.5 Specific Distributions

We mainly use Gaussian distribution for elastic components and log-normal distribution for inelastic components to do the best-fit of polar scattering angular distribution profiles.

3.5.1 The Normal (Gaussian) Distribution

Normal (or Gaussian or Gauss) distributions are important in statistics and are often used in science to represent a real-valued random variable. The general form of normal (Gaussian) distribution is defined as

$$f_N(x;\sigma,x_0) = \frac{1}{\sigma\sqrt{2\pi}}\, e^{-\frac{(x-x_0)^2}{2\sigma^2}}$$

Where the parameter σ is the standard deviation, the variance of the distribution is σ^2. The parameter x_0 is the mean or expectation of the distribution (and also its mode and median). If the considered function is the density of Normal distribution of the form, then the full width at half maximum (FWHM) is: FWHM $= 2\sqrt{2ln2}\sigma \approx 2.355\sigma$.

3.5.2 The Log-normal Distribution

The log-normal distribution is defined as

$$f_{LN}(x;w,x_0) = \frac{1}{xw\sqrt{2\pi}}\, e^{-\frac{(\ln\frac{x}{x_0})^2}{2w^2}}$$

where x_0 and w are the median and width, respectively, of the random variable $x = e^y$ The log-normal distribution $LN(x_0, w^2)$ and the normal distribution $N(x_0, \sigma^2)$, also known as Gaussian distribution, are closely linked, $\sigma^2 = e^{w^2}(e^{w^2} - 1)x_0^2$ where x_0 is the mean value in the Gaussian distribution and is the median value in the log-normal. Reversely, knowing, x_0 and σ from a Gaussian distribution, the equivalent relative width $w = \sqrt{\ln\frac{1+\sqrt{1+4\sigma^2/x_0^2}}{2}}$. The mean value of a log-normal distribution is $\langle x\rangle$ or $\bar{x} = x_0\, e^{w^2/2}$, $\bar{x} = x_0\, \exp\left(\ln\frac{1+\sqrt{1+4\sigma^2/x_0^2}}{2}\right)$.

The QBCM has some predictive power but fails to explain the increase of the inelastic scattering profile at low values of $E_\perp$. More precisely, during an E-scan, where the angle of incidence θ_i stays constant, the QBCM predicts that the number of collision sites should remain constant and that each inelastic event has a fixed contribution in scattering angle. At low values of $E_\perp$, in the quasi-elastic regime, only one inelastic collision is expected to contribute ($p_i << 1$), and therefore the inelastic scattering profile should stay constant. This is not what we observe. We try below to develop a model that considers the attractive forces and evaluates the consequences. The application of normal distribution and log-normal distribution in GIFAD see Appendix C.

3.6 Elastic Diffraction and Inelastic Scattering Patterns

Taking advantage of the wave-particle duality of matter, such as atoms or molecules. particle-surface scattering(more considered particle nature), or diffraction(wave nature) experiments were observed more than a hundred years ago. The mechanism is generally regarded from the standpoints of two extreme regimes: the quantum regime and the classical regime[70, 71].

The scattering of particles, such as atoms and molecules, is one of the most fundamental particle-surface interactions. It consists of elastic and inelastic scattering such as single-collision and multi-collision. The dominant scattering channel is governed by the collision parameters of particles with the surface, such as the mass of probe and surface atoms, surface temperature, incident angle, energy transfer of incident primary beam, the property, and quality of the surface, etc.

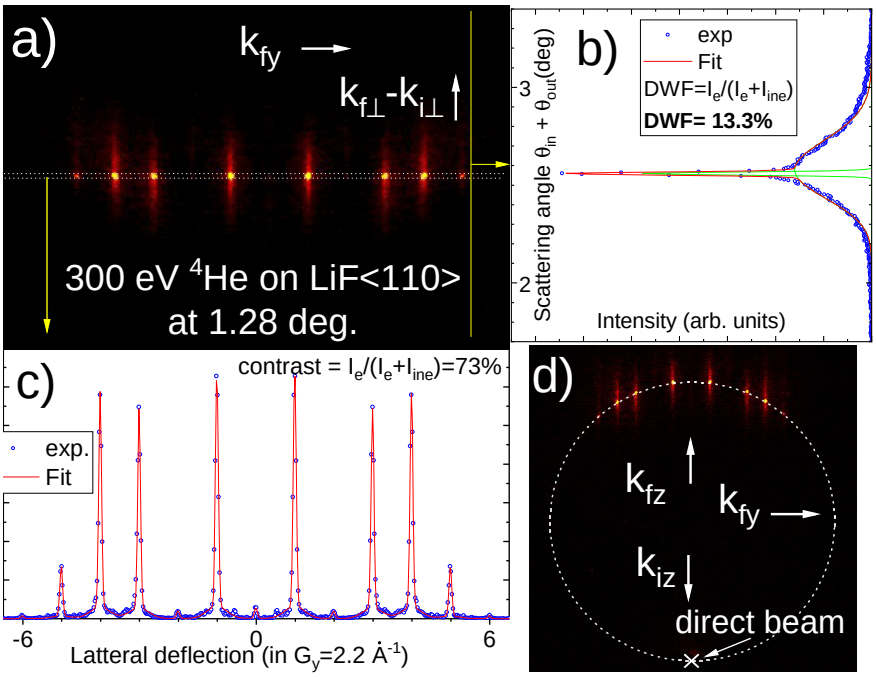

Figure 3.11 a) Quasi polar transform of the raw diffraction image in panel d). Panel b) corresponds to a full projection onto the vertical axis producing the polar scattering profile. Experimental data are fitted using the sum of a narrow Gaussian and a broad log-normal profile. Panel c) corresponds to the intensity in a narrow horizontal band centered on the specular reflection. From ref.[72].

3.6.1 Polar Profiles

Here, first, we will focus on the polar scattering angular distribution profiles (See Fig. 3.11 b).).*i.e.*, we focus on the atom-surface interaction along the z-direction, see the scattering geometry in the x-z plane Fig. 3.12. After the polar-like transform, such a complex 2D (y-z plane) problem reduced to the 1D problem. Through appropriate data processing and transformation, the elastic and inelastic components can be well separated along the Laue circle (see Fig. 3.11). Such distribution along z regardless of crystal orientation, as shown in Fig. 6.4.

3.6.2 Lateral(Transverse) Profiles

The lateral profile (See Fig. 3.11 c).). In Ref.[73], the lateral profile of He/LiF is described as made of two components, a broad and a narrow one. This empirical approach suggested a modified Debye-Waller factor (DWF) where divided by N_{eff} where N_{eff} is the effective number of scattering centers involved in the classical trajectory. This effective number of

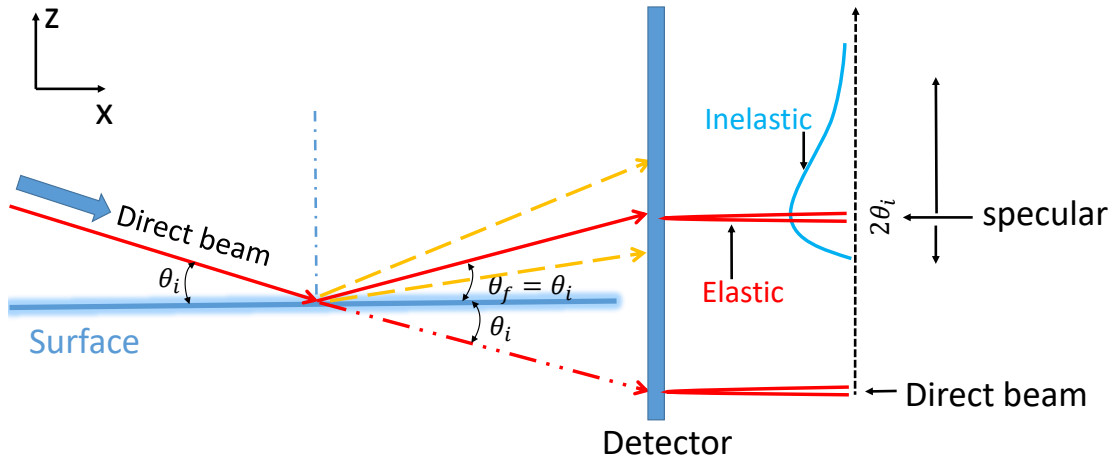

Figure 3.12 Schematic illustration of elastic (specular peak) and inelastic scattering geometry in the x-z plane. The direct beam can be easily recorded by removing the sample.

scattering centers was linked to the DWF in more detail in Ref.[74] using the Classical energy loss associated with such a grazing trajectory.

In Ref. [75], the transverse scattering profile recorded with He/LiF along a Random direction was analyzed in terms of a Lorentzian profile. However, this profile is a trade-off combining elastic and inelastic contributions.

In ref[71], a first attempt was made to derive an inelastic lateral scattering profile based on classical trajectory simulation and a Lamb-Dicke model. The line shape could not be confirmed unambiguously. Experimentally, the Lorentzian profile gives a decent description, but the detailed comparison with the experiment shows that it has too long tails, so that -1) the contrast is reduced, impairing the de-convolution of weak peaks -2) the rainbow peaks where several diffraction orders contribute extend too far outside (Airy peak).

We propose a new empirical description of an exponential attenuation of the intensity. The resulting line profile is obtained by convolution by the primary beam profile.

The lateral scattering profile is $P(\phi) \propto e^{-|\phi|/\phi_0}$. Its mean values is centered at the elastic diffraction location and the second moment of this distribution is $m_2 = 2\int_0^\infty (e^{|\phi|/\phi_0})^2 d\phi = \phi_0$ where ϕ_0 is the typical range of the momentum transfer. After convolution by the primary beam profile, the distribution has a broader tail than a Gaussian profile but significantly less than a Lorentzian profile.

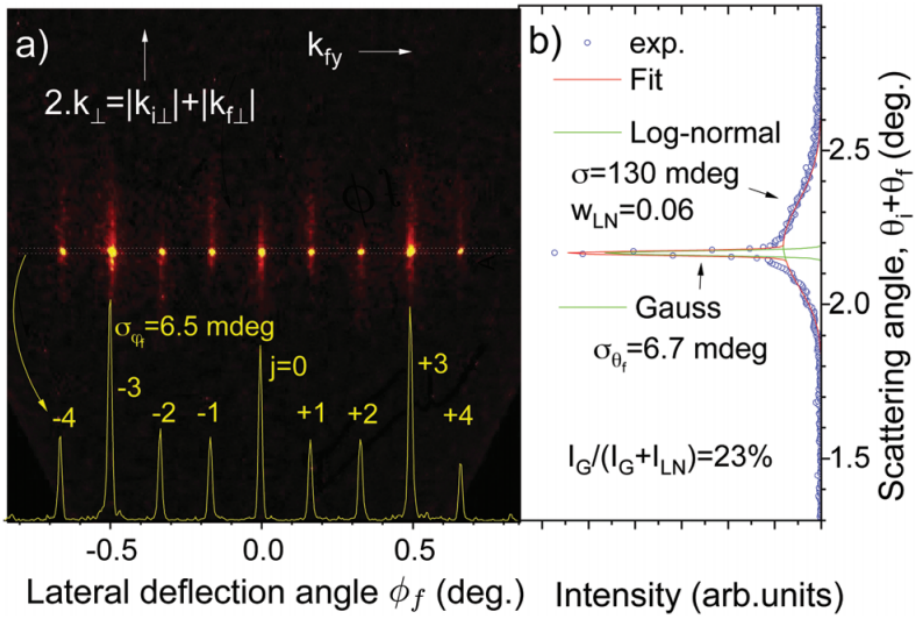

Figure 3.13 (a) A typical diffraction pattern after the polar transform, the Laue circle is now a horizontal line. (b) The polar profile (scattering angular distribution) shows well-separated components, the narrow one fitted by Gaussian distribution and the much broader one fitted by a quasi log-normal distribution, from ref.[72]

3.6.3 Separation into Elastic and Inelastic Scattering

For most of the systems investigated, the polar profile (see Fig. 3.13 b).) is well-fitted by the sum of log-normal distribution and a Gaussian distribution having the same Gaussian width σ_e as the primary beam, see Fig. 3.3. To make the best separation between elastic and inelastic scattering components, the following analysis method is applied to the several polar angular intensity distributions of scattered atoms from the surface obtained at different experimental conditions, by varying incident angles (θ_{scan}), primary beam energy (E_{scan}), and surface temperature (T_{scan}). As shown in Fig. 3.13 b). Equation used for the fitting analysis is described as

$$I_{total}(E,\theta,T) = I_{elastic} + I_{inelastic} = A_N + A_{LN} + B$$

where A_N is the elastic scattering component is best fitted by Normal (or Gaussian) distribution, which has the same width and shape as the direct beam. A_{LN} is an inelastic scattering component is fitted by Log-Normal distribution. B is the background noise. Now, the elastic and inelastic linked by Normal distribution and log-normal distribution have such a

relationship:

$$\text{Elastic}: \; G[\theta_i;\sigma](\theta) = \frac{A_N}{\sigma\sqrt{2\pi}} \exp\left(\frac{-(\theta-2\theta_i)^2}{2\sigma^2}\right)$$

$$\text{Inelastic}: \; LN[\theta_m;w](\theta) = \frac{A_{LN}}{w\theta\sqrt{2\pi}} \exp\left(\frac{-\left(\ln\frac{\theta}{\theta_m}\right)^2}{2w^2}\right)$$

with a variance $\sigma_{ine}^2 = e^{w^2}(e^{w^2}-1)\theta_m^2$

and reversely $w = \left(\ln\frac{1+\sqrt{1+4\sigma_{ine}^2/\theta_m^2}}{2}\right)^{1/2}$

3.6.4 Elastic and Inelastic Scattering Width and Intensity

After we separated the elastic and inelastic components of the polar profiles, the best-fit by the sum of log-normal distribution and a Gaussian distribution having the same Gaussian width σ_e as the primary beam, see Fig. 3.3. However, the elastic contribution is not clearly resolved when the elastic ratio is less than a few percent. We usually impose the elastic width used in the fit to be the same as the primary beam's. It should be stated that sometimes, the direct beam which is systematically recorded before or after target insertion, is better fitted by a non-Gaussian profile, in these cases, the same profile is used in the fitting de-convolution. In some cases, with our best angular resolution, there could be indications of a slight broadening at the base of the elastic peak compared with the direct beam's shape. However, the effect could also be due to the deformation of the inelastic profile that a log-normal profile would poorly describe. This aspect will not be discussed further.

Chapter 4

Elastic Diffraction and Theoretical Description

If, in some cataclysm, all of the scientific knowledge were to be destroyed, and only one sentence passed on to the next generations of creatures, what statement would contain the most information in the fewest words? I believe it is the atomic hypothesis (or the atomic fact, or whatever you wish to call it) that all things are made of atoms—little particles that move around in perpetual motion, attracting each other when they are a little distance apart, but repelling upon being squeezed into one another. In that one sentence, you will see, there is an enormous amount of information about the world, if just a little imagination and thinking are applied[76].
-Richard Feynman

4.1 Overview

In this chapter, we try to model the interaction of the fast atom with a surface. First, the basic concepts for understanding probe atoms, then the description of crystal surface (*e.g.* LiF). Same as any other diffraction technique, the fast atom elastic diffraction information reveals the periodic structure of the crystals. So far, fast atom elastic diffraction on surfaces has been treated as the quantum dynamics of the projectile atoms evolving in the potential energy landscape (PEL) or PES, assuming that all surface atoms rest at equilibrium positions.

4.2 Description of Probes: Neutral Atoms

Elastic Diffraction of fast ions on surfaces has never been observed. The reason is probably that ions interact too strongly with the surface. The electric field of the ions polarises the surface, inducing displacements of the surface electrons and ions with specific time scales. This is usually modeled by image force attraction with a typical eV magnitude [77, 34]. Atoms interact much less. At a large distance from the surface, the forces are dominated by van de Waals forces, more precisely by long-range dispersion forces. The short-range repulsive forces responsible for the reflection of the probe atom are the Pauli repulsion which is expected to scale with the surface electronic density. The ideal probe of this electronic density would be an atom as compact as possible and hardly polarizable. In this respect, the best candidate is helium, the most compact atom and the hardest to ionize and deform. Compared with atomic force microscope (AFM), which also probes surface electronic density, the helium atom is an ideal tip. We also used Ne, which has a comparable ionization potential, and other noble gas atoms in the chapter 8.

4.3 Description of Surface

Every real solid is bounded by surfaces. The surface atoms are only visible in surface-sensitive experimental microscopic techniques or by studying properties or processes determined by surface atoms only. Most aspects of surface descriptions and surface crystallography are natural extensions of the concepts used in the concept of bulk materials. Since the main concepts of bulk crystallography can be found in every textbook about solid-state physics. (*e.g.* [81, 82]). Here, we pay more attention to the crystal surface. A geometrical construction in describing crystal surfaces is that of a lattice plane, which is usually denoted by *Miller indices (hkl)* where *h, k, l* are the integer reciprocal axis intervals given by the intersections of the lattice planes with the three crystallographic axes. They have a simple meaning in the case of rectangular crystal systems, such as the cubic system. For example, the symbol (100) denotes lattice planes perpendicular to the cubic x-axis, and (110) means the lattice planes perpendicular to the face diagonal in the first quadrant of the XY-plane of the cubic unit cell.

In the case of lattice planes, it is convenient to relate them to a linear combination.

$$\tilde{\mathbf{n}} = \frac{1}{2\pi}\left[h\mathbf{b_1} + k\mathbf{b_2} + l\mathbf{b_3}\right]$$

Where $\mathbf{b_j}$ (j=1,2,3) are the primitive vectors of the reciprocal lattice with the integer number *h, k, l*. The vectors $\mathbf{b_j}$ are directly related to the primitive lattice vector $\mathbf{a_i}$ (i=1,2,3) by the

Table 4.1 Crystal properties* of LiF(001), KCl(001).

Property (at 300K)	LiF(001)	KCl(001)
Bulk lattice constant (Å)	4.03	6.29
$\langle 110 \rangle$ surface lattice constant (Å)[a]	2.84	4.45
$\langle 100 \rangle$ surface lattice constant (Å)	2.02	3.15
Melting temperature (K)	1115	1049
Bulk Debye temperature (K)[b]	734	235
Surface Debye temperature (K)	350-610, 550[c]	159
Density (10^3 kg m^{-3})	2.635	1.984
Ionization Energy (eV)	11.3[d]	8.4
Surface stiffness (Å^{-1})	3.45	2.97

*Most of parameters from Ref. [78]. [a]For a simple cubic lattice. [b]Ref. [79] [c]Ref. [72]. [d]Ref. [80]

relation

$$\mathbf{a_i} \cdot \mathbf{b_j} = 2\pi\delta_{ij}.$$

A lattice plane can be characterized by the *Miller indices (hkl)*, hence, a normal parallel to the reciprocal lattice vector.

$$\mathbf{G}_{hkl} = h\mathbf{b_1} + k\mathbf{b_2} + l\mathbf{b_3}$$

The property of the vector $\mathbf{G}_{hkl}$ of the reciprocal lattice can be proven to characterize the lattice planes by all possible Bravais lattice points.

$$\mathbf{R}_l = \sum_{i=1}^{3} n_{li}\mathbf{a_i}$$

4.3.1 Structure of LiF Crystal

This manuscript mainly uses lithium fluoride(LiF) as a standard sample. It has been used for a long history in Helium atom scattering (HAS) investigation. In recent years, LiF are employed

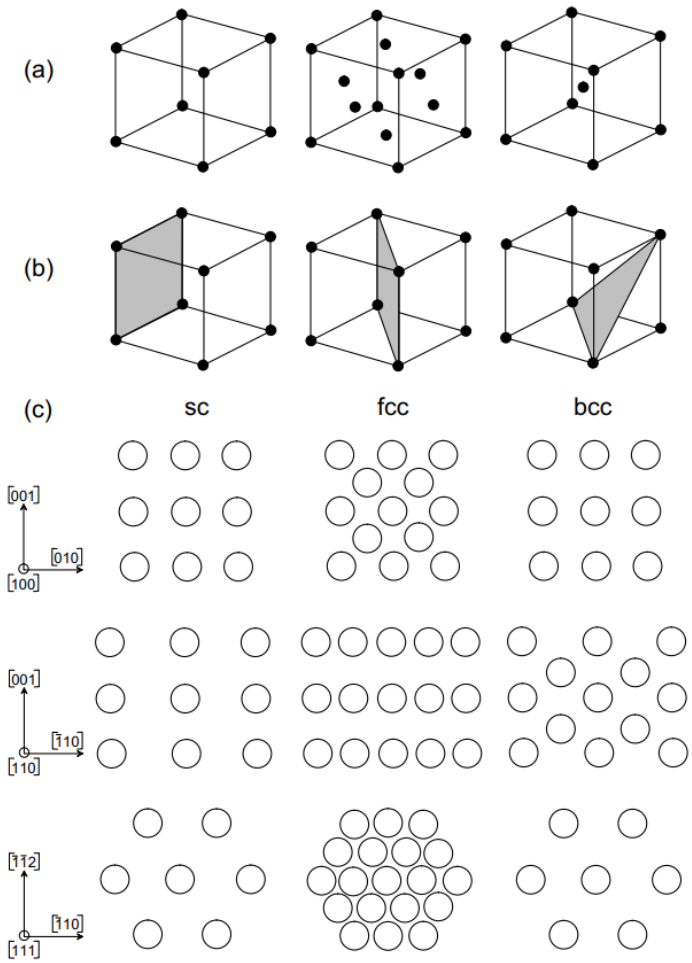

Figure 4.1 (a) Cubic Bravais lattices sc, fcc, bcc; (b) low-index planes (100), (110), (111) in a sc cell; (c) low-index planes resulting from cubic lattices. Bravais lattice points are indicated as dots (a,b) or spheres (c) and taken from Ref. [54]

in various applications such as lithium (Li)-ion batteries[83], organic electroluminescence devices[84], and solar cell[85]. Among the alkali halide thin films, LiF has the smallest lattice constant (a=4.03Å) and largest bandgap (E_g=13.6 eV) [86, 87].

A complete characterization of a solid surface requires knowledge of not only atoms of "what elements" are present but also "where" they are. Furthermore, how are they moving on the surface? Just as in bulk, it is not that the atomic coordinates are of much direct interest. Instead, besides the chemical nature of the atoms, their geometrical arrangement governs the electronic, magnetic, optical, and other properties of surfaces.

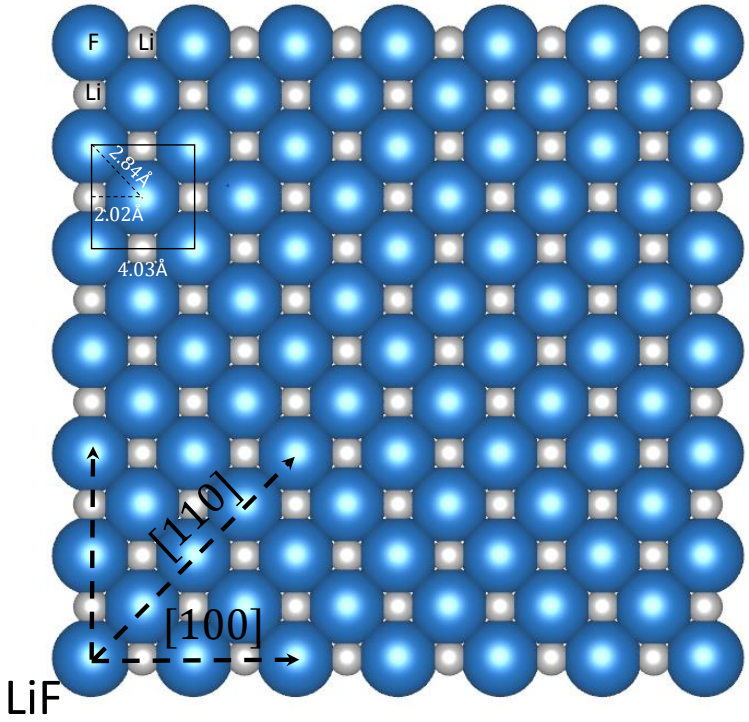

Figure 4.2 Schematic representation of the LiF(001) surface is shown,for the incident beam along the $\langle 100 \rangle$ and $\langle 110 \rangle$ direction. The Fluorine (blue) and Lithium (grey) atoms form a separated row. Physical parameters from Material Projects[88] and drawn by VESTA software[89].

4.3.2 Surface Work Function

Work function is a fundamental property of any surface. It is defined as the minimum amount of energy required to remove the most loosely bound electron from the surface to the vacuum. For the LiF crystal used in our experiment, the reported work function or binding energy is between 11.3 eV[80] and 13 eV[64].

4.4 Theory of Elastic diffraction at Surfaces

The elastic diffraction information reveals the periodic structure of the crystals. So far, fast atom elastic diffraction on surfaces has been treated as the quantum dynamics of the projectile atoms evolving in the potential energy landscape (PEL), often called potential energy surface (PES). $V_{3D}(x,y,z)$ is created by assuming that all surface atoms at equilibrium positions. In other words, quantum dynamics is a powerful tool linking the unknown PEL

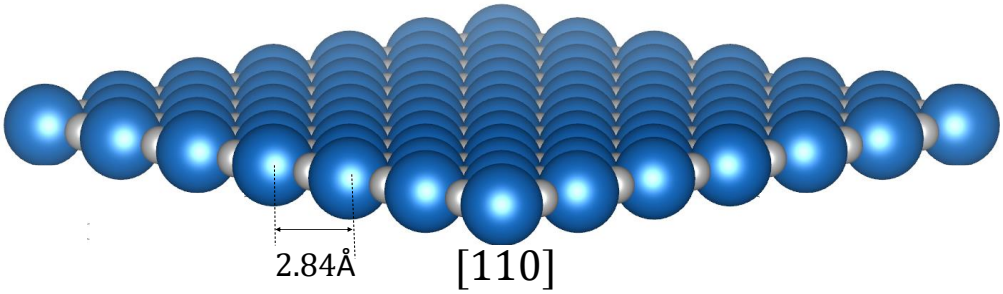

Figure 4.3 Schematic view of the $\langle 110 \rangle$ direction of LiF(001) surface. The Fluorine (blue) and Lithium (grey) atoms form separated rows. Physical parameters as shown in the figure with a_y=2.84 Å.

to the measured diffracted intensities. Assuming that the quantum scattering can be treated exactly, both theoretical calculations and experiments are trying to measure the PEL as precisely as possible, and to provide physical parameters such as atomic positions, surface work function, and attractive physisorption well depth.

4.4.1 Axial surface channeling approximation

The axial surface channeling approximation (ASCA) states that, at grazing incidence, the individual surface atoms are invisible. In Fig. 4.3 above, we see well-aligned rows of atoms, but we also clearly see the individual atoms, so why is the ASCA so strongly established in GIFAD? There are two arguments: one is energetic, and the other states that the coupling is very weak and almost geometric. From a perturbation point of view, the transition probability between two discrete states $|\Psi_0\rangle, |\Psi_1\rangle$ separated by an energy ΔE and coupled by a term $\langle \Psi_0 | W | \Psi_1 \rangle$ is $P = (W/\Delta E)^2$ where both the coupling W and the energy difference ΔE are important.

Let us consider one state associated with specular reflection where no reciprocal lattice vector is exchanged with the surface and the other where a surface reciprocal lattice vector $\vec{G}(mG_x, nG_y, 0)$ is exchanged between the crystal and projectile with momentum $\vec{k_i}(k_{ix}, k_{iy}, k_{iz})$.

The final momentum is now $\vec{k_f}(k_{fx}, k_{fy}, k_{fz}) = (k_{ix} + mG_x, k_{iy} + nG_y, k'_{iz})$ and its energy is $\propto (k_{ix} + mG_x)^2 + (k_{iy} + nG_y)^2 + k'^2_{iz}$. At this point, there is no apparent difference between the x and y directions, except that in GIFAD, $k = \sqrt{2mE}/\hbar \sim k_x$ is 100 to 1000 Å^{-1} for He, much larger than $G = 2\pi/a \sim \text{Å}^{-1}$. Grazing incidence also means that $k_{ix} \gg k_{iz}$ since $\theta = \text{atan}\,\frac{k_{iz}}{k_{ix}}$. k_{iy} is also supposed to be much smaller than k_{ix}, we can even simplify considering a projectile

well-aligned with the crystal axis so that $k_{iy} = 0$. The energy is then $k_{ix}^2 + m^2 G_x^2 + 2mk_{ix}G_x + n^2 G_y^2 + k_{iz}'^2$. We see that the price to pay for $m \neq 0$ is much more than for $n \neq 0$ because of the cross term $2mk_{ix}G_x$ which is much larger than G_x^2 or G_y^2 because typical value of k_{ix} are at least two orders of magnitude larger than the unit reciprocal lattice vector $G_x \sim G_y$. So the energy needed for diffraction along x is much more than for diffraction along y. What about the coupling terms? The one deflecting the projectile to the left or the right (y direction) is the integral of the lateral forces along y. It should be similar in magnitude to the term responsible for specular reflection (along z), since lateral deflection can be of the same order of magnitude as the angle of incidence, producing scattering up to 45° on the Laue circle (see Fig. 3.12) While the one coupling to the x has a specific peculiarity that it tends to be almost zero. The deceleration when approaching each atom is almost equal to the acceleration when receding. Since the velocity along x is almost constant, the action of the force is very close to zero. This is visible in Fig. 4.5 where the red line standing for γ_x is plotted. As a result, exchanging a reciprocal lattice vector parallel to x costs more than 100 to 1000 times more energy and has a much smaller coupling than in the y direction. How much smaller is the coupling? It is exactly equal to zero in the trajectory section where z is constant, *i.e.*, close to the turning point z_t where the force is maximum. Due to the small slope ($\dot{z}$) on the way in, the re-acceleration on each atom could be slightly larger than the deceleration, but this should be almost exactly opposite on the way out where the slope has changed sign. All these arguments were presented in one of the first GIFAD papers [5] using wave packets. They were analyzed in detail in a dedicated theoretical paper [90] using close coupling and confirmed by many other authors, for instance, in Diaz *et al.* [91] using Multi-configuration time-dependent Hartree (MCTDH). The reduced coupling was also identified in TEAS,[92] but surprisingly, emphasis was given to "Pronounced out-of-plane diffraction" whereas out-of-plane has always been present and that the specificity is more a reduction of the in-plane scattering.

Another estimate was given by Debiossac and Roncin [32] when adapting to GIFAD. The work of Carsten Henkel[93] derived in the context of cold atom diffraction in an optical lattice. In this work, the efficiency of the coupling under oblique incidence is estimated from the Kapitza-Dirac incidence factor[94] predicting, in 1933, the stimulated Compton scattering *i.e.*, the diffraction of electrons by optical standing waves:

$$\beta_{KD} = exp(-\frac{1}{2}(kw\ cotan\theta)^2) \tag{4.1}$$

It describes the exponential attenuation quantitatively due to the spatial averaging of the potential modulation. The damping is much faster than exponential due to the vertical

asymptotic branch of the tan function for grazing angle. The term kw in Eq. 4.1 describes the attenuation of the light intensity and can be related to the range $R_c = 1/\Gamma$ of the surface interaction potential [32]. Note that the formula derived by Henkel from first-order perturbation theory did not reproduce the time-reversal symmetry correctly[95]. Debiossac and Roncin empirically restored this symmetry[32], but precisely calculated by second-order perturbation theory by Miret-Artés and Pollak [96–99].

The interesting aspect is that the longer the range of the potential ($R_c = 1/\Gamma$, the better is the ASCA. This is why it is not visible in Fig. 4.3 where the hard sphere model corresponds to $R_c = 0$, if a finite dumping of the electronic density could be used, then it would be impossible to distinguish the individual atoms below a given angle. Then, if no exchange of momentum

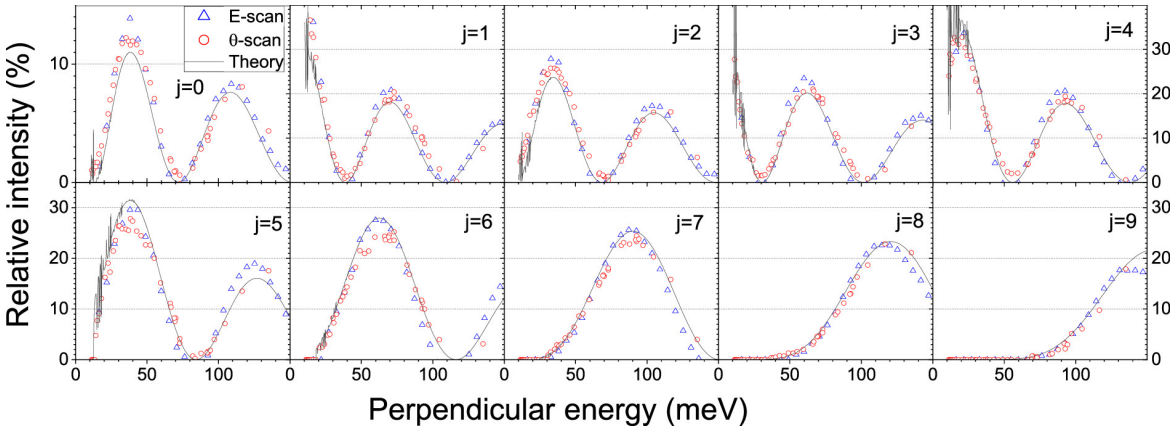

Figure 4.4 For Ne atoms scattered along the $\langle 110 \rangle$ direction. The intensity of the j_{th} diffracted beams are shown as a function of $E_\perp$, the energy of the motion in the (y, z) plane. For the degenerate $\pm$j diffraction orders, the summed intensity is shown. Diffracted intensities were measured during an E-scan (blue triangles and Fig.3.9) or θ-scan (red circles and Fig.3.8 right panel). The black line is for theoretical results. The very narrow peaks calculated at low energies reveal the bound state resonances. The PEL fit parameters are listed in Sec.4.5.3. Taken from Ref. [67].

along x is possible, this means that a uniform translation can replace the movement along x at velocity $v_\parallel$ and that we can replace the actual 3D potential energy surface $V_{3D}(x,y,z)$ by it 2D average along x, $V_{2D}(y,z) = \int_0^{ax} V_{3D}(x,y,z)dx$, as illustrated in Fig. 4.6 and Fig. 4.10 with a_x the unit cell along the probed crystal direction. For elastic diffraction, GIFAD is equivalent to a 2D problem with projectile impinging the potential averaged along the crystallographic direction with a wave vector $\vec{k}_\perp(k_{iy}, k_{iz})$. Therefore, the central prediction of ASCA is that, for a given crystallographic axis, the elastic diffracted intensity should only depend on $E_\perp = E\sin^2\theta_i$, so that varying the primary beam energy or the angle of incidence should produce identical results when plotted as a function of $E_\perp$. This is illustrated in Fig.

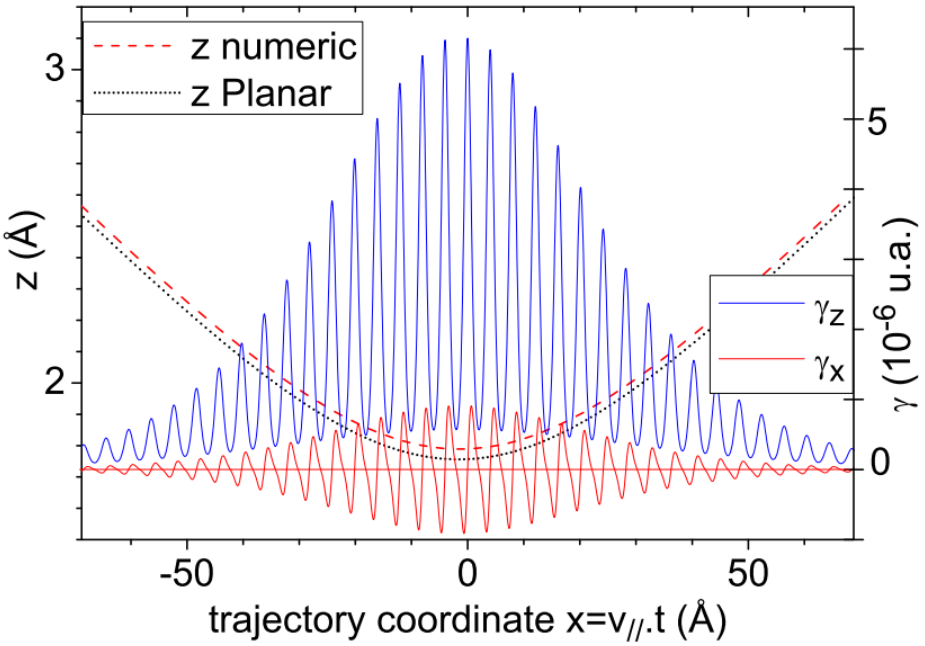

Figure 4.5 Classical trajectory z(x) of a 1 keV He projectile calculated on top of a row of fluorine atoms. Note that the z scale (left) is $\sim$ 100 times the x scale. The smooth trajectory is made of successive localized interactions with the surface atoms as illustrated by the components γ_x, γ_z of the acceleration along the trajectory (right scale), from ref.[71, 105].

4.4 where the blue triangle and red circles recorded during an E-scan and θ-scan respectively fall on top of each other.

As long as the ASCA holds (for limitations, see Ref. [90] for theory and Ref. [100] for the experiment), all theoretical methods developed for elastic diffraction at thermal energies should apply to GIFAD. These will be briefly discussed in the following sections.

In fact, the ASCA already had a long history in grazing incidence classical scattering on surfaces[101, 102, 34, 26, 59, 18, 103] where it was only an approximation since thermal movement ruins the exactitude, whereas it can be neglected in elastic diffraction, making ASCA a more 'exact' approximation. It was implicitly present in the prediction of GIFAD by Andreev [104] in 2002, but the paper did not attract proper attention, probably because there was no attempt to estimate the probability that diffraction is not blurred by decoherence.

In the left panel of Fig. 4.6, H. Winter*et al.* [18] showed a He atom in front of a LiF(001) surface the equipotential energy surface $V_{3D}(x,y,z)$=3 eV. The right panel shows the corresponding averaged potential $V_{2D}(y,z)$= 3 eV for channeling along the [110] direction(indicated by the arrow in the left panel).

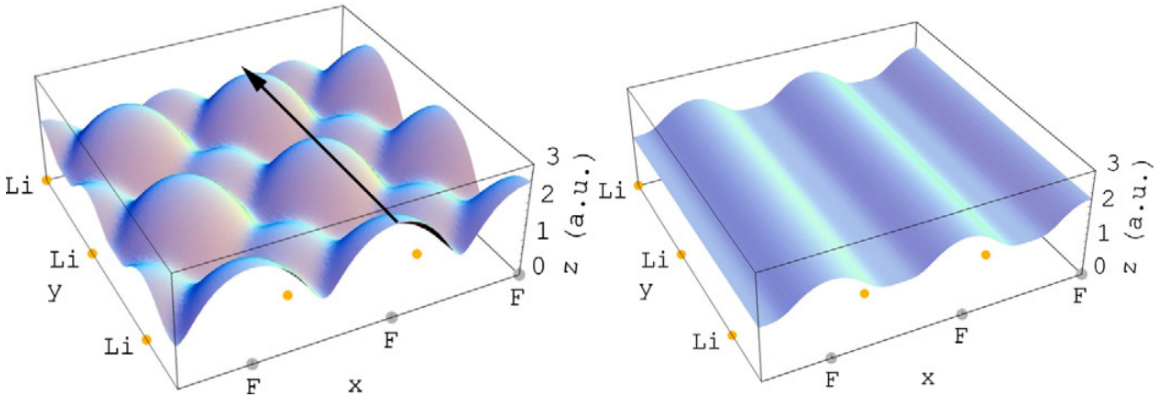

Figure 4.6 Left panel: Equipotential surface V (x,y,z) = 3 eV of interaction potential of He atom at LiF(001) surface from superposition of individually calculated interatomic pair potentials. Arrow indicates direction for averaging of V along y = [110] direction. Right panel: Effective potential for grazing scattering, equipotential surface V (x, z) = 3 eV for averaging of V (x, y, z) along y = [110] direction. Adapted from Ref. [18].

4.4.2 Theoretical methods in elastic diffraction

We start by indicating the methods developed in the context of GIFAD before extending to atomic diffraction, in general. According to the ASCA, elastic diffraction consists in calculating the quantum dynamics of an effective particle with energy $E_\perp$, and wave vector $\vec{k}_\perp(k_{iy}, k_{iz})$ in the potential energy surface averaged along the probed crystal axis. From the theoretical point of view, the ASCA is a considerable simplification since the effective wavelength $\lambda_\perp$ is much larger than the actual wavelength, reducing the numerical effort by orders of magnitude because of the typical quantization cell is on the order of $\lambda_\perp^2$ instead of λ^3. We assume here that the 3D PEL describing the projectile's energy at any point (x, y, z) above the surface is known so that its 2D average is a simple integration. For a crystal as simple as LiF, a 2D PEL is plotted in Fig. 4.10 for a neon projectile at LiF along $\langle 110 \rangle$ direction. The first method applied to GIFAD was a wave packet approach[106] developed by A.G. Borisov [5]. A similar technique was used by Aigner *et al.*[107]. The same wave packet technique also described the bound state resonance where the projectile is temporarily trapped into bound states above the surface. These were discovered by Frisch and Stern[108] soon after the first observation of atomic diffraction [4] and are considered as the most accurate determination of the attractive-well of the potential energy surface[109]. The general method of Multi-configuration time-dependent Hartree (MCTDH) was adapted to GIFAD by Diaz *et al.* [91] offering interesting perspectives for molecular projectiles. The close-coupling formalism, well suited to the discrete nature of diffraction was adapted to GIFAD by Zugarramurdi and Borisov[90]. Using a decomposition of the PEL onto a basis

set that have analytic Fourier transform, the method is fast enough to allow closed loop optimization of the PEL onto the experimental data [16].

Within the ASCA, all methods developed for TEAS should also apply to GIFAD. This is the case of atomic wave-packets[110] and close-coupling approaches[111, 112] but also the description in terms of Bohmian trajectories[113–115]. This also applies to all the classical, semi-classical, and optical models developed to simplify the quantum calculations. The semi-classical approach consists mainly in attaching a local WKB phase (see *e.g.*, Ref. [116] for a recent review) to classical trajectories, and then letting all trajectories with identical final momentum interfere. Such model have been developed by H. Winter and A. Schüller[18, 117] and Gravielle *et al.*[118–121] with specific additions to avoid the classical singularities at the extrema of the deflection function [122]. To explore the full 3D PEL, the semi-classical method can have a significant advantage because the short wavelength along x has a very strong classical character. However, using the ASCA, the benefit of semi-classical approaches is not very clear for elastic diffraction because the quantum methods are now quite efficient.

4.4.3 The Hard Corrugated Wall Model

These singularities are naturally absent in wavelike approaches such as optical models explaining the popularity[123, 124, 14] of the Hard Corrugated Wall model (HCW). The HCW model considers that all of the momentum transfer takes place at the turning point of the trajectory, close to the iso-energy curve $\tilde{z}(y)$. Such that $V_{2D}(y,\tilde{z}(y) = E_\perp$, where the force is maximum and the projectile at rest during a time $\tau \sim 1/\Gamma v_\perp$ (or lenght $x = v_\parallel \tau$ see Fig.5.4). The PEL $V_{2D}(y,z)$ is replaced by an infinite wall at location $\tilde{z}(y)$ and free propagation otherwise. No effect of a massive particle is considered and optical formulas can be used to predict the diffraction intensities I_m by a Fourier-like transform of the corrugation function $\tilde{z}(y)$.

$$I_m = \frac{k_{fz}}{k_{iz}} \left| \frac{1}{a_y} \int_0^{a_y} e^{-imG_y y - i(k_{fz}+k_{iz})\tilde{z}(y)}\, dy \right|^2 . \tag{4.2}$$

The simplest corrugation function of periodicity a_y is

$$\tilde{z}(y) = \frac{z_c}{2} \cos\left(y \cdot \mathbf{G_y}\right) = \frac{z_c}{2} \cos\left(y \cdot 2\pi/a_y\right) \tag{4.3}$$

for which the HCW Eq. 4.2 predicts diffracted intensities given by J_m the Bessel function of rank m:

$$I_m = J_m^2(2\pi z_c/\lambda_\perp) = J_m^2(k_\perp z_c) \tag{4.4}$$

The model is therefore extremely easy to implement and is already semi-quantitative at a surprisingly good level in view of the simplifications. The model does not account for multiple reflections corresponding to large corrugation amplitude nor for misaligned geometry corresponding to $k_{iy} \neq 0$ in the 2D plane. The model can be further simplified by considering only the flat section of the corrugation function $\tilde{z}(y)$ in Eq. 4.3 which contribute most to quasi specular reflection. Such points are indicated in red in Fig. 4.8, there are only two per projected lattice unit $\tilde{z}_{min}$ and $\tilde{z}_{max}$ and these give rise to the very specific evolution visible in Fig. 3.8 where the angle where the odd diffraction orders are intense correspond to weak even diffraction orders because the minimum $\tilde{z}_{min}$ sits at a location y in between that of $\tilde{z}_{min}$ and the next one. Along the vertical direction k_{iz}, the succession of maxima and minima is well reproduced by the simple equation $\delta k_{iz} z_c = n\pi$ with z_c the quasi constant corrugation amplitude. Below 100 meV, the shape of the corrugation function $\tilde{z}(y)$ does not depend strongly on $E_\perp$ as visible in Fig.4.7). The second-order perturbation theory developed by Miret-Artés and Pollak [96–99] corrects this lack by considering the finite range of the interaction. This is easily understood in Fig. 4.8b), where a trajectory flying over the next row is depicted. Within the HCW, it is not deflected at all, neither on the way-in, nor on the way-out. Whereas taking into account the extension of the interaction potential over a finite range, the forces acting on this trajectory can be taken into account.

For GIFAD, elastic diffraction of helium was observed for $E_\perp < 1$ eV. The classical turning points are typically 2-3 Å above the plane of ion core centers of the surface from Fig. 4.7.

4.5 The Atom-Surface Potential Energy Landscape (PEL)

The scattering and diffraction of atoms on the surface are determined by the interaction potential between the probe atom and the surface forming the potential energy landscape $V_{3D}(x,y,z)$ (PEL) above the surface. Classically, the energy landscape relevant for the scattering of the projectile requires the knowledge of all exact positions of the thermally displaced surface-atoms $(\delta x_i, \delta y_i, \delta z_i)$ at the moment of the scattering. We have seen that elastic diffraction only requires the Potential Energy Landscape associated with equilibrium positions so that the PEL is perfectly periodic. The calculation usually contains two steps, calculate the surface structure and electronic density, then place the projectile atom at all possible locations within x,y inside a lattice unit and z ranging from a few Å to $\sim$ ten Å. As a simplification, the surface structure is frozen during the second step because, with fast projectiles, the surface atoms do not have time to move (see e.g. Ref. [10] or Ref. [127]). Both steps can be performed by density functional theory (DFT, e.g. in Fig. 4.9)

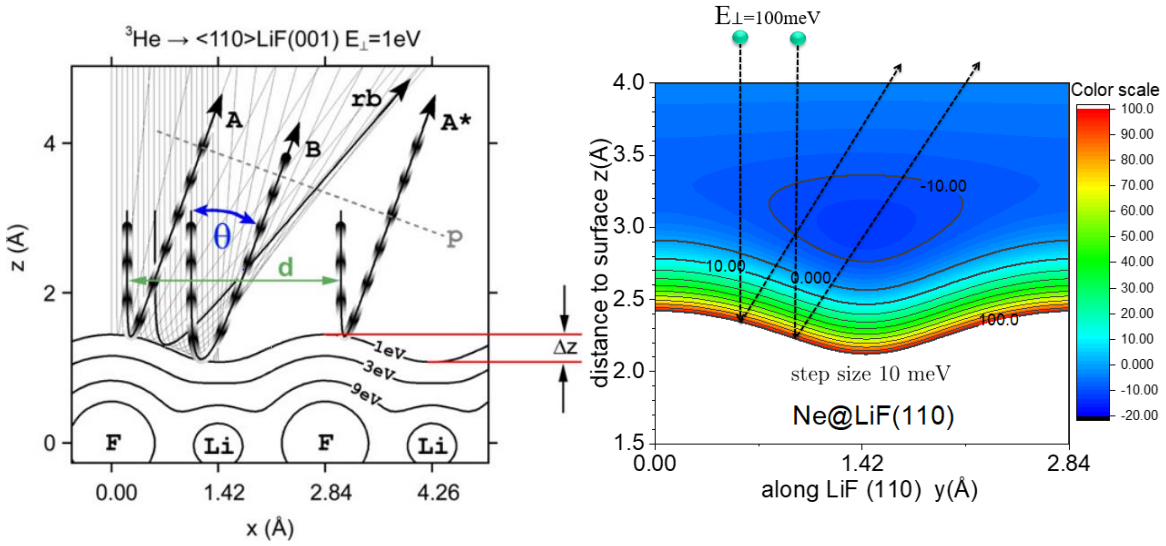

Figure 4.7 (a) Projectile trajectories z(y) and equipotential lines of the 2D interaction potential V2D(y,z) relevant for the scattering of He-LiF(001) in the (y,z) plane (taken from Ref. [18]). (b) The contour of Ne-LiF(001) along ⟨110⟩ 2D potential energy landscape (PEL) below 100 meV. The lines marked the potential energy level with a step size 10meV[125].

but the second one is very demanding since it has a very limited periodicity. Therefore, the calculation is performed with a reduced grid so that interpolation is needed.

4.5.1 Decomposition into Binary Interaction Potentials

One convenient way to interpolate is to fit the measured on the grid used to calculate binary interaction potentials attached to the surface atoms. It does not guarantee that the binary potential has a genuine physical meaning, but it guarantees that their sum reproduces the calculated PEL. If needed, a planar component can be added to mimic delocalized electrons. In some cases, such as ionic insulators where the valence electrons are localized on the atoms, the interatomic interaction potential between the projectile atom and each atom of the surface can be calculated directly by modeling the surrounding atoms as an array of point charges [34, 128].

Whatever the approach, it is convenient to expand the 3D PEL as $V_{3D}(\vec{r}) = \Sigma_{ij}\Sigma_n V^n_{bin}(|\vec{r}_n + i\vec{a}_i + j\vec{a}_j - \vec{r}|)$ where $\vec{a}_i, \vec{a}_j$ are the surface lattice vectors and $\vec{r}_n$ the coordinates of the n atoms inside the lattice unit. $V^n_{bin}(|\vec{r}|)$ is the binary interaction potential that depends only on the

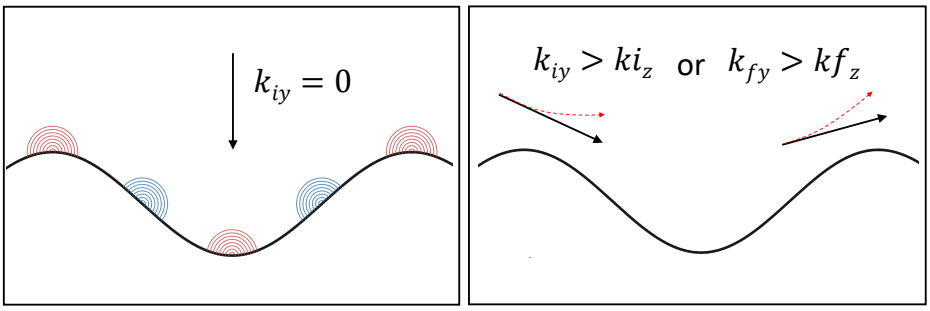

Figure 4.8 Left panel: The HCW is an optical model that can be understood from the Huygens principle and wavefront propagation. As a weakness, the light rays propagate freely, which is a good approximation at normal incidence of the equivalent ASCA particle, *i.e.* for $k_{iy} = 0$ but a poor approximation when the rays are close to the surface plane $k_{iy} \geq k_{iz}$ (Right panel). In this case, the HCW fails rapidly because long-range components of the interaction potential modify the trajectory. A situation illustrated by the red dashed trajectories and well described by a second-order perturbation theory [97, 98].

modulus of the inter-nuclear distance to the atom n in the lattice cell . In practice, at a given location, the sum Σ_{ij} runs only on the closest lattice sites around the projectile.

For elastic diffraction, the ASCA indicates that the 2D PEL is needed $V_{2D}(y,z) = \int_0^{ax} V_{3D}(x,y,z)dx$. Using the binary decomposition, it writes.

$$\begin{aligned} V_{3D}(\vec{r}) &= \Sigma_{i,j,n} V^n_{bin}(|\vec{r} - \vec{r}_n + i\vec{a}_i + j\vec{a}_j|) \\ V_{2D}(\vec{\rho}) &= \Sigma_{j,n} V^n_{row}(|\vec{\rho} - \vec{\rho}_n + j\vec{a}_j|) \\ V^n_{row}(\rho) &= \int_{-\infty}^{+\infty} V^n_{bin}(r)dx \\ V_{1D}(z) &= \Sigma_n V^n_{plan}(z - z_n) \end{aligned} \tag{4.5}$$

Of course, it can be interesting to use binary potentials for which the integration is analytic. This is the case of Yukawa type screened coulomb potentials $V_{SC}(r) = \frac{B}{r} e^{-\Gamma r}$ which have shown to be well-suited to describe inter-atomic potential (see *e.g* Ziegler-Biersack-Littmark(ZBL)[129]).

$$\int_{-\infty}^{+\infty} \frac{e^{-\Gamma r}}{r} dx = 2K_0(\Gamma\rho) \text{ with } \rho = \sqrt{y^2 + z^2} \tag{4.6}$$

where K_0 is the modified Bessel function of the second kind that, for x>0.7, can be approximated by [130] :$K_0(x) \approx (\frac{e^{-x}}{\sqrt{x}}) \cdot (1.25331414 + \frac{2}{x} \cdot (-0.07832358 + \frac{2}{x} \cdot (0.02189568 + \frac{2}{x} \cdot (-0.01062446 + \frac{2}{x} \cdot (0.00587872 + \frac{2}{x} \cdot (-0.0025154 + \frac{2}{x} \cdot 0.00053208))))))$

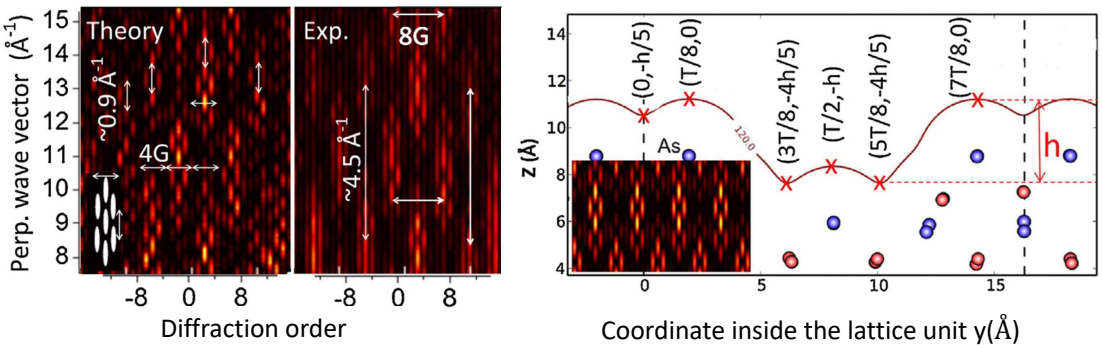

Figure 4.9 For the $\beta_2(2\times4)$ reconstruction of the GaAs(001) surface, the left panel reports the experimental diffraction chart (θ-scan) and the wave packet results from an ab-initio DFT calculation of the GaAs surface on the one hand and of the PEL with a helium atom on the other hand [10]. The right panel shows that the complex chain-ring features can be understood from a simple optical model where only six point source interfere[126]. The six red crosses correspond to the red point source in Fig.4.8.

So that, the contribution of each atom in the 3D cell to the 2D averaged cell can be evaluated directly without any numerical integration. Before presenting different forms of binary potentials used in atomic diffraction, we introduce the mean planar potential, which will be useful to discuss the depth of the attractive well responsible for physisorption. And also to discuss important properties of the atom trajectory. The mean planar potential can be defined as $V_{00}(z)$ in the Fourier expansion of the PEL in x,y, it can also be defined simply as $V_{plan}(z) = \int\int V_{3D}(x,y,z)dxdy$ over a lattice unit. However, $V_{3D}(x,y,z)$ is calculated using, in principle a sum over all the binary potential of the surface atoms. Again, expanding the binary potential over a basis set with specific properties can be very efficient to directly connect the binary potential to the mean planar potential using only the atomic elevation z_n inside the lattice unit. This corresponds to the final equation in the list of Eq. 4.5. When available we will give the analytic form of $V^n_{plan}(z)$ associated with $V^n_{bin}(|\vec{r}|)$.

4.5.2 A Purely Repulsive Single Exponential Model

This most simple form has been used in many descriptions of atomic collisions at the surface, where the projectile energy perpendicular to the surface exceeds ten's of eV, allowing penetration below the first layer. In this case, attractive forces can usually be neglected. A single repulsive form is enough to understand the concept of shadow cone focusing and many other processes involved in secondary ion mass spectroscopy. Very often, these calculations use purely repulsive ZBL form with excellent results. It is also enough to understand the main features of the projectile trajectory above the surface plane, such as the length of the trajectory

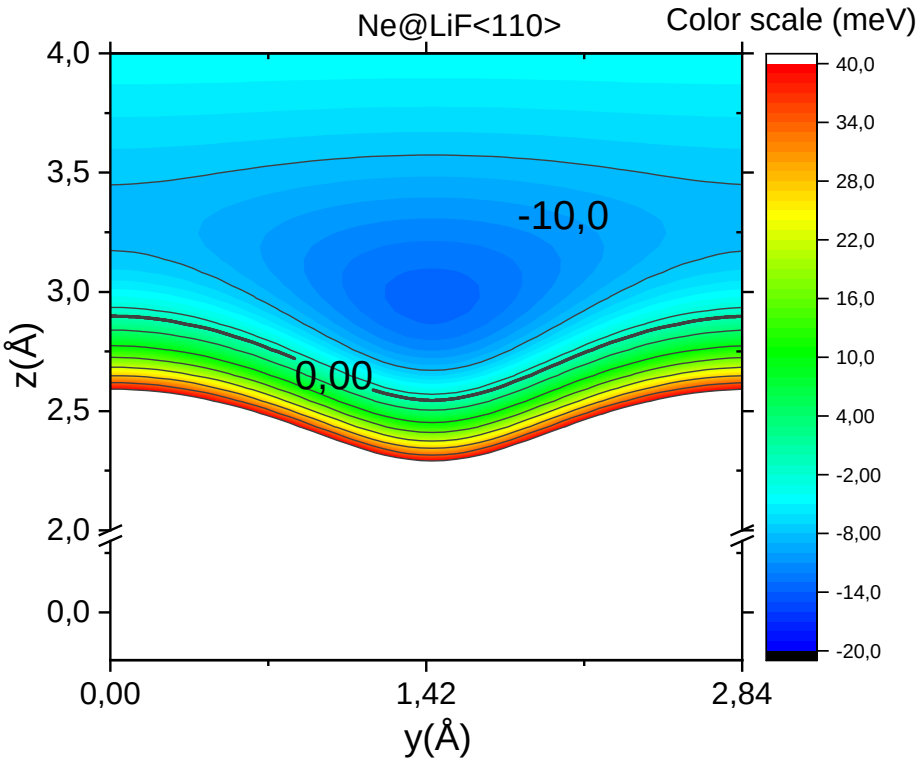

Figure 4.10 Equi-potential lines for the interaction of a Ne atom at LiF⟨110⟩ surface. The attractive(negative) potential energies are given in terms of the depth of the potential well D.

and the distance of the minimum approach. This simple model will be useful for discussing inelastic diffraction in simple terms, but the proper values of Γ need to be discussed. In ZBL, the values have been optimized to reproduce all possible pairs of projectile and target atoms in bulk. As semi-empirical forms with well-justified analytic forms and parameters adjusted to experiment, they cannot be entirely wrong. They are probably the best that one can get with a reduced effort. It was shown to perform well under grazing incidence to describe the evolution of the rainbow, but for values of $E_\perp$ between a few eV and up to 100 eV [131] where the projectile starts to penetrate the first atomic layer.

However, inside the bulk, inter-atomic distances larger than 2Å have no meaning, in this respect, using these potentials above these distances is an extrapolation. An extrapolation of proven values but an extrapolation cannot describe the physics that it did not contain initially. The weakness of the ZBL approach is the absence of attractive components and the fact that it does not contain any "chemistry of the surface". A valence electron in LiF is different from a valence electron in CaF_2, and this governs the repulsive behavior for

distances larger than Å above the surface. We assume that, above the surface, the repulsive forces should be dominated by the Pauli principle, which was shown to scale with the electron density. In the case of helium, binding is $1s^2$ outer electrons the most tightly in the periodic table. It is believed that the target surface electrons will have to move. So that the energy associated with a helium atom at a location $\mathbf{r_{he}}$, should be proportional [132] to the electron density ρ_{surf} of the surface at this same location $\mathbf{r} = \mathbf{r_{he}}$. $V_{rep}(\mathbf{r}) = \alpha\rho_{surf}(\mathbf{r})$ and should be valid when only conduction or valence electrons are concerned. The proportionality factor α was estimated to be $\alpha = 364$ eV a_0^3[133]. Above the surface, we expect that the wave function electrons should decay exponentially with a constant given by $\sqrt{2W}$. This derives from the Schrodinger equation $H\Psi = E\Psi$ in a region where the potential energy term V is close to zero, where W is the surface work function, the energy required to extract an electron, *i.e.* its binding energy E. Since the electronic density is given by the squared modulus of the wave function $\Psi(z)$, the decay rate should follow $\Gamma \approx 2\sqrt{2W}$ with W the surface work-function.The Fig.4.11 illustrates the displacement of the surface electrons by the presence of He and Ne atoms.

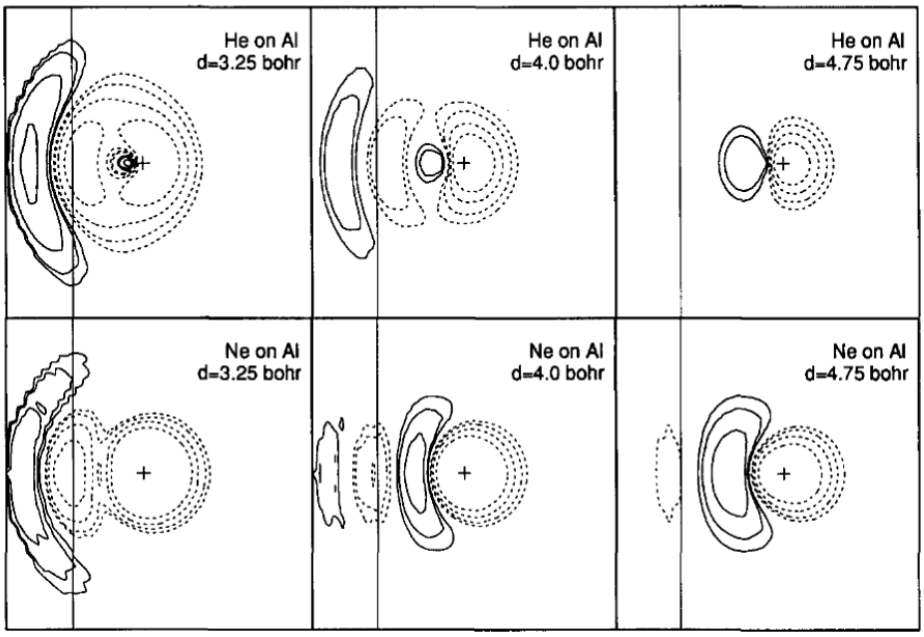

Figure 4.11 Contours of the displacement of the electron density induced by: (upper row) a He atom is impinging to the Al-jellium surface at three different distances: $3.25a_0$ (left panel), $4.0a_0$ (central panel) and $4.75a_0$ (right panel); (lower row) the same for Ne. Contour values shown are +0.001, +0.0005, +0.0003, +0.0001 electron/a_0 (the solid line refers to positive excess charge, the dashed line to negative excess charge). Ref. from[134, 135].

Under grazing incidence and when the energy $E_\perp$ is less than a few eV, the purely repulsive ZBL potentials were considered too repulsive, and the addition of attractive terms was needed[34, 136].

$$V_{tot}(\vec{r}) = V_{repulsive}(\vec{r}) + V_{attractive}(\vec{r})$$

4.5.3 A Bi-exponential Model

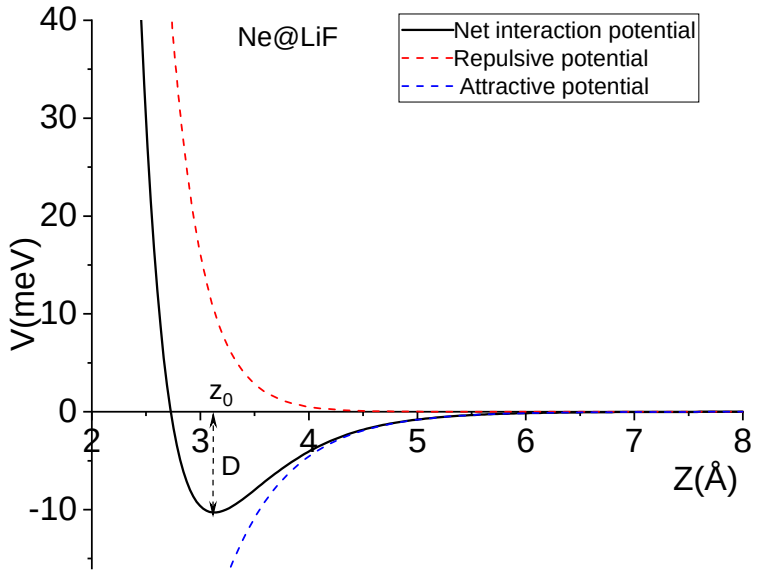

Figure 4.12 1D Ne-LiF mean planar potential as a Morse potential, the parameters are D=10.3 meV, $\Gamma = 3.46$ Å^{-1}, $z_0 = 3.129$ Å.

The minimum effort to reproduce an attractive and a repulsive part is to combine two exponential terms, one positive and one negative. If attraction dominates at large distance, then the range of the negative term should be larger than that of the positive one representing repulsion. We have seen that, for helium projectiles, the leading repulsive term should be on the order of $\alpha\rho e^{-\Gamma.z}$ (See sec.4.5.2). Can we estimate the attractive term of the binary potential? From a molecular point of view, the long-range attraction between two atoms is dominated by the van der Waals interaction between instant dipoles and induced dipoles, also known as London dispersion forces[137]. It is expected to scale as C_6/r^6. On an ionic crystal an important component of the attractive forces is due to the polarisation of the projectile by the electric of the surface resulting from the Madelung field. Away from the surface, it is expected to decay exponentially with a decay range close to the lattice unit, justifying an exponential form. This form has been used to reproduce all the diffraction orders for the

Ne-LiF[110] system over a wide range of $E_\perp$ as seen in Fig. 4.4.

$$V(r) = \sum_{i=1}^{2} \frac{a_{i,s}}{|\mathbf{R}-\mathbf{r}|} e^{-\Gamma_{i,s}|\mathbf{R}-\mathbf{r}|} \tag{4.7}$$

The parameters of the binary potential in Eq. 4.7 are : a_i = (39.84495, -1.6984), Γ_i = (2.1082, 1.246) for the Ne-Li^+ potential, a_i = (79.5900, -1.6632), Γ_i = (1.6364, 1.0165) for the Ne-F^- potential. The turning point is easily calculated at the equilibrium distance and the binary well depth. The 2D PEL displayed in Fig. 4.10 can be calculated immediately from these parameters using the 2D form $V^n_{row}(\rho)$ in Eq.4.6. The mean planar potential is also easily calculated with a simple spreadsheet or plotting software using Eq.4.5.

4.5.4 The Lennard-Jones potential

The Lennard-Jones (L-J), or Kihara Potential [138, 139] is probably the best-known form of diatomic molecular potential. The most commonly used form is the Lennard-Jones($6-12$ form)

$$V_{LJ}(r) = \frac{A}{r^{12}} - \frac{B}{r^6} = D_{LJ}\left[\left(\frac{r_0}{r}\right)^{12} - 2\left(\frac{r_0}{r}\right)^6\right] \tag{4.8}$$

Where D_{LJ} is the well depth, and r_0 is the equilibrium inter-nuclear separation, where $V_M(r_0) = -D_{LJ}$. The L-J potential in Eq. 4.8 is widely used because of its simplicity and inverse sixth-power, asymptotically-correct attractive van der Waals term. This form of binary interaction potential was used to represent the diffraction of fast helium atoms on a graphene surface grown on a 6H-SiC(0001) crystal.

The Moiré pattern was directly visible along the armchair direction [140]. In this case, the HCW model was applied along the armchair direction to describe a uniform graphene surface [141]. The HCW formula (eq.4.2) is the same, but $\tilde{z}(y)$ now describes the shape of the Graphene overlayer with its moiré pattern. For this system, the Fig. 4.13 shows the evolution of the well-depth between the binary radial form, the 2D axial form, and the mean planar form.

$$\begin{aligned}
V_{LJ,bin}(r) &= 4\varepsilon\left(\frac{r_c^{12}}{r^{12}} - \frac{r_c^6}{r^6}\right), \varepsilon = 1.4 \text{ meV is the well depth} \\
V_{LJ,row}(\rho) &= n\pi\varepsilon\left(\frac{63r_c^{12}}{64\rho^{11}} - \frac{r_c^6}{\rho^5}\right), n \text{ is the linear density} \\
V_{LJ,plan}(z) &= 2a_s\pi\varepsilon\left(\frac{2r_c^{12}}{5r^{10}} - \frac{r_c^6}{r^4}\right), a_s \text{ is the surfacic density}
\end{aligned} \tag{4.9}$$

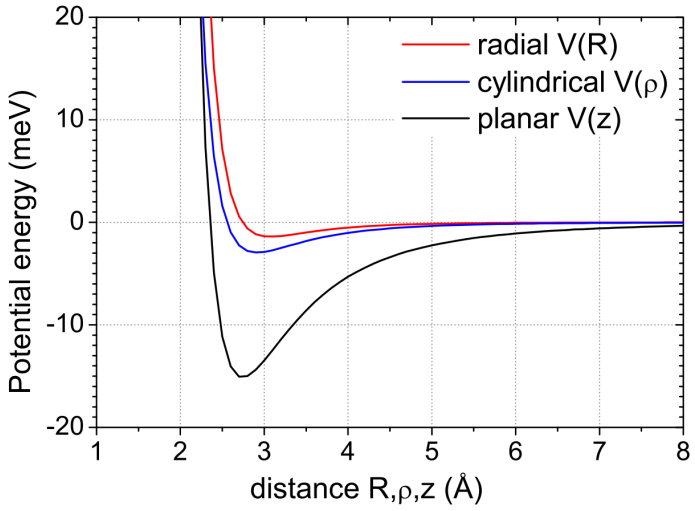

Figure 4.13 The interaction potential between a helium atom and a graphene surface; the binary interaction potential $V_{bin}(r)$, the same potential integrated along the armchair direction taken as x to produce $V_{row}(r)$ (note that it is the contribution of only one atom whereas the two atoms of the cell are aligned the [110] armchair direction and integrated over x and y to produce $V_{plan}(r)$.

These three different interaction potentials in Eq. 4.9 display quite different well depths. The increase of the well-depth from binary to row and planar form can be understood by comparing the distance between neighbor atoms along the row and in the plane. When these are located within 6-7Å, the attractive parts add up, whereas the compact repulsive overlap only for the closest atoms. This also outlines that several layers could contribute to the attractive part, but this is not the case for a single layer of Graphene. In principle, if the long range attractive forces could be added from all possible contributors, including the bulk atoms, the proper integration among the half 3D volume should yield a $\frac{r_c^6}{r^3}$ asymptotic behavior [142].

4.5.5 Buckingham Potential

The Buckingham potential is a formula proposed by Richard Buckingham in 1938[143], which describes the Pauli exclusion principle (Pauli repulsion) and van der Waals potential energy $V_B(z)$ for the interaction of two-atom or molecules in a correct asymptotic form. It keeps the six-power term of the attractive part of the L-J potential and the exponential repulsion term.

$$V_B(z) = A \cdot \exp(-Bz) - \frac{C}{z^6} \tag{4.10}$$

Where A, B, and C are parameters, several approaches may determine those values in Eq. 4.10. This potential also has been used in Fast Atom Diffraction by Schuller *et al.*[127] and Helium Atom Scattering (HAS) by Zhu *et al.*[144].

4.5.6 Tang-Toennies Potential

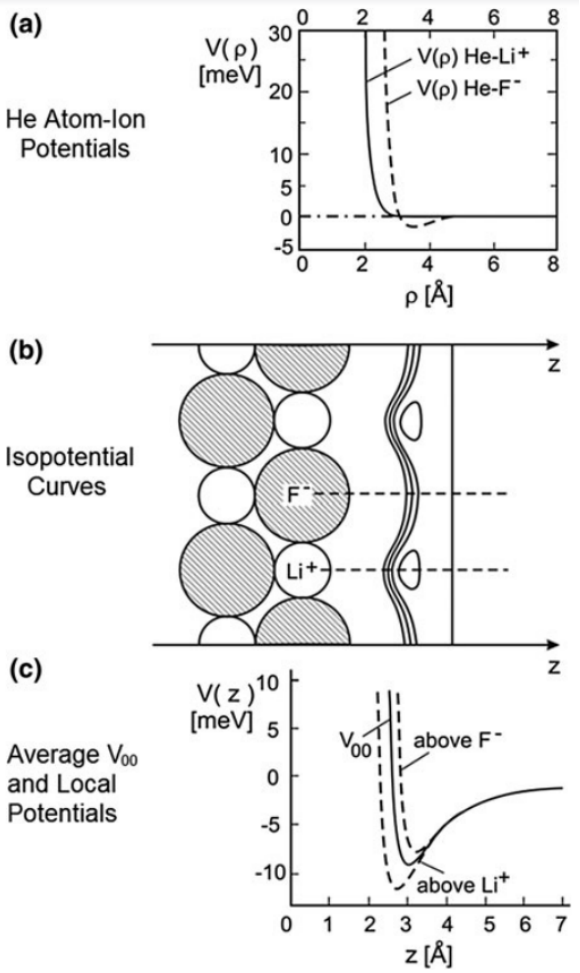

Figure 4.14 The He-LiF (001) surface potential based on the Tang-Toennies model. (a) Two-body potentials between He- and He-F^- as a function of the distance between the nuclei R. (b) The geometry and some iso-potential lines for the interaction of He atom with the surface from a summation of the atom-ion potentials in (a). (c) The solid curve shows the $V_{00}(z)$ Fourier component of the potential between He-LiF surface on the same distance scale as in (b). The two dashed curves show the local potentials above the Li^+ and F^-. From [142].

Tang and Toennies [145] developed an inter-atomic potential model, give He-LiF (001) surface potential in Fig. 4.14, which provides an accurate description of the intermediate

overlap region and covers the full range of inter-atomic distances. In this potential model, which provides good description of two-body van der Waals potentials between atoms. A simple exponential gives the repulsion and long-range attractive dispersion terms are those of the usual London power-law expansion, corrected, however, by damping function $f_{2n}(\beta r)$ which account for the overlap effects at intermediate distance. The inter-atomic potential given by

$$\begin{aligned} V_{tot}(\vec{r}) &= V_{repulsive}(\vec{r}) + V_{attractive}(\vec{r}) \\ &= Be^{-\beta r} - \sum_{n\geq 3} f_{2n(\beta r)} \frac{C_{2n}}{r^{2n}} \end{aligned} \tag{4.11}$$

Where the C_{2n} are the theoretical coefficients in the expansion of the attractive dispersion potential in Eq. 4.11, they can be accurately calculated from the optical properties of the separate atoms[142]. The damping functions $f_{2n}(\beta r)$ are defined as

$$f_{2n}(x) = 1 - e^{-x} \sum_{k=0}^{2n} \frac{x_k}{k!}$$

Based on this form, Sheng, Toennies, and Tang recently proposed a conformal potential for all noble gas dimers valid at all internuclear distances [146]. The adaptation to ionic crystal seems possible since the ionic electronic structure is that of a close shell noble gas, but electrostatic effects should be included.

4.6 The 1D means planar potential V(z)

We have introduced the 1D mean planar potential and some analytic expressions derived from specific binary potentials. We try to indicate here some interesting physical properties of these 1D potentials. We start with a specific form of 1D mean planar potential that will be used for inelastic diffraction, the Morse potential.

4.6.1 The Morse planar potential

indicate the binary forms giving rise to Morse, there are two possibilities, one is from Yukawa or pure exponential.

The Morse potential is widely used in chemical physics and by the STM and AFM community, [13] and many of its properties can be easily calculated (Tab. 4.2.).

$$\begin{aligned} V &= D\, e^{-\Gamma(z-z_0)} - 2D\, e^{-\Gamma(z-z_0)/2} \\ \dot{V} &= -D\,\Gamma(\, e^{-\Gamma(z-z_0)} - e^{\Gamma(z-z_0)/2}\,) \end{aligned} \tag{4.12}$$

4.6.2 Equilibrium Position, well-depth

The equilibrium distance is defined here as the coordinate z_0 where energy is minimum. For each analytic form of the 1D mean planar potential, the equilibrium distance z_0 can be found by solving $\dot{V}(z) = 0$.

Stable equilibrium: z_0 is at a potential minimum position, and therefore it will feel a force restoring it to z_0 as it moves away from z_0. An example of the Ne atom approach to the LiF surface is illustrated in the Fig. 4.15:

In surface physics and surface chemistry discriminate between two types of adsorptions-physisorption and chemisorption[147]. The physisorption or physical adsorption is the state of inert-gas atoms or molecules weakly bound to a surface that involves no chemical reaction. This weak interaction is mainly due to Van der Waals forces [148, 149, 72], with well depths D of order 1 to 300 meV [150]. The strength of the physisorption supports such classification: physisorbed atoms or molecules desorb under heating at typical temperatures, that are rarely above the bulk-boiling point of the adsorbate(*e.g.* 77 K for physisorbed N_2)[147]. This low value means that binding for times long enough to form ordered structures occurs only at low temperatures, $T < D/k_B$ *i.e.* a few K to hundred K, depending on the system. Higher desorption temperatures indicate chemisorption.

4.6.3 Turning Points and Allowed Regions of Motion

For a projectile of effective energy $E_\perp$, it is interesting to know how close it will approach the surface. More precisely, we want to determine the minimum distance z_t reached along the 1D mean planar potential.

Using Morse planar model Eq. 4.12, the turning point is given by

$$z_t = z_0 - \frac{2}{\Gamma}\ln\left(1+\sqrt{1+\frac{E_\perp}{D}}\right) \tag{4.13}$$

Since the kinetic energy goes to zero when $V(z_t) = E_\perp$, all the kinetic energy convert into potential energy, the particle must come to a stop as it approaches the classical turning point z_t in Eq. 4.13. At this turning point, the repulsive force is usually maximum, and the particle will be at rest for a short moment so that the action of the force is maximum. This is the place where most of the momentum transfer will take place. This partly explains why the HCW is successful, and this will be important when discussing energy transfer for inelastic diffraction.

In practice, the classical turning points are about 2-3 Å above the surface, which is also the typical nearest-neighbor distance of adjacent atoms of materials[13].

4.6.4 The Atom-surface Interaction Forces

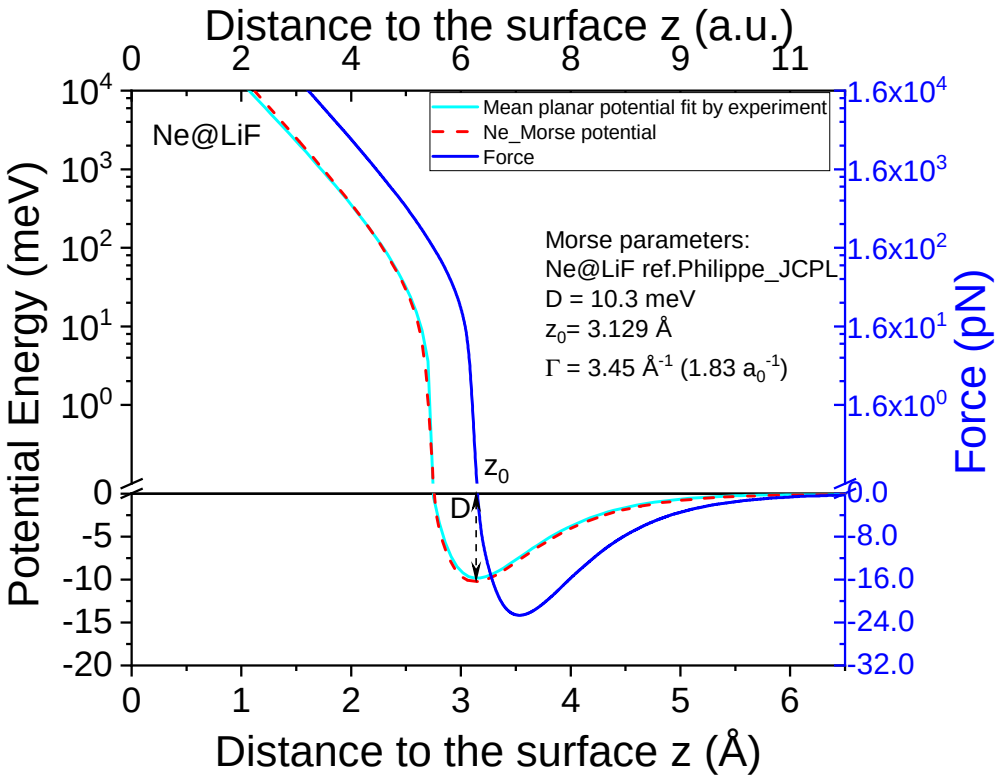

Figure 4.15 Ne atom at LiF surface, potential curve $V(z)$, and force curve $F(z)$, the Morse potential fitted by parameters D=10.3 meV, $\Gamma = 3.45$ Å, $z_0 = 3.129$ Å. ($1\ meV/\text{Å} = 1.6\ pN$)

In one dimensional case, we know the force on the particle at any point. It is determined by $\vec{F}_z = -\frac{\partial V}{\partial z} = -\dot{V}(z)$

4.6.5 Beeby Correction in GIFAD

As discussed in Sec. 4.4.1, GIFAD is sensitive to the 2D PEL, and if only Pauli repulsion would be involved, this 2D PEL would be proportional to the electronic surface density. Since this electronic density decreases away from the surface, the corrugation function, as evaluated by the HCW model, should decrease with the effective energy $E_\perp$. On many

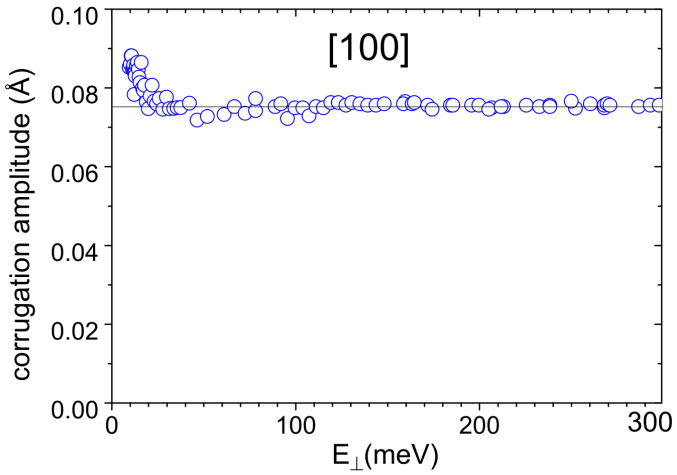

Figure 4.16 For He diffraction on Graphene, when fitting the diffracted intensities by the HCW Bessels formula of Eq. 4.2, the corrugation amplitude increases at low values of $E_\perp$[141]

occasions, the opposite is observed, as shown in Fig. 4.16 for the graphene/SiC system[141]. This un-physical behavior is suppressed by using the Beeby correction, which simply states that, due to the well depth D, the energy at impact is not $E_\perp$ but $E_\perp + D$. This correction is important only for $E_\perp$ that are comparable with D. The other underlying assumption is that the shape and magnitude of the corrugation function do not change significantly at low values of $E_\perp$, *i.e.*, far from the surface. This can be understood from Fig. 4.10 where one can see that all the equipotential lines are rather parallel to each other for positive values of the energy. This is again due to the weak attraction forces that compresses all the equipotential line around the distance z_{cross} immediately below the equilibrium distance z_0, as visible in Fig. 4.12 and Fig. 4.13 and even more when using a log scale as in Fig. 4.15. Without this attraction, the equipotential line would expand progressively to the vacuum and becomes less and less corrugated as the electron density does. In summary, the well depth contracts the equipotential lines and gives them a constant shape on a range significantly larger than D before they start progressively shrinking around the atom nuclei above one 1 eV, as visible in Fig. 4.7a). This behavior was already well investigated in TEAS, where the Beeby correction is broadly used, see *e.g.* [14].

4.6.6 Summary of 1D potentials

This chapter introduces a wide range of "empirical" or "semi-empirical" analytical expressions of inter-atomic potentials, based on mathematical approximations of the forces acting between atomic systems. They all contain two parts: a repulsive one and an attractive one dominating respectively at short or large distances to the surface.

Some of their analytic properties are listed below in Tab. 4.2.

Table 4.2 Main quantities are needed for the Morse and Lennard-Jones type potentials. *i.e.* $\Gamma_{att} = \Gamma_{rep}/2$.

Symbol	Morse Model	Bi-exponential Model	Lennard-Jones Model
$V(z)$	$D \cdot e^{-\Gamma(z-z_0)} - 2D \cdot e^{-\frac{\Gamma}{2}(z-z_0)}$	$A \cdot e^{-\Gamma z} - B \cdot e^{-\frac{\Gamma}{2}z}$	$D\left[\left(\frac{z_0}{z}\right)^{12} - 2\left(\frac{z_0}{z}\right)^{6}\right]$
$-\dot{V}(z)$	$D\,\Gamma(\, e^{-\Gamma(z-z_0)} - e^{-\frac{\Gamma}{2}(z-z_0)}\,)$	$\Gamma A \cdot e^{-\Gamma z} - \alpha B \cdot e^{-\alpha\Gamma z}$	$\frac{12D}{z}\left[\left(\frac{z_0}{z}\right)^{12} - \left(\frac{z_0}{z}\right)^{6}\right]$
D	D	$\frac{B^2}{4A}$, $Ae^{-\Gamma z_0}$ or $\frac{B}{2}e^{-\frac{\Gamma}{2}z_0}$	D
z_0	z_0	$\frac{2}{\Gamma} \cdot \ln\left(\frac{2A}{B}\right)$	z_0
z_c	$z_0 - \frac{2\ln 2}{\Gamma}$	$\frac{2}{\Gamma}\ln\left(\frac{A}{B}\right)$	$2^{-1/6}z_0$
z_t	$z_0 - \frac{2}{\Gamma}\ln(1+\sqrt{\frac{E_\perp}{D}+1})$	$\frac{2}{\Gamma} \cdot \ln\left(\frac{2A/B}{1+\sqrt{\frac{4AE_\perp}{B^2}+1}}\right)$	$z_0\left(1+\sqrt{\frac{E_\perp}{D}+1}\right)^6$
Γ	Γ	Γ	$12\frac{\ln z - \ln z_0}{z - z_0}$
Γ_{eff}	$\frac{\Gamma}{1-e^{\Gamma(z-z_0)/2}}$	$\frac{\Gamma}{1-\frac{B}{2A}e^{\Gamma z/2}}$	$\frac{12}{z\left[1-\left(\frac{z}{z_0}\right)^6\right]}$

These binary potentials have mainly interesting integration properties, so that the effective 2D potential can be evaluated directly from the atomic position of each atom in the lattice cell. Each of these atoms with a binary potential $V_{bin}(r)$ at position (x,y,z) will contribute to an axial potential $V_{2D}(\rho)$ centered at position (y,z) and to the mean planar potential $V_{1D}(z)$, so that the sums needed for 3D calculation are more simple in the 2D averaged plane and even more simple to evaluate the trajectory in the mean planar potential.

$$V_{row}(\rho) = \int_{-\infty}^{+\infty} V_{bin}(r)dx$$
$$V_{plan}(z) = \int_{-\infty}^{+\infty}\int_{-\infty}^{+\infty} V_{bin}(r)dxdy$$

$$V_{3D}(\vec{r}) = \Sigma_{i,j,n} V^n_{bin}(|\vec{r} - \vec{r}_n + i\vec{a}_i + j\vec{a}_j|)$$
$$V_{2D}(\vec{\rho}) = \Sigma_{j,n} V^n_{row}(|\vec{r} - \vec{r}_n + j\vec{a}_j|)$$
$$V_{1D}(z) = \Sigma_n V^n_{plan}(z - z_n)$$

Where i, j run over lattice vectors $\vec{a}_i$, $\vec{a}_j$ while n runs over the atoms of the unit lattice cell.

4.7 Summary of elastic diffraction

At least for simple systems, the problem of elastic diffraction is well-understood. The ASCA is well-established and allows exact treatment of the quantum dynamics of the helium projectile inside the PEL above the surface. Simple optical models can be used to derive semi-quantitative values of the surface topology. These results were progressively established in the past decade, mainly in Orsay and Berlin for the experimental aspects where both groups were involved in surface investigations at grazing incidences. Numerous thesis have progressively established the proper methods to derive the associated fundamental parameters. At Berlin, several PhD students were involved; Christian Auth, Stephan Wethekam[151], Andreas Schüller[152], and Jens Lienemann, Eric Meyer[153], Jan Seifert[154] and Marco Busch. At Orsay these are Jérôme Villette[155], Anouchah Momeni[156], Patrick Rousseau[157] Pierre Soulisse[158] and Maxime Debiossac[66]. The following chapters continue these studies focusing on the inelastic effects and attractive forces.

Chapter 5

Inelastic Diffraction, Models and Challenges

The grand aim of all science is to cover the greatest number of empirical facts by logical deduction from the smallest number of hypotheses or axioms.
-Albert Einstein

5.1 Overview

The elastic diffraction was derived on the assumption that atoms are standing still at equilibrium positions in the crystal. However, these definite equilibrium positions are only average positions around which the atoms oscillate. Even at zero temperature, an atom may be displaced from its average position, this corresponds to the so-called zero-point motion associated with the spatial extent of the ground state wavefunction limited by the Heisenberg uncertainty principle. As discussed above, GIFAD has strong similarities with thermal energy scattering (TEAS or HAS). Because the axial channeling approximation indicates that, in the elastic regime, GIFAD is equivalent to a particle with energy $E_\perp$ or momentum $\vec{k}_\perp(k_{iy}, k_{iz})$ evolving in the mean 2D planar potential. We now focus on the difference with TEAS, the inelastic diffraction regime which produces intensity on either side of the Laue circle. Since the Laue circle is defined by energy conservation, inelastic diffraction should be associated with where energy is exchanged with the surface. It can also be viewed from a spatial point of view. In principle, any part of the interaction which is not perfectly periodic should be visible in the inelastic diffraction. These can be defects such as missing atom of ad-atom, step edges, and islands, all these contributions illustrated

in Fig. 5.1 are often hidden in the concept of coherence-length of the surface indicating the mean distance without defects. Ultimately, GIFAD could help identify the nature of the most important structure, but this will be possible only in the inelastic scattering profiles or in the reflectivity curves as well as in the triangulation curves or large-angle scattering. All the aspects except elastic diffraction. It should be mentioned that inelastic diffraction

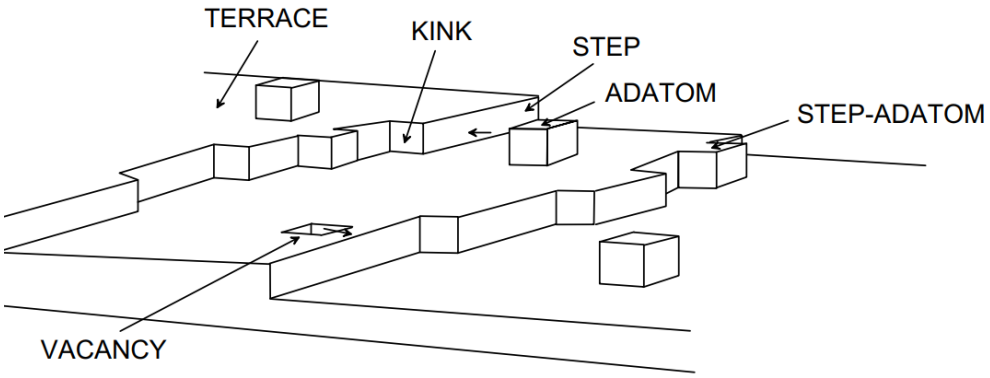

Figure 5.1 Illustration of structural imperfections of crystal surfaces. Atoms and their electron shells are indicated by little cubes. The figure adapted from Ref. [54].

is diffraction. The Fig. 5.2 shows elongated diffraction spots which are not sitting on the Laue circle, some are above, and some are below. In this figure, a weak signal of elastic diffraction can be filtered out by a differentiating Mexican-hat profile. When analyzed using the quasi-polar transformation defined in Fig.3.10b) and considering an effective wavelength $\lambda_{eff} = (\lambda_{in} + \lambda_{out})/2$, then the inelastic diffracted intensities are rather close to the elastic one. This interesting property was evidenced only when elastic diffraction is observed and for a distance to the Laue circle, which is less than a polar standard deviation σ_θ. Important work has already be performed in this direction by calculating some specific signatures from classical mechanics [102, 159, 59, 160]. In this manuscript, we investigate only LiF. In this wide band-gap insulator, electronic excitation can be ruled out for noble gas atoms projectiles with energy below a few keV having an energy $E_\perp$ less than one eV. Therefore, we will focus on the influence of thermal motion and its associated non-periodic positioning of the surface atoms. It is intimately linked to the phonon system, and this later is also specific at the surface. We will see that the specific kinematic conditions of GIFAD give rise to a different type of energy exchange than with TEAS. From the collisional point of view, we switch from "head-on" collisions with slow atoms to grazing collisions with fast atoms. There are several associated challenges. Can we measure online the exact surface temperature? Can we better understand some aspects of the quantum nature of the surface? Can we see specific surface phonons or their influence?

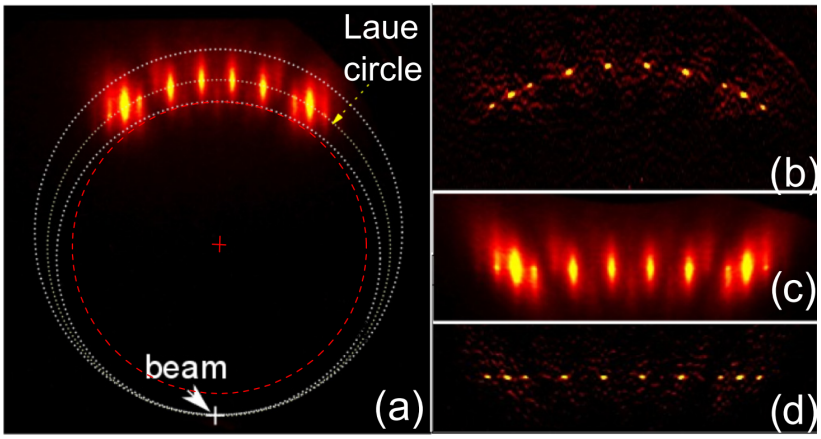

Figure 5.2 For 460-eV He^4 at 1.57° *i.e.* $E_\perp$ = 345 meV, the diffraction circles containing the beam position in the raw image (a) are transformed into horizontal lines in (c). The effect of the doubly differential filter applied in the z direction and isolating the elastic k_y profile and intensity is illustrated in (b) and (d), the k_z vertical extension is then given by the bandwidth of the filter. From Ref.[71].

5.2 Lattice Dynamics

The subject of lattice dynamics is the study of the thermal vibrations of the atoms in a crystal. The atoms or ions are not fixed to their equilibrium positions, but always vibrate with an energy that is governed by the temperature of the solid. In fact, inelastic diffraction, X-rays, neutrons, and thermal atoms have greatly contributed to measuring these vibration amplitudes via the Debye-Waller factor that will be discussed later (see Sec. 5.3). They found that the vibration amplitude can be in the order of 10% of an interatomic distance. In the study of lattice dynamics, atomic motions are frequently found to be adequately described as harmonic traveling waves. Each wave can be fully characterized in terms of its wavelength λ, pulsation ω, amplitude, and direction of propagation. The wavelengths have values ranging in scale from infinity down to the distances of interatomic separations. The standard approach uses reciprocal space and the wave-vector $\mathbf{k}$ defined as the vector parallel to the direction of propagation of the wave, and normalized such that $|\mathbf{k}| = 2\pi/\lambda$. We will find that ω is a function of both $\mathbf{k}$ and the forces between atoms, and the amplitude of any wave is a function of ω and temperature. The evolution of the energy of the mode with the wave vector is called the dispersion relation, and inelastic diffraction of atoms[161], electrons (HREELS), [162–164] and neutrons[165] have also contributed to these measurements respectively at the surface, close to the surface, or in the bulk as these three techniques have different penetration depth. On the theoretical side, within the harmonic approximation of the thermal vibration model, the solutions of the equation of the motion are then non-interacting normal modes,

and their quanta are called phonons. The phonon dispersion curve can be calculated for each Cartesian direction as a phonon spectrum. These are usually related to the thermal vibration of the atoms determined from inelastic diffraction studies (see the Debye-Waller factor, next chapter). The study of quantized surface vibrations, surface phonons, enables us to get knowledge about the forces at a solid surface, or between the surface and absorbed molecules. In the case of thin films such as graphene layers, the vertical vibration modes indicate the nature of the bounding [166]. This helps to understand and exploit a wide variety of transport and optical properties and functions involving phonons, either directly or via electron-phonon interaction [167].

We know that the mean energy of an oscillator is twice its mean potential energy, $\langle E \rangle = M\omega^2 \langle u^2 \rangle$ where $\langle u^2 \rangle$ is the mean square vibrational amplitude of the oscillator. We get [148]

$$\langle u^2 \rangle = \frac{\hbar}{2M\omega} \coth \frac{\hbar\omega}{2k_B T} \tag{5.1}$$

In a isotropic crystal, the mean square displacement (eq. 5.1) of the atoms in direction $\alpha = x, y \; or \; z$ is given by

$$\langle u_\alpha^2 \rangle = \frac{\hbar}{2M} \int_0^\infty \frac{1}{\omega} \coth \frac{\hbar\omega}{2k_B T} n_\alpha(\omega) d\omega \tag{5.2}$$

where $n_\alpha(\omega)$ is the spectral density for vibrations in α direction (eq. 5.2). The simplest example of oscillator-phonon coupling in the Debye model, in which the one-phonon continuum density of states is given by

$$n(\omega) = \begin{cases} \frac{3\omega^2}{\omega_D^2}, & 0 \leq \omega \leq \omega_D \\ 0, & other case \end{cases} \tag{5.3}$$

where ω_D (in eq. 5.3) is Debye frequency corresponding to the high frequency limit of the local oscillator with a value usually ≤ 50 meV, for LiF surface Debye temperature $T_D \approx 550$ K[127, 72, 168], so that $\hbar\omega_D = k_B T_D \approx 47.3$ meV.

For a bulk crystal in 3D space, the total mean square vibration amplitude is $\langle u^2 \rangle = \langle u_x^2 \rangle + \langle u_y^2 \rangle + \langle u_z^2 \rangle$. Due to the reduced number of close neighbors for surface atoms at the surface. The vibration frequency is reduced, but the energy in each mode should be constant at a given temperature. So that the vibrational amplitude of surface atoms normal to the surface is greater than in the bulk[148, 170] $\langle u_\perp^2 \rangle_T > \left\langle u_\parallel^2 \right\rangle_T$. Shichibe *et al.*[171] reported that the surface normal vibration $u_\perp$ makes a large contribution to the classical scattering processes

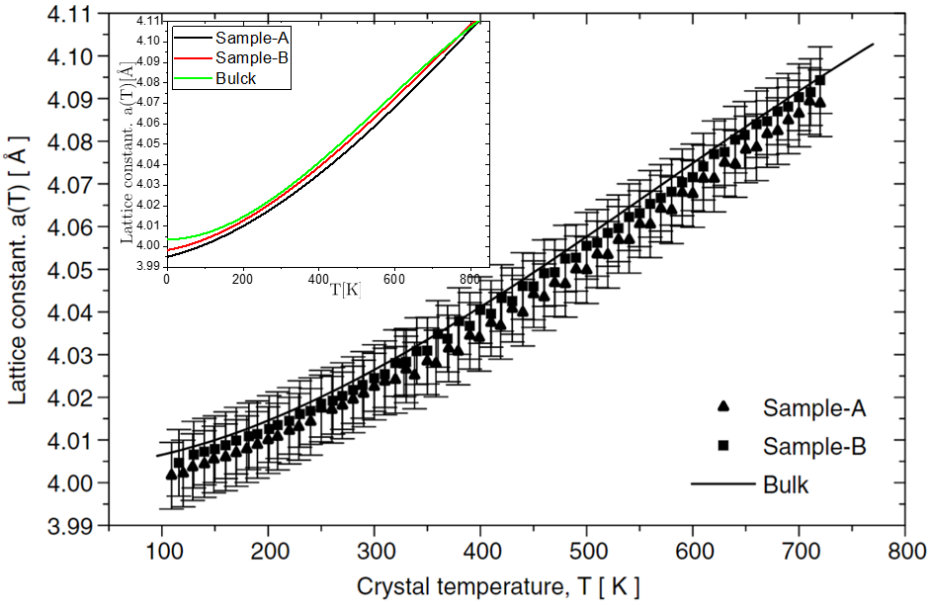

Figure 5.3 At different surface temperatures, the lattice constants measured by *Y. Ekinci et al.* [169] form two different crystal samples. The total error bars are also shown. The difference between the two crystals is about 0.002Å, which is attributed to the adjustment error of the azimuthal angle. The inset is the fitting curve plotted by using their recommended parameters.

of rare-gas atoms, such as Ar, Kr, and Xe. It is sometimes convenient to define a specific Debye temperature at the surface $k_B T_D = \hbar\omega_D$, and this latter is systematically lower than in bulk. From a naive description of a cubic crystal, the absence of one of the two neighbor atoms along z gives a force divided by two and a vibration amplitude multiplied by $\sqrt{2}$. The variation of the mean square amplitude of surface atoms can be calculated as a function of its temperature T.

$$\langle \sigma_z^2 \rangle = \frac{3\hbar^2}{2Mk_B T_D} \coth \frac{T_D}{2T} \tag{5.4}$$

Where T_D is surface Debye temperature. At high temperatures, $T > T_D$, the above formula (eq. 5.2) can be simplified to a linear form using $coth(T_D/2T) \sim 2T/T_D$. $\langle \sigma_z^2 \rangle = \frac{3\hbar^2 T}{Mk_B T_D^2}$ For bulk LiF at 300 K, we used the value calculated in ref.[127] $\langle u_{F\perp}^2 \rangle or \langle \sigma_z^2 \rangle = 0.0097\text{Å}^2$, at surface Debye temperature $T_{D\perp} = 547$ K, which is agree with the value of Hoinkes[168], $T_{D\perp} = (568 \pm 56)$ K, obtained by the thermal hydrogen atomic beam scattering method. A.Schueller *et al.* [127] calculated $\langle u_{Li}^2 \rangle = 0.0118\text{Å}^2$ and $\langle u_F^2 \rangle = 0.0081\text{Å}^2$ for LiF bulk and perpendicular vibrational amplitudes for LiF surface: $\langle u_{Li\perp}^2 \rangle = 0.0135\text{Å}^2$ and $\langle u_{F\perp}^2 \rangle = 0.0097\text{Å}^2$. which are increased by about 20% compared to bulk vibrational amplitude. Frisco

et al. in Ref.[172] use linear form for Li and (F) atoms : $\langle u(r_B)^2\rangle_T \approx [1+B(r_B)(T/T_{ref}-1)]\langle u(r_B)^2\rangle_{T_{ref}}$, with $B(r_B)=0.795(0.890)$

5.3 The Debye-Waller Factor in TEAS

The Debye-Waller factor (DWF) is a very important quantity needed for modeling all diffraction processes in materials in which lattice atoms displacements are involved. DWF is often interpreted as the probability of the coherent processes in the diffraction context. The main observable effect of the temperature is the attenuation of the elastic diffracted intensities $I(T)=I_0e^{2W(T)}$. It was introduced for X-rays historically, then used for electrons, neutrons, and atoms as well, where the Debye-Waller factor is described[14, 173, 74].

$$DWF = e^{-2W(T)} \tag{5.5}$$

where $-2W(T)$ in Eq. 5.5 is the Debye-Waller exponent and

$$W(T) = \frac{1}{2}\left\langle (\mathbf{u}\cdot\Delta\mathbf{k})^2 \right\rangle_T \tag{5.6}$$

Where $\Delta\mathbf{k}$ is the momentum transfer in the collision events, $\mathbf{u}$ is the displacement of a lattice atom from its equilibrium position, and the outer brackets refer to the thermal average. Equation (5.6) can be simplified by assuming that the average of the product is the product of the averages and that the parallel momentum transfer to the surface is zero. So we can rewrite Eq. (5.6) as:

$$W(T) = \frac{1}{2}\left\langle \mathbf{u}_z^2 \right\rangle_T \cdot (\Delta\mathbf{k}_z)^2 \tag{5.7}$$

Defining $k_BT_D = \hbar\omega_D$, equation 5.7 becomes:

$$W(T) = \frac{3(\hbar\Delta\mathbf{k}_z)^2T}{2Mk_BT_D^2} \tag{5.8}$$

In a single collision model where all the momentum is transferred to a single surface atom

$$(\Delta\mathbf{k}_z)^2 = (2ksin\theta_i)^2 = \frac{8mE}{\hbar^2}\sin^2\theta_i = \frac{8mE_\perp}{\hbar^2} \tag{5.9}$$

From a spatial point of view, the DWF can be derived as the reduction of the coherence due to the displacement $\mathbf{u}_z$ from equilibrium positions. This induces a path difference $2\mathbf{u}_z$ and a phase shift $2\Delta\mathbf{k}\mathbf{u}_z$. The resulting coherence of this gaussian phase distribution having a variance $(2\Delta\mathbf{k}\mathbf{u}_z)^2$ is simply the DWF. From a momentum point of view, the DWF indicates

the probability for a harmonic of pulsation ω_D to exchange a momentum $\Delta\mathbf{k}_z$ (in eq. 5.9)and remain in the ground state. DWF= $\langle\psi_0|e^{i\Delta\mathbf{k}}|\psi_0\rangle^2$

Note that the value is independent on the shape of the binary interaction potential $V^n_{bin}(r)$. However, it was rapidly understood[174] that the attractive well near the surface increases the projectile energy before the impact so that the effective energy is $E'_\perp = E_\perp + D$, where D is the well depth.

$$W(T) = \frac{12m(E_\perp + D)T}{Mk_BT_D^2} \tag{5.10}$$

Where m is the mass of the incoming atoms, M is the mass of the surface atom, $E_\perp$ is the incident beam energy $E_\perp$ normal to the surface, k_B is the Boltzmann constant, T_D is the surface Debye temperature. As a result, even at zero initial kinetic energy, the projectile is accelerated at an energy D and this prevent the DWF to reach unity, there is a saturation effect [14]:

$$\begin{aligned} DWF = \exp\{-2W(T)\} &= \exp\{\frac{-24m(E_\perp + D)T}{Mk_BT_D^2}\} \\ &= \exp\{\frac{-24mDT}{Mk_BT_D^2}\} \cdot \exp\{\frac{-24mE_\perp T}{Mk_BT_D^2}\} \end{aligned} \tag{5.11}$$

In TEAS, this can be seen as the low energy limit of the DWF during an energy scan (E_{scan}) or incident angle scan (θ_{scan}), note Eq. 5.11 as:

$$DWF = A(T) \cdot B(E_\perp, T) \tag{5.12}$$

where the Saturation factor in Eq. 5.12, $A(T) = \exp\{\frac{-24mDT}{Mk_BT_D^2}\}$ or $B(E_\perp) = \exp\{\frac{-24mE_\perp T}{Mk_BT_D^2}\}$. In T_{scan} mode, $A(T)$ is a constant at a certain temperature, or $B(E_\perp)$ is a constant at fixed $E_\perp$, *i.e.* fixed primary energy and incident angle θ. Obviously, the Saturation factor is within range $A, B \in (0,1)$. It means DWF never reach to 1, even with $E_\perp or T \to 0$, although at low temperature, small value of T, where zero point motion becomes effective the curve saturates to a constant value[175]. For instance, for He-LiF system at room temperature, $A_{He-LiF} = 0.61$, with $m(He) = 4\ u,\ D = 8.5meV,\ T = 300K,\ M(F) = 19\ u,\ k_B = 0.08617meV/K,\ T_D = 550K$. For Ne-LiF system, $A_{Ne-LiF} = 0.05$, with $m(Ne) = 20,\ D = 10.3meV$.

In such a single collision model, it predicts that DWF obeying an exponential decay as a function of $E_\perp$, $E_\perp = E\sin^2\theta \approx E\theta^2$, but it's not the case in GIFAD experimental results, see Fig. 6.5. The first naive attempt to estimate the DWF specific to GIFAD was to consider[176, 74] that the length of the trajectory can be converted into a mean number of

binary collisions and that the position fluctuations of this ensemble N is $\sigma_z/\sqrt{N}$ so that eq.5.7 becomes

$$W(T) = \frac{1}{2N}\sigma_z^2 \cdot (\Delta k_z)^2 \tag{5.13}$$

5.4 Classical Motion in an Exponential Potential

Since the ASCA has to be abandoned, we return to the 3D trajectory. Since the polar inelastic profile was found independent from the crystallographic axis probed, we return to the model trajectory $z(t)$ in the 1D mean planar potential (see chapter 4.6.1). We start with the simplest model, the purely repulsive exponential model $V(z) = V_0 e^{-\Gamma z}$ for which the trajectory and its derivative are analytic (see *e.g.* Ref. [71]). E_{iz} is the energy at $z = \infty$, the velocity $v_{iz} = \sqrt{2E_{iz}/m}$, the minimum distance z_0 corresponds to $\dot{z}(t) =$ and to the origin of time, $t = 0$ taken at the turning point z_0.

$$\begin{aligned}
z(t) &= z_0 + v_{iz}t + \frac{2}{\Gamma}\ln\left(\frac{1+e^{-\Gamma v_{iz}t}}{2}\right)\\
\dot{z}(t) &= v_{iz} - \frac{2v_{iz}}{e^{\Gamma v_{iz}t}+1}\\
\ddot{z}(t) &= -\frac{2v_{iz}^2\Gamma e^{\Gamma v_{iz}t}}{(e^{\Gamma v_{iz}t}+1)^2}\\
dE(t) &\sim \frac{\mu E a \Gamma^2 \theta^4}{4\cosh^4(\Gamma\theta x/2)}
\end{aligned} \tag{5.14}$$

In this model, the movement along x is a perfect translation at velocity $v_{parallel}$, and one considers the force given by $\ddot{z}(t)$ to evaluate the momentum-transfer curve to the surface atoms with the underlying atomic density $1/a_x$. In Fig. 5.4 such a trajectory is compared with a complete trajectory simulation on a 3D surface with binary potentials attached to the successive atoms within an atomic row. The figure also displays discrete momentum deposition curves having a quasi Gaussian profile. For each of the binary collisions identified along this trajectory, the momentum transfer $\delta\vec{k}$ is well-defined as the integral of the associated acceleration peak and the associated recoil energy $E_r = \delta k^2/2m_t$ of each surface atom of mass m_t along the trajectory. In this analytic form, the sum of all these classical recoil energies, which is the energy lost by the projectile, can be calculated, giving the classical energy loss $\Delta E_{Cl} = \frac{2}{3}\mu E \Gamma a \theta_i^3$[74].

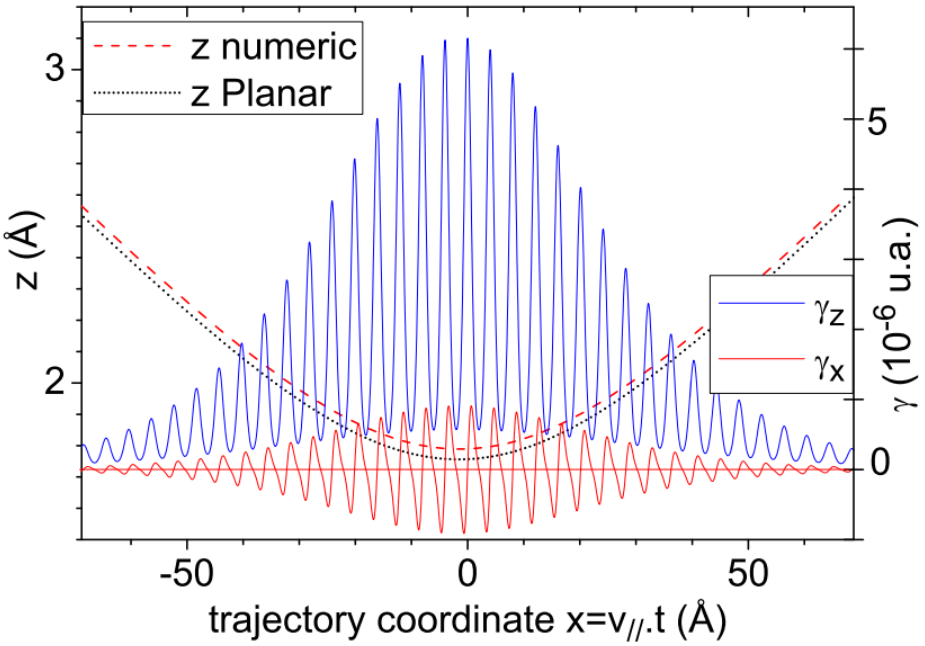

Figure 5.4 Classical trajectory $z(x = v_{\|}t)$ of a 1 keV He projectile calculated on top of a row of fluorine atoms. Note that the z scale (left) is $\sim$ 100 times the x scale. The smooth trajectory is made of successive localized interactions with the surface atoms as illustrated by the components γ_x, γ_z of the acceleration along the trajectory (right scale). From[71, 105].

5.5 Quantum Binary Collision Model (QBCM)

The quantum nature of the surface is introduced by considering that the surface atoms are bound in the Debye harmonic oscillator. Then for each surface atom, the local DWF can be estimated in TEAS as DWF=$e^{-\delta k^2 \cdot \sigma_z^2}$. At the end of the trajectory, the probability that all the binary collisions were elastic *i.e.* that none of the collisions was inelastic, is the product of all these probabilities. $P_e = \Pi p_e$, and since the product of exponential is the exponential of the sum, the resulting probability takes the simple form $P_e = e^{-\Delta E_{Cl}/\hbar\omega}$ where $\Delta E_{Cl} = \Sigma E_r$ is the sum of recoil energies already calculated in eq.5.17. Both the spatial approach replacing σ_z by $\sigma_z/\sqrt{N}$ and the momentum approaches are quite naive and oversimplified but they give exactly the same resulting DWF if we define N not from the FWHM of the momentum deposition curve ($\dot{z}(t)$ in Eq. 5.14 but as the effective number of equivalent binary collisions such that $N_{eq}E_r = \Delta E_{Cl}$, *i.e.* $N_{eq} = \frac{6}{\Gamma a \theta_{in}}$. The real problem of TEAS, where a slow moving wave-packet is hitting a quantum harmonic oscillator. It is far from trivial, as Schram and Heller illustrated in a recent paper "Hitting a ball on a spring: a simple model for understanding decoherence with wavefunctions" [177]. It is even more complex on a surface where the harmonic oscillator is no more an Eigenstate and

should be replaced by phonons modes. In TEAS, this situation has been addressed with a close coupling calculation [178] so that the excitation number in each mode can be traced. A statistical approach to the phonon bath has also proven qualitative results, including the adsorbates' effect[179]. Much less work was adapted to GIFAD[180, 181]. On the one hand, the sudden approach of the binary collision is even better justified than in TEAS because each collision lasts only $a/v_{\|}$ so that the surface atom has no chance to move during the collision. On the other hand, it isn't easy to evaluate the effect of the coherent transfer of momentum along the trajectory. The momentum transfer curve of Fig. 5.4 has a definite length and should have coupled more efficiently to specific phonon modes. Far from a detailed description of these effects, the interest of the above momentum approach is that if offers an opportunity to estimate the inelastic scattering profile because the projectile also receives the same momentum from the target atom, only directed in the opposite direction. If the collision is elastic (with a probability p_e). Then, the vibrational wave function of the surface atom is left unchanged. So that the elastic scattering probability p_e can be identified with the Lamb-Dicke probability of recoilless emission (or absorption), discovered as a line narrowing at high pressure in emission spectroscopy. Nowadays, it's widely used to laser-cool an ensemble of atoms without transferring any recoil energy.

5.6 The Modified Debye-Waller factor

Under grazing angle of incidence, the reflection of the projectile occurs in multiple collisions. The Debye-Waller argument 2W for each of these small collisions is smaller than that of Eq. 5.8, because $|\Delta k| \approx 2k_{\perp} = 2k\sin\theta_{in}$, for N times collisions, each small collision $\theta \approx 2\theta_{in}/N$. Thus, the Debye-Waller factor is transformed according to

$$e^{-2W} \rightarrow e^{-2W/N} \tag{5.15}$$

The DWF from Eq. 5.15 adapted to grazing incidence is now.

$$DWF = \exp\{-\frac{3\Delta E_{Cl}}{\hbar\omega_D}\coth\frac{T_D}{2T}\} \tag{5.16}$$

Where the classical energy loss ΔE_{Cl} is the sum of the recoil energies surface atoms is the classical energy loss. [74, 71] Where μ is the projectile to target mass ratio, $\mu = \frac{m_p}{m_t}$, and can be used to define $N = 6/(\Gamma a\theta_i)$. The mean number of equivalent binary collisions producing the same energy loss.

$$\Delta E_{Cl} = \frac{2}{3}\mu E\Gamma a\theta_i^3 \equiv \mu E(2\theta_i)^2/N \tag{5.17}$$

Where the last term is N times the binary recoil energy, resulting from each individual deflection by $2\theta_{in}/N$.

Statistics of inelastic events

What about the scattering profile? The local Debye-Waller factor $e^{-Er/\hbar\omega_D} = |\langle\Psi_0|e^{i\delta k}|\Psi_0\rangle|^2$ is interpreted as the probability that the surface atom is not vibrationally excited, *i.e.* that its wave function $\Psi_0\rangle$ is left unchanged. What is the consequence in terms of scattering distribution? We consider that if the collision is elastic, *i.e.*, if the surface atom wave function is unchanged, then we do not know anything about the position of this atom except the center of its wave function. At variance, if the collision is inelastic, then all possible excitation schemes should be considered. We assume that this leads to broadening that we evaluate from classical mechanics, by considering the position probability distribution. $P(z) = |\Psi_0(z)\rangle^2$ which is known to be Gaussian for a harmonic oscillator $P(z) = e^{-z^2/2\sigma_z^2}$. As a result, the inelastic scattering profile is a lognormal distribution and contributes to the overall inelastic scattering profile.

As a handy simplification, one can assume that the specular deflection is due to N equivalent binary collisions, *i.e.*, replacing the quasi-gaussian probability distribution (Eq.5 in Ref.[71]) with a square probability distribution. Mathematically, the convolution of N log-normal distributions is not a log-normal distribution. However, for comparatively small values of the width $w \approx \sigma_\theta/\theta_e = \sigma_\theta/2\theta_i \leq 0.1$, the property is numerically well verified [71] and, for N identical deflections, the resulting relative width parameter is reduced by $\sqrt{N}$ indicating simply that the final variance is the sum of individual variances. We note that Eq. 5.17 can be written as $\Delta E_{Cl} = 4\mu E\theta_{in}^2/N$ where $4\mu E\theta_{in}^2$ is the energy loss that would arise if only one atom would deflect the projectile by $2\theta_i$. The number $N = \frac{6}{\Gamma a\theta_{in}}$ is hence well-defined and interpreted as the mean number of collisions, each deflecting the projectile by $d\theta_1 = 2\theta_{in}/N$ with an associated recoil energy, $E_r = \mu E d\theta_1^2$ so that $\Delta E_{Cl} = NE_r$. The statistics is then easily expanded in terms of the number n of inelastic collisions.

$$P(n) = \binom{N}{n} p_e^{N-n}(1-p_e)^n/(1-p_e^N) \tag{5.18}$$

where the last term in Eq. 5.18 is here to normalise among the inelastic events only. The final variance $\sigma_{\theta_f}^2$ can be evaluated from the variance $\sigma_{\theta_1}^2 = (d\theta_1\Gamma\sigma_z)^2 \approx (\theta_{in}^2\Gamma^2 a\sigma_z/3)^2$ of

an individual inelastic collision.

$$\begin{aligned}
&(a)\ \sigma^2_{\theta_f} = \Sigma_n P(n)\ n\sigma^2_{\theta_1} \\
&(b)\ \text{for } p_e \approx 0,\ \ \sigma^2_{\theta_f} \approx \sigma^2_{Cl} = N\sigma^2_{\theta_1} = \frac{2a}{3}\theta^3_{in}\Gamma^3\sigma^2_z \\
&(c)\ \text{for } p_e \approx 1,\ \ \sigma^2_{\theta_f} \approx \sigma^2_{Qu} = \sigma^2_{\theta_1} = \frac{a^2}{9}\theta^4_{in}\Gamma^4\sigma^2_z
\end{aligned} \tag{5.19}$$

The limiting cases are given by the classical limit σ_{Cl} where all collisions are inelastic and the quasi-quantum limit σ_{Qu} where inelastic events (trajectories) are dominated by a single inelastic collision.

$$\begin{aligned}
\sigma_{\theta\ Cl} &= (\frac{2a\Gamma^3\theta^3_{in}}{3})^{1/2}\cdot\sigma_z \quad \text{or} \quad w_{Cl} = (\frac{a\Gamma^3\theta_{in}}{6})^{1/2}\cdot\sigma_z \quad (a) \\
\sigma_{\theta\ Qu} &= \frac{a\Gamma^2\theta^2_{in}}{3}\cdot\sigma_z \quad \text{or} \quad w_{Qu} = \frac{a\Gamma^2\theta_{in}}{6}\cdot\sigma_z \quad (b)
\end{aligned} \tag{5.20}$$

Both predictions indicate that the measured relative width $w \approx \sigma_{\theta_f}/2\theta_i$ should decrease at small angle of incidence during a θ_{scan} or stay constant during an E_{scan}. In this latter case, the angle of incidence is fixed, and increasing $E_\perp$ only brings the trajectory closer to the surface but does not change its shape nor the number of collisions or their relative strength $\delta k_z/k_x$ so that the relative width w should stay fixed.

This simple description of the scattering width as a perturbative broadening of the elastic scattering from an ideal surface with atoms fixed at equilibrium positions was developed as the quantum binary collision model (QBCM) [71]. We suggest in the next chapter, that the purely repulsive approach is too restrictive, much more than it is in TEAS where the most important correction, known as the Beeby correction is assumed to be qualitatively important only for values of $E_\perp \sim D$. In next chapter, a modified classical model take surface effective stiffness and Beeby correction both into account, the classical inelastic width $w_{Cl} = (\frac{a\Gamma^3_{eff}\theta_{eff}}{6})^{1/2}\cdot\sigma_z$.

5.6.1 conclusion

As the main difference with TEAS, we have seen that the stiffness of the repulsive potential plays a direct role in the scattering process. It governs the length of the trajectory above the surface, the number of binary collisions, and the violence (strength) of these binary

collisions. The minimum distance of approach to the surface, z_{min} is the same as in TEAS (when considering $E_{\perp}$), and the force $\dot{V}(z_{min})$ is also the same as in TEAS. However, the velocity and collisions are parallel to the surface in the grazing geometry. The repulsive force action is $\propto$ the time that the projectile is exposed to this force, and this scales as $1/v_{\parallel}$. In its crude form, the QBCM model predicts that the elastic or inelastic behavior is a property of each binary collision. This assumption does not affect the elastic scattering probability because this implies that all collisions are elastic. The question is more on the inelastic scattering. The QBCM suggests that only a few collisions could be inelastic, so the overall broadening could be much less than the classical limit. This is examined in the next chapter, together with the influence of the attractive forces.

Chapter 6

Experimental Results: Polar Inelastic Profiles in Fast Atom diffraction at Surfaces

This chapter corresponds to a publication by Peng Pan, Maxime Debiossac, and Philippe Roncin in *Physical Review B* under the same title[72].

6.1 GIFAD Polar Inelastic Profiles

Elastic diffraction was shown the be sensitive to the surface topology. This chapter discusses a complementary aspect. The probability for a projectile atom to be deflected away from the Laue circle, and how to interpret this deviation. More precisely, we define the inelastic polar scattering profile or angular distribution $P(\theta)$ as the probability for the projectile to be deflected by an angle θ different from the specular angle, where θ is the deviation from the primary beam direction: $\theta = \sqrt{\theta_y + \theta_z}$. This distribution does not display any diffraction feature, but our results below suggest that it is sensitive to the thermal amplitude of surface atoms multiplied by the stiffness of the mean surface potential at a distance z_t where the projectile velocity towards the surface changes sign. The increase of the stiffness at low values of $E_\perp$ will be related to the attractive well-depth.

The chapter is structured as follows: Sec. 6.1.1 presents experimental data recorded with helium and neon projectiles on a LiF crystal surface at room temperature (except for Fig. 6.4 recorded at -93 ° C). The image transformation used to produce the polar scattering

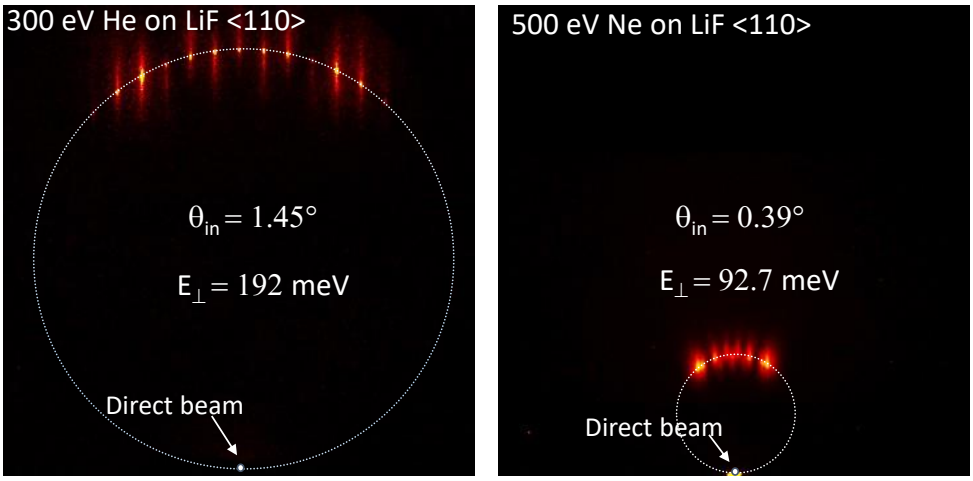

Figure 6.1 The raw images of the diffraction pattern of 300 eV Helium at $\theta_i = 1.45°$ (Left) and of 500 eV neon atoms at $\theta_i = 0.39°$ (right). The white line where bright spots are observed represents the Laue circle of energy conservation corresponding to elastic diffraction. The Bragg angle from eq. 3.1is much smaller for neon. Inelastic diffraction extends below and above this circle and, at comparable values of $E_\perp$, it is systematically more important for neon which has a larger mass.

profiles are presented, and within the explored conditions, these polar profiles are found to be independent of the probed crystallographic axis. A fit through these profiles is used to isolate the elastic and inelastic components as well as widths and positions and their evolution with the projectile energy and angle of incidence.

Section 6.1.2 briefly recalls properties of elastic and inelastic diffraction in GIFAD and simple models developed to retrieve physical properties of the system such as the shape of the electronic density profile, the depth of the attractive well, the surface stiffness, and the thermal movement of surface atoms. The model is adapted to take into account the role of the attractive part of the mean planar interaction potential, drastically improving the agreement with the experiment. Sec. 6.1.3 addresses the gaps in the model, trying to draw perspectives for future work.

6.1.1 The Polar Profiles

The raw diffraction images, such as the one in Fig. 6.1 and Fig. 6.3 show bright spots having a similar dimension to the primary atom beam and located on a circle. The z direction is normal to the surface plane in these figures. The x, y directions on the surface plane are defined as parallel and perpendicular to the low index direction probed, respectively, see Fig. 1.3. Away from the Laue circle, clear signs of inelastic diffraction remain visible in the

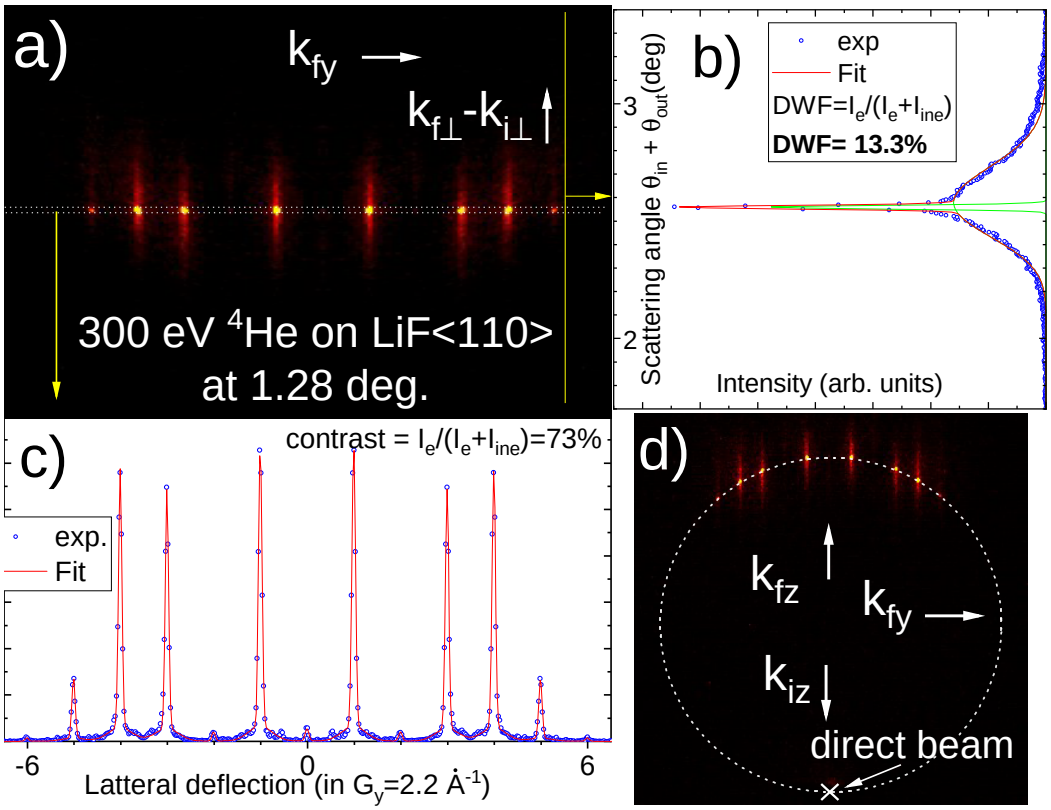

Figure 6.2 a) quasi polar transform of the raw diffraction image in panel d). The panel b) corresponds to a full projection onto the vertical axis producing the polar scattering profile, it is fitted by a sum of a narrow Gaussian and a broad log-normal profile. The panel c) is the intensity in a narrow horizontal band centered on the specular reflection[72].

form of vertical stripes extending on both sides as in Fig. 6.2a), or preferentially upward or downward as in Fig. 6.3a) and Fig. 6.3d). The intensity integrated along the y direction produces the polar scattering profiles in Fig. 6.2b) and Fig. 6.3b), where the diffraction features have disappeared. These polar scattering profiles visible in Fig. 6.2b) and Fig. 6.3b) are well-fitted by the sum of a narrow Gaussian profile, *a priori* identical to those visible in Fig. 6.2c) and Fig. 6.3c) on top of the broader log-normal distribution. This log-normal profile (6.1) was empirically adopted as a data-reduction procedure [155] because it was found to reproduce the asymmetry of the scattering profile in the classical scattering regime [34, 65] when diffraction was not considered. It was also observed in quantum Monte Carlo [107] or semi-classical [172] and classical [34] scattering approaches or inelastic diffraction. For small values of $w \leq 0.1$ as measured here, $\sigma_{ine}^2 \approx w^2\theta_m^2$, so that w is simply the relative width $w \approx \sigma_{ine}/\theta_m$ where θ_m is the median value very close to the specular scattering angle $\theta_s = 2\theta_{in}$.

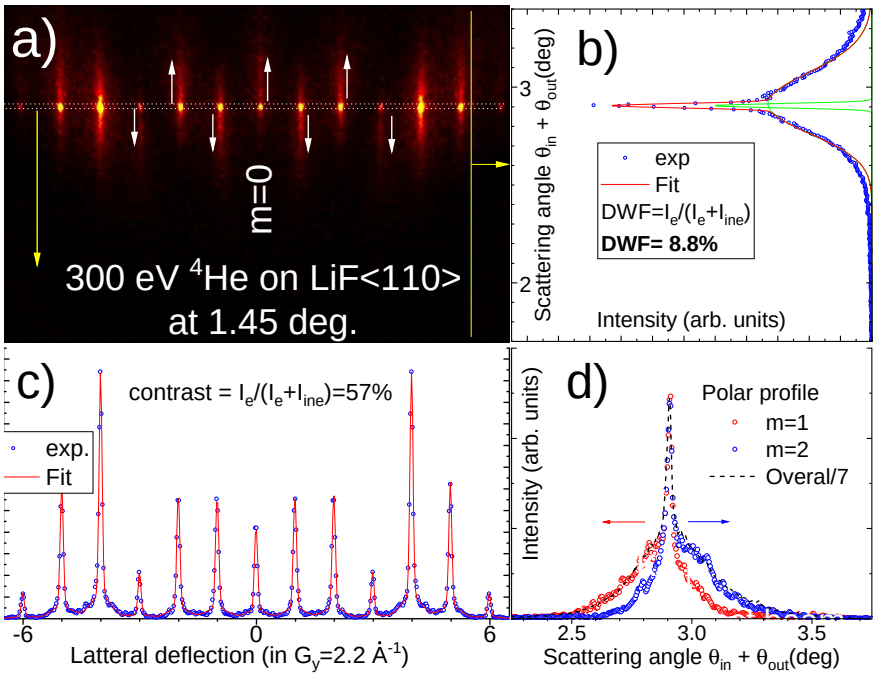

Figure 6.3 a) For 300 eV He impinging on Lif at 1.45° quasi polar transform of the raw diffraction image in panel d). The panel b) corresponds to a full projection onto the vertical axis producing the polar scattering profile. It is fitted by a sum of a narrow Gaussian and a broad log-normal profile. The panel c) corresponds to the intensity in a narrow horizontal band centered on the specular reflection. Same as Fig. 6.1 with identical scales but with an angle of incidence θ_i= 1.45° corresponding to an energy $E_\perp = 192$ meV. Panel d) now displays the polar scattering profile associated with the m=±1 and m=±2 diffraction orders showing an inelastic component pointing mainly towards low (•) or large (•) scattering angles, respectively. From ref.[72].

$$LN[\theta_m;w](\theta) = \frac{A}{w\theta\sqrt{2\pi}} \exp\left(\frac{-\left(\ln\frac{\theta}{\theta_m}\right)^2}{2w^2}\right)$$
$$\text{with a variance } \sigma_{ine}^2 = e^{w^2}(e^{w^2}-1)\theta_m^2 \tag{6.1}$$
$$\text{and reversely } w = \left(\ln\frac{1+\sqrt{1+4\sigma_{ine}^2/\theta_m^2}}{2}\right)^{1/2}$$

Figure 6.4 shows three almost identical polar scattering profiles recorded at the same incidence angle but along three different crystal orientations. This suggests that, for $E_\perp$ <1 eV where the distance to the surface is probably more than 2 Å, the magnitude of the momen-

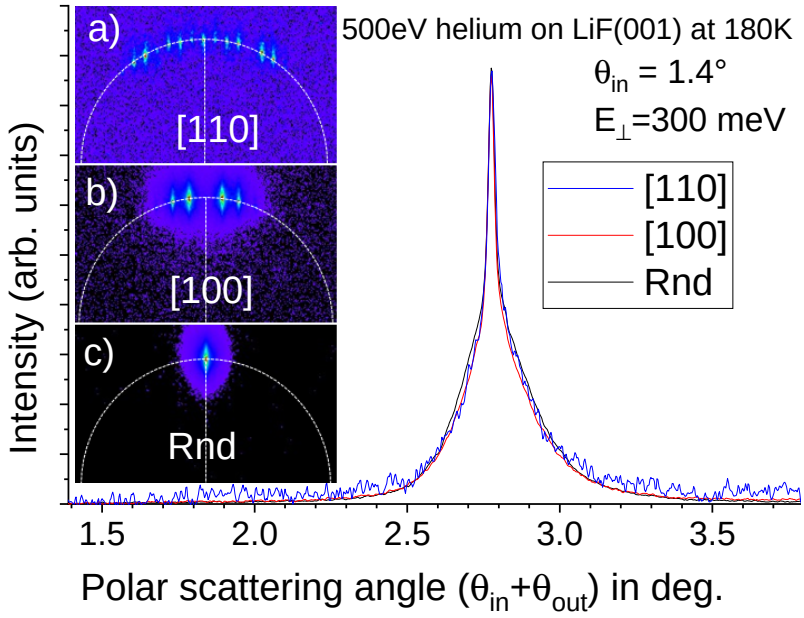

Figure 6.4 (a-c) Raw diffraction images of 500 eV helium incident at 1.4° on LiF at 180 K oriented along the [110], [100] and random direction respectively [72]. The resulting polar scattering profiles are almost identical, showing a narrow elastic peak at $\theta_{out} = \theta_{in}$ on top of a quasi-log-normal inelastic profile having a relative width $w = \sigma_\theta/\theta \approx 0.042 \pm 0.002$.

tum exchanged along z is not very sensitive to the exact crystallographic direction as also suggested in Ref. [75] when investigating the azimuthal line profile of inelastic diffraction peaks.

Four independent pieces of information can be extracted from the analysis of these polar scattering distributions as a sum of gaussian and log-normal profiles:

- (1) The intensity ratio of these profiles.
- (2) The elastic scattering width σ_e of the Gaussian profile.
- (3) The inelastic scattering width w of the log-normal inelastic profile (or its std deviation σ_{ine}).
- (4) The shift $\delta\theta = \theta_m - \theta_s$ between the inelastic and elastic polar profiles.

These four items are first presented separately, and will be discussed together after a few theoretical considerations.

The elastic diffraction ratio

The ratio of elastic scattering is considered to be a direct measure of the Debye-Waller factor describing the overall coherence when the projectile wave is scattered by a single impact, *e.g.* X-ray, neutron, and atoms at thermal energies (TEAS, see *e.g.*[14] for a review) on thermally displaced surface atoms at a temperature T: $I(T)/I_0 = e^{-2W(T)}$ with $2W(T) = \langle(\vec{u}\cdot\vec{\Delta k})^2\rangle_T$ where $\vec{u}$ describe the displacement vector of surface atoms (see Sec. 5.6).

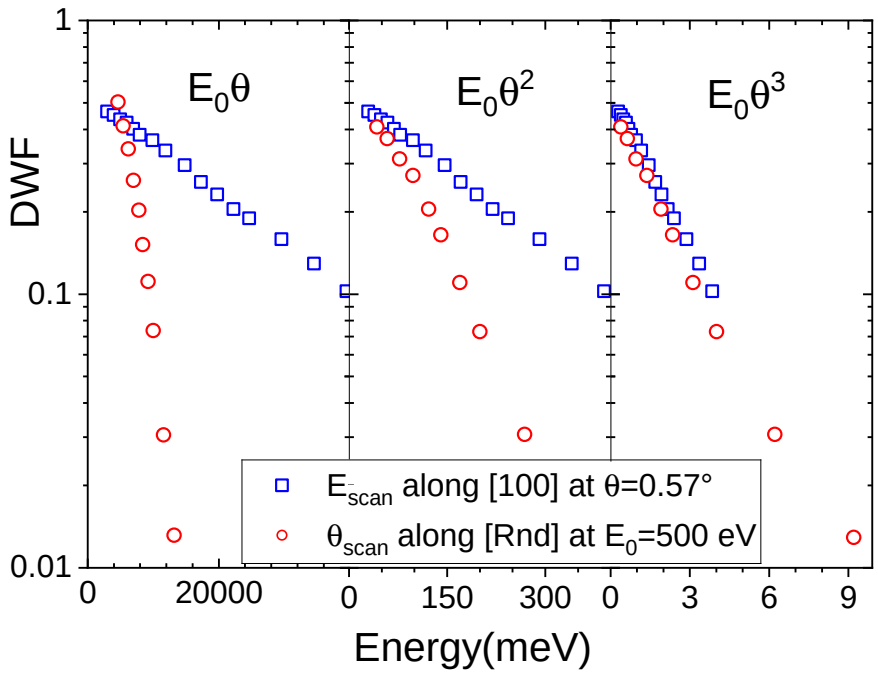

Figure 6.5 The DWF, measured as the relative intensity of elastic diffraction of He projectiles on LiF during an E_{scan} (□) or a θ_{scan} (○) are reported as a function of $E_0\theta$, $E_0\theta^2$ and $E_0\theta^3$. The log scale underlines the exponential decay whatever the abscissa. From ref.[182].

Reversely, this reduced decoherence allows large values of $E_\perp$, up to one eV for He, where attraction forces play a negligible role and where, due to small wavelength, the topological accuracy can be in the pm range [127, 16].

The measured DWF decays exponentially both with increased collision energy and with increased angle of incidence. However, when plotted as a function of $E\theta^3$, the data recorded during an E_{scan} or a θ_{scan} tend to fall on top of each other as illustrated in Fig. 6.5. this is fully consistent with the formula 5.16with the classical energy loss ΔE_{CI}. Figure 6.6 displays the DWF measured with helium and Ne projectiles in various initial conditions as a function of $E\theta^3$. In spite of a significant scattering of the experimental points, partly due to different samples, a dominant exponential decay is observed. The corresponding prefactor and a decay rate are indicated in Fig. 6.6 and will be discussed later.

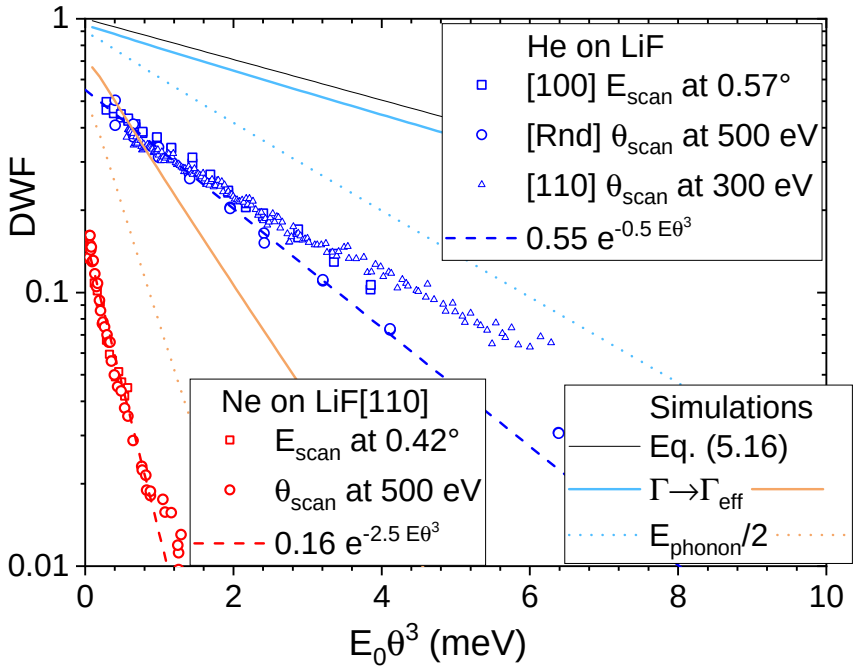

Figure 6.6 The DWF, measured as the relative intensity of elastic diffraction, is reported for He and Ne projectiles on LiF along various orientations as a function of $E\theta^3$. The (○,○) symbols were recorded on the same surface and the associated dashed lines are only to guide the eye, outlining the effect of the projectile mass on the decay constant. The (△) symbols correspond to a different target suggesting a possible influence of the surface coherence length (defect density). The simulations are described in the discussion. From Ref.[182].

The elastic scattering width.

The polar profile is well-fitted by the sum of a Gaussian distribution width σ_e, identical to that of the primary beam, and a log-normal profile width w_{LN}. However, when the elastic ratio is less than a few percent, the elastic contribution is not resolved. We usually impose the elastic width used in the fit to be the same as that of the primary beam. It should be stated that sometimes, the direct beam, which is systematically recorded before or after target insertion, is better fitted by a non-Gaussian profile. In these cases, the same profile is used in the fitting de-convolution. In some cases, with our best angular resolution, there could be indications of a slight broadening at the base of the elastic peak as compared with the shape of the direct beam, but the effect could also be due to the deformation of the inelastic profile that would be poorly described by a log-normal profile. This aspect is not important here and will not be discussed further.

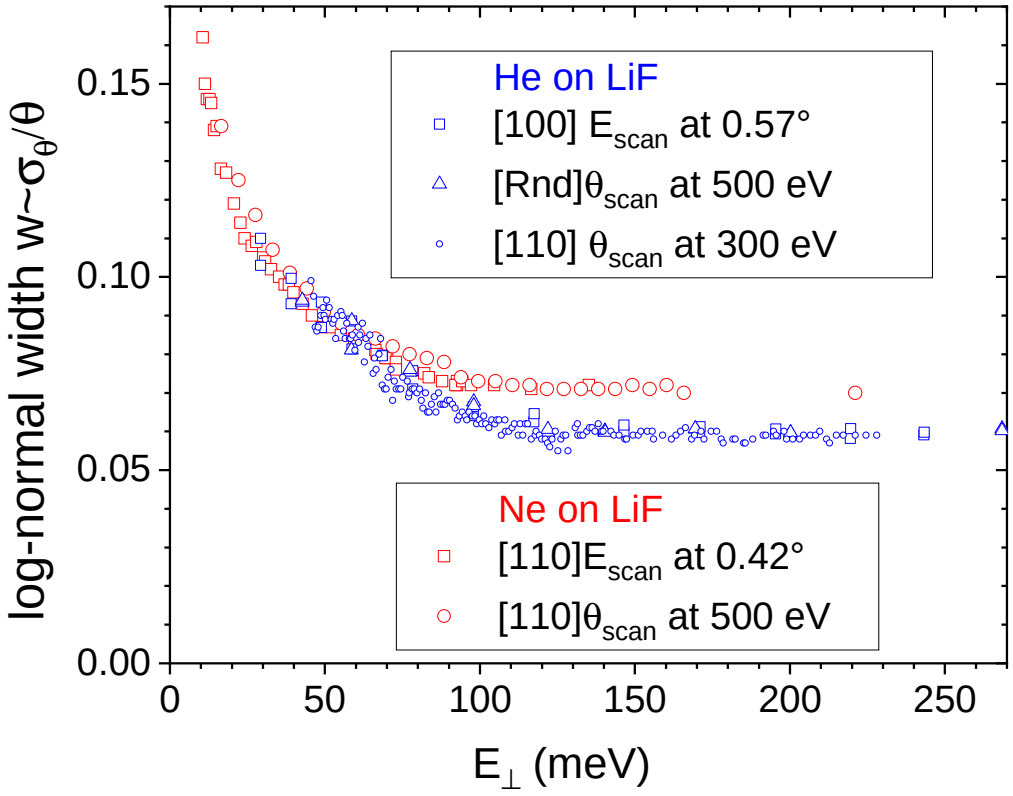

Figure 6.7 The log-normal width $w \approx \sigma_\theta/\theta_{scat}$ of the inelastic scattering polar profile is reported as a function of the perpendicular energy $E_\perp$, for helium (○) and neon (○) atoms impinging on LiF under various conditions indicated in insets. From ref.[72].

The inelastic scattering width w of the log-normal inelastic profile.

Figure 6.7 reports the evolution of the relative width of the polar profile measured with neon and helium projectile under various conditions of energy and angle on a LiF surface at room temperature. The data indicate that the polar relative width is not too sensitive to the crystallographic axis. When plotted as a function of the perpendicular energy $E_\perp$, the data reasonably align with each other irrespective of major differences in the Debye-Waller factor and of the absolute magnitude of the measured standard deviation σ_θ. The observed width seems to level at a fixed value for perpendicular energies larger than 100 meV and to increase significantly below. The data recorded with helium and neon appear rather similar, with a slightly different plateau value at large values of $E_\perp$. This rapid increase of the relative width starting at energies $E_\perp$ much larger than the well-depth D is at the heart of the present chapter suggesting a new experimental approach to estimate the well-depth D from purely inelastic scattering profiles. This behavior was first identified in a recent paper devoted mainly to the elastic diffraction of neon atoms on a LiF surface [67] where a calculated [128] potential

energy landscape could be optimized to data. Starting from these results, a model analysis is developed in Sec. 6.1.2 on a more general basis of Morse potentials. For helium, we use for the mean planar potential a well-depth $D = 8.5$ meV from TEAS spin-echo measurement, [183] while for neon, we took the value of $D = 10.3$ meV derived in Ref.[67] slightly below the recommended value in Ref.[184].

The angular shift $\delta\theta$ between the elastic and inelastic polar profiles.

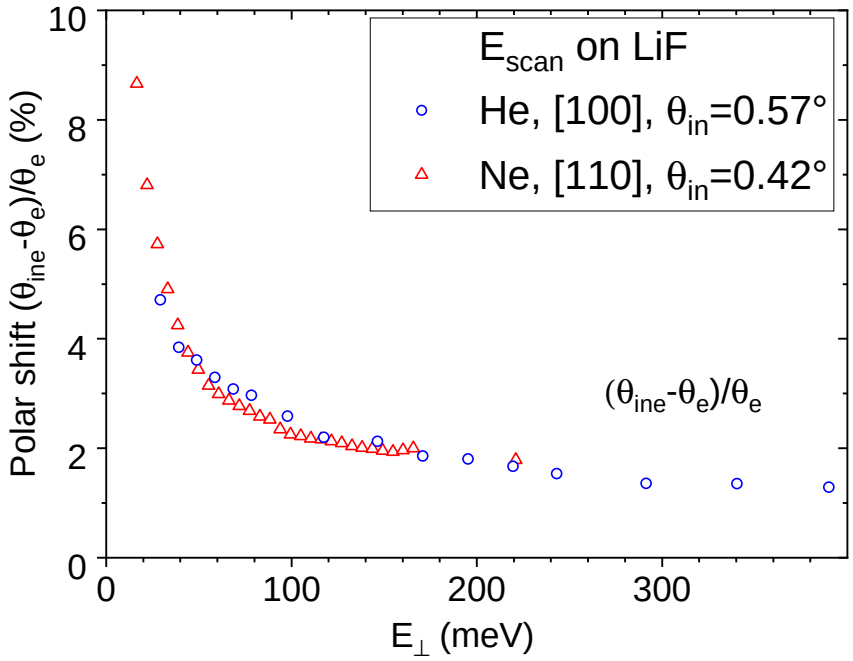

Figure 6.8 The relative shift between the peak position of the elastic peak and the median value of the inelastic profile, as modeled in Fig. 6.2 is reported for helium and neon projectiles. From ref.[72].

The fitting procedure illustrated in Fig. 6.2 and Fig. 6.3 was first developed with a constraint forcing a common value for the center of the elastic and inelastic scattering profiles. The reduced number of free parameters was expected to ensure better stability. However, we rapidly identified situations where the fit is much better with an inelastic scattering profile located at slightly larger angles: $\theta_{ine} = \theta_s + \delta_\theta$, with θ_s the specular angle and $\delta_\theta \geq 0$. Figure 6.8 indicates that this shift increases rapidly below 100 meV. The shift is arbitrarily plotted relative to the elastic scattering angle, the absolute deviation is comparatively small. For instance, the shift does not exactly reach zero at large values of $E_\perp$ obtained around 1-2 $^\circ$ incidence, the value of 1-2% corresponds to only 0.004 $^\circ$, which could be affected by our angular resolution [16]. More relevant probably, as can be seen in Fig. 6.3, the fit is not perfect, leaving a clear residue in the rising and trailing edges indicating possible

contributions from defects, and/or from the fact that the log-normal profile used here in the deconvolution is only an approximation as will be discussed in Secs. 6.1.1 and 6.1.3. Figures 6.7 and 6.8 display the evolution of the inelastic scattering width σ_θ and shift δ_θ relative to the specular angle $\theta_e = 2\theta_i$, both have a comparable behavior.

Summarizing the experimental findings:

- The inelastic polar profile hardly depends on the crystallographic direction investigated (Fig. 6.4).
- The Debye-Waller factor depends primarily on the reduced variable $E\theta^3$ (see Fig. 6.5).
- The relative inelastic width σ_θ/θ_s, as measured by w in Eq. 6.1 in a log-normal fit, depends mainly on the perpendicular energy $E_\perp$. It appears stable above 100 meV but increases rapidly below (see Fig. 6.7).
- The median position of the inelastic scattering polar scattering profile tends to become significantly over-specular at low values of $E_\perp$ (see Fig. 6.8).

We now rapidly present a model developed to describe the inelastic scattering profiles in fast atom scattering at grazing incidence.

6.1.2 Inelastic diffraction, the surface stiffness Γ

Aside from the probability (DWF), let us focus on a fundamental difference of the inelastic collision in TEAS and GIFAD. During a head-on collision at hyper-thermal energy, all the projectile momentum is reversed independently from the surface atom protruding or recessing from the mean surface plane. At variance, under grazing incidence, the distance of closest approach, and therefore the magnitude of the momentum transfer will be directly (exponentially) affected by this departure from equilibrium. At grazing incidence, the binary collision approximation where the overall momentum transfer is decomposed in terms of successive binary collisions with the closest surface atoms is still relevant due to the exponential character of the repulsive forces [71]. The momentum transfer can be evaluated from a straight line approximation [119] with a projectile flying at a distance z_t above the surface and, for a purely repulsive binary potential such as $V(z) \propto e^{-\Gamma z}$, the scattering angle also depends exponentially on the closest distance between the projectile and the surface atom. As a result of a surface atom protruding or receding by $\pm dz$ is scattered at angles $\theta_\pm \propto e^{-\Gamma(z_t \pm dz)}$. Considering $dz = \sigma_z(T)$ as the standard deviation of Gaussian atomic displacement defined above, the scattering distribution due to this single collision is a

log-normal distribution where the specular angle corresponding to the equilibrium position is the median value while the relative width is $w = \Gamma\sigma_z(T)$ [74, 71].

Both He and Ne have much larger binding energy than LiF so that most of the energy variation when approaching the surface should be related to the deformation of the Fluorine atoms. He and Ne are therefore expected to have a similar decay rate of the mean planar potential, and only the absolute magnitude of the repulsive term should be larger for neon which has more outer electrons.

Since the valence band is located on F^- ions, the Li^+ play a limited role in the momentum transfer associated to diffraction, as confirmed by trajectory simulations [105].

Note that the simple relation $w = \Gamma\sigma_z$ holds only for a single scattering event. The overall elastic scattering probability is the product of all the individual elastic probabilities but the overall inelastic scattering profile, depends on how many individual inelastic events contribute to the polar inelastic profile.

The attractive forces, the effective stiffness $\Gamma_{\mathbf{eff}}$

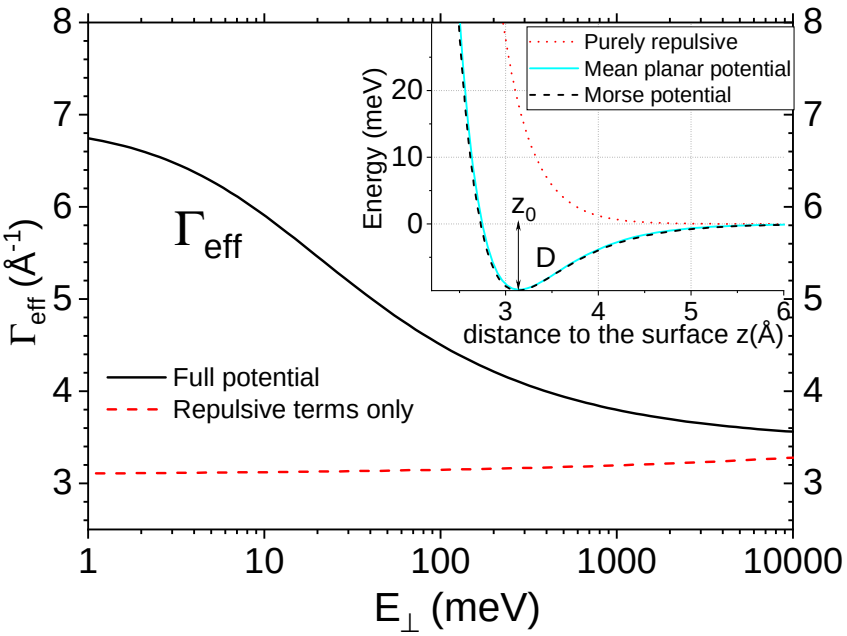

Figure 6.9 The mean interaction potential for Ne-LiF from Ref.[67] is reported in the insert together with the fitted Morse potential. The logarithmic derivative $\Gamma_{\text{eff}} = -V'(z)/(V(z)+D)$ is expressed as a function of the energy $E_\perp$ (see text). From ref.[72].

The main properties of the QBCM described above derive from the exponential form of the repulsive part of the interaction and could remain valid after adding a weak attractive part. These are the polarisation forces due to the Madelung electric field of the LiF surface which should also exhibit exponential decay with a typical range on the order of the lattice unit and the van der Waals forces which should have a polynomial form (see *e.g.* ref[146] for a recent discussion in noble gas dimers). The resulting physisorption well can host bound state resonances whose exact locations are sensitive to both sides of the trapping well. These can be observed in GIFAD [185] but the TEAS has demonstrated exceptional resolution [183] (or [186] for a recent review), providing a challenging description of the attractive part.

Here, the width of the polar profile originates from the part of the trajectory close to the surface and is expected to be sensitive mainly to the shape of the repulsive wall. We decided to use an exponential form also for the attractive part because of its simple form and analytic properties. It can also be justified by the fact that part of the attractive forces are due to the polarisation of the projectile in the Madelung field of the ionic crystal surface. This latter is known to decrease exponentially with a range close to the lattice constant. We choose a Morse potential of the form.

$$V_M(z) = De^{-\Gamma(z-z_0)} - 2De^{-(\Gamma/2)(z-z_0)} \tag{6.2}$$

Where the attractive part has a decay range twice larger than the repulsive one. Compared with the pure repulsive potential where only Γ was found important, two additional parameters are needed: the well-depth D and the equilibrium distance z_0. Using Eq. 6.2, the turning point z_t when an atom of energy $E_\perp = V_M(z_t)$ bounces back from the surface is given by

$$z_t = z_0 - \frac{2}{\Gamma}\ln\left(1+\sqrt{1+\frac{E_\perp}{D}}\right) \tag{6.3}$$

The parameters Γ=3.46 Å^{-1}, D=10.3 meV, and z_0=3.13 Å have been fitted to the *ab initio* potential energy landscape calculated in Ref.[128] and optimized to elastic diffraction data with a fast quantum scattering code for the Ne-LiF system for $E_\perp$ ranging between 20 and 200 meV [67]. Both the empirically adjusted mean planar potential and the Morse potential used hereafter are displayed in the inset of Fig. 6.9. They look very similar as we have imposed equal depth and equilibrium distance as well as the value of Γ, note that this value is very close to the one derived from the asymptotic behavior attached to the workfunction $W \simeq 13$ eV [64], $\Gamma \sim 2\sqrt{2W} = 3{,}7$ Å^{-1}.

Rather than a direct evaluation of the momentum transfer along the projectile trajectory, we compare in Fig. 6.10 neon data recorded during an E_{scan} with prediction using the QBCM and the Morse potential. We first recall that for an E_{scan} and a purely repulsive potential, the classical limit of Eq. 5.19 predicts a constant value of the log-normal width w, as illustrated by the horizontal dotted line in Fig. 6.10 corresponding to neon atoms at θ_{in}=0.42 ° [67]. To better illustrate the role of the attractive forces we have tried to evaluate its contributions to three separated parts of the atom trajectory, i) the way in of the trajectory, ii) the comparatively closer collisions with surface atoms, and iii) the way out.

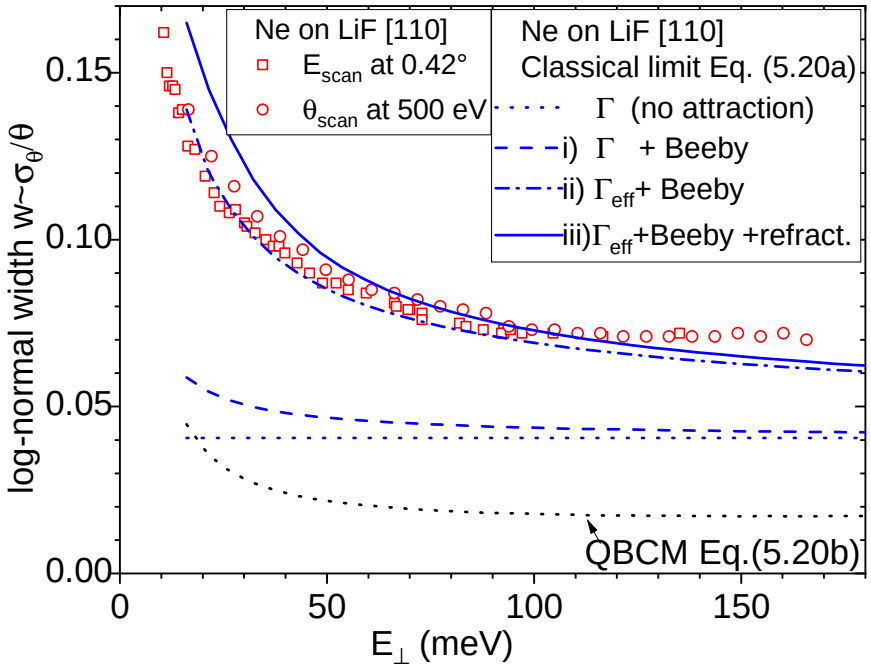

Figure 6.10 The log-normal relative width $w \approx \sigma_\theta / \theta_{scat}$ of the inelastic scattering polar profile is reported for conditions indicated on the left inset. To outline the different contributions, incomplete models are presented and discussed in the text, the QBCM model in Eq. 5.20 . From ref.[72].

- (i) The modification of the perpendicular energy before the impact on the surface ($\infty > z \geq z_0$).

This correction corresponds to the well-known Beeby correction factor [174] widely used in TEAS [187]. It considers that the attractive part of the mean planar potential has the effect of changing the effective perpendicular kinetic energy before the projectile evolution on the repulsive wall. The Beeby correction considers that elastic diffraction probability can be evaluated as that of a particle with an effective energy $E'_\perp = E_\perp + D$.

For grazing incidences, the situation is similar to the image charge acceleration increasing the impact energy of ions before impact on a surface, [188, 25] and it is usually modeled as an effective angle of incidence $\theta_{\text{eff}} = \sqrt{\theta_i^2 + D/E}$ providing the same impact energy $E_\perp + D$. The polar straggling $\sigma_\theta = w \times \theta_{\text{eff}}$ acquired at impact should be preserved so that the relative width is now $w' \approx w \times \theta_{\text{eff}}/\theta_i$. The corresponding dashed line in Fig. 6.10 indicates a moderate increase of w at low values of $E_\perp$ but only for values of $E_\perp$ close to D. The value of $\sigma_z = 0.098$ Å considered here for data recorded at 300 K, is taken from ab initio extensive calculations [127, 172] of the LiF crystal and corresponds to a Debye temperature T_D=550 K at the surface, very close to the recommended value derived from TEAS measurements [168].

- (ii) The modification of the stiffness of the surface at the moment of impact ($z < z_0$).

We now take into account that the actual stiffness at the moment of impact is not Γ that of the sole repulsive term of the potential but the logarithmic derivative $-V'/V$ of the actual potential combining repulsive and attractive part at the turning point in eq. 6.3. More precisely, taking into account the above Beeby correction that the effective energy is $E_\perp + D$, the effective stiffness is defined as $\Gamma_{\text{eff}} = -V'/(E_\perp + D)$ which remains well-defined even for low values of $E_\perp$. Using the Morse potential $V_M(z)$ from Eq. 6.2 as a mean planar potential, the effective stiffness of the repulsive wall is given by (A detailed derivation in Appendix A)

$$\Gamma_{\text{eff}}(z) = \Gamma \left[1 + \left(1 + \frac{E_\perp}{D} \right)^{-1/2} \right] \tag{6.4}$$

The figure 6.9 reports the evolution of the effective stiffness with the energy $E_\perp$ and shows an increase that is maximum at low values but remains significant above 100 meV. The dashed-dot line in Fig. 6.10 now shows a sharp increase of w also starting at perpendicular energies around 100 meV.

- (iii) The refraction of the atoms inelastically scattered when leaving the surface ($z_0 \leq z < \infty$)

This last contribution is the reverse transformation of i). When climbing the attractive branch of the mean planar potential, the particles scattered from the surface at an angle θ_{emi} will give back the energy D along the z direction so that the observation angle is $\theta_{obs} = \sqrt{\theta_{emi}^2 - D/E}$. The median value θ_{emi} of the log-normal scattering profile is restored at the specular angle. However, the associated Jacobian $J = \mathrm{d}\theta_{obs}/\mathrm{d}\theta_{emi}$ induces a nonlinear stretching of the log-normal distribution at low scattering angles. The effect on the scattering profile was

estimated by fitting the resulting scattering profile by a log-normal distribution to produce a relative width w and correspond to the full line in Fig. 6.10.

The sharp increase is qualitatively well reproduced a dominant contribution coming from the account of Γ_{eff} in Eq. 6.4. The agreement with the observation seems better for the classical limit, as if a single inelastic collision (among N) is enough to induce a fully classical behavior. This quantitative agreement should not be overestimated because, as discussed below, a proper account of phonons can probably affect the absolute magnitude. However, we consider that the influence of the well-depth D on the effective stiffness Γ_{eff} is a very robust effect that has to be taken into account to estimate the polar width. It is the main finding of the present paper. Note that in TEAS, using diffracted intensities recorded between 17 and 270 meV on a Ni(110) surface, a mean potential energy curve could be extracted, indicating a similar twofold increase of the surface stiffness at low energy [189].

The consequence of the well depth D on the Debye-Waller factor is less quantitative. Taking into account the attractive terms, the DWF in Eq. 5.16 can be written using the classical energy loss of Eq. 5.17 but evaluated with the effective stiffness Γ_{eff} and effective angle of incidence θ_{eff} defined above. The result reported in Fig. 6.6 as full lines in light blue or orange indicates that neither the offset nor the slope is well reproduced and the improvement compared with the purely repulsive form is only marginal. This is quite different from TEAS where the Beeby correction is widely used to adapt the Debye-Waller factor to measurements [174, 190]. In particular, it is responsible for a significant offset at very low impact energy. In GIFAD, changing θ to θ_{eff} increases the impact energy but the angle remains grazing so that the momentum is still shared among several surface atoms with a limited consequence on the Debye-Waller factor. The situation is even worse concerning the angular shift in Fig. 6.8, the asymmetric stretching of the polar profile on the way out produces a shift that is much less than the one observed and tended to decrease the mean inelastic polar profile. These discrepancies are discussed in the next section.

6.1.3 Discussion

The similarities between Fig. 6.7 and Fig. 6.8 suggest that a common origin could explain both behaviors but our simulations do not confirm this. A possible explanation could be related to the reduction of the surface reflectivity at the most grazing incidences. One important aspect of grazing angle collision is the sensitivity to the presence of obstacles such as ad-atoms or step edges etc... These are becoming increasingly important as the angle of incidence is decreased, and their influence can be measured by the reflectivity, the ratio of reflected particles intensity related to that of the primary beam before target insertion.

Below 1 ° of incidence, this reflectivity becomes challenging to measure because, even with a beam diameter ϕ below 100 μm, the length of the zone illuminated $\sim \phi/\theta_{in}$ becomes larger than the typically crystal dimension around 10 mm. However, this restriction alone does not explain that the surface quality usually limits the lowest possible incidence. We observed optimum reflectivity with large wafers and freshly grown layers of semi-conductor directly measured inside the molecular beam epitaxy chamber [10]. It was then possible to measure the influence of incomplete layers on the inelastic scattering angle during growth [126]. In the present case, even with freshly cleaved LiF surfaces (see sec.,2.7) the observed reflectivity usually drops drastically below a few percent for incidence angles below 0.3°. This dependency may be of limited importance for elastic diffraction, which is spot-like and cannot be deformed, but the inelastic scattering profile is probably affected since particles scattered under-specular have fewer chances to reach the detector without encountering an obstacle. The tendency of over-specular reflection observed in Fig. 6.8 could reflect the reduced probability for particles scattered under-specular to reach the detector. The effect would probably reduce the measured inelastic intensity and its width at the lowest incidences. Therefore, it would also affect the Debye-Waller factor but probably only by a few percent, as suggested by the effect on the mean position of the inelastic polar profile.

The disagreement between the measured and predicted Debye-Waller factor probably indicates a lack in the model. A major weakness of the QBCM is that surface vibrations are treated only through the local Debye oscillator, thus neglecting the phonons mode, which are the genuine eigenstates of vibrations at surfaces. Only a few authors have developed approaches where phonons are explicit, most are adapted to TEAS [191, 192, 177, 193] but also to grazing incidences [180, 181].

In GIFAD, the successive momentum transfer to the surface atoms occurs in a timescale $\tau = 1/(\Gamma v_\perp)$ with $v_\perp = \sqrt{2E_\perp/m_p}$ much shorter than the vibration time. So that momentum transfer along the N successive collisions of the trajectory should be coherent, exciting preferentially transverse phonons having a wavelength close to $N \cdot a \sim 6/(\Gamma\theta)$. Since the interaction with Fluorine ions dominates, the vector of exchanged momentum should decompose with almost equal weight to acoustic and optical surface phonons, the former having associated low energy while the second should have flat dispersion curves with an energy close to the high-frequency limit of the Debye oscillator considered here. The model described above does not take phonons into account. The easiest way to improve the agreement with data is to reduce the Debye temperature to 310 K (which also provided a better qualitative agreement in Ref.[71]). The associated prediction of the DWF is depicted by dotted lines in Fig. 6.6 and is much closer to the experimental data with slopes that now

compare to the measured ones. This low value of the Debye temperature is probably not a good description of the amplitude of the thermal displacement but should be considered as an indication that low energy phonons can contribute to GIFAD [180] and suggested in Fig.6.11. This part has not been developed so far and deserves deeper investigations.

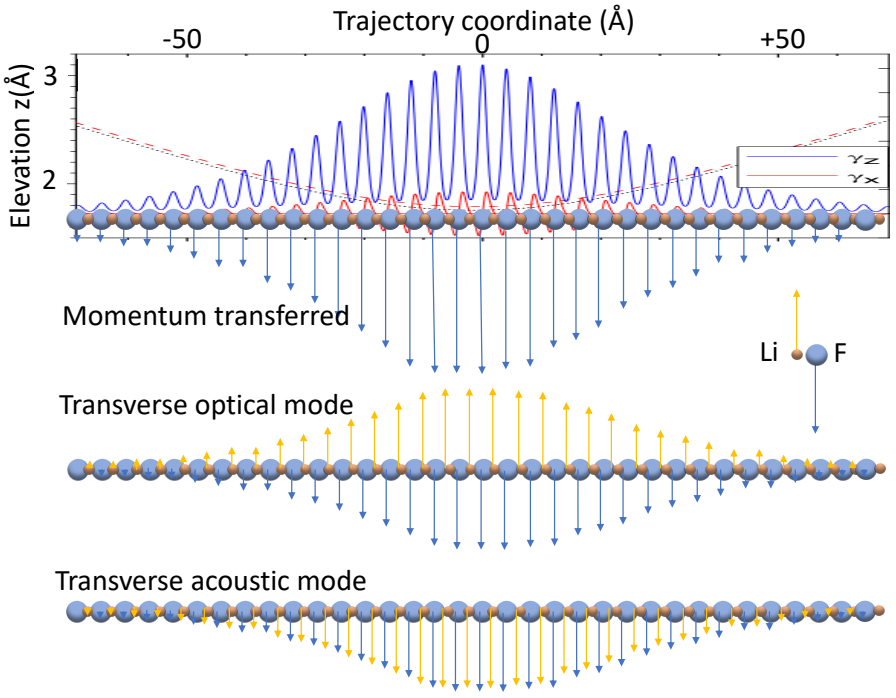

Figure 6.11 Assuming that only the Fluorine atoms interact with the projectile, the momentum transfer curve could be decomposed into an equal weight into optical and acoustic phonons. The former should have a flat dispersion curve with $E \sim \hbar\omega_D$ while the second should belong to a low energy linear dispersion curve $E \propto k$. The typical length L of the trajectory should indicate the wavelength of the modes.

6.1.4 Conclusion

We have presented measurements of the polar scattering profile of fast helium and neon atoms with energies ranging from 0.2 keV to 5 keV diffracted at the surface of a LiF single crystal under grazing incidence. These profiles were found to be independent on the crystallographic axis probed by the primary atomic beam. The fit of the inelastic profile by a log-normal function provides an estimate of the DWF which is found to depend on $E\theta_{in}^3$, a quantity proportional to the classical energy loss in Eq. 5.17 as suggested in [176, 74, 71]. The relative width w derived from the log-normal fit is found to depend primarily on the energy $E_\perp \sim E\theta_{in}^2$ *i.e.*, for a given system projectile-surface, on the distance of closest approach.

This is consistent with eq.7.3 and E-scan. Our result do not show evidence of the quantum regime where only one collision could be inelastic, it seems that either all collision are inelastic either none of them. It does not affect the elastic or inelastic probability but it does affect the predicted angular profiles. In this respect, the QBCM becomes identical to the model proposed by Manson *et al.*[74] The value of w is found stable for larger than 100 meV but increases rapidly below. Both He and Ne projectiles display comparable values and similar behavior. Using a Morse potential fitted to a potential energy landscape previously adjusted to elastic diffraction data and a binary collision model together with a well-accepted value of the Debye temperature, the sharp increase of w is well reproduced and the analysis suggests a dominant role of the effective stiffness $-V'/(E_\perp + D)$ at the distance of closest approach.

To our knowledge, this rather simple effect was not documented so far, but a quick look at the inset of Fig. 6.9 indicates that the mean planar potential is seriously affected by the attractive forces. The repulsive wall is brought significantly closer to the surface. It has to grow at a faster rate to merge with the high energy values (low z) where the attraction is usually neglected. Our work suggests that under grazing incidence specific phonon mode may participate to the inelastic scattering which takes place on a relatively long distance $L \sim 6/(\Gamma\theta)$ (typically around $\sim$ 100 Å for θ=1 °) and where all surface atoms receive a momentum coherently oriented towards the bulk.

To first order, elastic diffraction is qualitatively well described by a hard corrugated wall model where the surface is modeled as an infinitely hard surface. We show here that its counterpart, the inelastic polar profile, is mainly sensitive to the stiffness Γ_{eff} of the hard wall and that this later is very sensitive to the attractive forces. The method can probably be applied to estimate the physisorption well-depth for heavier elements where the diffraction features are more difficult to obtain, and attractive forces can be more significant.

Chapter 7

Experimental Results: Temperature Dependence in Fast-atom Diffraction at Surfaces

The present chapter corresponds to a publication by Peng Pan, Maxime Debiossac, and Philippe Roncin, Accepted to *Physical Chemistry Chemical Physics*[182].

7.1 Introduction

Compared with thermal energies atom diffraction (TEAS), one of the distinct features of GIFAD is its ability to operate at elevated temperatures (*e.g.* Fig. 7.1 taken from [10]). The surface temperature is a decisive parameter in controlling the growth conditions in Molecular Beam Epitaxy (MBE). A delicate balance between the supply of material to the surface, its mobility, and the surface structure are to be found. Surprisingly, to our knowledge, there is no extensive experimental study published. In principle, a temperature scan (T-scan) is one of the easiest measurements. There is no change of the beam or target positioning parameter, and one simply increases the current of the heating coil. This is much more complex in practice because the thermal effect and mechanical deformations strongly affect both the exact target position and direction. This chapter describes the experimental approach to circumvent this difficulty. It presents experimental investigations on temperature dependence under a wide variety of experimental conditions of energy, angle of incidence, and temperatures.

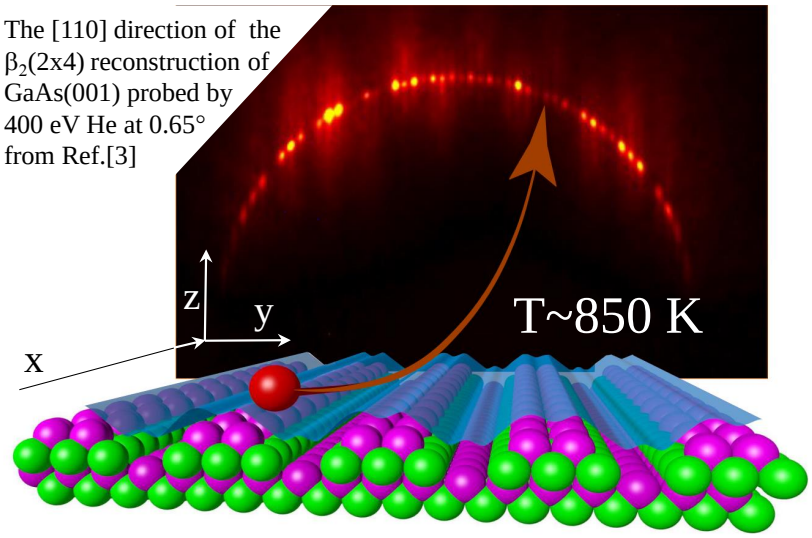

Figure 7.1 Recall the schematic GIFAD setup illustrating the interest in Molecular Beam Epitaxy (MBE). The diffraction image of a $\beta_2(2\times4)$ reconstructed GaAs(001) surface at 850 K was recorded inside a MBE vessel at Institut des Nanosciences de Paris (INSP)[11].

7.2 Experimental procedure

First, Fig.7.2 insists on the importance of the temperature effects. It shows three diffraction images recorded almost under identical conditions but at three different temperatures. The temperature increase triggers a transition from a spotty pattern where elastic diffraction dominates to a stripy pattern and then to a comparatively broad diffraction pattern where adjacent peaks start to overlap.

In GIFAD, the target surface is easily positioned within 10 to 20 μm from the beam. If it is not enough inserted, the primary beam is still present on the image, whereas if it is too much inserted, even the scattered beam disappears. However, thermal expansion of the target crystal and of the manipulator induce much larger displacements as well as minor angular tilts producing major effects in GIFAD (see e.g. the θ^3 dependence of the DWF displayed in Fig.6.5). For this reason, we were not able to record the three images displayed in Fig. 7.2 one after each other. Instead, we waited for a stable temperature before realigning the target and performing a θ-scan. From these variations, we interpolate between measured angular values to restore a temperature variation. Our target surface temperature is measured with a type-N thermocouple mechanically pressed on the backside of the Omicron-type sample plate. We have check consistency between different measuring devices by putting the thermocouples in liquid nitrogen and in an oven. The estimated accuracy is around a few K.

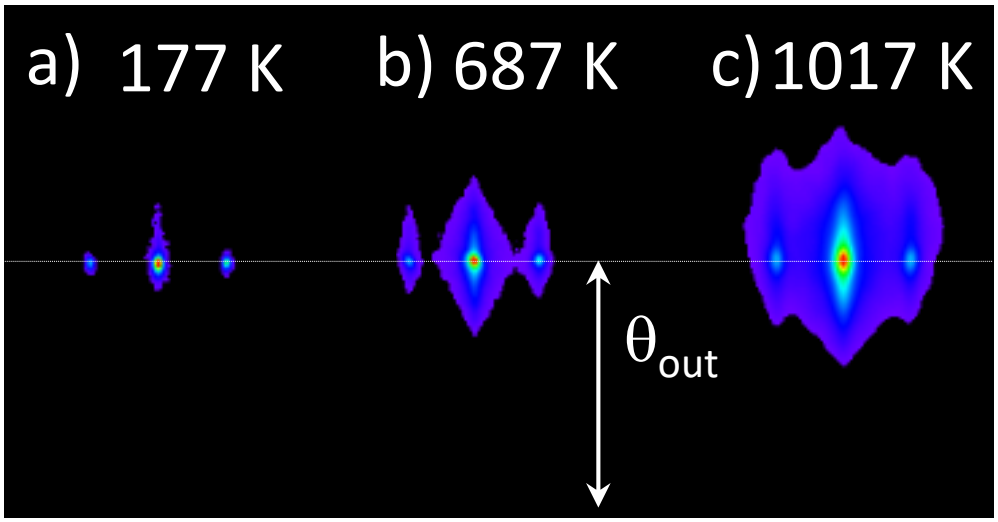

Figure 7.2 Three diffraction images recorded with 500 eV helium impinging with θ_{in}=0.75 °. on LiF [100] direction at temperatures of 177 K a), 687 K b), and 1017 K c). The images are normalized to the maximum intensity I_{max} corresponding here to the elastic specular spot. The rainbow color palettes are identical with a threshold value of 3% of I_{max}. From ref.[182].

On Fig. 7.3 a) the intensity distribution recorded on the Laue line is displayed in log scale for the three images of Fig.7.2. Within experimental uncertainty due to slightly different beam conditions, the narrow elastic peaks do not change shape but the inelastic contribution increases both in intensity and in width as outlined by the full-color lines suggesting an exponential decay of the inelastic component with the lateral deflection from the elastic position. More precisely, in this example, the extrapolated inelastic intensity increases quasilinearly with the temperature while the exponential delay constant decreases. The broad inelastic profile is also clearly identified with a relative height and a width growing with temperature so that the relative elastic intensity decay rapidly. At this stage, it is useful to compare with the first investigation of the temperature dependence performed when elastic diffraction was not yet demonstrated and where all peak shapes seemed to depend on temperature [9, 100, 10], probably because of a limited surface coherence. In this context, the Debye-Waller factor was tentatively attributed to the ratio of the narrow peak relative to the total intensity observed on the Laue circle [176, 194, 195], similar to the one that could be derived from Fig. 7.3 a) rather than from Fig. 7.3 b). This point of view, which is meaningful to analyze the elastic diffraction intensities, obviously underestimates the overall inelastic intensity and strongly depends on the primary beam profile.

Theoretically, a wave packet approach perturbed by random kicks to the wave function[107] to mimic thermal displacement was able to reproduce qualitatively a full inelastic diffraction

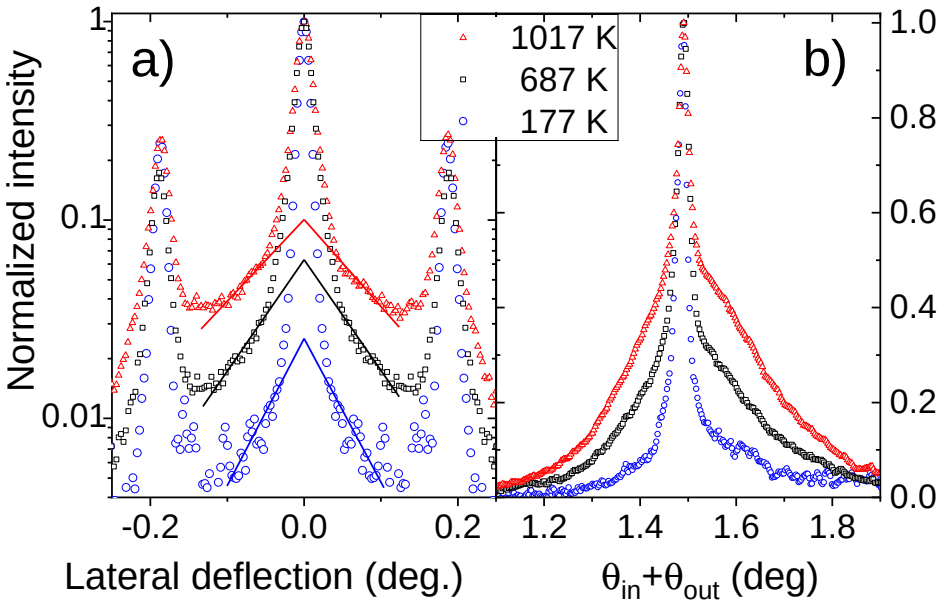

Figure 7.3 For the three images in Fig6.2. Panel a): lateral profiles on the Laue circle, the lines are here to outline the exponential decay of the peak tail. Panel b): polar scattering profiles as defined in previous chapters, for instance in Fig.6.3 or Fig.7.4. From ref.[182].

image but without any elastic signature. In addition, the statistic of these kicks and their amplitude was somewhat arbitrary, and no elastic diffraction was predicted hence the conclusion and title are partly incorrect. A similar problem is present in the semi-classical approaches of Gravielle and Frisco [181, 172], they could predict a broadening of the (inelastic) polar profile with temperature but using an elastic model while the elastic profile is absent. This outlines the difficulties of addressing together elastic and inelastic effects in GIFAD. As detailed in the previous chapter (eq.5.13), the DWF proposed[176, 74, 71] for GIFAD writes:

$$DWF = \exp\left(-\frac{3\Delta E_{Cl}}{\hbar\omega_D}\coth\frac{T_D}{2T}\right),\ \Delta E_{Cl} = \frac{2\,m_p}{3\,m}\Gamma a E\theta_i^3 \equiv NE_r \tag{7.1}$$

For the He-LiF system, the product Γa is close to 14 [67, 72] so that $N \approx 2/\theta$ can be large explaining why elastic diffraction could be observed with $E_\perp$ close to one eV [18, 16] whereas TEAS is usually limited below 100 meV. Alternately, with this reduced decoherence, GIFAD can explore the higher temperatures needed for MBE.

In the previous chapter, this naive, purely repulsive description was improved by taking into account an attractive part of the potential, for instance, van der Waals contributions [174, 121, 196], responsible for the physisorption well of depth D. In elastic diffraction, the effect of such attraction is the presence of bound-state resonances [109, 185] and the

increase of the rainbow angle at low energy [67]. These are naturally accounted for using a quantum approach [185, 67] or modeled in a semi-classical [149] or optical method such as the hard corrugated wall by the Beeby correction, indicating that the effective impact energy $E_\perp$ increases to $E_\perp + D$ [174, 197, 141] or considering a modified angle of incidence $\theta_{\text{eff}} = \sqrt{\theta_{in}^2 + D/E}$. The Beeby correction also significantly decreases the DWF in TEAS [198]. In GIFAD, we also found that the mere presence of a tiny well significantly modifies the stiffness of the potential by bringing the turning point much closer to the surface plane [72]. This can be expressed quantitatively using a Morse potential(Sec. 4.6.1) $V_M(z) = D(e^{-\Gamma(z-z_0)} - 2e^{-\Gamma/2(z-z_0)})$ and looking for the turning point z_t where $V_M(z_t) = E_\perp$ the effective stiffness is :

$$\Gamma_{\text{eff}}(E_\perp) = \Gamma\left[1 + \left(1 + \frac{E_\perp}{D}\right)^{-1/2}\right] \tag{7.2}$$

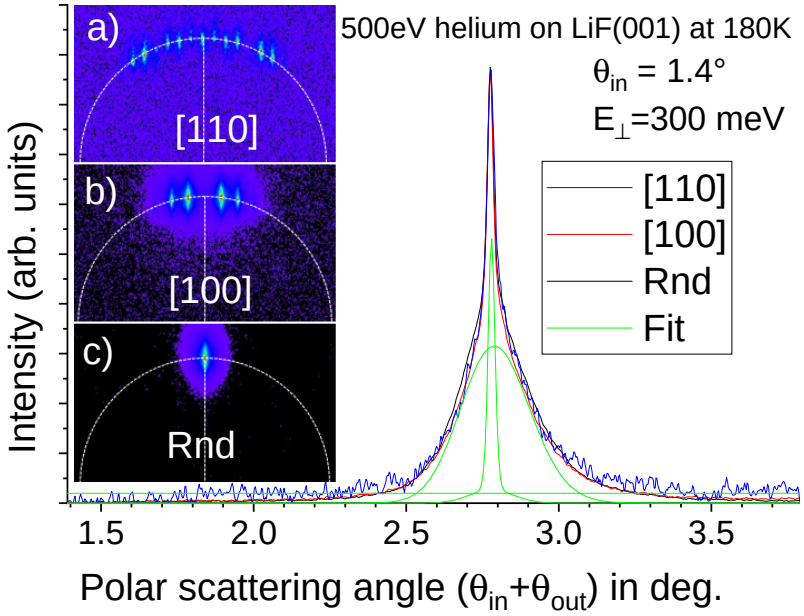

Figure 7.4 same figure as Fig.6.4 recalling that the polar profiles recorded along with the a)[110], b)[100], and c)random direction are identical. From ref.[72].

This increased stiffness was already identified in TEAS, [189] but it has much less consequence since at normal incidence the projectile hits a single surface atom, only the time scale $\tau \approx \Gamma/v_\perp$ depends on Γ not the magnitude of the exchanged momentum $2q$ and therefore not the coherence ratio. It is the reverse in grazing scattering, for identical values of $E_\perp$ the time scale τ for bouncing from the surface are identical in TEAS or GIFAD, but the

time needed for a single quasi binary collision is now $\tau' \approx v_{//}/a = \tau/N$ independent on Γ_{eff}, while its magnitude $\approx 2q/N$ depends directly on the effective stiffness Γ_{eff}. In summary, for GIFAD, the stiffness Γ_{eff} governs the momentum transferred in each collision, a stiffer interaction potential needs fewer collisions for specular reflection and each of them becomes more violent leading to an overall reduction of the DWF.

At the atomic level, the temperature is modeled by the spatial extend of a surface atom of mass m, which, in a Debye harmonic model is a Gaussian profile with $\sigma_z^2(T) = \frac{3\hbar}{2m\omega}\coth\frac{T_D}{2T} \sim \frac{3\hbar}{2m\omega}\frac{2T}{T_D}$, where T_D is the Debye temperature such that $\hbar\omega = k_B T_D$ with k_B the Boltzmann constant.

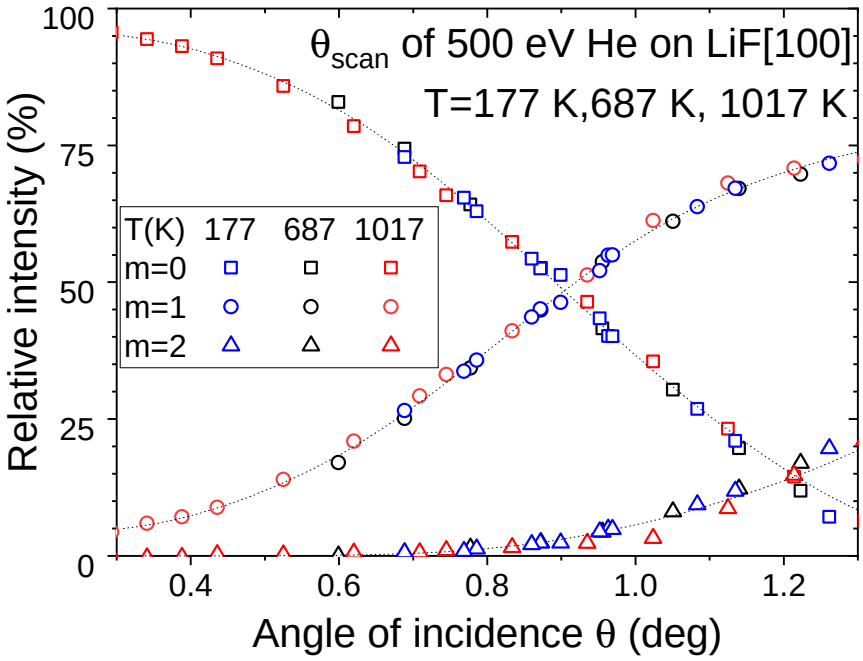

Figure 7.5 The relative intensities of (○)$m = 0$, (□)$m = \pm 1$ and (△)$m = \pm 2$ recorded in three θ-scan performed at temperatures of ○ 177 K, ○ 687 K, ○ 1017 K, fall on top of each other, I_m predict by Eq. 4.4. From ref.[182].

7.3 Results

We concentrate here on the impact of the thermal movement of surface atoms on the inelastic diffraction and its relative intensity but the temperature also affects the elastic diffraction via the thermal expansion of the crystal. Measuring the thermal expansion coefficient is simply tracking the evolution of the Bragg angle with temperature. In practice, the Bragg angle of 500 eV helium on LiF [100] is only 0.1826 ° at room temperature, and even with a

0.005 ° resolution, the native accuracy is only a few percent. A fit if Fig. 6.2c) can provide an accuracy ten to a hundred times better depending on the statistics. Keeping this relative accuracy during successive images requires complex procedures to ensure that the position illuminated by the beam stays fixed, and that all angles are measured with the same accuracy. We observe a variation of the reciprocal lattice vector with temperature compatible with previous measurements but less precise than the one measured in TEAS [199]. Along the [100] direction (Fig. 7.2 and 7.3), we have checked that the relative diffracted intensities, needed to extract the structure factor, do not depend significantly on the temperature. Fig. 7.5 reports the intensities recorded during three θ-scan at three different temperatures.

7.3.1 DWF: Sample quality issues

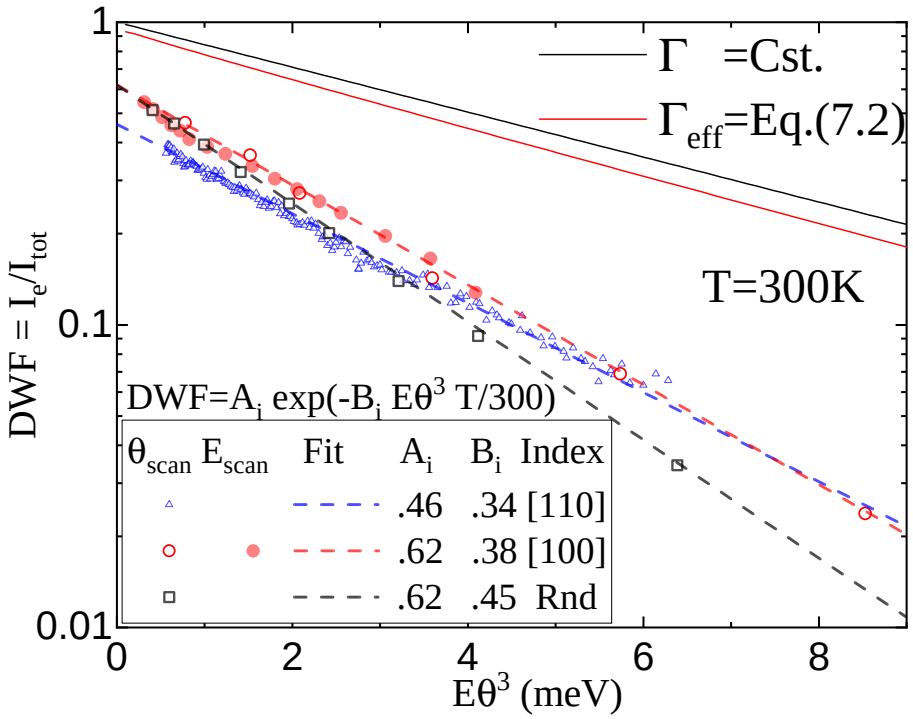

Figure 7.6 Energy dependence of the DWF from 3 samples at room temperature $T_r = 300K$, measured as the relative intensity of elastic diffraction, is reported for He atoms on LiF along random orientations as a function of $E\theta^3$, the tendency indicates $2W \propto E\theta^3$ at a fixed temperature. The dotted lines fit the data and provide the decay rate, which is proportional to temperature, 2W ∝ T. From ref.[182].

All our samples have been prepared by cleaving at air LiF crystals previously irradiated by γ rays [55]. However, the Debye-Waller factor (see Sec. 5.6 seems to vary from sample to sample and may also depend on the actual spot investigated. We also observed a slow degradation of the diffraction images with time, even at a few 10^{10} mbar pressure. We try

to perform a complete set of experiments within a day or two but, for instance, cooling to a low temperature usually takes a whole day. When taking a sample left in a vacuum for a few weeks, the measured DWF is systematically lower, even after a short thermal treatment. This is illustrated in Fig. 7.6 where three sets of data recorded on the different samples are reported. In spite of a scattering of data points in each set, the measured DWF are different.

7.3.2 DWF: Energy dependence

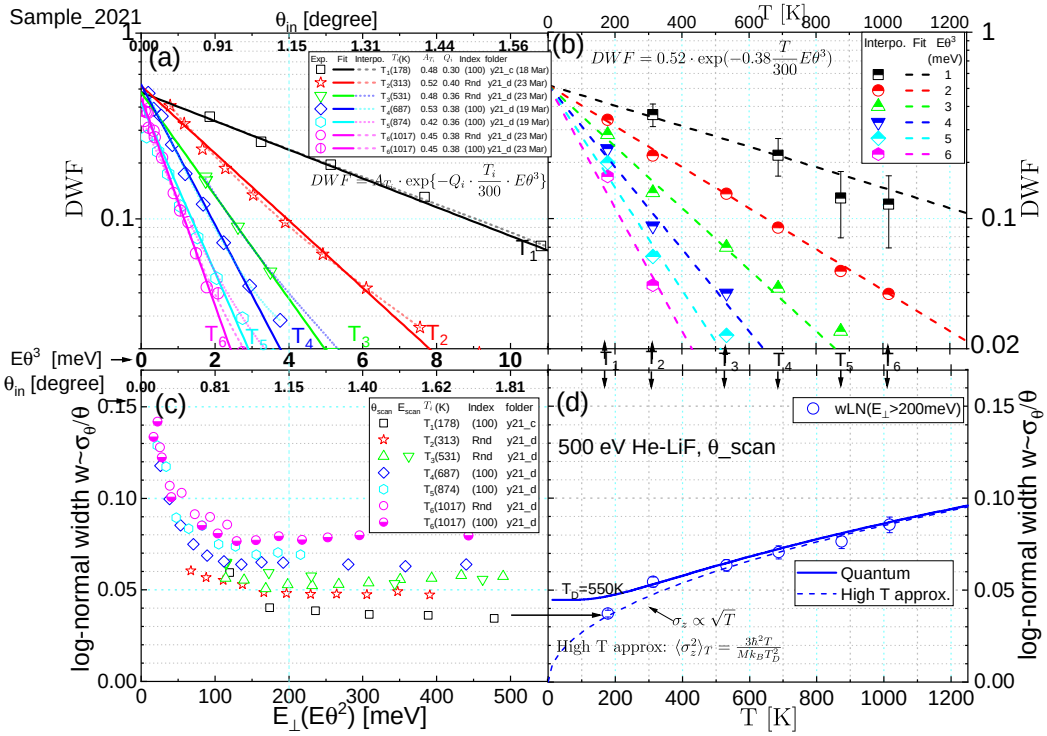

Figure 7.7 Results from sample A. (a) Energy dependence of the DWF at temperature T_i. (b) Temperature dependence of the DWF, the data interpolated from (a) at $E\theta^3$ from 1 to 6 meV. (c) Energy dependence of the inelastic scattering width w of the log-normal inelastic profile. (d) Temperature dependence of the inelastic scattering width w, which is the statistical mean of the data in (c) having a normal energy above 200 meV. The error bar is the standard deviation. From ref.[182].

As predicted from the spatial approach [176] considering a reduced thermal amplitude $u^2 = u_z^2/N$ or from momentum transfer along the trajectory [74, 71], the effective DWF adapted for GIFAD was predicted to scale with $E\theta_{in}^3$ where E is the primary beam energy and θ_{in} the angle of incidence. This was verified at room temperature [72] by reporting DWF measured on a large set of energy and incidence angles.

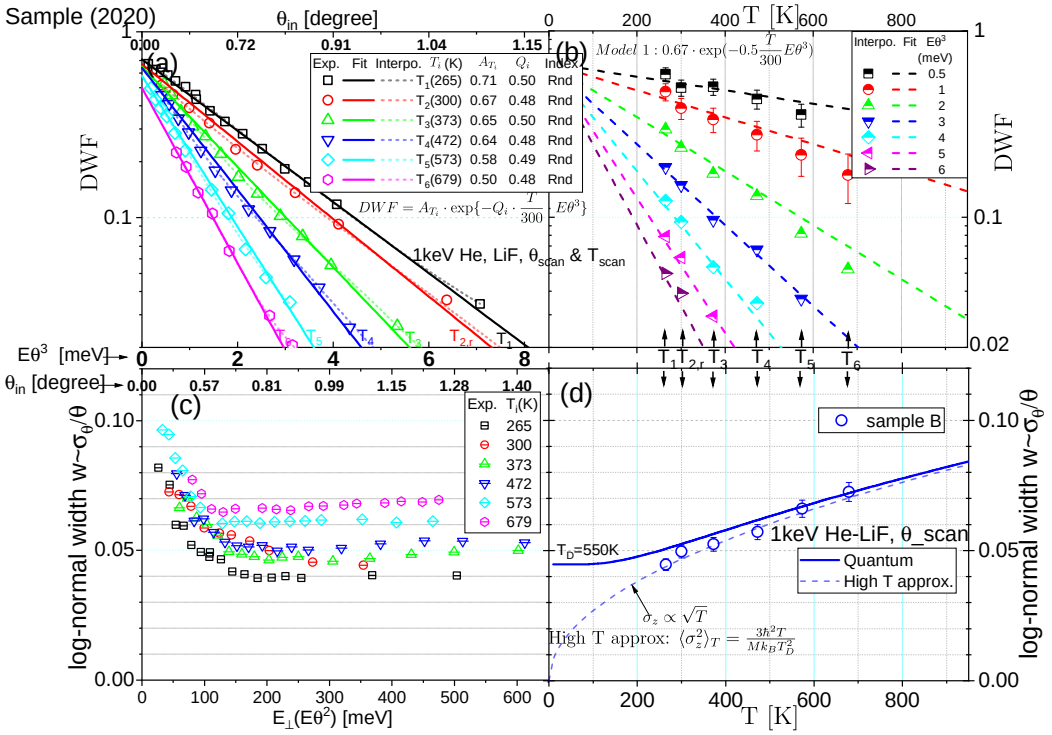

Figure 7.8 Same as Fig.7.8 but with sample B. (a) Energy dependence of the DWF at temperature T_i. (b) Temperature dependence of the DWF, the data interpolated from (a) at $E\theta^3$ from 0.5 to 6 meV. (c) Energy dependence of the inelastic scattering width w of the log-normal inelastic profile. (d)Temperature dependence of the inelastic scattering width w, which is the statistical mean of the data in (c) having a normal energy above 200 meV. The error bar is the standard deviation. From ref.[182].

The figure. 7.8 display the DWF measured with helium projectiles for seven temperatures ranging from 177K to 700K on LiF along a random direction. The dotted lines fit the data and provide the exponential decay rate, which indicates that the Debye-Waller exponent $2W(T)$ is proportional to surface temperature.

7.3.3 DWF: Temperature dependence

In grazing angle fast atom diffraction experiment, it's very sensitive to the incident angle, $2W \propto E\theta^3 T$, For fixed beam energy E and incident angle θ, *i.e.* $E\theta^3$=constant, the DWF should exponentially decay as a function of temperature T. The measured DWF or elastic ratio exponentially decays with increased collision energy, and also exponentially decays with increased incident angle. However, when plotted as a function of $E\theta^3$, the data recorded during an E_{scan} or a θ_{scan} tend to fall on top of each other as reported in Ref.[72]. The figure

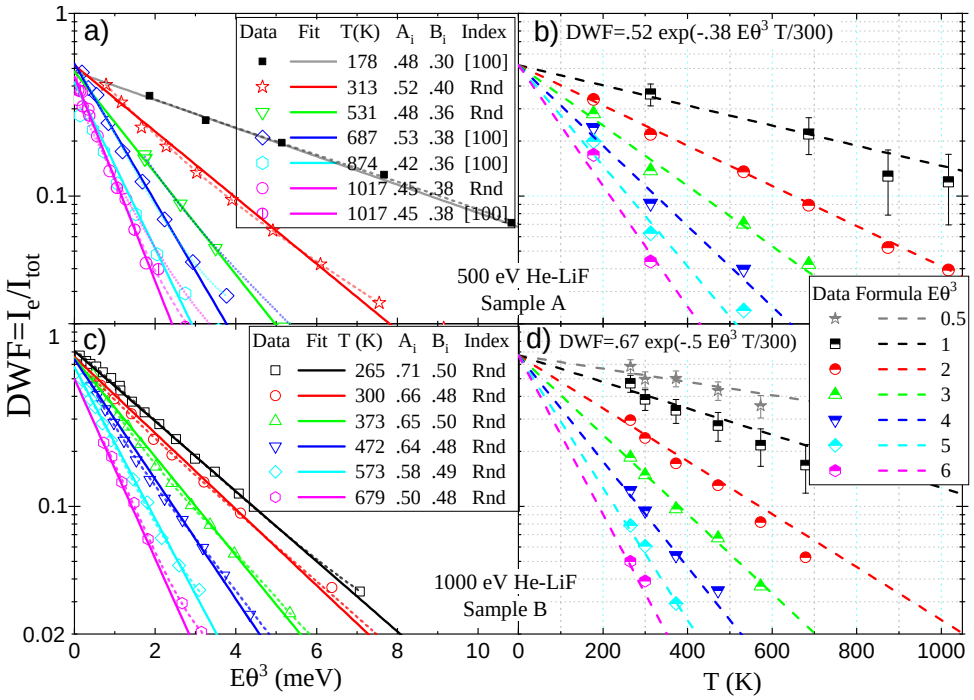

Figure 7.9 Panels a) c), report the DWF as a function of the reduced parameter $E\theta^3$ for the two different LiF samples of Fig.7.8 and Fig.7.7. The dotted lines are B-spline interpolation used to derive the temperature dependence at fixed values of $E\theta^3$ in b) d) and reproduced by a global formula. At very low angles of incidence, corresponding to $E\theta^3 \leqslant 1$ meV, where a scattering background is present an error bar estimated at 5% is plotted. From ref.[182].

7.6, 7.8, and 7.7 displays the DWF measured with helium as probes in a wide variety of initial conditions as a function of $E\theta^3$.

7.3.4 The inelastic scattering width w

The polar inelastic scattering profile is fitted log-normal form, [200] and the relative width w are reported in Fig. 7.10a) and 7.10b) as a function of the perpendicular energy $E_\perp$, a quantity that governs the distance of closest approach to the surface. The fact that this width was found [72] to depend mainly on $E_\perp = E\theta^2$ indicates that it is sensitive to the magnitude of the most violent inelastic collisions along the trajectory rather than to the integral effect of such collision, which would be closer to $E\theta^3$. Assuming that the inelastic collision is well-modeled by classical mechanics, the thermal motion $\sigma_z(T)$ of the surface atom induces, for each collision a log-normal scattering profile having a width $\mathrm{dw} = \Gamma\sigma_z$ [74, 71] or, equivalently a contribution to the angular straggling $d\sigma_\theta = \Gamma\sigma_z d\theta$ where $d\theta$ is the elastic deflection angle in this collision already estimated as $d\theta = (\theta_{in} + \theta_{out})/N$. Adding the N individual variances $d\sigma_\theta^2$ or using the mean log-normal width $\mathrm{w} = \mathrm{dw}/\sqrt{N}$

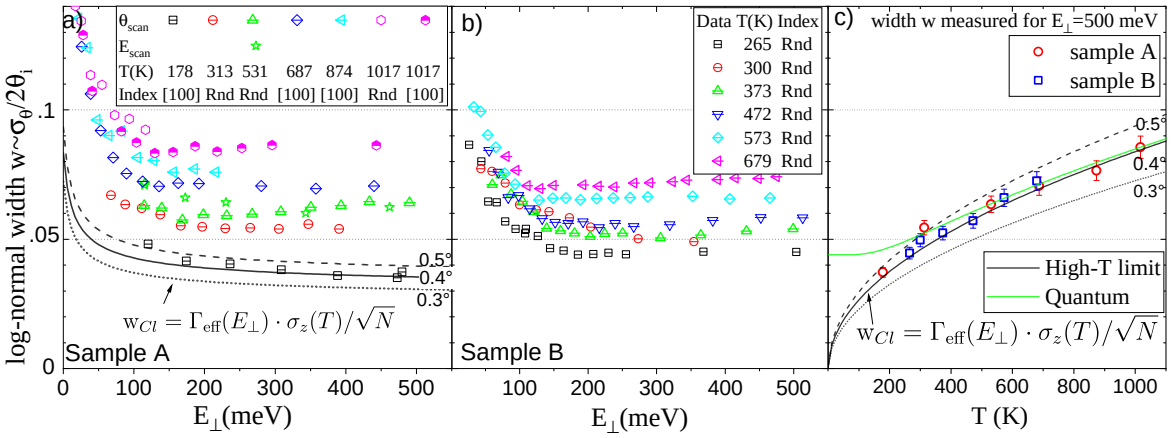

Figure 7.10 a) and b) inelastic scattering width w as a function of $E_\perp = E\theta^2$. The increase at low $E_\perp$ is mainly due to $\Gamma_{\text{eff}}(E_\perp)$. The w measured at $E_\perp$=500 meV are reported in panel c) with the mean thermal amplitude $\sigma_z^2(T)$. The lines in a) and c) correspond to Eq. 7.3 with different angles in the evaluation of N. (see text) The green curve marked as Quantum takes the zero-point energy into account. From ref.[182].

the classical scattering width is predicted:

$$w_{Cl} = \Gamma \cdot \sigma_z/\sqrt{N}, \text{with } N = 6/(\Gamma a \theta_{in}) \tag{7.3}$$

The comparison with the experiment is tricky, the Eq. 7.3 reproduced the evolution during an E-scan but not during a θ-scan while the experiment gives similar results during E-scan and θ-scan [72]. In this respect, the following discussion is only qualitative. More precisely, during an E-scan where θ_i is fixed N would stay constant so that, neglecting for here the Beeby correction, $w_{Cl} \propto \Gamma\sigma_z$ would remain constant. However, as already observed at room temperature [72] and in Fig. 7.10a) and 7.10b) a sharp increase of w is observed at low $E_\perp$. The agreement was established by taking into account the attractive forces *i.e.* by replacing Γ with Γ_{eff} from Eq. 7.2. The increase at low energy could then be attributed to the enhanced stiffness at low energy [72]. The full dashed and dotted lines indicate how the absolute values of w_{Cl} depend on the angle of incidence of the hypothetical equivalent E-scan. The 7.10c) reports the value of w measured at $E_\perp$ = 500 meV where is becomes stable. The lines using the same Eq. 7.3 now indicate that the evolution of the plateau values in Fig. 7.10a) and 7.10b) is compatible with the expected variation of σ_z even if the low-temperature zero-point motion (green curve) is not visible. The physical parameter D=8.5 meV [109] and T_D=550 K [127] correspond to well-accepted values in the literature, and Γ=3.5 Å^{-1} was produced in a quantum calculation [185]. It is close to the asymptotic value $\Gamma = 2\sqrt{2W} = 3.55 \pm 0.15$ Å^{-1} where $W = 12.2 \pm 0.5$ eV is the work-function of LiF. Once again, the semi-quantitative

agreement should be balanced by the fact that the model does not predict the observed similar behavior of w($E_\perp$) during an E-scan and a θ-scan. So far, the classical model Eq. 7.3 consider both surface effective stiffness Γ_{eff} and Beeby correction, $\theta_{\text{eff}} = \sqrt{\theta_{in}^2 + D/E}$, the classical inelastic width $w_{Cl} = (\frac{a\Gamma_{eff}^3 \theta_{eff}}{6})^{1/2} \cdot \sigma_z$.

7.4 Discussion

With the LiF samples used here, Fig. 7.9b and d) indicate that GIFAD is not able to provide an internal value of the temperature with an accuracy better than 20-50 $°C$. Combining consistently the width w and the DWF could improve the accuracy but the sensitivity to sample quality appears as a severe limitation. In contrast, if the main focus is to optimize the growth parameters to improve the surface quality in terms of coherence length, *i.e.* mean distance L_C between defects, GIFAD offers a unique handle with a very broad range of operation. First, a simple ϕ-scan [58] can identify the crystallographic axis even without diffraction, offering the first estimate of L_C via the peak to background ratio of the ϕ-scan [16]. When diffraction becomes visible, the presence of elastic diffraction, and its associated elastic peak width, readily gives insights on L_C. Then, optimizing the DWF could give real-time access to very large defect-free surfaces with the advantage that the diagnostic is performed simultaneously on an illuminated surface $S \approx \oslash^2/\theta$ on the order of 1 mm^2 for a diaphragm size of $\oslash$=100 μm. This diagnostic is complementary to the elastic diffracted intensity, which indicates the detailed topology of the terminal layer in real-time. We have shown here that the width w of the scattering profile can be understood qualitatively in terms of a classical model using an effective stiffness $\Gamma_{\text{eff}}(E_\perp)$ and a thermal amplitude $\sigma_z(T)$. This suggests that classical scattering simulation in grazing incidence, in general, [160] and in the context of GIFAD [181, 172] should produce a fair estimate of the inelastic profile. However, *In fine*, a quantum inelastic treatment as developed in TEAS [178] and recent attempts to encompass both elastic and inelastic aspects under grazing incidence [180] should help connect to the real world of surface phonons and their possible specific coupling to the multiple collision regime.

7.5 Conclusions

Using a definition based on the analysis of the polar scattering profile to isolate the elastic and inelastic components, the DWF can be evaluated for each diffraction image. At comparable energy and incidence angle, the DWF is found independent of the crystal axis probed. Due

to the extreme sensitivity to mechanical deformations associated with temperature variations, the T-scans were performed indirectly via interpolation of θ-scan and E-scan at different temperatures. At each temperature, the DWF specific to the multiple collision regime of GIFAD is shown to depend primarily on $E\theta^3$, differing from $E\theta^2$ in TEAS, where a single collision regime prevails. Within the present accuracy, a simple exponential decay with temperature is observed but, different LiF samples produce slightly different decay parameters and maximum coherence, suggesting an important contribution of the defect density and terrace size distribution. The effect of the attractive forces on the surface has been investigated in TEAS. It produces increased impact energy, known as the Beeby correction, and increased stiffness of the surface mean-planar potential-energy-surface due to a closer approach towards the surface [189]. They also have the same consequences regarding the elastic diffracted intensities in GIFAD or TEAS but very different consequences in the inelastic behavior of GIFAD and TEAS. In TEAS, the Beeby correction is known to limit the maximum possible DWF, [174] while in GIFAD, the Eq. 7.1 and Fig. 7.6 c) indicate only a weak influence on the maximum DWF. As to the effective stiffness Γ_{eff}[189], it does not directly affect the DWF in TEAS, whereas, it enters the DWF factor in GIFAD because each binary collision becomes more violent as evidenced by the sharp increase of the inelastic scattering width w at low values of $E\theta^2$ in Fig. 7.10 a), b). The effect of Γ_{eff} on the DWF, though larger than the Beeby correction, is also limited because it is, in part, balanced by the reduced number of collisions needed for specular reflection. Our results also suggest an important contribution of surface defect to decoherence in grazing conditions, but this aspect is yet unexplored.

Chapter 8

Experimental Results: Noble Gases Atoms (Ar Kr Xe) as Probes in GIFAD

8.1 Overview

The experimental results of He and Ne atoms in GIFAD have been discussed in the Chap. 6 and 7. The present chapter presents preliminary results obtained with heavier noble gases: Ar, Kr, and Xe, the properties of noble gas in Tab. 8.1.

All noble gases have a close shell electronic structure with a comparatively large ionization potential I_p. As a crude approximation, we could consider that I_p is larger than the work function of the LiF surface so that the range $\Gamma = 2\sqrt{2I_p}$ of the repulsive term is constant. In practice, we expect that the effective range is slightly longer as heavier atoms are more willing to deform. The other parameter of the repulsive forces is its magnitude. Within this simple description of the Pauli repulsion, the magnitude is expected to scale with the number of valence electrons. We a helium projectile, the surface has to provide room for two electrons, while with neon, six electrons of the $2p^6$ outer shell are trying to find space. The scaling parameter[132] $V(x,y,z) = \alpha\rho(x,y,z)$ should grow accordingly. Ar is $3p^6$ Kr $4p^6$ and Xe is $5p^6$. It should be possible to explain the scattering images in terms of Morse potential and to relate the associated parameters to the atomic properties of the projectile. So far, none of the diffraction results have been fully analyzed. We only present general images recorded at comparatively large $E_\perp$ to illus similarities and differences between these noble gases. Then preliminary results on the evolution of the rainbow angle and the polar profile are presented for Ar.

Property	He	Ne	Ar	Kr	Xe
Atomic number	2	10	18	36	54
Atomic Mass (amu)	4.0026	20.180	39.948	83.798	131.29
Atomic radius[a] (pm)	31	38	71	88	108
First ionization energy[b] (eV)	24.587	21.564	15.759	13.999	12.130
Polarizability	1.38	2.66	11.1	16.8	27.30

Table 8.1 Properties of noble gas atoms, [a] Ref.[201] and [b] Ref.[202]

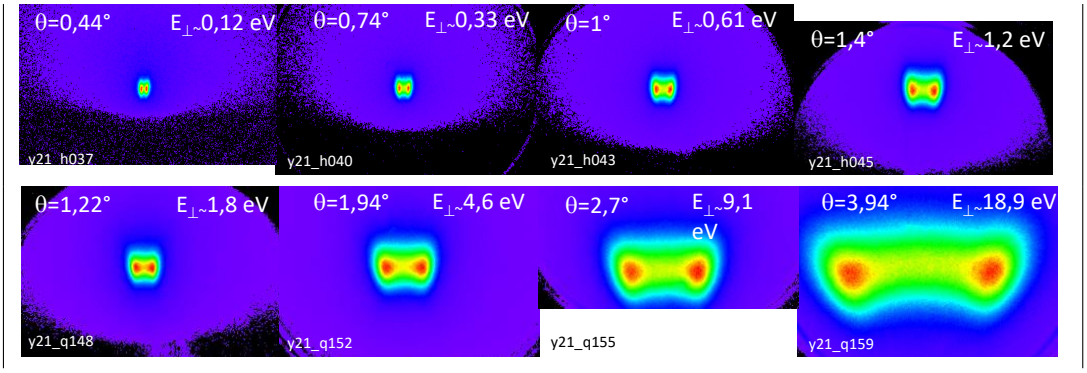

Table 8.2 Raw images of 4 keV Kr and Xe atoms scattered off LiF ⟨100⟩.

8.2 A brief comparison of noble gases

We do not present the diffraction result obtained at the lowest values of $E_\perp$. We focus first on the high energy values where the semi-classical behavior merges into a classical behavior with remaining quantum features. Using our flexible below allowing large angle scattering, we have been able to push the investigation towards significantly larger values of $E_\perp$.

Fig.8.2 shows the raw scattering profiles of Kr and Xe atoms impinging LiF along the ⟨100⟩ direction at 4 keV. At a glance, the scattering profiles do not exhibit clear modifications. They show two maxima corresponding to the rainbow angle and scale with the angle of incidence.

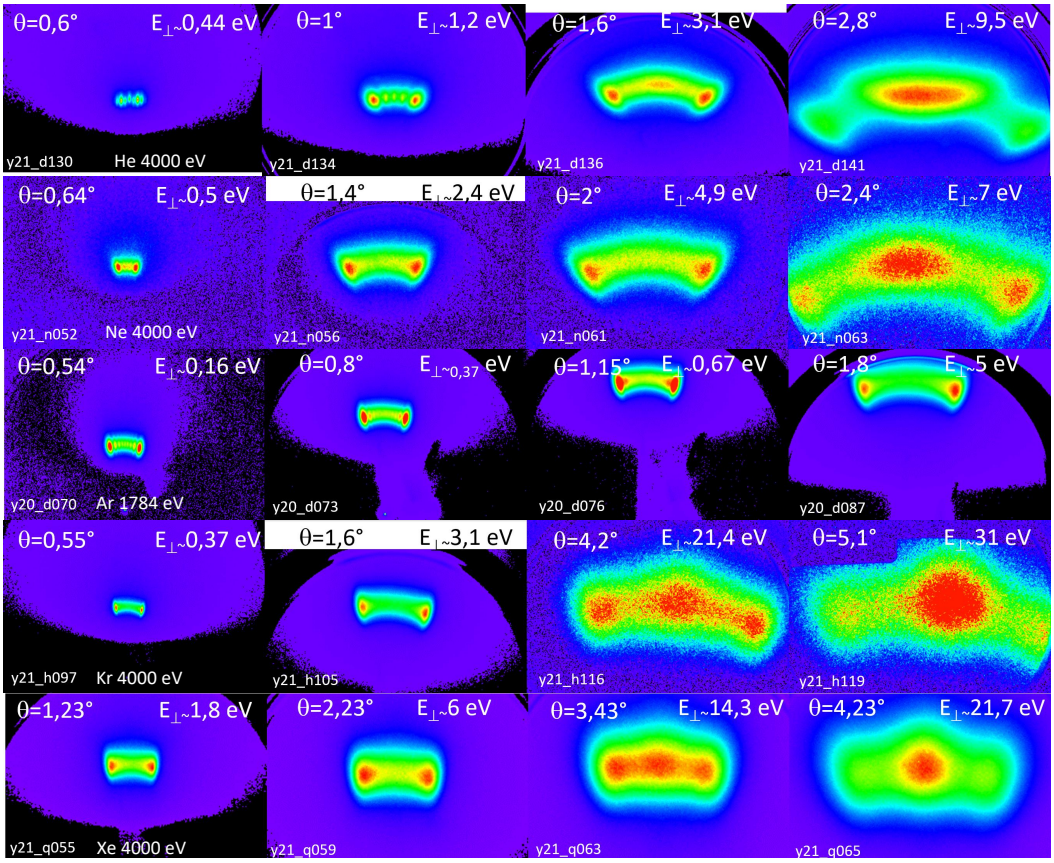

Figure 8.1 Raw images of He, Ne, Ar, Kr and Xe atoms scattered off LiF⟨100⟩.

8.3 Ar results

With Ar projectiles, we have started to analyze two properties already observed with Ne and He. These are the evolution of the polar scattering width w, and the evolution of the outer rainbow angle also called the principal rainbow angle. These two properties are described in Fig.8.2 obtained with 1784 eV Ar ($\hbar k_{||} \simeq 5850 \text{Å}^{-1}$) on LiF⟨100⟩, similar to Fig.6.2 which was recorded with He. The raw scattering image (as in Fig.8.1) is polar transformed as a function of $k_{f\perp}$ in Fig.6.2a). This 2D intensity Map is projected onto the vertical axis to produce a Polar scattering profile in Fig.6.2b). This latter is fitted by a log-normal profile providing the relative width parameter $w \simeq \sigma_\theta / \theta$. In contrast, only a narrow horizontal slice at the specular angle is used to plot Fig.8.2c). The supernumerary rainbow structure visible is fitted in Fig.8.2c) by a HCW model which with eq.4.2 and only two Fourier components $z_1, z_2 << z_1$ to describe the corrugation function $\tilde{z}_c(y) = z_1 \cos(G_y y) + z_2 \cos(2G_y y)$. All diffraction order with an intensity I_m given by eq.4.2 were given a constant line profile, and the sum of these intensities is the red line. The HCW model assumes perfect coherence of both projectile

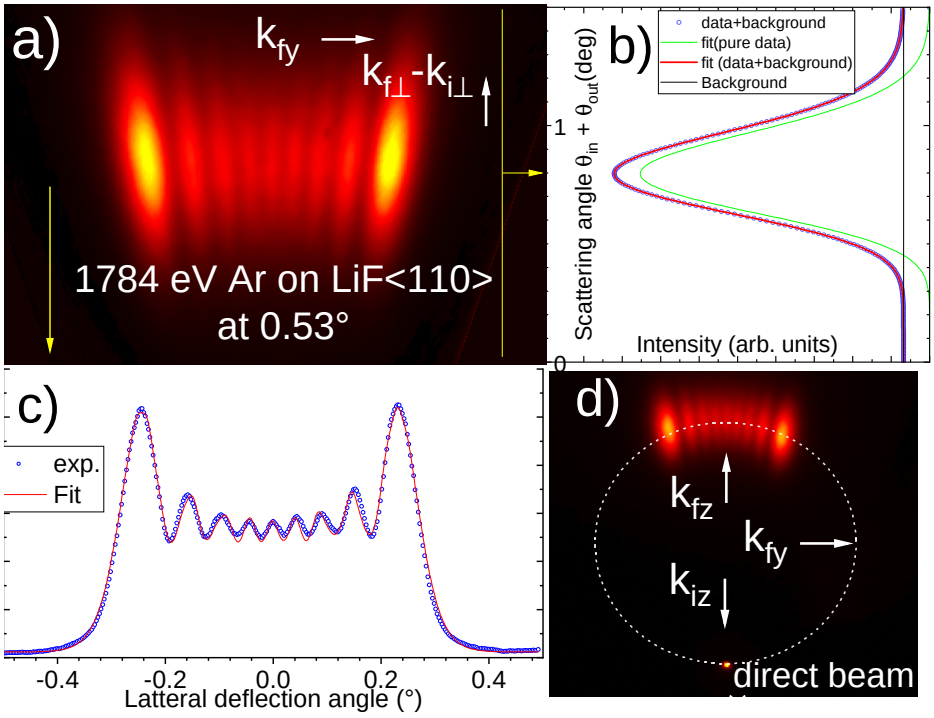

Figure 8.2 a) quasi polar transform of the raw diffraction image in panel d). The panel b) corresponds to a full projection onto the vertical axis producing the polar scattering profile. Since elastic components are negligible, it is fitted by a log-normal profile. The panel c) corresponds to the intensity in a narrow horizontal band centered on the specular reflection.

and surface so that the reasonable quality of the Fit indicates that this line broadening is enough to model the decoherence. It also suggests that a very detailed description of the corrugation function is possible because a two component Fourier transform is too naive to fit exactly the shape and positions of the supernumerary rainbows. With this strategy, it should be possible to build a PEL as in Fig.4.7 directly from the experiment and compare different noble gases. The Fig.8.3 reports the evolution of the log-normal width w as a function of the normal energy $E_\perp$ corresponding to a θ-scan with 1784 eV Ar. It displays the characteristic shape of Fig.6.10 obtained with Ne and He. The redline is a curves representing the effective stiffness (Eq. 6.4) Γ_{eff} corresponding to a Morse potential with $D = 50.2$meV and Γ=3.46 Å^{-1}, the same as for Ne.

Fig.8.4 displays a 2D map of the lateral scattering profile versus the angle of incidence θ expressed in values of $k_\perp$. Rather than the lateral scattering profile, as in Fig.8.2c), the horizontal scale is the 2D scattering angle $\varphi = \text{atan}\left(k_{fy}/k_{fz}\right)$ as sketched above the 2D map. Together with the complex pattern of supernumerary rainbows in the center of the image, we also observe the characteristic shape of the outer rainbow as in Fig.3.9 obtained during an

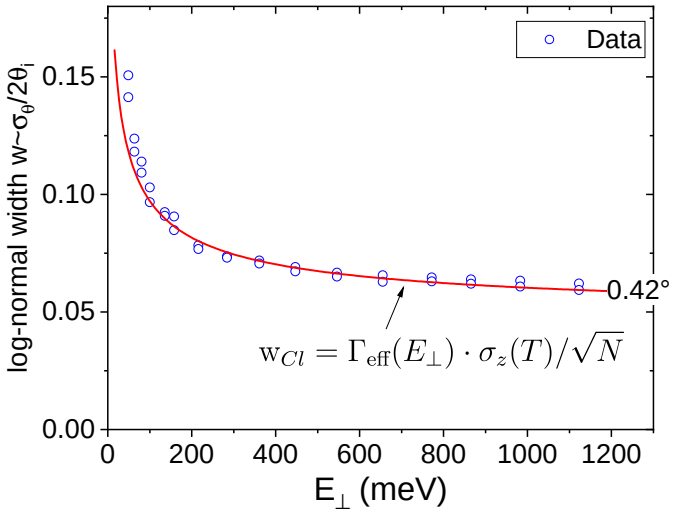

Figure 8.3 Ar scattering at LiF$\langle 110 \rangle$ surface at 300K, the inelastic scattering with w as a function of $E_\perp$. The red line is for eq.5.10 with D=50.2 meV, Γ=3.46 Å^{-1} and T_D=550 K, the inelastic scattering width increase at low $E_\perp$ mainly comes from the surface stiffness Γ_{eff} (eq.6.4).

E-scan with Ne atoms. To be more quantitative, the evolution of the rainbow angle φ with the energy $E_\perp$ is reported in Fig.8.5. The redline is also derived from the same attraction parameter $D = 50.2$ meV. In this curve, the stiffness is not present, and only the asymptotic value of the rainbow angle (indicated by vertical bars in Fig.8.4 is needed in the optical refraction formula. It corresponds to the Snell-Descarte law of refraction:

$$\begin{aligned} n_1 \sin\varphi_{rb} &= n_2 \sin\varphi_{obs} \quad \text{with } n_1, n_2 \text{ proportional to the local velocity} \\ \sqrt{E_\perp}\sin\varphi_{rb} &= \sqrt{E_\perp + D}\sin\varphi_{obs} \end{aligned} \tag{8.1}$$

where φ_{rb} is the emission angle close to the surface, where the energy is given by $E_\perp + D$ giving a refraction index (velocity ratio) $n_1 = \sqrt{E_\perp/(E_\perp + D)}$, and φ_{obs} is the observation angle far away from the surface (in vacuum) where the energy is $E_\perp$ giving a refraction index $n_2 = \sqrt{E_\perp/E_\perp}$=1. In the experiment, φ_{rb} is the asymptotic value of the rainbow angle measure for $E_\perp >> D$ as outlined by the vertical line in Fig. 8.4.

8.4 Conclusion

We have presented scattering patterns of He, Ne, Ar, Kr and Xe under comparable conditions. Only some Ar data have been analyzed suggesting that an estimate of the attractive well-depth

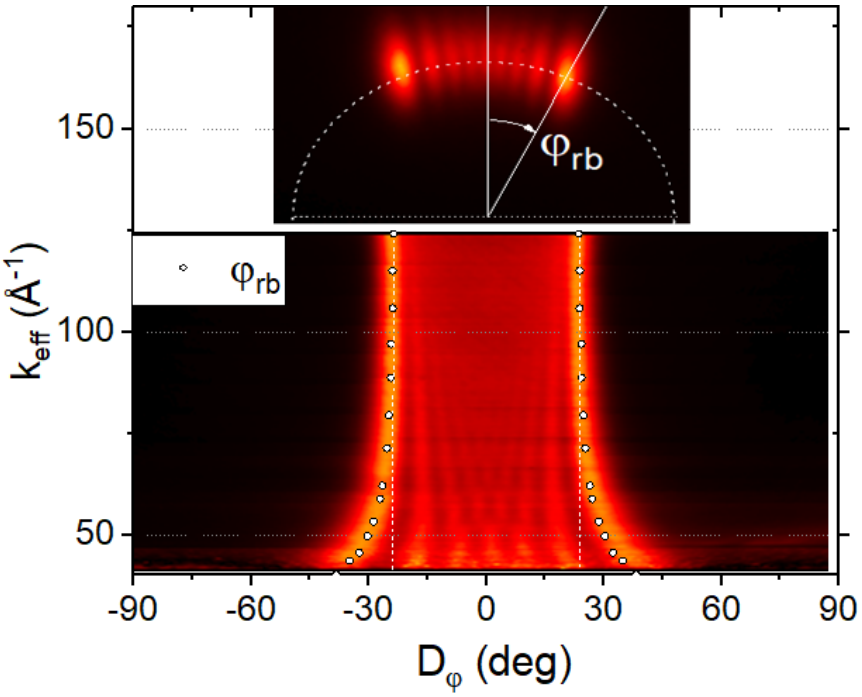

Figure 8.4 The diffraction chart is derived from a θ-scan of Ar at LiF$\langle 110 \rangle$ at 1784 eV. Each horizontal line reports the intensity on the Laue circle but in units of the angle $\varphi = atan(k_{fy}/k_{fz})$, *i.e.* of the scattering angle in the (y,z) 2D perpendicular plane. Vertical axis is in momentum $k_\perp = k_{iz} \propto \theta_{in}$. The vertical dashed line indicates the asymptotic value of the rainbow angle. The white circle is from an optical refraction model using the Snell-Descarte law in Eq. 8.1.

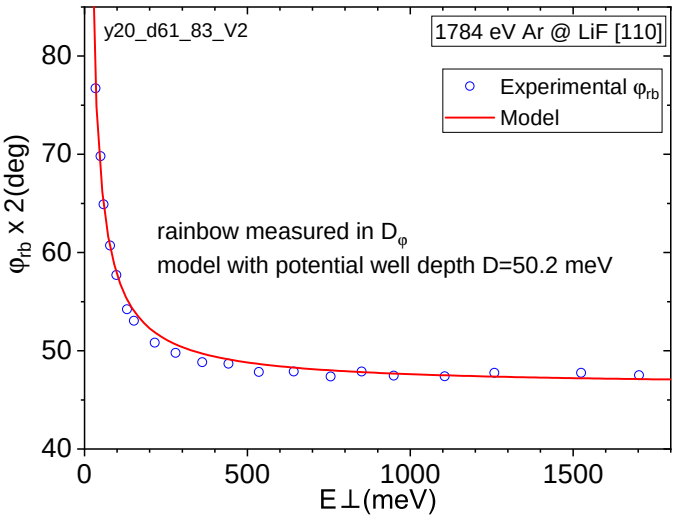

Figure 8.5 The full rainbow angle of Ar at LiF$\langle 110 \rangle$ as a funtion of $E_\perp$. The horizontal axis corresponds to the angle $\varphi = atan(k_{fy}/k_{fz})$ while the vertical one is in momentum $k_\perp = k_{iz}$.

could be derived from the analysis of the Polar inelastic profile and of the rainbow angle as was suggested in Chapter 6. Work is in progress to analyze all the gases.

Chapter 9

Measuring physisorption well-depth with fast atom scattering

This chapter corresponds to a presentation[203] at the APS March meeting by Peng Pan and Philippe Roncin under the same title on March 16th 2022 in Chicago, USA.

9.1 Overview

This chapter summarizes the different approaches used to measure the physisorption well-depth using fast atoms. We start with the most accurate one, namely bound state resonances. We then explore less and less demanding techniques where the observation of elastic diffraction is not required. Even the need for inelastic diffraction is relaxed with a possible application to heavier atoms interacting with surfaces with applied perspectives.

9.2 Bound states resonances BSR

In 1930, Estermann and Stern[4] published the first observation of the diffraction of an atom, *i.e.*, the first demonstration that a complex particle made of a nucleus surrounded by electrons can behave as a wave. Only three years later, Frisch and Stern[108] published the first observation of bound state resonance where the projectile atom temporarily oscillates in the attractive well above the surface. The technique has been turned extremely precise using the spin-echo technique with slow ^{3}He atoms[109] at thermal energies. The situation turned out to be much more complex with keV atoms, probably because the distance spent during each oscillation now corresponds to a comparatively large distance $L = v_{\|}\tau$ where τ

is the oscillation period. If any defect is present during this distance, the wave packet cannot interfere properly with the specular one, and the resonance is damped. In his thesis, Maxime Debiossac succeeded in measuring these resonances shown in Fig. 9.1. The agreement with wave packet calculation by Asier Zugarramurdi and Andrei Borisov could reproduce both the positions and the line width, assuming a coherence length of 0.2 μm [185].

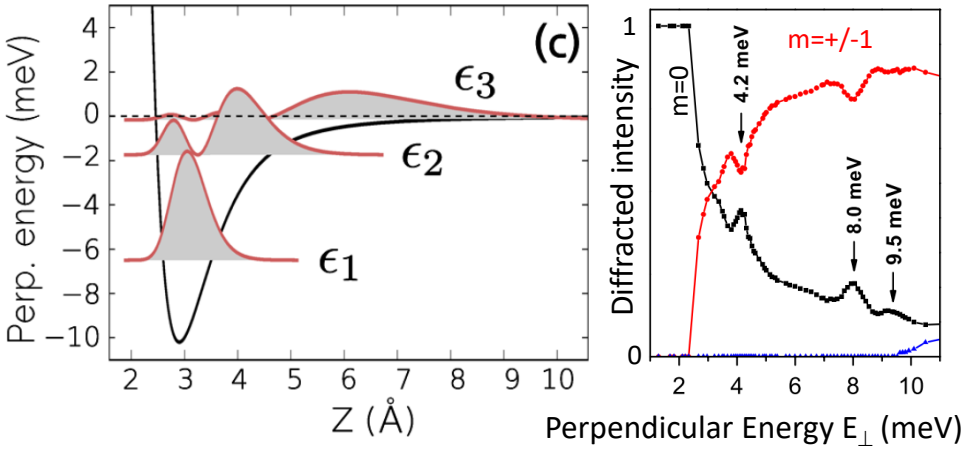

Figure 9.1 Left is a schematic view of the mean planar potential of the He LiF system. It hosts three vibrational bound states along z while the movement along the surface is subject to Bloch conditions. Taken from [185]

Measuring the position of bound states offers a unique opportunity to explore the shape of the attractive well. Because these bound states can be estimated from the mean planar potential $V_{plan}(z)$, for instance, using the Wentzel-Kramers-Brillouin (WKB) semi-classical approach. Intuitively, the shallow slope far away from the surface where the outer re-turning point is located, will strongly influence the position of these states because this is where the atoms stay longer. A critical limitation of this approach is that only a few bound states should be present and only a few diffraction orders. Otherwise, it is not possible to identify all possible combinations accurately. In practice, helium was used with several target surfaces, and only very few examples were published with neon.

9.3 Beeby correction

When fitting the diffracted intensities by a hard corrugated wall model (HCW) sec.4.4.3, the derived corrugation may increase at low values of $E_\perp$. For simple systems, this is quite often unphysical as the equipotential lines are expected to extend further away and get smoother (flatter). This is sometimes corrected simply by adding the well-depth D to the energy, a

correction known as the Beeby correction. See *e.g.* Fig. 4.16. Generally, the apparent corrugation is modified only in an energy region comparable to the well-depth D.

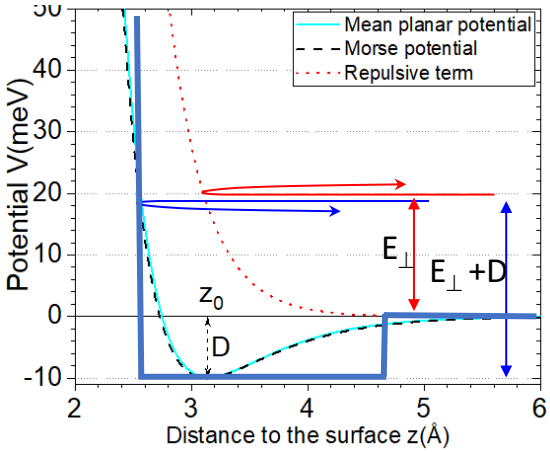

Figure 9.2 In the Hard Corrugated Wall model (see sec.4.4.3, the mean planar potential is replaced by an infinite Wall. The Beeby correction is equivalent to let it be preceded by a uniform well of depth D so that the energy at impact is now $E_\perp + D$.

9.4 Comparing elastic intensities with the exact quantum scattering

Recently, Debiossac *et al.*[67] published another determination using neon projectile on LiF, where the intensity of elastic diffraction orders could be measured and quantitatively compared with an empirically adjusted PEL shown in fig 9.3.

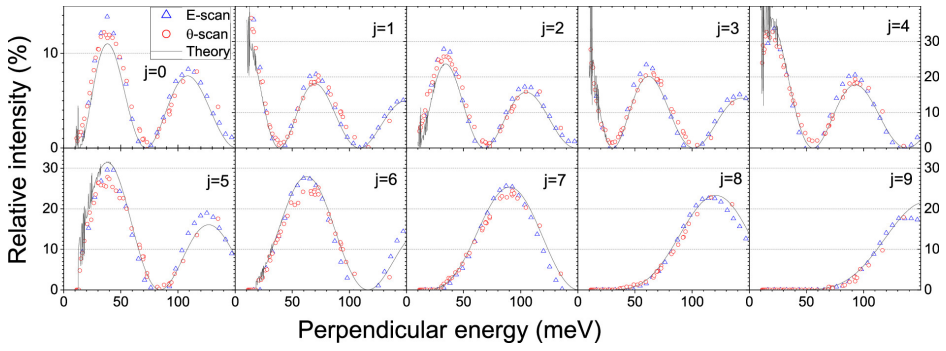

Figure 9.3 For Neon atoms scatter along the $\langle 110 \rangle$ direction. By adjusting the PEL model to the measured diffraction intensities, a well-depth of 10.3 meV of the mean planar potential could be derived. Taken from Ref. [67] and from Fig. 4.10 in chapter 4.

From the GIFAD, experimental point of view, the technique is much easier because a simple E-scan or θ-scan is enough to measure the evolution of all elastic diffraction orders in a day or two. This is true only if the elastic diffraction ratio (DWF) is large enough. However, Fig. 6.5 shows that neon is already much weaker than helium, and heavier noble gas did not exhibit significant elastically diffracted intensity.

9.5 Refraction effect

In the paper described above, the authors observed a rapid increase of the rainbow angle at low values of the perpendicular energy $E_\perp$ (see Fig. 3.9). The effect was modeled with a model saying that the effective energy inside the well is $E_\perp + D$ while it is only $E_\perp$ far from the surface. For low values of $E_\perp$, we have seen in the section 4.5 that a tiny well-depth is enough to "attract" the crossing point z_c closer to the surface, and give an almost constant shape of the HCW at values of $E_\perp$ close to the threshold (this is well-illustrated in Fig. 4.10). So that the rainbow angle at the moment of impact is also expected to be constant. Then, using a simple optical model and the Snell-Descartes law, the variation of the detected rainbow angle could be reproduced. The optical model is the same as depicted in Fig. 9.2 where the depth D indicates the refraction index.

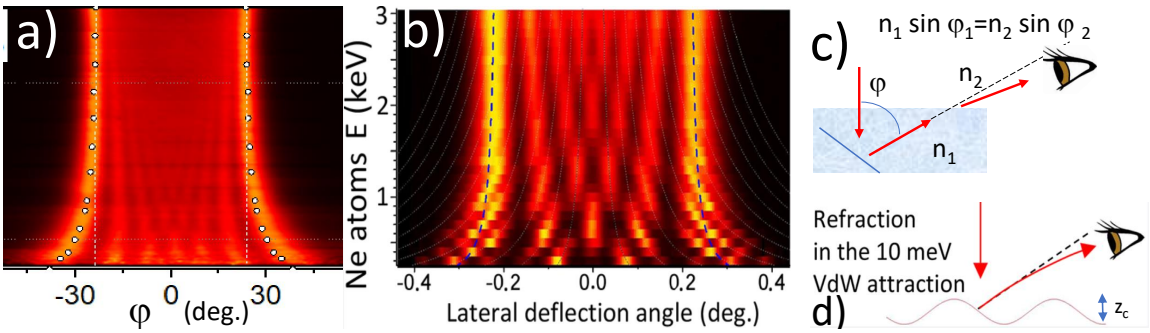

Figure 9.4 a) is the diffraction chart of an θ-scan recorded with 1784 eV Ar on LiF $\langle 110 \rangle$ (see Fig. 8.4).b) represent the diffraction chart of an E-scan recorded with Neon on LiF (see Fig. 3.9). c) recalls typical geometry of the Snell-Descarte law. d) applies this scheme to explain the evolution of the measured rainbow angle with $E_\perp$, Taken from [67].

The technique does not require the detection of elastic diffraction, it works better for large masses because several diffraction orders are populated so that the notion of rainbow angle is well defined. This is not the case for helium at low $E_\perp$ as in Fig. 3.12. In this respect, the method is well adapted to more complex systems. In the previous chapter, it was applied to Argon, Krypton, and Xenon projectiles and the data are under quantitative evaluation. The

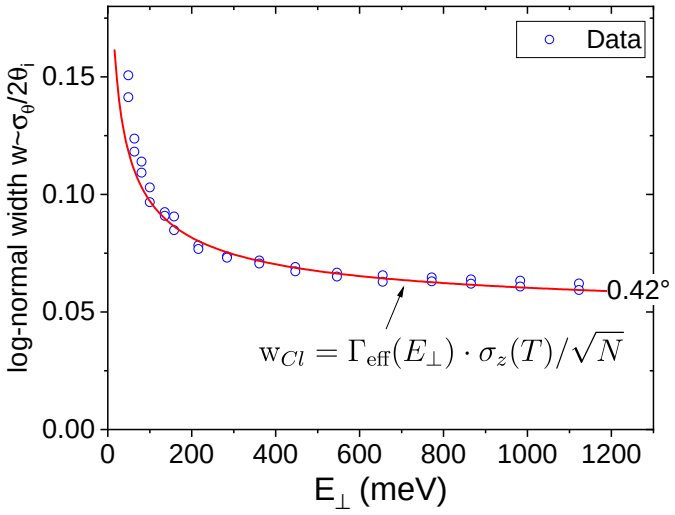

Figure 9.5 same as Fig. 8.3 the evolution of the log-normal inelastic scattering width w of Ar is compared with the prediction of the Classical limit w_{Cl} using the effective stiffness (eq.6.4).

rainbow angle is a quantum feature that persists in the classical regime. Indeed the interfering trajectories responsible for the rainbow can be selected as infinitely close to each other (on each side of the inflection point). So that quantum interference does not require a significant coherence length, neither from the beam, nor from the surface.

9.6 Inelastic scattering width, the effective stiffness

In the chapter,6 we have shown that the width of the inelastic profile is also quite sensitive to the well-depth D. Fig. 9.5 compares the measure evolution of the polar scattering profile with our analytic formula developed with a Morse potential. It does not require any quantum feature in the scattering profile since the analysis is based on the inelastic polar profile, which was not found to display any diffraction feature.

9.7 Conclusion

The five techniques reported here to estimate the well-depth are quite different. The first and third require detailed knowledge of the PEL. With bound state resonance, the shape of the PEL far from the surface (on the attractive branch) will be needed to estimate the position of the observed resonance. It is accurate but demanding in terms of resolution and does not appear well adapted to GIFAD with atoms heavier than helium. A quantum scattering code

can predict the diffracted intensities in the third technique. In case of agreement, the part of the PEL close to the turning point, and the well-depth can be derived with confidence, but the technique is poorly sensitive to the exact shape of the attractive branch. The second one uses the Beeby correction based on a HCW description. The advantage is that this description can be empirical. Only the shape variation at low values of $E_{\perp}$ is used to derive a well-depth.

The fourth technique requires only one quantum feature, the rainbow scattering angle should be applicable to almost all systems. However, It requires a significant corrugation of the surface because refraction effects are negligible if the rainbow angle is close to the normal direction in the perpendicular plane. Could it then be interesting to use misaligned conditions? The last one does not require any quantum feature but is not firmly established. One advantage is that it is insensitive to corrugation and works in a random direction. It seems that the last techniques should be able to analyze well-depth on the order of a few 100 meV opening perspectives in physical chemistry since these attractive wells are driving the adsorption of gases on surfaces. An important property for catalytic application where the initial binding of reactant is a crucial step.

Chapter 10

Outlook and Conclusion

Stay hungry. Stay foolish.

by Steve Jobs at Stanford

10.1 Outlook

From the material side, One important application of GIFAD is monitoring the growth in the MBE environment, especially working under high temperatures or high magnetic or electric field. For instance, the thermoelectric materials like Bi_2Te_3 and Bi_2Se_3 could be interesting systems to investigate under external field.

From the probe side, we have seen that grazing incidences could provide an estimate of the well-depth above the surface. These encouraging results may be extended to systems with applications in catalysis. Not to mention the difficult problem of fast molecule diffraction[204].

10.2 Conclusion

This thesis describes experimental investigations using the technique of grazing incidence fast atom diffraction at surfaces (GIFAD). We identify two components in the diffraction images. One is associated with elastic diffraction, and the other is inelastic diffraction, where energy has been exchanged with the surface. Elastic diffraction provides information about the surface structure in the form of the potential energy landscape (PEL), closely associated with the surface symmetry, atomic positions and electron density at the surface. Since its discovery at LCAM (Orsay-France) and at HMI (Berlin-Germany), most experimental and

theoretical efforts have assumed elastic diffraction. For elastic diffraction, the axial surface channeling approximation has been extensively investigated and is well-established, both theoretically and experimentally. It shows that when the atomic beam is aligned with a low index crystallographic axis, GIFAD is equivalent to a particle with effective energy $E_\perp$ evolving in the mean axial PEL. With $E_\perp = E_0 \sin^2 \theta_{in}$, typically three to four orders of magnitude smaller than E_0 for $\theta \approx 1^\circ$. The main focus of the thesis is inelastic diffraction related to the thermal movement of the surface atoms. Using fast helium and neon atoms with energies ranging from 0.2 keV to 5 keV scattered at the surface of a LiF(001) crystal along $\langle 110 \rangle$, $\langle 100 \rangle$, and random directions, we use specific polar transform to define the scattering profile referred to the beam position and showing no diffraction feature other that the elastic scattering peak. This profile is found to be independent of the probed crystallographic axis. The inelastic component is well-fitted by a log-normal profile where the relative width parameter w scales as σ_θ / θ.

Within a purely repulsive model, this width w is expected to be an invariant during an E-scan, where the incidence angle θ is fixed. However, we observed a rapid increase of this relative width w on $E_\perp$ energies below 100 meV. We propose a new model taking into account the attractive forces. It is based on the description of the mean planar potential as a Morse potential, and predicts that the width w is governed by the effective stiffness depending on the physisorption well depth D. The model significantly improves the description of the scattering profile with only one physical parameter D. We have used this model to investigate the Debye-Waller factor (DWF) defined as the ratio of elastic diffraction and its temperature dependence between 130K and 1017 K. Contrarily to the diffraction of atoms at thermal energies, we found that the well-Depth D has only a very limited influence of the saturation of the DWF at low values of $E_\perp$. Using helium and neon projectiles with different mass m_p, we could establish experimentally a generic $DWF = exp(-\alpha m_p E_0 \theta_{in}^3 T)$ dependence.

The main investigations were performed with helium and neon projectiles having an energy between 300 eV and 5 keV. We extend these studies using Ar, Kr, and Xe noble gases. Compared with the previous thesis on GIFAD, we demonstrate the significant role of the attractive forces. In conclusion, we compare five different methods to measure the physisorption well-depth with GIFAD. Three methods are related to elastic diffraction. (1) The identification of bound state resonances. (2) The "Beeby correction" to the hard corrugated wall (HCW) model. (3) Comparing measured diffraction intensities with exact quantum scattering codes. (4) One method can be applied to both the elastic and inelastic diffraction, an optical model explaining the refraction by analogy to the Snell-Descartes laws of refraction (here, the index represent the projectile velocity close to the surface). (5) And a new one, specific

to inelastic diffraction compares the observed log-normal inelastic width with our surface effective stiffness model.

10.3 Conclusion in French:

Cette thèse décrit une étude expérimentale utilisant la technique de diffraction d'atomes rapides sous incidence rasante sur les surfaces (GIFAD). Nous identifions deux composantes dans les clichés de diffraction. L'une est associé à la diffraction élastique, et l'autre à la diffraction inélastique, où de l'énergie a été échangée avec la surface. La diffraction élastique fournit des informations sur le paysage énergétique (PEL) au-dessus de la surface et est intimement lié à la symétrie de la surface, la position des atomes et la densité électronique en surface. Dans cette thèse nous montrons l'importance des forces attractives sur le paysage énergétique.

Pour la diffraction élastique, l'approximation de la canalisation axiale en surface à été largement validée. Elle indique que, le long d'un axe cristallographique principal, GIFAD est équivalent à une particule d'énergie effective $E_\perp = E_0 \sin^2\theta$ évoluant dans le PEL moyenné le long de cet axe. Pour un angle d'incidence $\theta \approx 1^\circ$, $E_\perp$ est typiquement trois à quatre ordres de grandeur plus petite que l'énergie totale E_0.

L'objectif principal de cette thèse est la diffraction inélastique liée au mouvement thermique des atomes de surface. Nous proposons une transformation polaire séparant d'une part le profil de diffraction élastique et inélastique associé à l'angle de diffusion et le profil de diffusion qui lui ne montre aucun signe de diffraction autre que la présence d'un éventuel pic élastique à l'angle de diffusion $2\theta_{in}$ correspondant à $\theta_{out} = \theta_{in}$. En utilisant des atomes d'hélium et de néon rapides avec des énergies allant de 0,2 keV à 5 keV diffusés à la surface d'un cristal LiF(001) le long de $\langle 110 \rangle$, $\langle 100 \rangle$, et dans des directions aléatoires, nous avons montés que ce profil de diffusion est indépendant de l'axe cristallographique sondé. le profil inélastique est bien ajusté par un profil log-normal où le paramètre de largeur relative $w \sim \sigma_\theta / \theta$, Dans un modèle purement répulsif, cette largeur w devrait être invariante lors d'un E-scan, où l'angle d'incidence θ est fixe. Cependant, nous observons une augmentation rapide de cette largeur relative w lorsque l'énergie $E_\perp$ est inférieure à 100 meV. Nous proposons un nouveau modèle prenant en compte les forces attractives à deux niveaux. La première est l'augmentation de l'énergie au moment de l'impact $E_\perp \to E_\perp + D$ ou D est la profondeur du puit attractif, un effet connu sous le nom de "correction de Beeby". La deuxième et plus importante pour GIFAD, est l'augmentation de la force entre le projectile et la surface au voisinage du point tournant. En partant d'une description du potentiel planaire

moyen de type "potentiel de Morse", nous parvenons à reproduire les observations et à établir l'importance relative des différentes contributions.

Le profil de diffusion inélastique log-normal permet aussi une évaluation directe du rapport de diffraction élastique et inélastique connu sous le nom de facteur Debye-Waller (DWF) qui s'avère être très différent de celui mesuré avec des atomes d'énergie thermiques. En utilisant des projectile d'hélium et de néon entre 300 eV et 5 keV et des températures de surface entre 130K et 1017 K nous avons montré que : -i) L'effet de la profondeur du puit de physisorption sur la saturation du DWF à basse énergie est fortement réduit et -ii) la forme générique est de type de type $DWF = exp(-\alpha m_p E_0 \theta_{in}^3 T)$. Nous étendons ces études en utilisant les gaz nobles Ar, Kr et Xe confirmant le rôle important des forces attractives. En conclusion, nous comparons cinq méthodes différentes pour mesurer la profondeur du puits de physisorption avec GIFAD. Trois méthodes sont liées à la diffraction élastique. (1) L'identification des résonances d'état lié. (2) La « correction Beeby » au modèle de tôle ondulée (HCW). (3) La comparaison des intensités de diffraction mesurées avec les valeurs calculées par dynamique quantique. (4) Dans l'esprit de la correction de Beeby, l'application de le loie de Snell-Descarte à l'angle de rainbow observé. (5) Et la mesure de la largeur polaire inélastique comparée à notre modèle de rigidité effective de la surface.

Bibliography

[1] Louis De Broglie. *Research on the theory of quanta*. PhD thesis, Paris University, 1924.

[2] C. Davisson and L. H. Germer. Diffraction of electrons by a crystal of nickel. *Phys. Rev.*, 30:705–740, Dec 1927.

[3] George P Thomson and Alexander Reid. Diffraction of cathode rays by a thin film. *Nature*, 119(3007):890–890, 1927.

[4] Immanuel Estermann and Otto Stern. Beugung von molekularstrahlen. *Zeitschrift für Physik*, 61(1):95–125, 1930.

[5] P. Rousseau, H. Khemliche, A. G. Borisov, and P. Roncin. Quantum scattering of fast atoms and molecules on surfaces. *Phys. Rev. Lett.*, 98:016104, Jan 2007.

[6] A. Schüller, S. Wethekam, and H. Winter. Diffraction of fast atomic projectiles during grazing scattering from a lif(001) surface. *Phys. Rev. Lett.*, 98:016103, Jan 2007.

[7] N. Bundaleski, H. Khemliche, P. Soulisse, and P. Roncin. Grazing incidence diffraction of keV helium atoms on a Ag(110) surface. *Phys. Rev. Lett.*, 101:177601, Oct 2008.

[8] M Busch, A Schüller, S Wethekam, and H Winter. Fast atom diffraction at metal surface. *Surface science*, 603(3):L23–L26, 2009.

[9] H. Khemliche, P. Rousseau, P. Roncin, V. H. Etgens, and F. Finocchi. Grazing incidence fast atom diffraction: An innovative approach to surface structure analysis. *Applied Physics Letters*, 95(15):151901, 2009.

[10] M. Debiossac, A. Zugarramurdi, H. Khemliche, P. Roncin, A. G. Borisov, A. Momeni, P. Atkinson, M. Eddrief, F. Finocchi, and V. H. Etgens. Combined experimental and theoretical study of fast atom diffraction on the $\beta_2(2\times4)$ reconstructed GaAs(001) surface. *Phys. Rev. B*, 90:155308, Oct 2014.

[11] P. Atkinson, M. Eddrief, V. H. Etgens, H. Khemliche, M. Debiossac, A. Momeni, M. Mulier, B. Lalmi, and P. Roncin. Dynamic grazing incidence fast atom diffraction during molecular beam epitaxial growth of GaAs. *Applied Physics Letters*, 105(2):021602, 2014.

[12] F.J. Giessibl. Advances in atomic force microscopy. *Rev. Mod. Phys.*, 75:949, 2003.

[13] J. Chen. *Introduction to Scanning Tunneling Microscopy Third Edition*. Monographs on the Physics and Chemistry of Materials. Oxford University Press, 2021.

[14] Daniel Farias and Karl-Heinz Rieder. Atomic beam diffraction from solid surfaces. *Reports on Progress in Physics*, 61(12):1575–1664, dec 1998.

[15] J.A. Barker and D.J. Auerbach. Gas—surface interactions and dynamics; thermal energy atomic and molecular beam studies. *Surface Science Reports*, 4(1):1–99, 1984.

[16] M. Debiossac, P. Pan, and P. Roncin. Grazing incidence fast atom diffraction, similarities and differences with thermal energy atom scattering (teas). *Phys. Chem. Chem. Phys.*, 11(12):4564–4569, 2021.

[17] J. Seifert, A. Schüller, H. Winter, R. Włodarczyk, J. Sauer, and M. Sierka. Diffraction of fast atoms during grazing scattering from the surface of an ultrathin silica film on mo(112). *Phys. Rev. B*, 82:035436, Jul 2010.

[18] H. Winter and A. Schüller. Fast atom diffraction during grazing scattering from surfaces. *Progress in Surface Science*, 86(9):169 – 221, 2011.

[19] M.A. Van Hove. From surface science to nanotechnology. *Catalysis Today*, 113(3):133–140, 2006. Catalysis, Nanomaterials and Environment.

[20] Xiao-Liang Qi and Shou-Cheng Zhang. Topological insulators and superconductors. *Rev. Mod. Phys.*, 83:1057–1110, Oct 2011.

[21] Klaus von Klitzing, Tapash Chakraborty, Philip Kim, Vidya Madhavan, Xi Dai, James McIver, Yoshinori Tokura, Lucile Savary, Daria Smirnova, Ana Maria Rey, et al. 40 years of the quantum hall effect. *Nature Reviews Physics*, 2(8):397–401, 2020.

[22] Manuel Angst, Thomas Brückel, Stephan Förster, Karen Friese, and Reiner Zorn. Scattering! soft, functional and quantum materials: Lecture notes of the 50th iff spring school 2019. Technical report, Streumethoden, 2019.

[23] G. Bracco and B. Holst. *Surface science techniques*. Springer Science, 2013.

[24] Gilles Renaud, Rémi Lazzari, and Frédéric Leroy. Probing surface and interface morphology with grazing incidence small angle x-ray scattering. *Surface Science Reports*, 64(8):255–380, 2009.

[25] A. Arnau, F. Aumayr, P.M. Echenique, M. Grether, W. Heiland, J. Limburg, R. Morgenstern, P. Roncin, S. Schippers, R. Schuch, N. Stolterfoht, P. Varga, T.J.M. Zouros, and H.P. Winter. Interaction of slow multicharged ions with solid surfaces. *Surface Science Reports*, 27(4):113–239, 1997.

[26] H. Winter. Collisions of atoms and ions with surfaces under grazing incidence. *Physics Reports*, 367(5):387–582, 2002.

[27] C. A. Volkert and A. M. Minor. Focused ion beam microscopy and micromachining. *MRS Bulletin*, 32(5):389–399, 2007.

[28] Satoshi Ninomiya, Kazuya Ichiki, Hideaki Yamada, Yoshihiko Nakata, Toshio Seki, Takaaki Aoki, and Jiro Matsuo. Precise and fast secondary ion mass spectrometry depth profiling of polymer materials with large ar cluster ion beams. *Rapid Communications in Mass Spectrometry*, 23(11):1601–1606, 2009.

[29] Bill Ward, John A Notte, and Nicholas P Economou. Helium ion microscope: A new tool for nanoscale microscopy and metrology. *Journal of Vacuum Science & Technology B*, 24(6):2871–2874, 2006.

[30] Horst Niehus, Werner Heiland, and Edmund Taglauer. Low-energy ion scattering at surfaces. *Surface Science Reports*, 17(4-5):213–303, 1993.

[31] Hidde H Brongersma, M Draxler, M De Ridder, and P Bauer. Surface composition analysis by low-energy ion scattering. *Surface Science Reports*, 62(3):63–109, 2007.

[32] Maxime Debiossac and Philippe Roncin. Atomic diffraction under oblique incidence: An analytical expression. *Phys. Rev. A*, 90:054701, 2014.

[33] H Winter. Image charge acceleration of multi-charged argon ions in grazing collisions with an aluminum surface. *EPL (Europhysics Letters)*, 18(3):207, 1992.

[34] J. Villette, A. G. Borisov, H. Khemliche, A. Momeni, and P. Roncin. Subsurface-channeling-like energy loss structure of the skipping motion on an ionic crystal. *Phys. Rev. Lett.*, 85:3137–3140, 2000.

[35] Steven M Girvin and Kun Yang. *Modern condensed matter physics*. Cambridge University Press, 2019.

[36] Peng Pan, Jaafar Najafi Rad, and Philippe Roncin. A setup for grazing incidence fast atom diffraction, 2022.

[37] M. Debiossac, P. Roncin, and A. G. Borisov. Refraction of fast ne atoms in the attractive well of a LiF(001) surface. *The Journal of Physical Chemistry Letters*, 11(12):4564–4569, 2020.

[38] C. W. Magee and R. E. Honig. Depth profiling by sims—depth resolution, dynamic range and sensitivity. *Surface and Interface Analysis*, 4(2):35–41, 1982.

[39] R. S. Gao, L. K. Johnson, D. A. Schafer, J. H. Newman, K. A. Smith, and R. F. Stebbings. Absolute differential cross sections for small-angle he^+-he elastic and charge-transfer scattering at kev energies. *Phys. Rev. A*, 38:2789–2793, Sep 1988.

[40] O.Jagutzki. Position sensitive anodes for mcp read-out using induced charge measurement. *NuIM-A*, 477:256 – 261, 2002.

[41] Sylvain Lupone, Pierre Soulisse, and Philippe Roncin. A large area high resolution imaging detector for fast atom diffraction. *NIM-B*, 427:95 – 99, 2018.

[42] *Xenon 0.95/17-0010 F0.95 aperture C-mount lens from Schneider-Kreuznach*.

[43] Maxime Debiossac and Philippe Roncin. Image processing for grazing incidence fast atom diffraction. *NIM-B*, 382:36 – 41, 2016.

[44] P Roncin, H Laurent, and M Barat. An electrostatic spectrometer for a simultaneous analysis of energy and scattering angle. *Journal of Physics E.*, 19(1):37, 1986.

[45] P Roncin, MN Gaboriaud, M Barat, and H Laurent. Transfer ionization in collisions involving multiply charged ions at low kev energy. *Europhysics Letters*, 3(1):53, 1987.

[46] M Barat, P Roncin, L Guillemot, MN Gaboriaud, and H Laurent. Single and double electron capture by c4+ ions colliding with helium target. *Journal of Physics B: Atomic, Molecular and Optical Physics*, 23(16):2811, 1990.

[47] X Flechard, S Duponchel, L Adoui, A Cassimi, P Roncin, and D Hennecart. State-selective double-electron capture in low-velocity collisions studied by recoil-ion momentum spectroscopy. *Journal of Physics B: Atomic, Molecular and Optical Physics*, 30(16):3697, 1997.

[48] P Roncin, AG Borisov, H Khemliche, A Momeni, A Mertens, and H Winter. Evidence for f- formation by simultaneous double-electron capture during scattering of f+ from a lif (001) surface. *Physical review letters*, 89(4):043201, 2002.

[49] A Cassimi, T Ikeda, L Maunoury, CL Zhou, S Guillous, A Mery, H Lebius, A Benyagoub, C Grygiel, et al. Dynamics of charge evolution in glass capillaries for 230-keV Xe^{23+} ions. *Physical Review A*, 86(6):062902, 2012.

[50] P Pan, ST Niu, HY Song, XM Chen, XY Qiu, and JX Shao. Transmission of kev o-ions through a single tapered glass capillary. *NIM-B*, 450:332–336, 2019.

[51] S. Lupone, S. Damoy, A. Husseen, N. Briand, M. Debiossac, S. Tall, and P. Roncin. Note: A large open ratio, time, and position sensitive detector for time of flight measurements in uhv. *Rev. Sci. Instrum.*, 86(12):126115, 2015.

[52] O. Grizzi, M. Shi, H. Bu, and J. W. Rabalais. Time-of-flight scattering and recoiling spectrometer (tof-sars) for surface analysis. *Review of Scientific Instruments*, 61(2):740–752, 1990.

[53] M. Sereno, S. Lupone, M. Debiossac, N. Kalashnyk, and P. Roncin. Active correction of the tilt angle of the surface plane with respect to the rotation axis during azimuthal scan. *NIM-B*, 382:123 – 126, 2016.

[54] Friedhelm Bechstedt. *Principles of surface physics*. Springer Science, 2012.

[55] J. J. Gilman, C. Knudsen, and W. P. Walsh. Cleavage cracks and dislocations in lif crystals. *Journal of Applied Physics*, 29(4):601–607, 1958.

[56] Alexander Hexemer and Peter Müller-Buschbaum. Advanced grazing-incidence techniques for modern soft-matter materials analysis. *IUCrJ*, 2(1):106–125, 2015.

[57] Felix E. Feiten, Jan Seifert, Joachim Paier, Helmut Kuhlenbeck, Helmut Winter, Joachim Sauer, and Hans-Joachim Freund. Surface structure of $v_2o_3(0001)$ revisited. *Phys. Rev. Lett.*, 114:216101, May 2015.

[58] Nataliya Kalashnyk, Hocine Khemliche, and Philippe Roncin. Atom beam triangulation of organic layers at 100 meV normal energy: self-assembled perylene on Ag(110) at room temperature. *Applied Surface Science*, 364:235 – 240, 2016.

[59] R. Pfandzelter, T. Bernhard, and H. Winter. Ion beam triangulation of ultrathin Mn and CoMn films grown on Cu(001). *Phys. Rev. Lett.*, 90:036102, Jan 2003.

[60] V A. Morosov, A. Kalinin, Z. Szilagyi, M. Barat, and P. Roncin. 2π spectrometer: A new apparatus for the investigation of ion surface interaction. *Rev. Sci. Instrum.*, 67(6):2163–2170, 1996.

[61] VA Morozov, FW Meyer, and P Roncin. Multi-coincidence studies as a technique for the investigation of ion-surface interaction. *Physica Scripta*, T80A:69–72, 1999.

[62] V. A. Morozov and F. W. Meyer. Path-dependent neutralization of multiply charged ar ions incident on au(110). *Phys. Rev. Lett.*, 86:736–739, Jan 2001.

[63] J Villette, J.P Atanas, H Khemliche, M Barat, V Morosov, and P Roncin. Grazing collision of kev protons on lif correlation between energy loss and electron emission. *NIM-B*, 157(1):92 – 97, 1999.

[64] P. Roncin, J. Villette, J. P. Atanas, and H. Khemliche. Energy loss of low energy protons on lif(100): Surface excitation and H^- mediated electron emission. *Phys. Rev. Lett.*, 83:864–867, jul 1999.

[65] H. Khemliche, J. Villette, A. G. Borisov, A. Momeni, and P. Roncin. Electron bihole complex formation in neutralization of Ne^+ on LiF. *Phys. Rev. Lett.*, 86:5699, 2001.

[66] Maxime Debiossac. *Diffraction d'atomes rapides sur surfaces : des résonances de piégeage à la dynamique de croissance par épitaxie*. PhD thesis, Université Paris sud-XI, 2014. Thèse de doctorat dirigée par P.Roncin.

[67] M. Debiossac, P. Roncin, and A. G. Borisov. Refraction of fast ne atoms in the attractive well of a lif(001) surface. *The Journal of Physical Chemistry Letters*, 11(12):4564–4569, 2020.

[68] T Narayanan, O Diat, and P Bösecke. SAXS and USAXS on the high brilliance beamline at the ESRF. *NIM-A*, 467:1005–1009, 2001.

[69] Maxime Debiossac and Philippe Roncin. Image processing for grazing incidence fast atom diffraction. *NIM-B*, 382:36 – 41, 2016.

[70] K Burke and W Kohn. Finite debye-waller factor for "classical"atom-surface scattering. *Physical Review B*, 43(4):2477, 1991.

[71] P Roncin and M Debiossac. Elastic and inelastic diffraction of fast atoms, Debye-Waller factor, and Mössbauer-Lamb-Dicke regime. *Phys. Rev. B*, 96:035415, 2017.

[72] Peng Pan, Maxime Debiossac, and Philippe Roncin. Polar inelastic profiles in fast-atom diffraction at surfaces. *Phys. Rev. B*, 104:165415, Oct 2021.

[73] Patrick Rousseau, Hocine Khemliche, Nenad Bundaleski, Pierre Soulisse, Anouchah Momeni, and Philippe Roncin. Surface analysis with grazing incidence fast atom diffraction (GIFAD). *Journal of Physics: Conference Series*, 133:012013, oct 2008.

[74] J. R. Manson, H. Khemliche, and P. Roncin. Theory of grazing incidence diffraction of fast atoms and molecules from surfaces. *Phys. Rev. B*, 78:155408, Oct 2008.

[75] J. Seifert, J. Lienemann, A. Schüller, and H. Winter. Studies on coherence and decoherence in fast atom diffraction. *NIM-B*, 350:99 – 105, 2015.

[76] Richard P Feynman, Robert B Leighton, and Matthew Sands. *The Feynman lectures on physics, Vol. I: The new millennium edition: mainly mechanics, radiation, and heat*, volume 1. Basic books, 2011.

[77] C. Auth, A. Mertens, H. Winter, A. G. Borisov, and F. J. García de Abajo. Resonant coherent excitation of fast hydrogen atoms in front of a lif(001) surface. *Phys. Rev. Lett.*, 79:4477–4480, Dec 1997.

[78] G Brusdeylins, R Bruce Doak, and J Peter Toennies. High-resolution helium time-of-flight studies of rayleigh surface-phonon dispersion curves of LiF, NaF, and KCl. *Physical Review B*, 27(6):3662, 1983.

[79] JT Lewis, Ao Lehoczky, and CV Briscoe. Elastic constants of the alkali halides at 4.2 k. *Physical Review*, 161(3):877, 1967.

[80] J. Berkowitz, H. A. Tasman, and W. A. Chupka. Double-oven experiments with lithium halide vapors. *The Journal of Chemical Physics*, 36(8):2170–2179, 1962.

[81] Charles Kittel, Paul McEuen, and Paul McEuen. *Introduction to solid state physics*, volume 8. Wiley New York, 1996.

[82] Steven H Simon. *The Oxford solid state basics*. OUP Oxford, 2013.

[83] Dingchang Lin, Yayuan Liu, Wei Chen, Guangmin Zhou, Kai Liu, Bruce Dunn, and Yi Cui. Conformal lithium fluoride protection layer on three-dimensional lithium by nonhazardous gaseous reagent freon. *Nano letters*, 17(6):3731–3737, 2017.

[84] L. S. Hung, C. W. Tang, and M. G. Mason. Enhanced electron injection in organic electroluminescence devices using an Al/LiF electrode. *Applied Physics Letters*, 70(2):152–154, 1997.

[85] James Bullock, Peiting Zheng, Quentin Jeangros, Mahmut Tosun, Mark Hettick, Carolin M Sutter-Fella, Yimao Wan, Thomas Allen, Di Yan, Daniel Macdonald, et al. Lithium fluoride based electron contacts for high efficiency n-type crystalline silicon solar cells. *Advanced Energy Materials*, 6(14):1600241, 2016.

[86] V. Romankov and J. Dreiser. Morphology of ultrathin lithium fluoride deposited on Ag(100): Dendrites versus islands. *Phys. Rev. B*, 104:195401, Nov 2021.

[87] D.M. Roessler and W.C. Walker. Electronic spectrum of crystalline lithium fluoride. *Journal of Physics and Chemistry of Solids*, 28(8):1507–1515, 1967.

[88] Anubhav Jain, Shyue Ping Ong, Geoffroy Hautier, Wei Chen, William Davidson Richards, Stephen Dacek, Shreyas Cholia, Dan Gunter, David Skinner, Gerbrand Ceder, and Kristin a. Persson. The Materials Project: A materials genome approach to accelerating materials innovation. *APL Materials*, 1(1):011002, 2013.

[89] K. Momma and F. Izumi. Vesta 3 for three-dimensional visualization of crystal data. *Journal of applied crystallography*, 44(6):1272, 2011.

[90] Asier Zugarramurdi and Andrei G Borisov. When fast atom diffraction turns 3D. *NIM-B*, 317:83–89, 2013.

[91] A.S. Muzas, F. Gatti, F. Martín, and C. Díaz. Diffraction of h from lif(001): From slow normal incidence to fast grazing incidence. *NIM-B*, 382:49 – 53, 2016.

[92] D. Farías, C. Díaz, P. Nieto, A. Salin, and F. Martín. Pronounced out-of-plane diffraction of H_2 molecules from a Pd(111) surface. *Chem. Phys. Lett.*, 390:250, 2004.

[93] C. Henkel, J.-Y. Courtois, and A. Aspect. Atomic diffraction by a thin phase grating. *J. Phys. II France*, 4(11):1955–1974, 1994.

[94] P. L. Kapitza and P. A. M. Dirac. The reflection of electrons from standing light waves. *Mathematical Proceedings of the Cambridge Philosophical Society*, 29(2):297, 1933.

[95] A Zugarramurdi, M Debiossac, P Lunca-Popa, LS Alarcón, A Momeni, H Khemliche, P Roncin, and AG Borisov. Surface-grating deflection of fast atom beams. *Physical Review A*, 88(1):012904, 2013.

[96] Salvador Miret-Artés and Eli Pollak. Classical theory of atom–surface scattering: The rainbow effect. *Surface Science Reports*, 67(7):161 – 200, 2012.

[97] Salvador Miret-Artés, Shauli Daon, and Eli Pollak. Semiclassical perturbation theory for diffraction in heavy atom surface scattering. *The Journal of Chemical Physics*, 136(20):204707, 2012.

[98] Eli Pollak and Salvador Miret-Artés. Second order classical perturbation theory for atom surface scattering: Analysis of asymmetry in the angular distribution. *The Journal of Chemical Physics*, 140(2):024709, 2014.

[99] Eli Pollak and Salvador Miret-Artés. Second-order semiclassical perturbation theory for diffractive scattering from a surface. *The Journal of Physical Chemistry C*, 119(26):14532–14541, 2015.

[100] M. Busch, J. Seifert, E. Meyer, and H. Winter. Evidence for longitudinal coherence in fast atom diffraction. *Phys. Rev. B*, 86:241402, 2012.

[101] D M Danailov and D S Karpuzov. Total reflection of energetic ions from crystal surfaces at glancing incidence. *Canadian Journal of Physics*, 75(4):197–209, 1997.

[102] Daniel M. Danailov. Angular spectra of rainbow scattering at glancing kev he+ bombardment of nial(100) surface with transverse energies in the range 1 to 10ev. *NIM-B*, 264(1):29 – 35, 2007.

[103] Donald S. Gemmell. Channeling and related effects in the motion of charged particles through crystals. *Rev. Mod. Phys.*, 46:129–227, Jan 1974.

[104] EA Andreev. Quantum and classical characteristics of glancing scattering of fast atoms on the surface of a crystal. *Russian Journal of Physical Chemistry A*, 76, 2002.

[105] P. Roncin, M. Debiossac, H. Oueslati, and F. Raouafi. Energy loss and inelastic diffraction of fast atoms at grazing incidence. *NIM-B*, 427:100–107, 2018.

[106] H. Tal-Ezer and R. Kosloff. An accurate and efficient scheme for propagating the time dependent schrödinger equation. *The Journal of chemical physics*, 81(9):3967, 1984.

[107] F. Aigner, N. Simonović, B. Solleder, L. Wirtz, and J. Burgdörfer. Suppression of decoherence in fast-atom diffraction at surfaces. *Phys. Rev. Lett.*, 101:253201, 2008.

[108] R Frisch and Otto Stern. Über die magnetische ablenkung von wasserstoffmolekülen und das magnetische moment des protons. i. *Zeitschrift für Physik*, 85(1):4–16, 1933.

[109] A.P. Jardine, S. Dworski, P. Fouquet, G. Alexandrowicz, D. J. Riley, Gabriel Y. H. Lee, J. Ellis, and W. Allison. Ultrahigh-resolution spin-echo measurement of surface potential energy landscapes. *Science*, 304(5678):1790, 2004.

[110] Bret Jackson and Horia Metiu. An examination of the use of wave packets for the calculation of atom diffraction by surfaces. *The Journal of chemical physics*, 82(12):5707–5716, 1985.

[111] M Hernández, Octavio Roncero, Salvador Miret-Artés, Pablo Villarreal, and Gerardo Delgado-Barrio. Study of the diffraction mediated selective adsorption through the close-coupling and diabatic distorted wave formalisms. application to the 4he–cu (110) system. *The Journal of Chemical Physics*, 90(7):3823–3830, 1989.

[112] M Minniti, C Díaz, JL Fernández Cuñado, A Politano, D Maccariello, F Martín, D Farías, and R Miranda. Helium, neon and argon diffraction from Ru (0001). *Journal of Physics: Condensed Matter*, 24(35):354002, 2012.

[113] AS Sanz, F. Borondo, and . Miret-Artes. Causal trajectories description of atom diffraction by surfaces. *Physical Review B*, 61(11):7743, 2000.

[114] AS Sanz, F. Borondo, and S. Miret-Artes. Particle diffraction studied using quantum trajectories. *Journal of Physics: Condensed Matter*, 14(24):6109, 2002.

[115] R Guantes, AS Sanz, Juan Margalef-Roig, and Salvador Miret-Artés. Atom–surface diffraction: a trajectory description. *Surface science reports*, 53(6-8):199–330, 2004.

[116] Davide Gaiotto, Gregory W Moore, and Andrew Neitzke. Wall-crossing, hitchin systems, and the wkb approximation. *Advances in Mathematics*, 234:239–403, 2013.

[117] A. Schüller, D. Blauth, J. Seifert, M. Busch, H. Winter, K. Gärtner, R. Włodarczyk, J. Sauer, and M. Sierka. Fast atom diffraction during grazing scattering from a mgo(001) surface. *Surface Science*, 606(3):161–173, 2012.

[118] M. S. Gravielle and J. E. Miraglia. Influence of the polarization in grazing scattering of fast helium atoms from lif(001) surfaces. *Phys. Rev. A*, 78:022901, Aug 2008.

[119] M.S. Gravielle and J.E. Miraglia. Quantum interference in grazing scattering of swift he atoms from lif(001) surfaces: Surface eikonal approximation. *NIM-B*, 267(4):610–614, 2009.

[120] M.S. Gravielle, A. Schüller, H. Winter, and J.E. Miraglia. Fast atom diffraction for grazing scattering of Ne atoms from a LiF(001) surface. *NIM-B*, 269(11):1208, 2011.

[121] G. A. Bocan, J. D. Fuhr, and M. S. Gravielle. van der Waals effects on grazing-incidence fast-atom diffraction for H on LiF(001). *Phys. Rev. A*, 94:022711, 2016.

[122] M.S. Gravielle and J. E. Miraglia. Semiquantum approach for fast atom diffraction: Solving the rainbow divergence. *Physical Review A*, 90(5):052718, 2014.

[123] U Garibaldi, AC Levi, R Spadacini, and GE Tommei. Quantum theory of atom-surface scattering: diffraction and rainbow. *Surface Science*, 48(2):649–675, 1975.

[124] G. Armand and J. R. Manson. Scattering of neutral atoms by an exponential corrugated potential. *Phys. Rev. Lett.*, 43:1839–1842, Dec 1979.

[125] Peng Pan and Philippe Roncin. Surface electron density probe by fast atomsAn online AFM in reciprocal space. ISMO workshop on charge transfer, October 2021. Poster.

[126] M. Debiossac, P. Atkinson, A. Zugarramurdi, M. Eddrief, F. Finocchi, V.H. Etgens, A. Momeni, H. Khemliche, A.G. Borisov, and P. Roncin. Fast atom diffraction inside a molecular beam epitaxy chamber, a rich combination. *Applied Surface Science*, 391:53 – 58, 2017.

[127] A. Schüller, S. Wethekam, D. Blauth, H. Winter, F. Aigner, N. Simonović, B. Solleder, J. Burgdörfer, and L. Wirtz. Rumpling of lif(001) surface from fast atom diffraction. *Phys. Rev. A*, 82:062902, 2010.

[128] J. E. Miraglia and M. S. Gravielle. Reexamination of the interaction of atoms with a LiF(001) surface. *Phys. Rev. A*, 95:022710, Feb 2017.

[129] James F. Ziegler and Jochen P. Biersack. *The stopping and range of ions in matter*, pages 93–129. Springer US, Boston, MA, 1985.

[130] William H. Press, Saul A. Teukolsky, William T. Vetterling, and Brian P. Flannery. *Numerical Recipes in C (2nd Ed.): The Art of Scientific Computing*. Cambridge University Press, USA, 1992.

[131] A Schüller, S Wethekam, A Mertens, K Maass, H Winter, and K Gärtner. Interatomic potentials from rainbow scattering of kev noble gas atoms under axial surface channeling. *NIM-B*, 230(1-4):172–177, 2005.

[132] N. Esbjerg and J. K. Nørskov. Dependence of the he-scattering potential at surfaces on the surface-electron-density profile. *Phys. Rev. Lett.*, 45:807–810, Sep 1980.

[133] G. Benedek, J.R. Manson, S. Miret-Artés, A. Ruckhofer, W.E. Ernst, A. Tamtögl, and J.P. Toennies. Measuring the electron–phonon interaction in two-dimensional superconductors with he-atom scattering. *Condensed Matter*, 5(4), 2020.

[134] F. Montalenti, M.I. Trioni, G.P. Brivio, and S. Crampin. Ab initio results for the adiabatic atom-surface interaction for helium and neon on a simple metal. *Surface Science*, 364(2):L595–L599, 1996.

[135] G. P. Brivio and M. I. Trioni. The adiabatic molecule–metal surface interaction: Theoretical approaches. *Rev. Mod. Phys.*, 71:231–265, Jan 1999.

[136] A. Schüller, K. Gärtner, and H. Winter. Interaction potential for fast Ne atoms in front of LiF(001) surface. *EPL (Europhysics Letters)*, 81(3):37007, jan 2008.

[137] H.C. Hamaker. The london—van der Waals attraction between spherical particles. *Physica*, 4(10):1058–1072, 1937.

[138] Taro Kihara. *Convex Molecules in Gaseous and Crystalline States*, pages 147–188. John Wiley & Sons, Ltd, 1963.

[139] Hendrik Heinz, R. A. Vaia, B. L. Farmer, and R. R. Naik. Accurate simulation of surfaces and interfaces of face-centered cubic metals using 12-6 and 9-6 lennard-jones potentials. *The Journal of Physical Chemistry C*, 112(44):17281–17290, 2008.

[140] A. Zugarramurdi, M. Debiossac, P. Lunca-Popa, A. J. Mayne, A. Momeni, A. G. Borisov, Z. Mu, P. Roncin, and H. Khemliche. Determination of the geometric corrugation of graphene on sic(0001) by grazing incidence fast atom diffraction. *Applied Physics Letters*, 106(10):101902, 2015.

[141] M. Debiossac, A. Zugarramurdi, Z. Mu, P. Lunca-Popa, A. J Mayne, and P. Roncin. Helium diffraction on SiC grown graphene: Qualitative and quantitative descriptions with the hard-corrugated-wall model. *Physical Review B*, 94(20):205403, 2016.

[142] Giorgio Benedek and Jan Peter Toennies. *Atomic Scale Dynamics at Surfaces*, volume 63. Springer, 2018.

[143] R. A. Buckingham and John Edward Lennard-Jones. The classical equation of state of gaseous helium, neon and argon. *Proceedings of the Royal Society of London. Series A. Mathematical and Physical Sciences*, 168(933):264–283, 1938.

[144] Xuetao Zhu. Temperature-dependent anomalies in the structural and dynamical properties of the (001) surface of lithium copper oxide. *Ph. D. Thesis*, 2011.

[145] K. T. Tang and J. Peter Toennies. An improved simple model for the van der Waals potential based on universal damping functions for the dispersion coefficients. *The Journal of Chemical Physics*, 80(8):3726–3741, 1984.

[146] Xiaowei Sheng, J. Peter Toennies, and K. T. Tang. Conformal analytical potential for all the rare gas dimers over the full range of internuclear distances. *Phys. Rev. Lett.*, 125:253402, Dec 2020.

[147] M. Schmidt, A. Masson, H.P. Cheng, and C. Bréchignac. Physisorption and chemisorption on silver clusters. *ChemPhysChem*, 16(4):855–865, 2015.

[148] D. Spanjaard M.-C. Desjonqueres. *Concepts in Surface Physics*, chapter 1-6, pages 1–528. Springer-Verlag Berlin Heidelberg, 1994.

[149] G. A. Bocan, H. Breiss, S. Szilasi, A. Momeni, E. M. Staicu Casagrande, E. A. Sánchez, M. S. Gravielle, and H. Khemliche. Dynamical effects as a window into van der Waals interactions in grazing-incidence fast he-atom diffraction from kcl(001). *Phys. Rev. B*, 104:235401, Dec 2021.

[150] Gianfranco Vidali, G Ihm, Hye-Young Kim, and Milton W Cole. Potentials of physical adsorption. *Surface Science Reports*, 12(4):135–181, 1991.

[151] Stephan Ernst Wethekam. *Ladungsaustausch schneller Edelgasatome und Fullerene mit Festkörperoberflächen*. PhD thesis, Humboldt-Universität zu Berlin, 2009. Under supervision of H.Winter.

[152] Andreas Schüller. *Quanten-Regenbogenstreuung bei axialer Oberflächen-Gitterführung schneller Atome*. PhD thesis, Humboldt-Universität zu Berlin, 2010. Under supervision of H.Winter.

[153] Eric Meyer. *Strukturuntersuchungen an Oxidkristalloberflächen mittels der streifenden Streuung schneller Atome*. PhD thesis, Humboldt-Universität zu Berlin, 2016. Under supervision of H.Winter.

[154] Jan Seifert. *Bestimmung der atomaren Struktur ultradünner Schichten auf Festkörperoberflächen mittels streifender Atomstreuung*. PhD thesis, Humboldt-Universität zu Berlin, 2012. Under supervision of H.Winter.

[155] Jérôme Villette. *Etude expérimentale de l'intéraction rasante d'atomes et d'ions sur des surfaces isolantes*. PhD thesis, Université Paris sud-XI, 2000. Thèse de doctorat dirigée par P.Roncin.

[156] Anouchah Momeni. *Etude expérimentale des processus multi-électroniques lors de collisions d'ions en incidence rasante sur une surface de LiF(001)*. PhD thesis, Université Paris sud-XI, 2003. Thèse de doctorat dirigée par P.Roncin.

[157] Patrick Rousseau. *Collisions rasantes d'ions ou d'atomes sur les surfaces : de l'échange de charge à la diffraction atomique*. PhD thesis, Université Paris Sud 11, 2007. Thèse de doctorat dirigée par Roncin, Philippe.

[158] Pierre Soulisse. *Développement d'un dispositif expérimental pour la diffraction d'atomes rapides et étude de surfaces d'isolants ioniques*. PhD thesis, Université Paris Sud 11, 2011. Thèse de doctorat dirigée par Roncin, Philippe.

[159] R. Pfandzelter. Effects of defect structures at surfaces and thin films on grazing scattering of fast ions. *Phys. Rev. B*, 57:15496–15506, Jun 1998.

[160] D.M. Danailov, R. Pfandzelter, T. Igel, H. Winter, and K. Gärtner. Test of the interatomic potential in the eV-region by glancing-angle scattering of He-atoms from Fe(0 0 1). *Applied Surface Science*, 171(1):113–119, 2001.

[161] A. Ruckhofer, S. Halbritter, H. E Lund, A.J.U. Holt, M. Bianchi, M. Bremholm, G. Benedek, P. Hofmann, W. E Ernst, and A. Tamtögl. Inelastic helium atom scattering from Sb_2Te_3 (111): phonon dispersion, focusing effects and surfing. *Physical Chemistry Chemical Physics*, 23(13):7806–7813, 2021.

[162] T Angot, M Portail, I Forbeaux, and JM Layet. Graphitization of the 6h–sic (0001) surface studied by hreels. *Surface science*, 502:81–85, 2002.

[163] A Lafosse, A Hoffman, M Bertin, D Teillet-Billy, and R Azria. Density-of-states effect on surface and lattice vibrational modes in hydrogenated polycrystalline diamond. *Physical Review B*, 73(19):195308, 2006.

[164] Nataliya Kalashnyk, Kawtar Mouhat, Jihun Oh, Jaehoon Jung, Yangchun Xie, Eric Salomon, Thierry Angot, Frédéric Dumur, Didier Gigmes, and Sylvain Clair. On-surface synthesis of aligned functional nanoribbons monitored by scanning tunnelling microscopy and vibrational spectroscopy. *Nature communications*, 8(1):1–9, 2017.

[165] G. Dolling, H. G. Smith, R. M. Nicklow, P. R. Vijayaraghavan, and M. K. Wilkinson. Lattice dynamics of lithium fluoride. *Phys. Rev.*, 168:970–979, Apr 1968.

[166] A. Politano, B. Borca, M. Minniti, J. J. Hinarejos, A. L. Vázquez de Parga, D. Farías, and R. Miranda. Helium reflectivity and debye temperature of graphene grown epitaxially on ru(0001). *Phys. Rev. B*, 84:035450, Jul 2011.

[167] Giorgio Benedek, Joseph R Manson, and Salvador Miret-Artés. The electron–phonon coupling constant for single-layer graphene on metal substrates determined from he atom scattering. *Physical Chemistry Chemical Physics*, 23(13):7575–7585, 2021.

[168] H. Hoinkes, H. Nahr, and H. Wilsch. Surface debye temperature by atomic beam scattering. *Surface Science*, 33(3):516–524, 1972.

[169] Y Ekinci and JP Toennies. Thermal expansion of the LiF (0 0 1) surface. *Surface science*, 563(1-3):127–134, 2004.

[170] A. U. MacRae and L. H. Germer. Thermal vibrations of surface atoms. *Phys. Rev. Lett.*, 8:489–490, Jun 1962.

[171] H Shichibe, Y Satake, K Watanabe, A Kinjyo, A Kunihara, Y Yamada, M Sasaki, WW Hayes, and JR Manson. Probing interlayer interactions between graphene and metal substrates by supersonic rare-gas atom scattering. *Physical Review B*, 91(15):155403, 2015.

[172] L. Frisco and M. S. Gravielle. Thermal effects on helium scattering from lif(001) at grazing incidence. *Phys. Rev. A*, 102:062821, Dec 2020.

[173] Branko Gumhalter. Single-and multiphonon atom–surface scattering in the quantum regime. *Physics Reports*, 351(1-2):1–159, 2001.

[174] J L Beeby and L Dobrzynski. The scattering of atoms from surfaces: a model. *Journal of Physics C: Solid State Physics*, 4(11):1269–1278, aug 1971.

[175] Giorgio Benedek, Joseph R. Manson, and Salvador Miret-Artés. The electron–phonon interaction of low-dimensional and multi-dimensional materials from he atom scattering. *Advanced Materials*, 32(25):2002072, 2020.

[176] Patrick Rousseau, Hocine Khemliche, Nenad Bundaleski, Pierre Soulisse, Anouchah Momeni, and Philippe Roncin. Surface analysis with grazing incidence fast atom diffraction (GIFAD). *Journal of Physics: Conference Series*, 133:012013, oct 2008.

[177] Matthew C Schram and Eric J Heller. Hitting a ball on a spring: a simple model for understanding decoherence with wavefunctions. *European Journal of Physics*, 41(2):025401, jan 2020.

[178] P. Kraus, A. Tamtögl, M. Mayrhofer-Reinhartshuber, F. Apolloner, Ch. Gösweiner, S. Miret-Artés, and W.E. Ernst. Surface structure of Bi(111) from helium atom scattering measurements. inelastic close-coupling formalism. *The Journal of Physical Chemistry C*, 119(30):17235, 2015.

[179] R Martínez-Casado, A S Sanz, and S Miret-Artés. Phonon lineshapes in atom–surface scattering. *Journal of Physics: Condensed Matter*, 22(30):304017, jul 2010.

[180] M.C. Schram and E.J. Heller. Approach to coherent interference fringes in helium-surface scattering. *Phys. Rev. A*, 98:022137, 2018.

[181] L. Frisco and M. S. Gravielle. Phonon contribution in grazing-incidence fast atom diffraction from insulator surfaces. *Phys. Rev. A*, 100:062703, Dec 2019.

[182] Peng Pan, Maxime Debiossac, and Philippe Roncin. Temperature dependence in fast-atom diffraction at surfaces. *Phys. Chem. Chem. Phys.*, 24:12319–12328, 2022.

[183] D. J. Riley, A. P. Jardine, S. Dworski, G. Alexandrowicz, P. Fouquet, J. Ellis, and W. Allison. A refined he–lif(001) potential from selective adsorption resonances measured with high-resolution helium spin-echo spectroscopy. *The Journal of Chemical Physics*, 126(10):104702, 2007.

[184] Gianfranco Vidali, G. Ihm, Hye-Young Kim, and Milton W. Cole. Potentials of physical adsorption. *Surface Science Reports*, 12(4):135 – 181, 1991.

[185] M. Debiossac, A. Zugarramurdi, P. Lunca-Popa, A. Momeni, H. Khemliche, A. G. Borisov, and P. Roncin. Transient quantum trapping of fast atoms at surfaces. *Phys. Rev. Lett.*, 112:023203, Jan 2014.

[186] Anton Tamtögl, Adrian Ruckhofer, Davide Campi, William Allison, and Wolfgang E Ernst. Atom-surface van der Waals potentials of topological insulators and semimetals from scattering measurements. *Physical Chemistry Chemical Physics*, 23(13):7637–7652, 2021.

[187] Gloria Anemone, Amjad Al Taleb, Giorgio Benedek, Andres Castellanos-Gomez, and Daniel Farías. Electron–phonon coupling constant of 2h-mos2(0001) from helium-atom scattering. *The Journal of Physical Chemistry C*, 123(6):3682–3686, 2019.

[188] H Winter. Image charge effects in ion surface scattering. *Journal of Physics: Condensed Matter*, 8(49):10149–10183, dec 1996.

[189] K. H. Rieder and N. Garcia. Energy dependence and softness of the potential for he scattering from ni(110). *Phys. Rev. Lett.*, 49:43–46, Jul 1982.

[190] A. Politano, B. Borca, M. Minniti, J. J. Hinarejos, A. L. Vázquez de Parga, D. Farías, and R. Miranda. Helium reflectivity and debye temperature of graphene grown epitaxially on ru(0001). *Phys. Rev. B*, 84:035450, Jul 2011.

[191] G. Benedek, J. P. Toennies, and R. B. Doak. Surface-phonon spectroscopy of lif(001) by inelastic scattering of he atoms: Theory and interpretation of time-of-flight spectra. *Phys. Rev. B*, 28:7277–7287, Dec 1983.

[192] S. Miret-Artès. Resonant inelastic scattering of atoms from surfaces. *Surface Science*, 339(1):205–220, 1995.

[193] G. Benedek, Salvador Miret-Artès, J. P. Toennies, and J. R. Manson. Electron–phonon coupling constant of metallic overlayers from specular he atom scattering. *The Journal of Physical Chemistry Letters*, 9(1):76–83, 2018.

[194] N. Bundaleski, P. Soulisse, A. Momeni, H. Khemliche, and P. Roncin. Decoherence in fast atom diffraction from surfaces. *NIM-B*, 269(11):1216–1220, 2011.

[195] please note that, when reproducing the fig.7 of ref.[176] in ref.[194] the data column was mistakenly replaced by the line to guide the eyes giving an impression of being perfectly aligned, the error was reproduced in ref.[18].

[196] M. del Cueto, A. S. Muzas, G. Füchsel, F. Gatti, F. Martín, and C. Díaz. Role of van der Waals forces in the diffraction of noble gases from metal surfaces. *Phys. Rev. B*, 93:060301, Feb 2016.

[197] A. Al Taleb, G. Anemone, L. Zhou, H. Guo, and D. Farías. Diffraction of CH_4 from a metal surface. *The Journal of Physical Chemistry Letters*, 10(7):1574–1580, 2019.

[198] G. Vidali and C. Hutchings. Measurement of the Debye-Waller factor for He-LiF. *Phys. Rev. B*, 37:10374–10377, Jun 1988.

[199] Y Ekinci and J.P Toennies. Thermal expansion of the lif(001) surface. *Surface Science*, 563(1):127–134, 2004.

[200] *The log-Normal distribution.* $f(x) = \frac{1}{x\sigma\sqrt{2\pi}} exp(\frac{(-\ln x-\mu)^2}{2\sigma^2})$.

[201] Jacob N. Israelachvili, editor. *Intermolecular and Surface Forces, Preface to the Third Edition*, page xvii. Academic Press, Boston, third edition edition, 2011.

[202] A. Kramida, Yu. Ralchenko, J. Reader, and NIST ASD Team. NIST Atomic Spectra Database (ver. 5.8), [Online]. Available: `https://physics.nist.gov/asd` [2021, October 28]. NIST, Gaithersburg, MD., 2020.

[203] Peng Pan et al. Measuring physisorption well depth with fast atom scattering. *Bulletin of the American Physical Society*, 2022.

[204] M. del Cueto, A. S. Muzas, M. F. Somers, G. J. Kroes, C. Díaz, and F. Martín. Exploring surface landscapes with molecules: rotationally induced diffraction of h2 on LiF(001) under fast grazing incidence conditions. *Phys. Chem. Chem. Phys.*, 19:16317–16322, 2017.

Appendix A

Surface effective stiffness derivation

Surface effective stiffness: The Effective Γ (Γ_{eff})

In the QBCM, the coupling strength between the projectile trajectory and the surface atoms is given by Γ, the logarithmic derivative of the interaction potential $\Gamma = -V'(z)/V(z)$. We know that Force along z-direction is $F_z = -\frac{\partial V}{\partial z} = -\frac{dV}{dz} = -V'(z)$. The physical meaning of Γ is Force over by potential energy at the classical turning point $\Gamma = F_z/V(z)$. It corresponds to the relative value of the derivative referred to the projectile initial energy $E_\perp$ evaluated at the turning point z_{turn}; where the coupling is most effective $V(z_{turn}) = E_\perp$.

Can we try to generalize this concept by introducing an effective stiffness? We cannot define it as the logarithmic derivative because it gives a singular value at z_{cross} where $V(z_{cross}) = 0$. This can be solved by taking into account the Beeby correction which considers that the effective energy when hitting the wall is $E_\perp + D$ where $D = V_{min}$. We therefore define $\Gamma_{eff} = -V'(z)/(V(z)+D)$. In a general potential form,

$$V_G(z) = A \cdot e^{-\Gamma_G(z-z_0)} - B \cdot e^{-\alpha\Gamma_G(z-z_0)} \tag{A.1}$$

If we set $A = D_G$ in Eq. A.1, with the known conditions:$z_{min} = z_{cross} - \frac{\ln\alpha}{\Gamma(1-\alpha)}$, $V_G(z_0) = -D_G$, $V_G(z_{cross}) = 0$, We get that $\alpha = 0.5$, then

$$V_G(z) = D_G \cdot e^{-\Gamma_G(z-z_0)} - 2D_G \cdot e^{-\frac{\Gamma_G}{2}(z-z_0)} \tag{A.2}$$

If we impose equal depth $D_G = D_M = D_{LJ}$ in Eq. A.2, and equilibrium distance, this implies that

$$V_G(z) = \begin{cases} D\cdot e^{-2\Gamma_M(z-z_0)} - 2D\cdot e^{-\Gamma_M(z-z_0)} \\ D\left[\left(\frac{z_0}{z}\right)^{12} - 2\left(\frac{z_0}{z}\right)^{6}\right] \end{cases} = \begin{cases} V_M(z),\ if\ \Gamma_G = 2\Gamma_M \\ V_{LJ}(z),\ if\ \Gamma_G = 12\frac{\ln z - \ln z_0}{z-z_0} \end{cases}$$

We need to know Γ_{eff} from the value of $V(z)$. Let us try to look for $(1-e^{\Gamma(z-z_0)/2})$
$V(z) = D\cdot e^{-\Gamma(z-z_0)} - 2D\cdot e^{-\frac{\Gamma}{2}(z-z_0)} = D\left[(e^{-\frac{\Gamma}{2}(z-z_0)}-1)^2 - 1\right]$
Then, we get

$$e^{-\frac{\Gamma}{2}(z-z_0)} - 1 = \begin{cases} \sqrt{\frac{V(z)}{D}+1},\ if\ z \le z_0 \\ -\sqrt{\frac{V(z)}{D}+1},\ if\ z > z_0 \end{cases}$$

$$\Gamma_{eff} = \frac{\Gamma}{1-e^{\Gamma(z-z_0)/2}} = \frac{\Gamma e^{-\Gamma(z-z_0)/2}}{e^{-\Gamma(z-z_0)/2}-1} = \begin{cases} \Gamma[1+(\frac{V(z)}{D}+1)^{-1/2}],\ if\ z < z_0 \\ \Gamma, \qquad\qquad if\ z = z_0 \\ \Gamma[1-(\frac{V(z)}{D}+1)^{-1/2}],\ if\ z > z_0 \end{cases} \tag{A.3}$$

We can also calculate it from the classical turning point $z_t : \Gamma_{eff}(E_\perp) = \Gamma_{eff}(z = z_t)$
$z_t - z_0 = -\frac{2}{\Gamma}\ln(1+\sqrt{\frac{E_\perp}{D}+1})$, so that V($z_t$) could simplify
$e^{\Gamma(z_t-z_0)/2} = e^{-(\ln(1+\sqrt{\frac{E_\perp}{D}+1}))} = (1+\sqrt{\frac{E_\perp}{D}+1})^{-1}$. So, in Morse potential model

$$\Gamma_{eff} = \frac{\Gamma}{1-\frac{1}{(1+\sqrt{1+\frac{E_\perp}{D}})}} = \Gamma\left[1+\left(1+\frac{E_\perp}{D}\right)^{-1/2}\right] \tag{A.4}$$

If we consider a particle approach to the surface, with kinetic energy $E_\perp$, with low kinetic energy $E_\perp \to 0$,

$$\Gamma_{eff} = \lim_{E_\perp\to 0}\Gamma\left[1+\left(1+\frac{E_\perp}{D}\right)^{-1/2}\right] = 2\Gamma \tag{A.5}$$

with high kinetic energy $E_\perp \to \infty$,

$$\Gamma_{eff} = \lim_{E_\perp\to \infty}\Gamma\left[1+\left(1+\frac{E_\perp}{D}\right)^{-1/2}\right] = \Gamma \tag{A.6}$$

This means the Γ_{eff} varies by a factor of two from high energy (low z_t, more close to the surface) to low energy (high z_t, far from the surface).

Appendix B

Wavelength calculation of atom beam

Using the de Broglie relations for wave vector and momentum for matter waves:

$$p = \hbar k \tag{B.1}$$

Due to the speed of the atom (keV) being much less than the speed of light c. The classical expression of the total energy E of a free particle of mass at rest m and momentum p is:

$$E = \frac{p^2}{2M} \quad and \quad k = \frac{\sqrt{2ME}}{\hbar} \tag{B.2}$$

Dimensional analysis: $\left[\text{Å}^{-1}\right] = \frac{\sqrt{[kg]\cdot\left[kg\cdot m^2\cdot s^{-2}\right]}}{\left[kg\cdot m^2\cdot s^{-1}\right]} \cdot 10^{-10} \cdot \frac{m}{\text{Å}}$

Then, the wave vector in the unit of Å^{-1} is, the fundamental Constants seen in Tab.B.1.

$$\begin{aligned} k\left[\text{Å}^{-1}\right] &= \frac{\sqrt{2M\cdot 1.66054\times 10^{-27}\,[kg]\cdot E\cdot 1.6022\times 10^{-22}\,[kg\cdot m^2\cdot s^{-2}]}}{1.05457\times 10^{-34}\,[kg\cdot m^2\cdot s^{-2}]}\cdot 10^{-10} \\ &= \sqrt{\frac{M[u]\cdot E[meV]}{2.09004075}} \end{aligned} \tag{B.3}$$

Where, k[Å^{-1}], M[u], and E [meV]. The kinematic relationships of an incident atoms beam linking the de Broglie wavelength λ_i (expressed in Å) wavelength is

$$\lambda_i[\text{Å}] = \frac{2\pi}{k_i[\text{Å}^{-1}]} = \frac{9.0836}{\sqrt{M[u]\cdot E_i[meV]}} \tag{B.4}$$

For the most often used ^{4}He monochromatic beam[142],

$$\lambda_i[\text{Å}] = \frac{4.5418}{\sqrt{E_i[meV]}} \tag{B.5}$$

Velocity in Classical Mechanics:

$$V_i = \sqrt{\frac{2E_i}{m}} = \sqrt{\frac{2E[eV]\cdot 1.602176634\times 10^{-19}}{m[u]\cdot 1.660539\times 10^{-27}}} = 1.38913884\times 10^4\sqrt{\frac{E[eV]}{m[u]}}(m/s) \tag{B.6}$$

Table B.1 Fundamental Physical Constants- Frequently used constants.

Quantity	Symbol	Value	Unit
Speed of light in vacuum	c	299 792 458	m s^{-1}
Planck constant	h	6.626 070 15 $\times 10^{-34}$	J Hz^{-1}
Reduced Planck constant	$\hbar$	1.054 571 817 $\times 10^{-34}$	J s
		6.582 119 569 $\times 10^{-16}$	eV s
Boltzmann constant	k	1.380 649 $\times 10^{-23}$	J K^{-1}
		8.617 333 262 $\times 10^{-5}$	eV K^{-1}
elementary charge	e	1.602 176 634 $\times 10^{-19}$	C
Bohr radius	a_0	5.291 772 109 03 $\times 10^{-11}$	m
Hartree energy	E_h	27.211386	eV
electron mass	m_e	9.109 383 7015 $\times 10^{-31}$	kg
proton mass	m_p	1.672 621 923 69 $\times 10^{-27}$	kg
neutron mass	m_n	1.674 927 498 04$\times 10^{-27}$	kg
atomic mass constant[a]	m_u	1.660 539 066 60 $\times 10^{-27}$	kg
proton-electron mass ratio	m_p/m_e	1836.152 673	
amu-electron mass ratio[b]	m_u/m_e	1822.8897707	
Standard gravity	g	9.80665	N kg^{-1}

* From NIST: http://physics.nist.gov/constants. [a] m_u=$\frac{1}{12}m(^{12}\text{C})$.

[b] In element table we usually use amu unit, we add this quantity here.

Appendix C

Application of the Distribution and Programming

Log-normal to Gaussian

If we know the log normal width w and the median scattering angle θ_m (from experimental measurement), the equivalent Gaussian variance is

$$\sigma_\theta^2 = e^{w^2}(e^{w^2}-1)\theta_m^2 \tag{C.1}$$

i.e. $\frac{\sigma_\theta}{\theta_m} = \sqrt{e^{w^2}(e^{w^2}-1)} = \sqrt{e^{2w^2}-e^{w^2}}$. (Note: the value σ_θ^2 is the variance of log-normal inelastic profile. σ_θ is the standard deviation.) We know the Taylor expansion of e^x:

$$e^x = \sum_{n=0}^{\infty} \frac{x^n}{n!} = 1 + x + \frac{x^2}{2!} + \frac{x^3}{3!} + \cdots \tag{C.2}$$

We know that the Log normal width $w \sim 0.1$, $w^2 \ll 1$. So that $e^{w^2} \approx 1 + w^2$, $e^{2w^2} \approx 1 + 2w^2$. $\sqrt{e^{2w^2}-e^{w^2}} \approx \sqrt{(1+2w^2)-(1+w^2)} = w$. In other words, we get the relation:

$$\frac{\sigma_\theta}{\theta_m} \approx w \tag{C.3}$$

So that w is simply the relative width, where θ_m is the median value, it's very close to the specular scattering angle $\theta_s = 2\theta_{in}$.

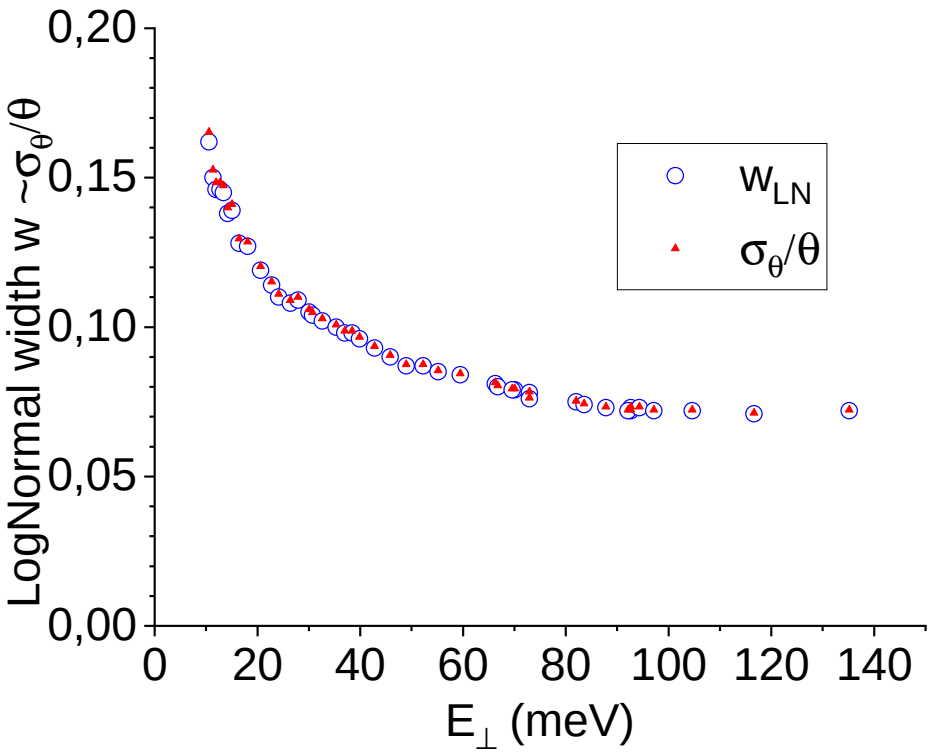

Figure C.1 Comparison of $\frac{\sigma_\theta}{\theta_s}$ and w as a function of $E_\perp$, where w_{LN} direct from experimental data fitted by LN, and $\frac{\sigma_\theta}{\theta_s}$ calculated from Eq. C.1.

Gaussian to Log-normal

If the coordinate x is well-defined (not within a constant), then if we know the standard deviation σ_x and the central value x, the equivalent log-normal width w is the positive solution of the second-order equation with $X = e^{w^2}$. $X = \frac{1+\sqrt{1+4\sigma^2/x^2}}{2}$ the final result is $w = \sqrt{\ln \frac{1+\sqrt{1+4\sigma^2/x^2}}{2}}$.

Checking the Transformation

Step 1- Using Origin, we generate with the origin, a gaussian distribution of atomic positions z having σ_z as a standard deviation (Normalized form). We calculate the scattering distribution assuming that $\theta = e^{-\Gamma.(b+z)}$ where b is a distance to the surface (an impact parameter) taken much larger than σ_z. It corresponds to a projectile initially parallel to the surface and then deflected by the unique atom. The resulting distribution is well fitted by a log-normal distribution of standard form $ln(x/x_0)/2w$ where x_0 corresponds to $2\theta_{in}$ is and with $w = \Gamma\sigma_z$.

$P(\theta_i) = \frac{A}{\theta_i} e(\frac{-\ln^2 \frac{\theta_i}{\theta_e}}{2w^2})$		$P(E_{ri}) = \frac{A}{2E_{ri}} e(\frac{-\ln^2 \frac{E_{ri}}{E_r}}{8w^2})$	
$\langle \theta_i \rangle$	$\theta_e e^{w^2/2}$	$\langle E_{ri} \rangle$	$E_r e^{2w^2}$
mode	$\theta_e e^{-w^2}$	mode	$E_r e^{-4w^2}$
$\sigma^2_{\theta i}$	$\theta_e^2 (e^{w^2} - 1) e^{w^2}$	σ^2_E	$E_r^2 (e^{4w^2} - 1) e^{4w^2}$

Table C.1 Properties of the log-normal polar scattering angular and energy loss distributions associated with an inelastic event.
$E_r = \mu E \theta_e^2$, $A = \frac{1}{w\sqrt{2\pi}}$, $w = \Gamma \sigma_z$

C.0.1 Application of Morse Potential

Numerical Examples

Case 1. Ar-LiF surface

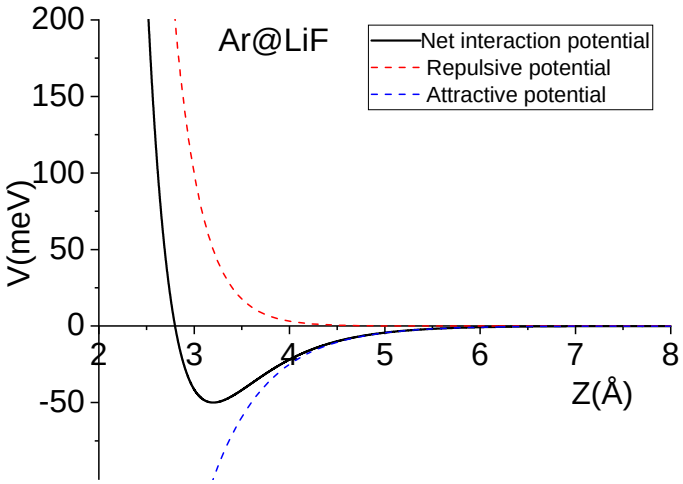

Figure C.2 Morse model with D=50meV, $\Gamma = 3.46$ Å^{-1} $(1.83\ a_0^{-1})$, $z_0 = 3.2$ Å

We want to predict angular profiles for a given projectile with mass M, energy E, and incidence angle θ_i. To start we will use the equivalent scattering model where the classical energy loss $\Delta E_{Class} = \frac{2}{3}\mu E\Gamma a\theta_i^3$ is equally shared among $N_{eff} = 6/\Gamma a\theta_i$. Each inelastic event is associated with a recoil energy $\Delta E_r = \Delta E_{Class}/N_{eff} = \frac{1}{9}\mu E\Gamma^2 a^2\theta_i^4$.

At a temperature T, we know σ_z (Eq. 11 in Ref. [71]). step one. calculated the modified incidence angle θ_i' such that $E_\perp' = E_\perp + D$. $E\sin^2\theta_i' = E\sin^2\theta_i + D$, in practice we define $\theta_i' = \arcsin\sqrt{\sin^2\theta_i + D/E}$. Second step evaluated Γ_{eff} for this value of $E_\perp'$. third step, calculate N_{eff}, ΔE_r, P_e and p_e and $p_i = 1 - p_e$. each inelastic event occurring with a probability p_i will produce an angular straggling by $w = \Gamma_{eff}\cdot\sigma_z$. The associated individual deflection is $\delta\theta = 2\theta_i'/N_{eq}$ and the variance is (standard deviation squared) is $\sigma_\theta^2 = e^{w^2}(e^{w^2} - 1)\delta\theta^2$ which is $\sigma_\theta^2 = e^{w^2}(e^{w^2} - 1)(2\theta_i'/N_{eq})^2$.

The next step is to evaluate the statistics of the single, double, triple, etc. inelastic collision. Since these are equivalent collisions, we only need to count them. The statistical weight of exactly p inelastic collisions is $f(p) = C_N^p\ p_i^p\ p_e^{N-p}$. Note that $N = N_{eq}$ and $f(p)$ is a probability and should always be lower or equal than 1, also, a safe way to evaluate the binomial coefficients is the following iterative form $C_N^p = \Pi_{i=1}^{i=p}\frac{N+1-i}{i}$. The variance associated with p inelastic events is $\sigma_p^2 = p\cdot\sigma_\theta^2 = p\cdot e^{w^2}(e^{w^2} - 1)\delta\theta^2$. the simplest strategy is to calculate the equivalent variance. $\sigma_{tot}^2 = \Sigma_{p=1}^{p=N} f(p)\sigma_p^2$. We can now transform back this variance into a log-normal width $w_{eff} = \sqrt{\ln\frac{1+\sqrt{1+4\sigma_{tot}^2/(2\theta')^2}}{2}}$

We now know the angular scattering profile after the collisions on the surface. We have to consider that the final angle is affected by the attractive well. we know the probability of leaving the wall with an angle θ_f P(θ)=$LN[2\theta_i', w_{eff}](\theta)$. However, this angle will be affected in the opposite way as in the way in, namely $E\sin^2\theta_{obs} = E\sin^2\theta_f - D$. or $E\sin^2\theta_f' = E\sin^2\theta_i - D$.

$\theta_f' = \arcsin\sqrt{\sin^2\theta_i - D/E}$ or $\theta_{obs} = \arcsin\sqrt{\sin^2\theta_f - D/E}$. We have to calculate the distribution, evaluate its mean value and variance, and compare it with the experiment.

C.0.2 Programming in CodeBlocks

Experimental Facts

We observe a narrow peak that we assume the elastic peak and a broader peak well fitted by a log-normal profile that corresponds to the inelastic collisions.

Classically, if we neglect the movement of surface atoms, then we can easily calculate the projectile trajectory z(t) or z(x) for the case of exponential potential. $V(z) = V_0 e^{-\Gamma z}$ Eq.5 [71] . Note that such a mean exponential potential is obtained 'exactly' as the mean planar potential resulting from individual screened coulomb binary potentials: $Ae^{-\Gamma z} = \int\int (A/r) e^{-\Gamma r} dxdy$, with $r = \sqrt{x^2 + y^2 + z^2}$.

Let us concentrate on a single classical binary collision. We have a single surface atom at a location $x = 0$. The projectile is coming from infinity far away. It is traveling parallel to the surface at an elevation z with a velocity $V_{//}$. If we know the binary interaction potential, we can calculate everything, $x(t)$ and $z(t)$ or $z(x)$ including the final scattering angle θ, Which is the ratio of v_z and v_x, at a large distance. If $V(z)$ is exponential, $V(z) = V_0 e^{-\Gamma z}$ then the final angle is also exponential is proportional to $e^{-\Gamma z}$ or, in other words it is equal to $\theta_0 e^{-\Gamma z}$.

Now, if we repeat the calculation 10^6 time and pick up a random position of the target within it probability distribution. We chose any value dz, and associated a probability given by the Gaussian distribution. We will built a polar scattering distribution. Since we have a formula, we do not need to calculate 10^6. For a value dz of the surface atom (its shift from equilibrium), the angle will be $\theta_0 = e^{-\Gamma(z-dz)}$. We can demonstrate that this give a log-normal distribution with $w = \Gamma_{eff} \cdot z$, this gives a variance $V_{individual} = e^{w^2}(e^{w^2} - 1)(\delta\theta)^2$.

If we have N such collisions, a possible model is that the resulting angle is the sum of individual mean scattering angles and that the resulting variance is the sum of individual variance. This defines the classical Variance $V_{Classical} = N \cdot V_{individual}$ and therefore the classical log-normal width $w_{Classical} = w_{individual}/\sqrt{N}$.

If we want to know the effect of temperature, we should calculate where each surface atom is displaced according to the Gaussian probability distribution. This is not what we do. We consider each collision individually. Each collision will be elastic with a probability $p_e \propto e^{-\frac{E_r}{\hbar\omega}}$.

In more detail, surface atoms are harmonic oscillators with a frequency ω_D, this means that they have a vibration amplitude σ_z [71].

$$\langle \sigma_z^2 \rangle = \frac{3\hbar^2}{2Mk_B T_D} \coth \frac{T_D}{2T} \tag{C.4}$$

Appendix D

Jacobian Transformation

Recall that if we have a distribution in one set of variables $\{x_1, x_2, ...x_n\}$ and want to change variables to another set $\{y_1, y_2, ...y_n\}$ the distribution in the new variables are given by

$$f(y_1, y_2, ...y_n) = \left\| \begin{matrix} \frac{\partial x_1}{\partial y_1} & \frac{\partial x_1}{\partial y_2} & \cdots & \frac{\partial x_1}{\partial y_n} \\ \frac{\partial x_2}{\partial y_1} & \frac{\partial x_2}{\partial y_2} & \cdots & \frac{\partial x_2}{\partial y_n} \\ \vdots & \vdots & \ddots & \vdots \\ \frac{\partial x_n}{\partial y_1} & \frac{\partial x_n}{\partial y_2} & \cdots & \frac{\partial x_n}{\partial y_n} \end{matrix} \right\| f(x_1, x_2, ...x_n) \tag{D.1}$$

Where the symbol $\|J\|$ denotes the absolute value of the determinant of the Jacobian J. Here, we want to transform the emitted angle θ_{emi} into the observed angle θ_{obs}, which is one-dimensional (1D) problem with the relation

$$\theta_{emi} = \sqrt{\theta_{obs}^2 + \frac{D}{E}} \;\; \Rightarrow \;\; \theta_{obs} = \sqrt{\theta_{emi}^2 - \frac{D}{E}} \tag{D.2}$$

Emitted angle is always larger than the observed angle due to refraction that reduces the angle. In other words, The observed angle is lower than the emitted angle.

Note that with the definition $0 < \theta_{emi} < \pi$. In order to obtain the joint probability density function in θ_{emi} we need to calculate the Jacobian.

$$\|J_1\| = \frac{\mathrm{d}\theta_{obs}}{\mathrm{d}\theta_{emi}} = \frac{\theta_{emi}}{\sqrt{\theta_{emi}^2 - \frac{D}{E}}} \tag{D.3}$$

The emission distribution $f(\theta_{emi})$ is given by

$$f(\theta_{emi}) = f(\theta_{obs})\,\|J_1\| \tag{D.4}$$

So that $f(\theta_{obs})$ is

$$f(\theta_{obs}) = \frac{f(\theta_{emi})}{\|J_1\|} \tag{D.5}$$

We know that due to the attractive well existing, see the Fig. 4.15 take Beeby correction into account,

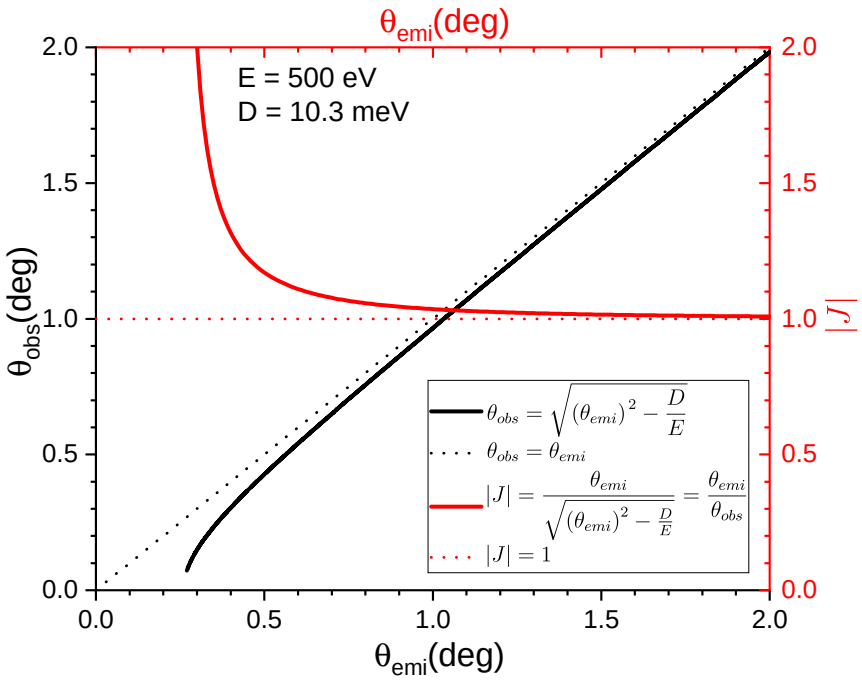

Figure D.1 E = 500eV,D = 10.3 meV

the emitted angles below 0.26° of scattered beams are not observable, see Fig. D.1.

In reality, we can not observe the emission angular distribution, but the observation angular distribution are measurable, so let's do it reversely, first of all, we assuming that we know the observation angular distribution, we know the observed angle and emitted angle has a relation as above Eq. D.2, we can

get the Jacobian:

$$\|J_2\| = \frac{\mathrm{d}\theta_{emi}}{\mathrm{d}\theta_{obs}} = \frac{\theta_{obs}}{\sqrt{\theta_{obs}^2 + \frac{D}{E}}} \tag{D.6}$$

and then take the Jacobian transform into account, So that the emission angular distribution $f(\theta_{emi})$ is

$$f(\theta_{emi}) = \frac{f(\theta_{obs})}{\|J_2\|} \tag{D.7}$$

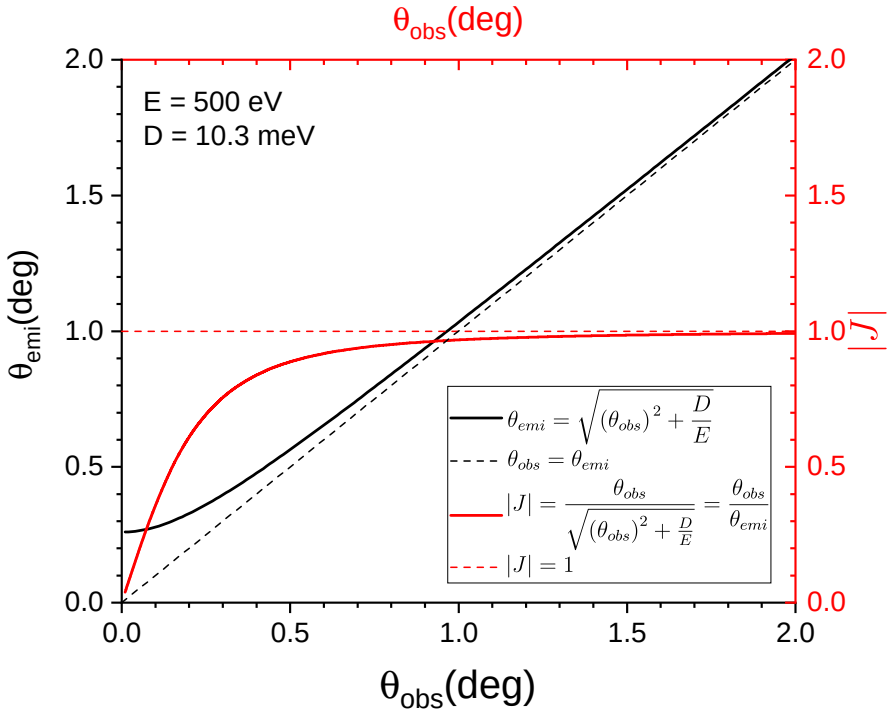

Figure D.2 E = 500 eV, D = 10.3 meV

In summary, for a typical beam primary energy, E=500 eV, and D = 10.3 meV, the Well depth of Neon on the LiF surface, whether in emission frame or observation frame, the effect of Jacobian transform at an angle below 1° is more significant than it above 1°. When the angle is larger than 1°, they are both in linear behavior with $\theta_{emi} \approx \theta_{obs}$.

Appendix E

Temperature Measurements with type N and type K thermocouples

During the first series of experiments, we could not reach temperatures below -100 °C. One of the possible reasons could have been an improper reading of negative temperatures. Therefore, we have decided to check our ability to read the negative temperature accurately with liquid nitrogen (LN2), which has a boiling point of about -195.8 °C (77K) at atmospheric pressure.

We are measuring temperature with type K thermocouples (Nickel-Chromium / Nickel-Alumel). We have quite several K-type thermocouples. All have thin wires and a single weld spot. We selected those purchased from Omega company specializes in temperature measurements. We also selected a readout via a dedicated FLUKE sensor have two inputs.

Measuring temperature with type N thermocouples (Nicrosil / Nisil): it shares the same accuracy and temperature limits as type K, See Tab.E.1, but it has better repeatability between 300 °C to 500 °C. Our manipulator and sample holder were delivered with a type K thermocouple, and we chose to keep it. We purchased a new type N thermocouple made of thin 0.3 mm wires from RS-pro (RS: 621-2192). To read the temperatures, we have purchased two low-cost universal temperature units, GM1312 able to read type N, K, J, T, or E thermocouples. the two units have been labeled GM1312-A and GM1312-B, See Fig. E.2.

Table E.1 Data sheet of different types of TC, Seebeck Coefficient (SC)

Sensor type	SC in µV/°C	Temp Range in °C	Material
N	36.256	-200 to +1300	Nisil Nicrosil
K	41.276	-200 to +1350	Alumel Chromel

We first started by positive temperature values using a simple heating tape. We put the thermocouple into LN2 and received an error message from the unit GM1312-A. After a few tests, we understood that this unit displays a temperature 5 °C below GM1312-B using the same thermocouple. Since the display is factory limited to -200 °C, the error is not too serious.

Temperature reading via a MAX31855N sensor and an Arduino

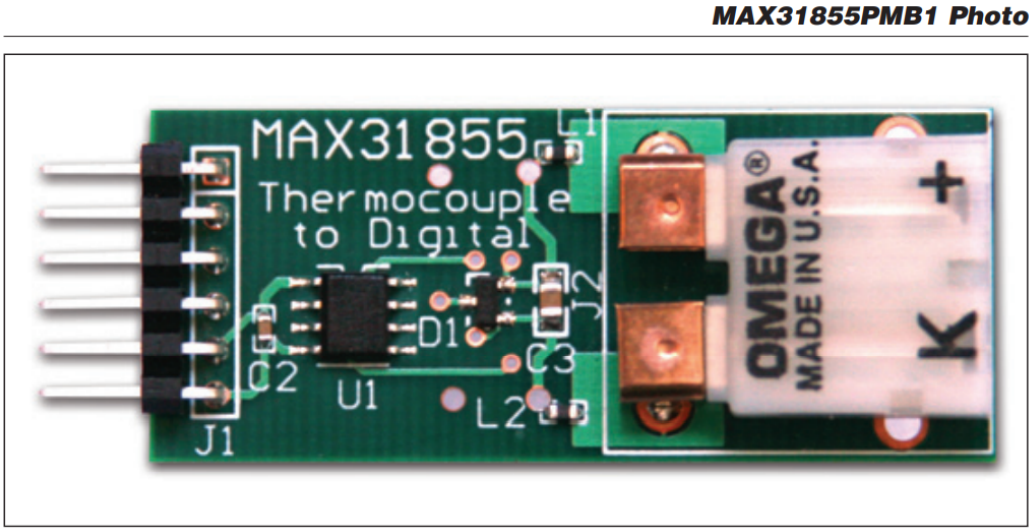

Figure E.1 A photo of MAX31855PMB1 board designed for K-type sensor. We have soldered a MAX31855N chip dedicated to type N readout.

We have a heating unit Heat-2, from the company PREVAC. Unfortunately, the unit requires a type K thermocouple, whereas our manipulator has a type N thermocouple. To use the power supply with the correct temperatures, we have tried to read the type-N TC with an Arduino and a MAX31855N temperature sensor. The idea was to use the Arduino to read the type-N TC and generate a voltage that would mimic the same temperature but as if a type-K would have generated it. We have purchased a printed circuit board equipped with a MAX31855K, and we have replaced the chip with a MAX31855N dedicated to type N. See Fig.E.1. The readout by the Arduino is performed with an SPI protocol using three wires: SELECT, DATA (MISO), and Clock. The Arduino put the SELECT signal LOW (0 volts) and emits a series of XX UP-LOW cycles of the CLOCK signal while reading the DATA signal from the MAX31855K at each rising edge of the CLOCK. The result is an integer number describing the temperature. We used a program available on the web (https://github.com/RobTillaart/MAX31855-RT). Unfortunately, the readout was much closer to that of reading a type N with a type K converter, indicating probably the use of specific resistors on the PCB. We did not proceed further in this direction. We used the HEAT-2 power supply directly with type-N but with a bit of graph indicating the temperature correspondence.

Test temperature results of LN2



Figure E.2 The temperature was measured by a type-N plug with GM1312B N mode (GM1312B-N), a type-N plug with GM1312B K mode (GM1312B-K), in addition, A type-K plug with Fluke as the reference temperature.

We measured liquid nitrogen (LN2) temperature by type-K and type-N thermocouples, we have two kinds of type N cables (RS and homemade), where the one from RS company has point-like contact, and homemade K has multiple-wire, see Fig.E.2. LN2 has a boiling point of about -195.8 °C (77K). We have four displays, fluke(type-k or J readable), GM1312-A (type N, K, J, T or E readable), GM1312-B (type N, K, J, T or E readable), and Arduino UNO with MAX31855N. In addition, GM1312 and fluke have measurement range from -200 $^{\circ}C$ to +1300 $^{\circ}C$. The LN2 temperature measurement results show in TableE.3.

In summary, the temperature results of LN2, -195.8 °C (77K), measured by fluke (type-K) and GM1312 (type-N) are comparable with a difference $\pm 3^{\circ}C$. And the LN2 temperature results have a 5 $^{\circ}C$ difference by using the same TC cable with different displays, GM1312-A and GM1312-B, i.e. A=B-5 [$^{\circ}C$]. In addition, the quality of TC cables is important. For instance, a wrong value of LN2 temperature, -245 $^{\circ}C$ from a bad type-K cable given by fluke. Our two homemade type-N (HM-N) TCs made by type-N extension cable have comparable results $\pm 1^{\circ}C$ difference inside LN2, but they give about 5$^{\circ}C$ higher values compared with the one from RS company (RS-N). We think it's due to the extension cable metal core is bigger than RS and can absorb more thermal energies from the room

Table E.2 Experimental results of type K from different readout devices

LN2 temperature measured by type K and type N ($^{\circ}C$)			
Fluke (K) (with type-K)	GM1312-A (with RS N)	GM1312-B (with homemade N)	Arduino (with N)
-193.9	-197	-190.5	-105.3 (RS)
-245 (bad K)	-196.5	-191.1	-103 (homemade)

Table E.3 Experimental results in LN2

TC/Display	Fluke (K) (K mode)	GM1312-B (N mode)	GM1312-B (K mode)
type-K	-193.3	out of range	-190.3
type-N	out of range	-196.3	-103.9

temperature environment. In temperature range from 25 $^{\circ}C$ to 150 $^{\circ}C$, HM-N and RS-N give $\sim \pm 1^{\circ}C$ difference.

E.0.1 General Description

We made a temperature measurement device by using a MAX31855N chip for N-type thermocouple and programming by Arduino.

The MAX31855PMB1 peripheral module provides the necessary hardware to interface the MAX31855N thermocouple-to-digital converter. The IC performs cold-junction compensation and digitizes the signal from a thermocouple. For every type of TC, there exist a MAX31855 variant, this module is set up to operate with a N-type thermocouple.

The working of thermocouples (TC) is based upon the Seebeck effect. Different TCs have a Seebeck Coefficient (SC) expressed in $\mu V/^{\circ}C$. See https://pdf1.alldatasheet.com/datasheet-pdf/view/415790/MAXIM/MAX31855NASA.html. This converter resolves temperatures to $0.25^{\circ}C$, allows readings from $-200^{\circ}C$ to $+1300^{\circ}C$, and for N-type thermocouples exhibits thermocouple accuracy of $\pm 2^{\circ}C$ for temperatures ranging from $-200^{\circ}C$ to $+700^{\circ}C$, and accuracy of $\pm 4^{\circ}C$ for temperatures ranging from $+700^{\circ}C$ to $+1300^{\circ}C$.

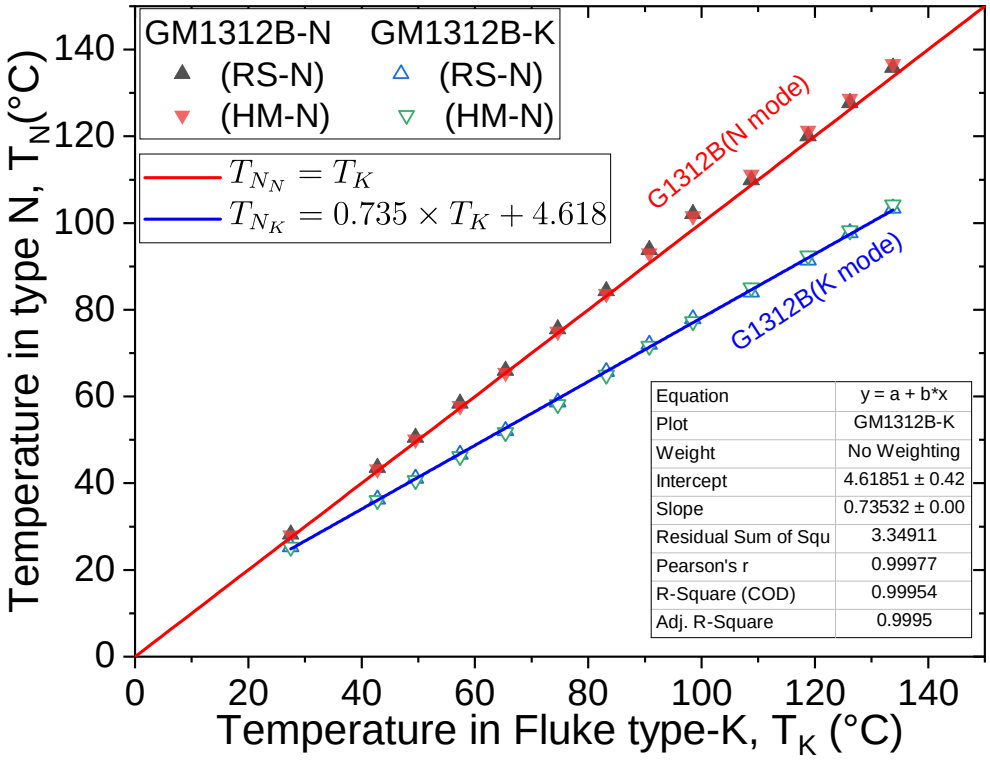

Figure E.3 Temperature is measured by a type-N plug with GM1312B N mode (GM1312B-N), a type-N plug with GM1312B K mode (GM1312B-K), in addition, A type-K plug with Fluke as the reference temperature plot as the x-axis.

The core formula to calculate the temperature is (Table E.1)

$$V_{out} = (36.256\mu V/^{\circ}C) \times (T_R - T_{internal}) \tag{E.1}$$

Hardware SPI vs. Software SPI

The hardware and software SPI pin connections are shown in Tab.E.4

Programming Codes in Arduino

The programming codes original from Rob Tillaart, Peng PAN modified the PINs according to our device connections as follows:

```
//    AUTHOR: Rob Tillaart
// VERSION: 0.1.4
// PURPOSE: thermocouple lib demo application
//     DATE: 2021-09-15
//      URL: https://github.com/RobTillaart/MAX31855_RT
```

Table E.4 Pin connections between the device and Arduino UNO

HW SPI	Arduino UNO	Notes
MISO	12	Data input
MOSI	11	not used
CLOCKPIN	13	CLK
SELECT	8	can be others too.

Table E.5 Experimental results from measuring different points of a cup of cold water

Temperature results from type K and type N ($°C$)			
$T_K(1)$	$T_K(2)$	$T_N(1)$	$T_N(2)$
1.2	1.0	6	6.25
9.1	7.9	12.5	12.5
13.6	13.4	15	15.25

```
#include "MAX31855.h"

const int doPin = 12;
const int csPin = 8;
const int clPin = 13;

MAX31855 tc(clPin, csPin, doPin);

void setup()
{
  Serial.begin(9600);
  Serial.print("Start␣max31855_demo0:␣");
  Serial.println(MAX31855_VERSION);
  Serial.println();

  tc.begin();
}

void loop()
{
```

```
  int status = tc.read();
  Serial.print("stat:\t\t");
  Serial.println(status);

  float internal = tc.getInternal();
  Serial.print("internal:\t");
  Serial.println(internal, 3);

  float temp = tc.getTemperature();
  Serial.print("temperature:\t");
  Serial.println(temp, 3);
  delay(1000);
}
```

Appendix F

Auto-control Camera by Labview

In our experiment, for instance, in an azimuthal scan (ϕ-scan), so-called atomic triangulation, we rotate the sample step by step (0.1°/step), a complete turn (360°) which will need to save images 3600 times in few hours. It's impossible to finish such a task manually. So we tried to develop an auto control system for such a task. We need to use external and start trigger mode in camera setting, and prepare a proper external trigger signal from the Labview side.It requires a hardware connection between the camera and LabVIEW (control sample manipulator) and software settings (HiPic and Labview).

a) Pin connections

No.	Signal
1	Ext. Trigger In
2	GND
3	NC
4	GND
5	Global Exposure Timing Out / Programmable Timing Out / Trigger Ready Out
6	GND

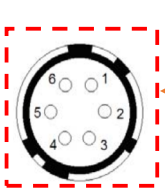

HR10A-7R-6S

b) After connecting with Labview

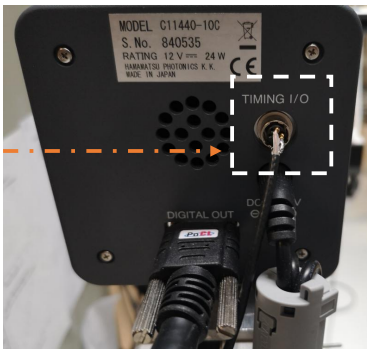

Figure F.1 We need to use connector pins No. 1, 2 (Ext. Trigger In and GND), and 4,5 (GND and Trigger ready out).

The timing logic recorded by an oscilloscope in Fig.F.2 with 1s and 10s pause. The motor action time $t_{motor} \approx 0.7$ s, the computer action time $t_{motor} \approx 40$ms. For both setting, One period time is $t_{tot} = t_{pause} + t_{motor} + t_{com}$.

PCM+sequence mode:

Camera: t_{tot}= ExposureTime*#ofExposure =100 ms*10=1 s

Labview : #ofSeq=10 ExposureTime :110 ms Motor speed:0.36°/s (~7s/° in real)

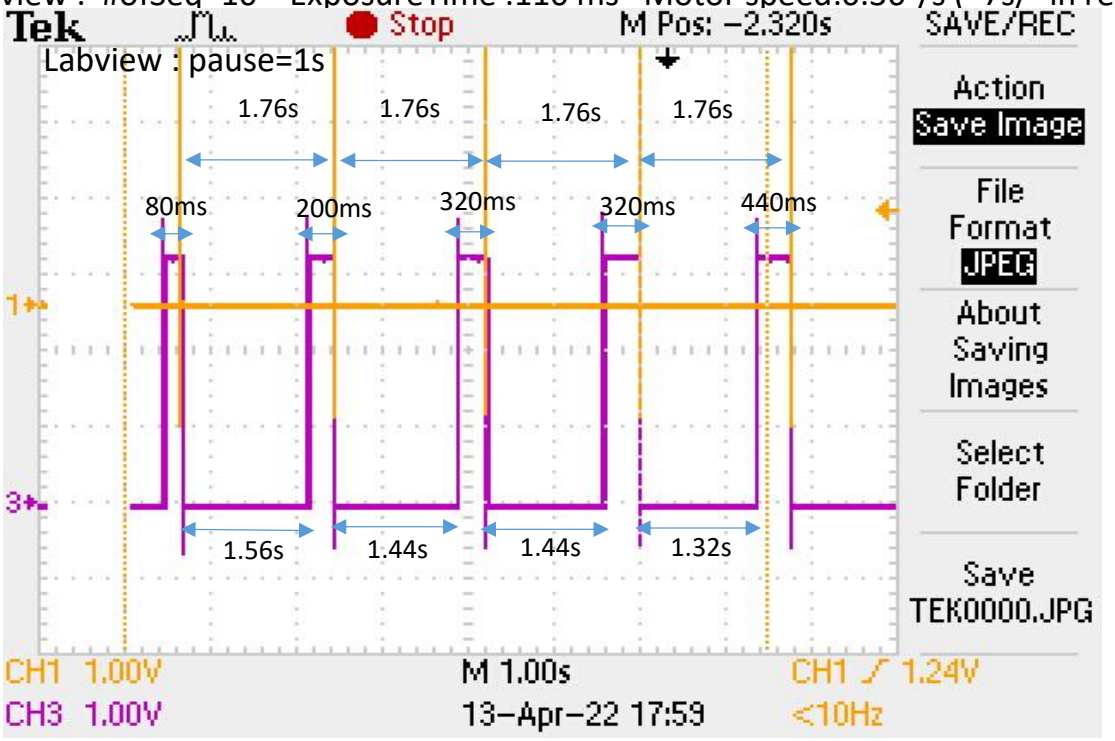

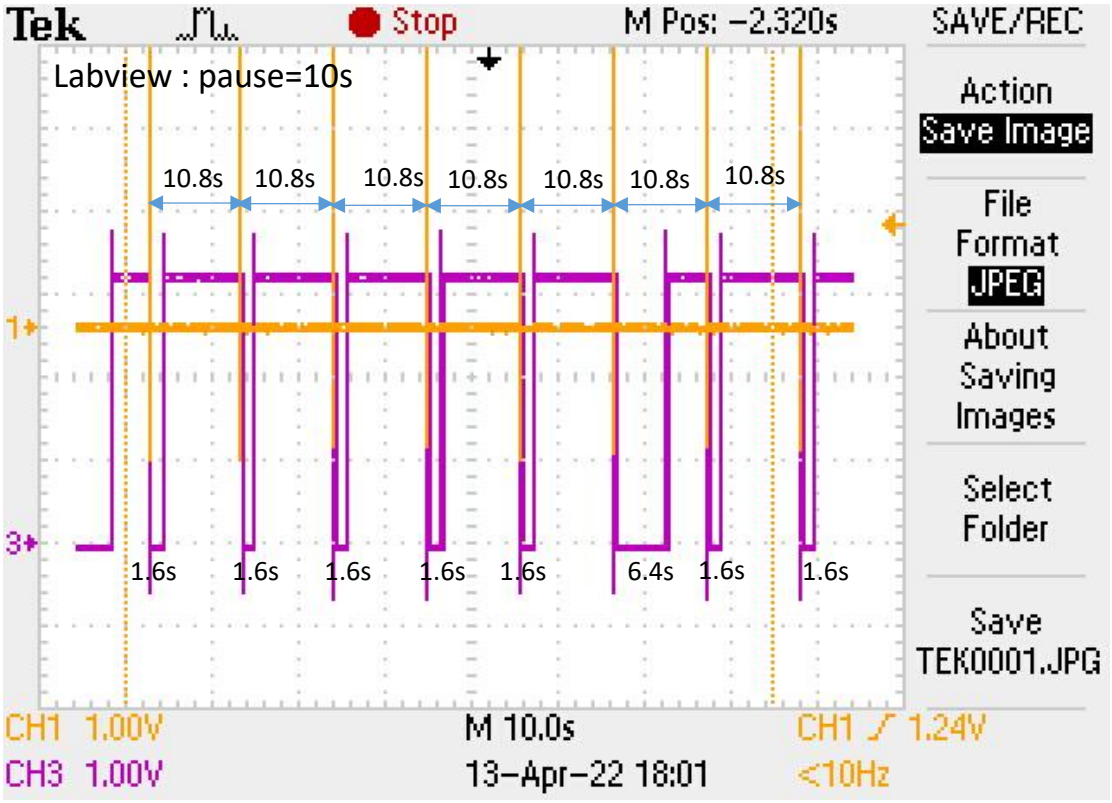

Figure F.2 Here, we use PCM and external trigger by Labview signal. Due to some nonlinear behavior of the camera, we switch to external start trigger mode, so we need one trigger at the beginning.

Appendix G

CAD design for retractable detector

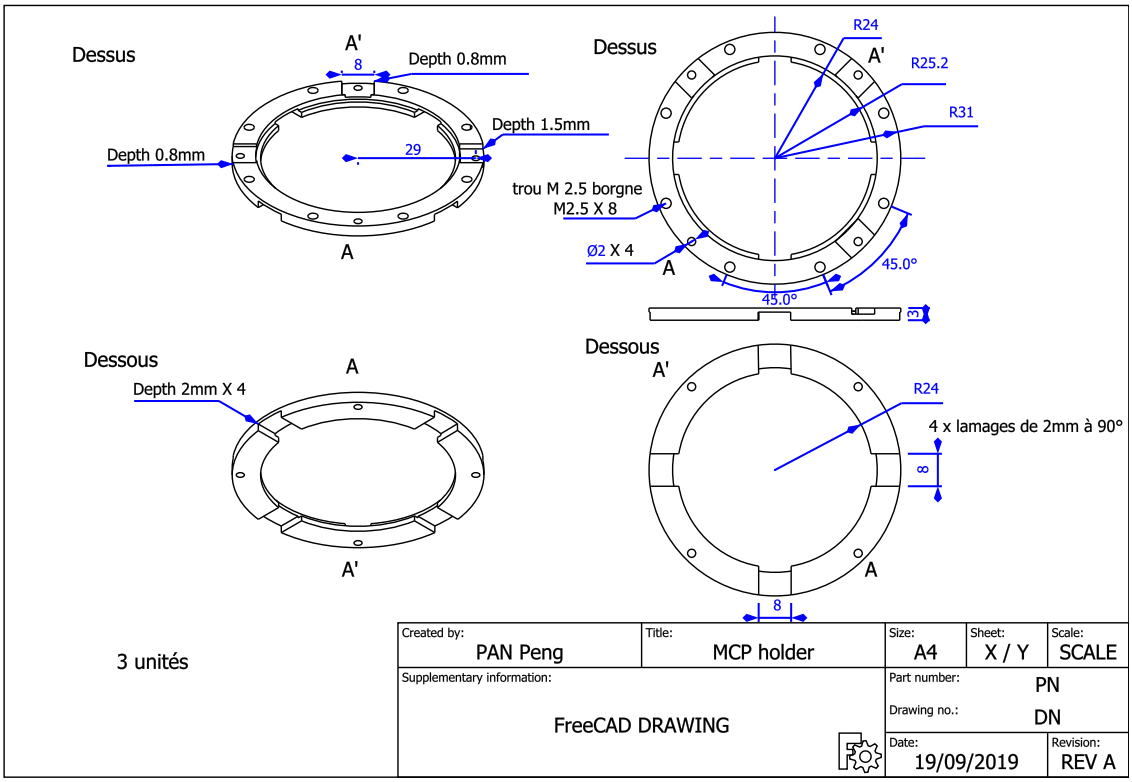

Figure G.1 MCP holder designed for detector